To the Graduate Council:
I am submitting herewith a dissertation written by Xin Wang entitled "Chemical Short Range Order in Complex Functional Ceramics." I have examined the final paper copy of this dissertation for form and content and recommend that it be accepted in partial fulfillment of the requirements for the degree of Doctor of Philosophy, with a major in Material Science & Engineering.

Katharine Page, Major Professor

We have read this dissertation
and recommend its acceptance:

Katharine Page

Veerle Keppens

Eric A. Lass

Haixuan Xu

Matthew G. Tucker

Accepted for the Council:

Carolyn R. Hodges

Vice Provost and Dean of the Graduate School

To the Graduate Council:
I am submitting herewith a dissertation written by Xin Wang entitled "Chemical Short Range Order in Complex Functional Ceramics." I have examined the final electronic copy of this dissertation for form and content and recommend that it be accepted in partial fulfillment of the requirements for the degree of Doctor of Philosophy, with a major in Material Science & Engineering.

Katharine Page, Major Professor

We have read this dissertation
and recommend its acceptance:

Katharine Page

Veerle Keppens

Eric A. Lass

Haixuan Xu

Matthew G. Tucker

Accepted for the Council:

Carolyn R. Hodges

Vice Provost and Dean of the Graduate School

(Original signatures are on file with official student records.)

Chemical Short Range Order in Complex Functional Ceramics

A Dissertation Presented for the

Doctor of Philosophy

Degree

The University of Tennessee, Knoxville

Xin Wang

May 2024

© by Xin Wang, 2024
All Rights Reserved.

To my family

Acknowledgements

I am incredibly grateful for the enriching experience of studying at the University of Tennessee, Knoxville (UTK), over the past four and a half years. The community here is truly exceptional, filled with kind-hearted and supportive individuals.

First and foremost, I am moved to express my deepest gratitude to my advisor, Prof. Katharine Page, as I attribute all my accomplishments to her unwavering guidance, encouragement, and support. Her mentorship has been instrumental in shaping my academic journey. During moments of confusion or uncertainty, she graciously provided valuable suggestions, fostering a positive conducive learning environment. I wholeheartedly believe that I wouldn't have successfully finished my Ph.D. study without her unwavering encouragement and support. I am forever indebted to her for the immeasurable impact she has had on my academic and personal growth.

I am immensely grateful for the invaluable contributions and support of my committee members, Prof. Veerle Keppens, Prof. Eric A. Lass, Prof. Haixuan Xu, and Dr. Matthew Tucker. Their collective affirmations of my work and insightful suggestions have not only enhanced my current research but have also provided invaluable guidance for my personal growth. I extend my heartfelt thanks to each of them. In particular, I would like to express my profound appreciation to Prof. Veerle Keppens for her willingness to dedicate her time and efforts to writing recommendation letters on my behalf during my job applications. I would also like to extend my sincerest thanks to Dr. Matthew Tucker for extending an invitation for

me to deliver a presentation on my neutron total scattering work at the 5^{th} National School on Total Scattering Analysis. This opportunity allowed me to share my knowledge and experiences in the field, and I truly appreciate the support provided. In addition to my committee members, I must express my sincere appreciation to Dr. Gabriel A. Geonaga, who expertly trained me on electrochemical measurements of oxygen evolution and reduction reactions. Not only did he confirm my work but he also went above and beyond by providing strong letters of recommendation on my behalf during my job applications. I am profoundly grateful for his contributions to my research and future career. I also want to express my grateful appreciation to Prof. Claudia J. Rawn, Prof. Gerd Duscher, and Dr. Michael Koehler for their assistance during my Ph.D. studies.

My Ph.D. research journey was made possible through the invaluable collaboration and contributions of Dr. Yuanpeng Zhang, Dr. Eleonora Calì, Prof. Young-Il Kim, Prof. Veerle Keppens, Dr. Brianna L. Musicó, Prof. Dustin A. Gilbert, Cameron Sparks Jorgensen, Dr. Corisa Kons, Prof. Eric A. Lass, Prof. Manashi Nath, Harish Singh, Kurt Lagemann, Dr. Palani Raja Jothi, Dr. Bo Jiang, and Dr. Peter C. Metz. I am truly indebted to their contributions, which have greatly enriched my research journey.

I am also grateful for the tremendous support I have received from our previous and present exceptional group mates, Dr. Palani Raja Jothi, Dr. Sreya Paladugu, Dr. Peter C. Metz, Dr. William R. Meier, Dr. Bo Jiang, Sean Drewry, Joshua C. Safin, Dr. Bernadette R. Cladek, Dr. Stephen C. Purdy, Kennedy Agyekum, Jade E. Holliman Jr, Lauren Miller, and Shripad Patil. They have created a strong and harmonious group dynamic, where everyone generously provides constructive suggestions that continuously motivate and uplift me. One of the most rewarding aspects of my Ph.D. journey has been mentoring talented undergraduate students, Nicole Liu and Austin J. Mattox, throughout their endeavors to tune and optimize our bifunctional oxygen evolution and reduction reaction electrocatalysts. I would also like to acknowledge the financial support provided by Prof. Page's Start-up Funding and University

of Tennessee-Oak Ridge Innovation Institute (UT-ORII) Seed Funding which has been instrumental in enabling my research endeavors and professional development activities. I am additionally grateful to the Department of Energy Basic Energy Sciences Neutron Scattering Program at Oak Ridge National Laboratory, which has provided me with rich opportunities to attend workshops, utilize mail-in neutron diffraction programs, and attend onsite experiments at the Spallation Neutron Source (SNS) Nanoscale-Ordered Materials Diffractometer (NOMAD).

In addition to the incredible individuals I have had the privilege of working with at UTK, I am deeply grateful for those who have inspired and supported me throughout my educational journey in China. Among them, one individual stands out in particular - my high school teacher, Mr. Zhao. He not only guided me in selecting a university but also instilled in me the belief that it is never too late to follow one's passion and set higher goals. His words resonated deeply within me and continue to shape my perspective. I am also indebted to the guidance and encouragement provided by Prof. Chao Zhou, one of the advisors of my master's research. He consistently encouraged me to excel in my research and provided invaluable insights to guide my research direction. Additionally, I would like to express my gratitude to Hongling Shu, my English teacher, who encouraged me when I applied to be a volunteer Chinese teacher in Benin. This experience in Benin proved to be transformative as it not only enhanced my English speaking abilities but also played a pivotal role in shaping my future. I am forever grateful for the impact this opportunity had on my life. Lastly, I want to acknowledge the special contribution of Prof. Kaifa Zhou, who was my Mechanics of Composite Materials teacher. He not only guided me through the Ph.D. application process but also provided invaluable advice on how to shape a brighter future. I am certain that I would not be the person I am today without his assistance. The memories of his support will forever hold a special place in my heart.

I am filled with profound gratitude for the unwavering support and love from my family, despite their initial concerns about me pursuing my education so far away.

My parents, Wei and Hengxi, have played a pivotal role in supporting me to come to the University of Tennessee and have provided me with tremendous support along the way. I am also immensely grateful to my grandparents, Hua and Qingchun, who have been a source of comfort and encouragement during moments of homesickness.

Finally, I thank Dr. Yuanpeng Zhang, my husband and best friend, and our daughter, Iris. I am incredibly fortunate to have the family Yuenpeng and I have created. We welcomed our precious daughter Iris during my first year of Ph.D. studies– she illuminates our lives. My husband, Yuanpeng, a dedicated Neutron Scattering Scientist at the SNS at ORNL, has been an unwavering pillar of support. His intelligence and relentless work ethic inspire me daily. He not only supports me in every aspect of our life together but also serves as a collaborator. Whenever I feel nervous or in need of encouragement, he provides solace and reassurance. Iris, our daughter brings us immeasurable joy and serves as a constant reminder of the greatest achievement in my life. Meeting my husband has profoundly shaped my trajectory, I am endlessly grateful for the abundant blessings we share and I am looking forward to the beautiful future we will make in sharing the rest of our lives.

"The fungus plant of a morning knows not the alternation of day and night. The cicada knows not the alternation of spring and autumn." – Zhuang Zhou, A Happy Excursion

"Ample preparations pave the path to victory, while insufficient preparations foretell the absence of triumph - all the more important, the absence of any preparations! (My translation)" – Sun Tzu, The Art of War

Abstract

Complex functional ceramics (CFCs) offer unique physicochemical properties across diverse promising applications in the fields of energy storage, chemical sensing, catalysis, magneto-electronics, and biomedicine, by their finely controllable chemical compositions and unique structural diversity. CFCs accommodate high levels of atomic disorder and lattice distortion, where the chemical short-range order (CSRO) of cations (or anions) decorating crystal structure sublattices may play special roles in directing structure-property trends. This work explores the relationship between CSRO and specific functional properties in three families of CFCs with combined experimental and theoretical approaches. First, our systematic exploration of local structure across the A cation size series (from the larger Ba to the smaller Ca) of $ATaO_2N$ (A=Ba, Sr, Ca) perovskite oxynitrides determines that local *cis* ordering and Ta off-centering play decreasing roles in overall lattice stability, overshadowed by the stabilizing effects of octahedral tilting. Second, we explore the sensitivity of ferrimagnetism to local cation order in spinel CFCs with compositions AFe_2O_4 (where A includes different combinations of Mg, Fe, Co, Ni, Cu, Mn, and Zn). The distinct populations of Fe and other magnetic cations on tetrahedral and octahedral sites in the materials are found to be impacted by thermal processing history and manifest in variation in the prevalence and propagation of local spin clusters, as revealed by detailed magnetometry data. Finally, we systematically examine the CSRO in a large new family of nano compositionally complex spinel oxides ACo_2O_4 (where A includes different combinations of Mn, Fe, Cu, Zn, Mg,

and Ni), prepared by an eco-friendly low-temperature soft-templating reaction route. Thermal processing history is shown to significantly influence various characteristics in the series, including phase purity, particle morphology, particle size, and the degree of cation site inversion. The inclusion or exclusion of specific cations is revealed to be an additional key design consideration. These characteristics are demonstrated to influence the family's electrocatalytic activities and magnetic properties, notably revealing promising bifunctional oxygen evolution reaction and reduction reaction performance. These efforts promote design principles and processing strategies for functional property tuning in CFCs and point to the importance and challenges of atomic structure characterization matching their complexity.

Table of Contents

1 Introduction **1**

1.1 Background and Motivation 2

1.1.1 Cation and anion substitution in Ta perovskite oxynitrides . . 2

1.1.2 High entropy ferrites made by special cation substitution . . . 3

1.1.3 Special cation substitution in nano compositionally complex cobalt oxides 5

1.1.4 Chemical short range order characterization and simulation . . 6

1.2 Objectives of the Study 14

1.3 Scope of the Dissertation 15

2 Influence of Cation Size on the Local Atomic Structure and Electronic Properties of Ta Perovskite Oxynitrides **17**

2.1 Introduction 18

2.2 Experimental and Computational Details 24

2.2.1 Materials synthesis 24

2.2.2 Neutron total scattering and data analysis 24

2.2.3 Computational details 28

2.3 Results and Discussion 28

2.3.1 Average structure from neutron diffraction 28

2.3.2 Local and intermediate range structure 33

2.3.3 Reverse Monte Carlo modeling, AIMD and DFT analysis . . . 38

2.4 Conclusion 46

3 Local Cation Order and Ferrimagnetism in Compositionally Complex Spinel Ferrites 48

3.1 Introduction 49

3.2 Methods 55

3.2.1 Materials synthesis 55

3.2.2 Magnetic measurement 57

3.2.3 Neutron total scattering 58

3.2.4 Reverse Monte Carlo modeling 60

3.3 Results and Discussion 62

3.3.1 Entropy, energy, and predicted site preference 62

3.3.2 Magnetic measurements 65

3.3.3 Distinct small magnetic clusters 67

3.3.4 Average structure 69

3.3.5 Chemical short range order 73

3.3.6 Large box reverse Monte Carlo (RMC) modeling 75

3.4 Conclusion 78

4 Phase Selectivity and Stability in Compositionally Complex Nano $(n\mathbf{A}_{1/n})\mathbf{Co_2O_4}$ 80

4.1 Introduction 81

4.2 Methods 84

4.2.1 Materials synthesis 84

4.2.2 Characterization 86

4.3 Results and Discussion 88

4.3.1 Composition and heat treatment effects 88

4.3.2 Case study: $(Mg_{0.2}Mn_{0.2}Fe_{0.2}Cu_{0.2}Zn_{0.2})Co_2O_4$ (5C1) 94

4.3.3 Line profile analysis as a screening tool 100

4.4 Conclusion 104

5 Excellent Bifunctional Oxygen Evolution and Reduction Electrocatalysts ($5A_{1/5}$)Co_2O_4 and their Tunability **106**

5.1 Introduction . . . 107

5.2 Experimental . . . 113

5.2.1 Material synthesis . . . 113

5.2.2 Structure and morphology characterization . . . 115

5.2.3 Electrochemical characterization . . . 116

5.3 Results and Discussion . . . 117

5.3.1 Bifunctional OER and ORR electrocatalysts . . . 117

5.3.2 Stability of MnFeNiCuZn-noMg-600 °C . . . 123

5.3.3 Tunability through cation selection and post-annealing . . . 127

5.4 Conclusion . . . 134

6 Impact of Thermal Annealing on Magnetic Properties in Nano Compositionally Complex Spinel Cobaltite - ($Mg_{0.2}Mn_{0.2}Fe_{0.2}Cu_{0.2}Zn_{0.2}$)$Co_2O_4$ **135**

6.1 Introduction . . . 136

6.2 Methods . . . 140

6.2.1 Materials synthesis . . . 140

6.2.2 Characterization . . . 140

6.2.3 Magnetic measurements . . . 141

6.2.4 Neutron total scattering measurements . . . 142

6.2.5 Rietveld and PDF refinement . . . 143

6.3 Results and Discussion . . . 144

6.3.1 Phase purity and nanoscale heterogeneity . . . 144

6.3.2 Magnetic phase segregation . . . 148

6.3.3 Average and local structure . . . 153

6.4 Conclusion . . . 157

7 Conclusions **161**

Bibliography **165**

Appendix **206**

A Supplemental Information for Chapter 2 207

B Supplemental Information for Chapter 3 220

C Supplemental Information for Chapter 4 231

D Supplemental Information for Chapter 5 234

E Supplemental Information for Chapter 6 241

Vita **248**

List of Tables

1.1 A brief summary of several merits and limitations of different local structure characterization techniques (Tech), including neutron and X-ray total scattering (NTS and XTS, respectively), Nuclear magnetic resonance spectroscopy (NMR), Extended X-ray Absorption Fine Structure (EXAFS[71]), X-ray absorption near-edge structure (XANES), Raman spectroscopy (RS), and Mössbauer spectroscopy (MS). 12

2.1 Average structures, tolerance factors and tilt systems for $ATaO_2N$ (A= Ba, Sr, Ca). 20

2.2 Lattice parameters, atomic positions, and isotropic atomic displacement parameters resulting from Rietveld refinement of neutron powder diffraction (NPD) data for $SrTaO_2N$ and $CaTaO_2N$ with anion site fixed 50/50-75/25 model and disordered O/N anion model, respectively. 30

2.3 Refined lattice parameters, atomic positions, atomic displacement parameters and fixed O/N fractional site occupancies from $SrTaO_2N$ and $CaTaO_2N$ local PDF refinements (from 1.5 to 6 Å) with anion site fixed 50/50-75/25 model and disordered O/N anion model, respectively. 35

2.4 Refined lattice parameters, atomic positions, atomic displacement parameters and fixed O/N fractional site occupancies from $SrTaO_2N$ and $CaTaO_2N$ PDF refinements over an intermediate range from 6 to 50 Å with anion site fixed 50/50-75/25 model and disordered O/N anion model, respectively. 35

3.1 A summary of powder sample high entropy spinel ferrite compositions appearing in the literature, including year reported (Year), chemical composition (Chem.), magnetic ground state (GS) (where FIM denotes ferrimagnetic), and the reference (Ref.). 53

3.2 High entropy spinels in this study, with firing temperatures and number of hours noted. Sample names correspond with those reported by Musicó *et al.*[157]. 56

3.3 Parameters for the best fitting model results among the normal, inverse and random solution F$d\bar{3}m$ spinel models applied for F1, F3, F4, and F5 Rietveld refinements. The table includes the refined magnetic moment (M), lattice parameter (a), oxygen position (u), isotropic atomic displacement parameters (U_{iso}) for the 8b, 16c, and 32e sites, and the resulting refinement goodness-of-fit, R_{wp}. 72

4.1 Compositions $(n\mathrm{A}_{1/n})\mathrm{Co}_2\mathrm{O}_4$ with $n \geq 5$ explored within this work, separated into groups (see main text for details). Samples are observed after calcination (*as formed* 400°C, AF4) and following post-annealing heat treatment (*post-treatment* 600°C, PT6, etc.). Check marks indicate the presence of specific elements in each composition. Conditions resulting in X-ray pure phases are colored green and conditions resulting in phase mixtures are colored purple. Impurities are coded: CuO ("c"); rock salt ("r"); secondary spinel ("s"); and $\mathrm{CoCl}_2{\cdot}2\mathrm{H}_2\mathrm{O}$ ("h"). 87

5.1 The target compositions with formula $(5A_{1/5})Co_2O_4$ involved in this work. Samples are obtained after calcination at 400 °C and following post-annealing heat treatment at 600 °C, 800 °C and 1000 °C. Conditions resulting in X-ray pure phases are labeled with check marks and conditions resulting in phase mixtures are labeled with impurity abbreviations. Impurities are coded: $CoCl_2{\cdot}2H_2O$ ("h"); tenorite CuO ("c"); rock salt ("r"); and secondary spinel ("s"). 114

5.2 The OER (overpotential η mV @ 10 mA cm^{-2}, Tafel slope (mV dec^{-1}), and ECSA (cm^2)) and ORR (onset potential E_0 (V), number of electrons n @ 0.3 V, and % H_2O_2) catalytic activities of the electrocatalysts involved in this work compared to the values from selected benchmark catalysts. 120

S2.1 Lattice parameters, occupancies and isotropic atomic displacement parameters and R_{wp} values resulting from Rietveld refinement of neutron powder diffraction (NPD) data for $SrTaO_2N$ and $CaTaO_2N$ with disordered, occupancy (occ.) refined, fixed *trans* and fixed 50/50-75/25 models. 208

S2.2 Anisotropic atomic displacement parameters and R_{wp} values resulting from Rietveld refinement of neutron powder diffraction (NPD) data for $SrTaO_2N$ and $CaTaO_2N$ with disordered anisotropic and fixed 50/50-75/25 anisotropic models. 209

S2.3 Total number (No.) of refined parameters, increased number (No.) of refined parameters comparing with the refinements which used average structures and R_{wp} values in the range from 1.5 to 6 Å PDF refinements for $SrTaO_2N$ and $CaTaO_2N$ with average structures and sub-lattice structures. 210

S2.4 Experimental[256] and Calculated (GGA+U) band gaps of most stable *cis* and *trans* configurations of $BaTaO_2N$, $SrTaO_2N$ and $CaTaO_2N$. . 217

S2.5 Neutron powder crystallographic data and refinement details for $SrTaO_2N$ and $CaTaO_2N$ with average models (fixed 50/50-75/25 model for $SrTaO_2N$ and disordered model for $CaTaO_2N$). 220

S3.1 Parameters for all the fitting model results of the normal, inverse and random solution F$d\bar{3}m$ spinel models applied for F1 Rietveld refinements. The table includes the refined magnetic moment (M), lattice parameter (a), oxygen position (u), isotropic atomic displacement parameters (U_{iso}) for the 8b, 16c, and 32e sites, and the resulting refinement goodness-of-fit, R_{wp}. 221

S3.2 Parameters for all the fitting model results of the normal, inverse and random solution F$d\bar{3}m$ spinel models applied for F3 Rietveld refinements. The table includes the refined magnetic moment (M), lattice parameter (a), oxygen position (u), isotropic atomic displacement parameters (U_{iso}) for the 8b, 16c, and 32e sites, and the resulting refinement goodness-of-fit, R_{wp}. 223

S3.3 Parameters for all the fitting model results of the normal, inverse and random solution F$d\bar{3}m$ spinel models applied for F4 Rietveld refinements. The table includes the refined magnetic moment (M), lattice parameter (a), oxygen position (u), isotropic atomic displacement parameters (U_{iso}) for the 8b, 16c, and 32e sites, and the resulting refinement goodness-of-fit, R_{wp}. 223

S3.4 Parameters for all the fitting model results of the normal, inverse and random solution F$d\bar{3}m$ spinel models applied for F5 Rietveld refinements. The table includes the refined magnetic moment (M), lattice parameter (a), oxygen position (u), isotropic atomic displacement parameters (U_{iso}) for the 8b, 16c, and 32e sites, and the resulting refinement goodness-of-fit, R_{wp}. 224

S3.5 Overall average atomic displacement parameters (ADPs) for tetrahedral and octahedral sites for F1 and F3, extracted from RMC configurations when a +2 valence state is assumed for all A cations in the AFe_2O_4 compositional series, and a +3 valence state is assumed for the remaining two Fe cations. "Tetra" designates the tetrahedral site, "Octa" the octahedral site, "Oxy" the oxygen site, "I" an inverse model and "R" a random model. ADPs are given in Å. 224

S3.6 Overall average atomic displacement parameters (ADPs) for tetrahedral and octahedral sites for F4 and F5, extracted from RMC configurations when a +2 valence state is assumed for all A cations in the AFe_2O_4 compositional series, and a +3 valence state is assumed for the remaining two Fe cations. "Tetra" designates the tetrahedral site, "Octa" the octahedral site, "Oxy" the oxygen site, "I" an inverse model and "R" a random model. ADPs are given in Å. 229

S3.7 The average magnetic moments (in μ_B) on tetrahedral and octahedral sites from RMC simulations assuming a +2 valence state for all A cations in the AFe_2O_4 compositional series, and a +3 valence state for the remaining two Fe cations. The net magnetic moment is calculated in the following way, $Net\ moment = (abs(2 \times MM_{Octa}) - abs(MM_{Tetra}))/3$. "Tetra" is for tetrahedral site, "Octa" for octahedral site, "MM" for magnetic moment, "I" for inverse model, "R" for random model and "abs" for absolute value. 229

S4.1 Compositions $(nA_{1/n})Co_2O_4$ with n from 1 to 4 explored within this work. Samples are observed after calcination (as-formed 400 °C, AF4) and following post-annealing heat treatment (post-treatment 600 °C, PT6, etc.). Check marks indicate the presence of a specific element in that composition. Conditions resulting in X-ray pure phases are colored green and conditions resulting in phase mixtures are colored purple. Impurities are coded: ZnO ("z"); CuO ("c"); Co ("Co"); rock salt ("r"); secondary spinel ("s"); and $CoCl_2{\cdot}2H_2O$ ("h"). 231

S5.1 The information of substrate and drop-casted mass (mass loading, ML) of OER and ORR catalytic measurements for the reference cited in Figure 1. The substrates are coded: carbon cloth ("CC"); glassy carbon ("GC"); nickel foam ("NF");pyrolytic graphite carbon ("PGC"); carbon fiber paper ("CFP"). 238

S5.2 The C_{DL} comparison for the 600 °C sample series. 240

S5.3 The R_{wp}, median of the lattice parameter (a_m, Å), crystallite size (CS), cation site inversion parameter (γ), and atomic positions of oxygen ($x = y = z = u$) of the Rietveld refinement with "continuous lattice" model[245] for the 600 °C sample series. The isotropic atomic displacement parameters of the tetrahedral site ($U_{iso,t}$, Å^2), octahedral site ($U_{iso,o}$, Å^2) and oxygen ($U_{iso,O}$, Å^2) were fixed as 0.005, 0.005, and 0.010 Å^2, respectively, for all compositions. 240

S6.1 Rietveld and PDF refinement parameters for the best fitting model results applied for the sample calcined at 400°C and the samples post-annealed at 600°C, 800°C, and 1000°C. The table includes the average scattering length for each site ($\langle b \rangle$), lattice parameter (a), phase percentage (p), oxygen position (u), isotropic atomic displacement parameters (B_{iso}) for the tetrahedral (8b), octahedral (16c), and oxygen (32e) sites, and the resulting refinement goodness-of-fit, R_{wp}. For the Rietveld refinement, the crystalline size (CZ), sample microstrain (MS), and refined magnetic moment (M) are also summarized. 246

List of Figures

1.1 (a) X-ray PDF and (b) neutron PDF comparison of three different samples with the composition $(Mn_{0.2}Fe_{0.2}Cu_{0.2}Zn_{0.2}Mg_{0.2})Co_2O_4$, each synthesized with a different weight percentage of polymer reactant and calcined at 400°C. Neutrons reveal local structure variations that are not distinguished with X-rays. 10

2.1 Average crystal structures of $ATaO_2N$ (A= Ba, Sr, Ca): (a) $BaTaO_2N$, $Pm\bar{3}m$, viewed almost along a-axis; (b) $SrTaO_2N$, $I4/mcm$, viewed almost along a-axis; and (c) $CaTaO_2N$, $Pnma$, viewed almost along c-axis. $Ta(O/N)_6$ octahedra are shown as yellow. Ba, Sr, and Ca are shown as brown, green, and mauve spheres, respectively. The blue spheres represent Ta, and the orange-purple mixed spheres represent the 2/3 and 1/3 partially O and N occupied anion sites. 20

2.2 (a) $SrTaO_2N$ and (b) $CaTaO_2N$ Rietveld refinement results for the NPD data (119° detector bank) with anion site fixed 50/50-75/25 and disordered O/N anion models, respectively. Data are given as green ($SrTaO_2N$) and mauve ($CaTaO_2N$) circles and the solid lines through the data are fits using the $I4/mcm$ and *Pnma* structures, respectively. The black difference curves are displayed below the data and fits. Phase markers are displayed as vertical lines between the fit and difference curves (red markers correspond to the hkl indices of the refined perovskite phase, while blue markers correspond to those of a parasitic vanadium phase resulting from incomplete container scattering subtraction). The vanadium phase markers are shown for reference only; the phase was not included in the Rietveld refinements. 29

2.3 Real space PDF refinement results for $SrTaO_2N$ using the $I4/mcm$ fixed 50/50-75/25 model, displaying: (a) 1.5 to 6 Å local PDF fit and (b) 6 to 50 Å intermediate length-scale PDF fit; and for $CaTaO_2N$ using the *Pnma* disordered anion occupancy model, displaying (c) 1.5 to 6 Å local PDF fit and (d) 6 to 50 Å intermediate length-scale PDF fit. Experimental PDF data are shown as black circles for both $SrTaO_2N$ and $CaTaO_2N$. The fits are shown as green and mauve lines through the data for $SrTaO_2N$ and $CaTaO_2N$, respectively. The black difference curves are shown at the bottom of each panel and the fit quality values are noted at the top right of each sub figure for each fitted region. . . 34

2.4 Real space PDF refinement results for $SrTaO_2N$ sub-space groups with *trans* N ordering ((a) $I\bar{4}2m$, (b) $I422$, (c) $I4m$, (d) $I\bar{4}$, and (e) $Ibam$) and *cis* N ordering (f) $Ima2$, with corresponding structures displayed beside them. Refinement results for $CaTaO_2N$, derived from the $Pnma$ parent structure, include sub-space group models with *trans* ordering ((g) $P2_1c$, (h) $P2_1m$), as well as sub-space groups with *cis* N ordering (including (i) $Pmn2_1$ (j) $P2_12_12_1$, (k) $Pmc2_1$, and (l) $Pna2_1$). Green and mauve circles correspond to the experimental PDF data for $SrTaO_2N$ and $CaTaO_2N$, respectively. Model fits are shown as black lines through the data. The difference curves are shown at the bottom of each panel and the fit quality values are noted at the top right (The best results for $SrTaO_2N$ and $CaTaO_2N$ are (f) and (i), respectively). 37

2.5 *cis* N ordered supercell structures (left) used in constructing RMC simulations and resulting point clouds of RMC simulations (right) of (a) $BaTaO_2N$, orthogonal to {001} (b) $SrTaO_2N$, orthogonal to {001} and (c) $CaTaO_2N$, orthogonal to $\{10\bar{1}\}$. The blue spheres represent Ta, the small orange spheres O, and the small purple spheres N. Ba, Sr, and Ca atoms are shown as brown, green, and mauve spheres, respectively. 40

2.6 The $ATaO_2N$ (A=Ba, Sr, Ca) partial pair distribution functions (pPDF) from RMCProfile (RMC) for (a) A-O, (b) A-N, (c) Ta_A-O, (d) Ta_A-N and radial distribution functions (RDF) from AIMD simulations for (e) A-O, (f) A-N, (g) Ta_A-O, and (h) Ta_A-N. The supercells used in RMC and AIMD feature *cis* N in TaO_4N_2 octahedra with '90-deg' configuration at axial N as proposed by Hinuma[79]. $BaTaO_2N$, $SrTaO_2N$, and $CaTaO_2N$ correlations are depicted in each panel in darkest (Ba) to lightest (Ca) hues, respectively). 41

2.7 (a,b) Illustration of the *cis* and *trans* N ordered configurations of $ATaO_2N$ (M=Ba, Sr, Ca) examined with DFT analysis. $P4/mmm$ and $Pbmm\_Ta_{fix}$ models entail metrically cubic symmetry (equivalent to $Pm\bar{3}m$ lattice, with *cis* and *trans* sublattice order lowering the symmetry, respectively). For the energetics of the cubic $P4/mmm$ and $Pbmm\_Ta_{fix}$ structures, only the structure volume and shape were allowed to relax (atomic positions were fixed). In the $P4mm\_O_{fix}$ and $Pbmm$ variants, anion positions are fixed, but Ta is allowed to displace, according to the $P4mm$ and $Pbmm$ lattice symmetry. (c,d) Relative energies for relaxed *cis* and *trans* configurations of $BaTaO_2N$, $SrTaO_2N$ and $CaTaO_2N$ with corresponding ordered phase indicated. The calculated energy level is shown relative to the energy of the $P4/mmm$ structure, which has the highest energy. 44

3.1 Schematic view of (a) the inverse spinel unit cell with blue tetrahedra (A-sites) and orange octahedra (B-sites). Cations on the octahedral site are drawn half blue and half orange to represent site mixing. Oxygen atoms sitting on polyhedral vertices are omitted for clarity. (b) The [0 0 1] projection of the cation substructure in the unit cell (black square) overlaid with the unit cell of the magnetic structure (blue frame). (c) The room-temperature zero-field magnetic spin structure composed of magnetic moments on the tetrahetral site (blue vectors pointing down) and octahedral site (orange vectors pointing up). . . . 51

3.2 (a) The CFSE calculations for F1 (□), F3 (★), F4 (×), and F5 (◊) with normal spinel, random solution, and inverse spinel structure models assumed (with a +2 valence state for all A cations in the AFe_2O_4 compositional series, and a +3 valence state for the remaining two Fe cations). (b) The calculated S_{config} of AFe_2O_4 high entropy spinels with the degree of inversion (γ) changing from 0 to 1 and the assumption that there are N (from 1 to 8, Fe is not included) cations occupying the A-site (the γ values 0, 2/3, and 1 were labeled according to the corresponding normal, random solution, and inverse spinel structure configurations). 64

3.3 The comparison of field-cooled (FC), zero-field-cooled (ZFC), and zero-field-warming (FCW) for all ferrite samples measured from 2K to 400K with an applied field of 10 mT: (a) F1, (b) F3, (c) F4, and (d) F5. The legend in (c) applies to all subplots. The insets are displayed in order to emphasize the cross-over and hysteresis in the FC and FCW curves. 66

3.4 The comparison of magnetic hysteresis loop data for ferrite compositions (F1,F3,F4,F5) measured at 300K with a ± 0.5 T range for (a) materials in this paper, measured with a 10 mT cooling; and (b) materials studied by Musicó et al., measured with a 100 mT cooling. The legend in (b) applies to both subplots. 66

3.5 The comparison of FORC measurements at 2 K and 300 K for sample F1 (a,b), F3 (c.d), F4 (e,f), and F5 (g,h), respectively. The directions of H_B and H_C are plotted for clarification and the scale bar indicates the rate at which the magnetic reversal speed changes for different H_R. 68

3.6 (a) The comparison of neutron Bragg data (31° detector bank) from F1 (orange line), F3 (purple line), F4 (red line), and F5 (green line) samples. Several hkl peaks featuring ferrimagnetic contributions are labeled. Best-fit Reitveld refinement of (a) F1 data using inverse spinel and ferrimagnetic spin order model and (c) F4 data using random solution spinel and ferrimagnetic spin order model. In (b) and (c) data are shown as black "x"s, fits are shown as solid orange lines, and difference curves fall below the data and fits in black lines. The blue and green solid curves displayed below the refinement results display the magnetic and nuclear contributions to the fits, respectively. 70

3.7 (a) The PDF data comparison of F1 (orange line), F3 (purple line), F4 (red line), F5 (green line). The 6 peaks (1, 5, 9, 12, 15, 17) highlighted with magenta dashed lines correspond to A-O pairs. The 4 peaks (2, 6, 10, 13) indicated with green dashed lines arise from A_{oct}-A_{oct} and O-O pair correlations. The 3 peaks (3, 11, 16) contributed by A_{oct}-A_{tet},A_{tet}-A_{tet} and A-O are identified in sky blue dashed lines. The peak (4) around 4 Å highlighted in a red dashed line corresponds to an O-O correlation. The combination of A_{oct}-A_{tet} and A_{tet}-O pair correlations contribute the 2 peaks (7, 14) indicated by orange dashed lines. The peak (8) highlighted by a pink dashed line arises from A_{oct}-A_{oct},A_{tet}-A_{tet} and A-O pair correlations. A comparison of the PDF refinements for (b) F1 sample data and (c) F4 sample data using different structure models (random, inverse, and normal spinel ferrite models). PDF data for F1 and F4 samples are shown in orange and red dots, respectively. The blue, lemon green and sky blue solid curves present fits to the data completed with the random solution spinel structure, inverse spinel structure and normal spinel structure model, respectively. The fit difference curves displayed below the data and fits are represented as black solid curves. 74

3.8 The proportion of magnetic moment vectors with projection on the XY plane for samples F1, F3, F4 and F5 falling into specified radii, relative to atoms of (a) tetrahedral (Tetra) and (b) octahedral (Octa) sites that the corresponding magnetic moments belong to. Results presented correspond to an inverse spinel structure model for F1 and F3 sample data and a random solution spinel model for F4 and F5 sample data. It is noted that similar results are obtained when the alternate models are used (inverse spinel model for F1 and F3 sample data and random solution spinel model for F4 and F5 samples). . . . 77

3.9 The HZ statistic for the distribution of (a) oxygen atom (O) coordinates and magnetic moment vectors (M) on (b) tetrahedral sites (Tetra) and (c) octahedral sites (Octa), for F1, F3, F4, and F5 samples. The horizontal dashed lines indicate a Gaussian distribution. 77

4.1 Schematic diagram of the LTST method used to synthesize a large family of compositionally complex cobalt-based nano spinels, $(n\mathrm{A}_{1/n})\mathrm{Co}_2\mathrm{O}_4$. First, a solution of inorganic precursors, structuring agent, and solvent is stirred for 30 mins. A wet gel is obtained after 24 h evaporation and a black powder is formed after calcination at 400 °C for 5 h (the *as-formed* (AF) sample). Finally, a spinel phase structure with 8 tetrahedral (green) sites and 16 octahedral (red) sites in the unit cell is identified by XRD (oxygen atoms are not shown in the image). . . 85

4.2 Spinel tolerance factore (τ) (top panels) and average ionic radii of tetrahedral site cations (bottom panels), assuming a normal spinel configuration, for (a) AF4 and PT6 samples, and (b) PT8 samples for each composition. Vertical lines in the bottom panels represent the calculated standard deviation of participating radii. The red dotted lines indicate the presence of "Mg" in a sample while black dotted lines indicate the presence of all other elements in the sample. Markers colored green indicate samples that appear X-ray phase pure. See Table 4.1 for sample compositions and further detail. 89

4.3 Phase formation energy, ΔH_f°, for possible binary oxide impurities resulting from the inclusion of single cations with different oxidation states. 93

4.4 (a) Logarithmic powder diffraction intensities collected step-wise in 11 °C intervals to 1100 °C, over an isothermal dwell, and free-cooling to room temperature. (b) Thermal analysis signals collected over a heating and cooling cycle with 300 °C/h ramp rate: temperature (blue —), weight change (green · · ·), and heat flow (red - - -). 95

4.5 STEM/EDS elemental mapping of *5C1* AF4, PT6, PT8, and PT10 samples. Color maps indicate heterogeneous cation distributions of Mg, Mn and Fe for certain grains in the AF4 sample. In PT6 and PT8 samples, the cation enrichments fade (samples feature more homogeneous cation distributions). In the PT10 sample, Mn and Fe atoms are found in separate grains from Mg, and a modest enrichment of Co is observed in those grains with Mn and Fe. Cu and Zn remain distributed throughout all particles. 97

4.6 Rietveld refinements for *5C1* AF4 X-ray diffraction data with (a) crystalline grain size broadening (1 phase, no strain, $R_{wp} = 3.870\%$), (b) size and strain broadening (1 phase, refined strain, $R_{wp} = 3.869\%$), (c) two spinel phase model (phase fraction and cubic lattice parameter refined, no strain, $R_{wp} = 2.171\%$), and (d) CL phase model ($R_{wp} = 2.113\%$) applied. The XRD patterns were analyzed with the Rietveld method as embodied in the TOPAS-V7[36] program. 99

4.7 Tetrahedral site ionic radius (r_A) distribution extracted from CL Rietveld refinement results for $(n\mathrm{A}_{1/n})\mathrm{Co}_2\mathrm{O}_4$ ($n \geq 5$) samples. The heat treatment conditions are listed at the top of each column, while the composition identities of each series is shown on the left of each row. The compositions are ordered by increasing calculated average octahedral site radius (where an inverse spinel structure is assumed) and calculated average tetrahedral site radius (where a normal spinel structure is assumed) for the compositions in the red box and green box, respectively. 102

4.8 The degree of inversion, γ, for samples $(n\mathrm{A}_{1/n})\mathrm{Co}_2\mathrm{O}_4$ ($n \geq 5$), obtained from CL refinements, with error bars included. The heat treatment condition for each sample is listed on the x-axis. The samples are grouped into two categories: those with Mg in the compositions (represented by red squares) and those without Mg in the composition (represented by green squares). The red and green arrows indicate the structural trend observed with increasing *post-treatment* temperature. 103

5.1 Overpotential (measured at 10 mA cm^{-2}) for OER versus onset potential for ORR for the best-performing $(5A_{1/5})Co_2O_4$ spinel CCOs in this work (solid colored circles) compared to existing ACo_2O_4 based electrocatalysts from references cited[302, 136, 111, 89, 23, 201, 151, 41, 242, 14, 301, 129, 40, 90, 31, 133, 212, 115, 283, 250, 299, 125, 111, 130, 285, 300, 270, 60, 9, 122, 128, 280, 24, 280, 4, 274, 43, 117, 76, 131, 239, 244, 3, 72, 26, 293, 283, 4, 250] (solid grey triangles). Several notable benchmarks are highlighted with hollow grey markers[133, 72, 301, 283, 90]. See text for further details. 109

5.2 (a) The cubic spinel oxide unit cell model with an inverse structure assumed. The red tetrahedral cation sites are completely occupied by Co atoms, while blue octahedral cation sites are occupied by 50% Co and 50% A atoms. Oxygen atoms decorating the corners of the shaded polyhedra are omitted for clarity. (b) XRD patterns of the MnFeNiCuZn-noMg cobaltite series, including the as prepared sample (400 °C), and samples post-annealed at 600 °C, 800 °C and 1000 °C. Impurities are coded: $CoCl_2{\cdot}2H_2O$ ("h"); tenorite CuO ("c"); rock salt ("r"); and secondary spinel ("s"). (c) Corresponding SEM images for samples in (b). 112

5.3 (a) OER LSV polarization curves, (b) OER Tafel plots, (c) OER ECSA, and (d) ORR LSV polarization curves at a rotating speed of 1600 rpm for the 600 °C sample series. 119

5.4 (a) Chronoamperometry plot of the catalyst MnFeNiCuZn-noMg-600 °C, shown to maintain the current density 10 mA cm^{-2} over 22 hr for OER. (b) The LSV polarization curves of sample MnFeNiCuZn-noMg-600 °C before and after chronoamperometry. The before OER XPS spectra of (c) Mn 2p, (d) Fe 2p, (e) Ni 2p, (f) Co 2p, (g) Zn 2p, (h) Cu 2p, and (i) O 1s are for the MnFeNiCuZn-noMg-600 °C electrode. The comparison of before and after OER XPS spectra can be found in SI Figure S5.5. 124

5.5 XRD patterns of (a) 600 °C series, MgMnFeCuZn-noNi, MgMnFeNiZn-noCu, MgFeNiCuZn-noMn, MnFeNiCuZn-noMg, MgMnNiCuZn-noFe, and MgMnFeNiCu-noZn samples. Impurities are coded: tenorite CuO ("c") and rock salt ("r"). SEM images in (b) reveal the morphology of the samples in (a). 130

5.6 Overpotential (η, measured at 10 mA cm^{-2}) of OER, crystalline size (CS, nm) and cation site inversion (γ) for all 6 compositions $(5A_{1/5})Co_2O_4$, MgMnFeCuZn-noNi (blue), MgMnFeNiZn-noCu (teal), MgFeNiCuZn-noMn (green), MnFeNiCuZn-noMg (orange), MgMnNiCuZn-noFe (pink), and MgMnFeNiCu-noZn (yellow). Left to right, correlations are depicted for as prepared samples (400 °C), and samples post-annealed at 600 °C and 800 °C. 132

6.1 (a) Normal spinel unit cell comprises pink tetrahedra (A-sites) and green octahedra (Co-sites), with atoms labeled in their respective colors. The A-site cations, including Mg, Mn, Fe, Cu, and Zn occupy the tetrahedral site, while Co occupies only the octahedral site. (b) The corresponding room-temperature zero-field magnetic spinel structure depicts calculated magnetic moments pointing down on the tetrahedral site and pointing up on the octahedral site. 138

6.2 (a) XRD pattern comparison of samples indicating a single spinel phase for 400°C and 600°C samples and impurity/secondary phases for 800°C and 1000°C samples. The small black solid (h k l) ticks placed in the bar on top of the XRD patterns indicate Bragg peak locations of the main spinel phase. (b-e) TEM image comparison of samples (b) calcined at 400°C, and post-annealed at (c) 600°C, (d) 800°C, and (e) 1000°C. The samples calcined at 400°C and post-annealed at 600°C display broad particle size distributions. In contrast, the sample post-annealed at 800°C exhibits particle sizes of 100 nm or more. The sample post-annealed at 1000°C consists of micron-scale sized particles. Note the same scale bar applies to all four TEM images in (b-e). . . . 145

6.3 STEM-EDS map of $(Mg_{0.2}Mn_{0.2}Fe_{0.2}Cu_{0.2}Zn_{0.2})Co_2O_4$ spinel (a) as prepared at 400°C, and after post-annealing heat treatment at (b) 600°C, (c) 800°C, and (d) 1000°C. Note the first column of images on the left are STEM high-angle annular dark-field (HAADF) images. The scale bar in the top left corner applies to all images. 147

6.4 The field-cooled (FC) comparison for all four samples over a temperature range of 2 K to 400 K with an applied field of 100 Oe. The accompanying inset reveals a slight bump in the sample post-annealed at 600°C, while no such feature is observed in the sample calcined at 400°C. The heat-treatment temperatures are indicated in the legend. The temperatures (5 K and 100 K) used in all FORC measurements are denoted by black dashed vertical lines. 149

6.5 Magnetometry data for all four samples measured at 5 K (top panels), and 100 K (bottom panels). The heat-treatment temperatures are indicated at the top of each column. Insets display the distinct widths and shapes of hysteresis loops near zero field at smaller scale 149

6.6 The comparison of FORC measurements at 5 K and 100 K for the sample calcined at (a, b) 400°C and the samples post-annealed at (c, d) 600°C, (e, f) 800°C, and (g, h) 1000°C. An intensity scale is displayed at the top right of (b). The feature labels "1" and "2" appearing in FORC plots for samples post-annealed at 600°C, 800°C, and 1000°C represent the primary feature orienting along the H_C axis, and the weak secondary feature along the H_B axis, respectively. 151

6.7 The comparison of neutron diffraction data from the 31° 2θ detector bank (bank 2) (a) and 154° 2θ detector bank (bank 5) (b) for the samples that were calcined at 400°C, and post-annealed at 600°C, 800°C, and 1000°C. (c) Corresponding PDF data of the sample series. The heat-treatment temperatures are specified by the legend in (c). The fit results for (d) Rietveld refinement of Bragg data (R_{wp}= 4.94%) and (e) total scattering data (R_{wp}= 11.97%) for the nanocrystalline CCO sample calcined at 400°C. The phase markers of the main spinel phase (main) and magnetic phase (mag) are displayed below the difference curve in (d). 154

6.8 Results of modeling neutron diffraction data (a, b, c) and PDF data (d, e, f) for the samples calcined at 400°C, and samples post-annealed at 600°C, 800°C, and 1000°C. (a, d) compares model phase percentages (p, %), (b, e) compares lattice parameters (a, Å), and (c, f) compares average scattering lengths of tetrahedral and octahedral sites obtained from refinement ($\langle b \rangle$, fm). Note that the red dashed line and red solid line indicate the calculated average scattering length on the tetrahedral site (n-tet) and octahedral site (n-oct) of a normal spinel structure, respectively. The red solid line and black solid line indicate the calculated average scattering length on the tetrahedral site (i-tet) and octahedral site (i-oct) with an inverse spinel configuration, respectively. The black dashed line represents the calculated average scattering lengths on both tetrahedral and octahedral sites in a random spinel configuration. 155

6.9 Idealized illustrations of cation populations possible within a CCO spinel cobaltite, representing two observed effects: site inversion, represented by a possible (a) normal spinel, and (b) random spinel; and phase segregation, represented with (c) $(Mg_{1/3}Cu_{1/3}Zn_{1/3})Co_2O_4$, and (d) $(Co)(Mn_{0.5}Fe_{0.5}Co)O_4$. (e) Calculated magnetic moments (M) for the models described in (a, b, c, d) on tetrahedral, and octahedral sites as well as the total sum of the magnetic moment. 158

S2.1 AC impedance data of polycrystalline $ATaO_2N$ (A = Ba, Sr, Ca) measured at 295 K, in the frequency range of 1 Hz-10 MHz. (a) Nyquist plots (Z in ohm for A = Ba and Sr, and kohm for A = Ca) and (b) frequency-dependence of dielectric constants. Taking into account the sample geometry, bulk electrical conductivities are evaluated as 1.6×10^{-4} S/cm, 1.3×10^{-4} S/cm, and 3.1×10^{-8} S/cm for A = Ba, Sr, and Ca, respectively. Note that the impedance (Z', Z") of $CaTaO_2N$ is plotted on a different scale. 207

S2.2 (a, b) Disordered anisotropic structure model and (c, d) fixed 50/50-75/25 anistropic structure model shown with 99% probability thermal ellipsoids for $SrTaO_2N$ and $CaTaO_2N$, respectively. 210

S2.3 (a) $SrTaO_2N$ and (b) $CaTaO_2N$ PDF sensitivity test of random/*cis*/*trans* models. Random models are given as blue, *cis* models are given as red and *trans* models are green. The black and orange difference curves describe the difference between random structure and *cis*/*trans*. . . . 211

S2.4 (a-c) Calculated PDFs and partial PDFs resulting from the first series of RMC fits to data. Data are shown as brown, green, and mauve circles for $BaTaO_2N$, $SrTaO_2N$, and $CaTaO_2N$, respectively. Fits are shown as black lines through the data, while blue, red, magenta, and orange solid lines are the partial PDFs of Ta-O, Ta-N, A-O and A-N. Resulting point clouds of corresponding model structures are shown at the right of each panel. 212

S2.5 (a-c) Calculated PDFs and partial PDFs resulting from the second series (with *cis* N ordering) of RMC fits to data. Data are shown as brown, green, and mauve circles for $BaTaO_2N$, $SrTaO_2N$, and $CaTaO_2N$, respectively. Fits are shown as black lines through the data, while blue, red, magenta, and orange solid lines are the partial PDFs of Ta-O, Ta-N, A-O and A-N. Resulting point clouds of corresponding model structures are shown at the right of each panel. 213

S2.6 (a-c) Calculated PDFs and partial PDFs resulting from the second series (with *trans* N ordering) of RMC fits to data. Data are shown as brown, green, and mauve circles for $BaTaO_2N$, $SrTaO_2N$, and $CaTaO_2N$, respectively. Fits are shown as black lines through the data, while blue, red, magenta, and orange solid lines are the partial PDFs of Ta-O, Ta-N, A-O and A-N. Resulting point clouds of corresponding model structures are shown at the right of each panel. 214

S2.7 (a-c) Calculated PDFs and partial PDFs resulting from the third series (with *cis* N supercell ordering) of RMC fits to data. Data are shown as brown, green, and mauve circles for $BaTaO_2N$, $SrTaO_2N$, and $CaTaO_2N$, respectively. Fits are shown as black lines through the data, while blue, red, magenta, and orange solid lines are the partial PDFs of Ta-O, Ta-N, A-O and A-N. Resulting point clouds of corresponding model structures are shown at the right of each panel. 215

S2.8 (a-c) Calculated PDFs and (d-f) S(Q) resulting from (third series) of RMC refinement. Data are shown as black circles, with resulting fits shown as solid lines through the data (brown lines for $BaTaO_2N$, green lines for $SrTaO_2N$, and mauve lines for $CaTaO_2N$). Black solid lines show the difference between data and fits. 216

S2.9 The corresponding partial pair distribution functions (pPDF) (a) A-O, (b) A-N, (c) Ta_A-O and (d) Ta_A-N, from RMCProfile(RMC), and radial distribution functions (RDF) (e) A-O, (f) A-N, (g) Ta_A-O and (h) Ta_A-N, from ab initio molecular dynamics (AIMD) simulations of $ATaO_2N$ (A=Ba, Sr, Ca). The supercells used in RMC and AIMD have anion ordering of *cis*-TaO_4N_2 octahedra with '90-deg' configuration at axial N as proposed by Hinuma[79]. 217

S2.10Total and partial density of electronic state of most stable *cis* and *trans* configurations of (a, b) $BaTaO_2N$, (c, d) $SrTaO_2N$ and (e, f) $CaTaO_2N$. 218

S2.11(a-c) Distinct *cis* N configurations accessible through anion ordering or tilting modification of a parent *Pnma* $CaTaO_2N$ structure. Each row contains configurations with a distinct motif of *cis* N order. The structures at the far left in each row involve no octahedral tilting (*Cccm*, *Pmma* and *Imma*), while the additional structures in each row include octahedral tilting ($P1$, $Pmc2_1$, $Pmn2_1$, $Pna2_1$, $P2_12_12_1$). (d) Relative energies for relaxed *cis* configurations of $CaTaO_2N$ shown in (a-c). The relative energies are shown in relation to the calculated energy of the $P2_12_12_1$ structure, which has the highest value. 219

S3.1 The calculated S_{config} of AFe_2O_4 HESOs with the degree of inversion (γ) changing from 0 to 1 and the assumption that there are N (from 1 to 8) cations ((a) with Fe included as one of the occupying 8 A site cations and (b) without Fe included as one of the occupying A site cations) (the γ values 0, 2/3, and 1 are labeled with the corresponding structure model (normal spinel, random solution, and inverse spinel, respectively.) It is shown that the samples in this study are better described as compositionally complex oxides (CCOs). 221

S3.2 Comparison of calculated neutron diffraction patterns with nuclear contributions (1^{st} column), magnetic contributions (2^{nd} column) and total calculations (3^{rd} column) delineated with normal spinel (a,b,c), inverse spinel (d, e, f), random solution (g, h, i) structure models for samples F1, F3, F4, and F5. 222

S3.3 The PDF data comparison of F1 (orange line), F3 (purple line), F4 (red line), and F5 (green line) shown for every 10 Å between 1.7 Å and 50 Å). The differences between F1 and F3 (black solid line), F1 and F4 (black dashed line), and F1 and F5 (black dotted line) are shown below the PDF data. 225

S3.4 The PDF data comparison of F1 (orange line), F3 (purple line), F4 (red line), F5 (green line). The 6 peaks (1, 5, 9, 12, 15, 17) highlighted with magenta dashed lines correspond to A-O pairs. The 4 peaks (2, 6, 10, 13) indicated with green dashed lines arise from A_{oct}-A_{oct} and O-O pair correlations. The 3 peaks (3, 11, 16) contributed by A_{oct}-A_{tet},A_{tet}-A_{tet} and A-O are identified in sky blue dashed lines. The peak (4) around 4 Å highlighted in a red dashed line corresponds to an O-O correlation. The combination of A_{oct}-A_{tet} and A_{tet}-O pair correlations contribute the 2 peaks (7, 14) indicated by orange dashed lines. The peak (8) highlighted by a pink dashed line arises from A_{oct}-A_{oct},A_{tet}-A_{tet} and A-O pair correlations). A comparison of the PDF refinements for (b) F3 sample data and (c) F5 sample data using different structure models (random, inverse, and normal spinel ferrite models). PDF data for F3 and F5 samples are shown in orange and red dots, respectively. The blue, lemon green and sky blue solid curves present fits to the data completed with the random spinel structure, inverse spinel structure and normal spinel structure model, respectively. The fit difference curves displayed below the data and fits are represented as black solid curves. These results are similar to results for F1 and F4 samples presented in the main body of this work. 226

S3.5 RMC fitting of $F(Q)$ data for (a) F1, (b) F3, (c) F4 and (d) F5 with inverse model assuming that a +2 valence state for all A cations in the AFe_2O_4 compositional series, and a +3 valence state for the remaining two Fe cations. 227

S3.6 RMC fitting of $F(Q)$ data for (a) F1, (b) F3, (c) F4 and (d) F5 with random model assuming that a +2 valence state for all A cations in the AFe_2O_4 compositional series, and a +3 valence state for the remaining two Fe cations. 227

S3.7 RMC fitting of Bragg data for (a) F1, (b) F3, (c) F4 and (d) F5 with inverse model assuming that a +2 valence state for all A cations in the AFe_2O_4 compositional series, and a +3 valence state for the remaining two Fe cations. 228
S3.8 RMC fitting of Bragg data for (a) F1, (b) F3, (c) F4 and (d) F5 with random model assuming that a +2 valence state for all A cations in the AFe_2O_4 compositional series, and a +3 valence state for the remaining two Fe cations. 228
S3.9 KDE for magnetic moments distribution in XY plane for all samples – (a) F1, (b) F3, (c) F4 and (d) F5 with inverse model assuming that a +2 valence state for all A cations in the AFe_2O_4 compositional series, and a +3 valence state for the remaining two Fe cations. "Tetra." denotes tetrahedral site, "Octa." denotes octahedral site. 230
S3.10KDE for magnetic moments distribution in XY plane for all samples – (a) F1, (b) F3, (c) F4 and (d) F5 with random model assuming that a +2 valence state for all A cations in the AFe_2O_4 compositional series, and a +3 valence state for the remaining two Fe cations. "Tetra." denotes tetrahedral site, "Octa." denotes octahedral site. 230
S4.1 XRD patterns measured with a Co X-ray source and shown at logarithmic scale for spinel samples, 5C1, 5C2, 5C3, 5C4, 5C5, 5C6, 5C7, 5C8, 6C1, 6C2, 6C3, and 7C1 after different heat treatments (AF4, PT6, PT8, and PT10). Panels containing X-ray pure phases are colored green. Detected impurity phases are coded: CuO ("c"); rock salt ("r"); secondary spinel ("s"); and $CoCl_2{\cdot}2H_2O$ ("h"). 232

S4.2 XRD patterns measured with a Co X-ray source and shown at logarithmic scale for spinel samples, 1C1, 2C1, 2C2, 2C3, 2C4, 2C5, 4C1 and 4C2 after different heat treatments (AF4, PT6, PT8, and PT10). Panels containing X-ray pure phases are colored green. Detected impurity phases are coded: ZnO ("z"); CuO ("c"); rock salt ("r"); secondary spinel ("s"); and Co ("Co"). 232

S4.3 First Two Columns: SEM/EDS maps of each cation in sample 5C1 AF4, corresponding to the SEM image in the top right panel. Sample 5C1 AF4 is compositionally homogeneous on the microscale. Last Column: SEM images of sample 5C1 AF4 shown at two different magnifications and in several regions. The sample's morphology is heterogeneous at the nanoscale. 233

S4.4 SEM images of samples 5C1 , 6C1, and 7C1 prepared AF4, PT6, PT8, PT10. Conditions resulting in X-ray pure phases are highlighted by green rectangles and conditions resulting in phase mixtures are highlighted by purple rectangles. 233

S5.1 Correlations between (a) OER overpotential (mV) at 10 mA cm^{-2} and heat treatment temperature; (b) OER overpotential (mV) at 10 mA cm^{-2} and crystalline size (nm), (c) cation site inversion (γ) and heat treatment temperature, and (d) OER overpotential (mV) at 10 mA cm^{-2} and cation site inversion for MgMnFeCuZn-noNi (light blue symbols), MgMnFeNiZn-noCu (teal symbols), MgFeNiCuZn-noMn (green symbols), MnFeNiCuZn-noMg (orange symbols), MgMnNiCuZn-noFe (pink symbols), and MgMnFeNiCu-noZn series (yellow symbols). In the plots, solid squares denote 400°C annealed samples, solid triangles indicate 600°C annealed samples, solid circles represent 800°C annealed samples, and 'x's denote 1000°C annealed samples. 234

S5.2 Linear sweep voltammograms of the MgMnFeCuZn-noNi, MgMnFeNiZn-noCu, MgFeNiCuZn-noMn, MnFeNiCuZn-noMg, MgMnNiCuZn-noFe, and MgMnFeNiCu-noZn 600 °C series of samples collected using the RDE set-up at rotating speeds of 400 rpm (black line), 800 rpm (red line), 1200 rpm (blue line), 1600 rpm (pink line), and 2000 rpm (green line). 235
S5.3 Plot of the H_2O_2 yields (red circle symbols) and electron-transfer numbers (black square symbols) for the MnFeNiCuZn-noMg-600 °C sample. 235
S5.4 The Koutechy-Levich (K-L) plots at different electrode potentials for the MnFeNiCuZn-noMg-600 °C sample. 236
S5.5 The before and after OER XPS spectra for (a) Mn 2p, (b) Fe 2p, (c) Ni 2p, (d) Co 2p, (e) Zn 2p, (f) Cu 2p, and (g) O 1s for the MnFeNiCuZn-noMg-600 °C sample electrode. 236
S5.6 SEM/EDS maps of a micron sized particle (left) and collections of nanoparticles (right) for the sample MnFeNiCuZn-noMg-400 °C. Each cation type appears to be present and homogeneously distributed across the distinct particle morphologies. 237
S5.7 High resolution SEM images of samples MgMnFeCuZn-noNi (top row) and MgFeNiCuZn-noMn (bottom row) subjected to different heat treatment temperatures (increasing from left to right). Note the difference in scale bar (lower magnification) for the 1000°C sample images at the far right. 237
S6.1 Comparison of refinement results for the 10 Å PDF data range for samples that were calcined at 400°C, post-annealed at 600°C, 800°C, and 1000°C, with a single spinel model (1-phase) on the left and a two component spinel model (2-phase) on the right. Goodness of fit factors are displayed in each panel. 241

S6.2 Comparison of refinement results for the 30 Å PDF data range for samples that were calcined at 400°C, post-annealed at 600°C, 800°C, and 1000°C, with a single spinel model (1-phase) on the left and a two component spinel model (2-phase) on the right. Goodness of fit factors are displayed in each panel. 242

S6.3 For the samples that were calcined at 400°C, post-annealed at 600°C, 800°C, and 1000°C– comparison of phase percentage (p, %), lattice parameter (a, Å), average scattering length ($\langle b \rangle$, fm), and the atomic displacement parameters (B, Å^2) of tetrahedral cation, octahedral cation, and oxygen sites extracted from refinement with 10 Å PDF data range with one-spinel phase (1-phase) model (left column) and two-spinel phase (2-phase) model (right column), respectively. 243

S6.4 For the samples that were calcined at 400°C, and post-annealed at 600°C, 800°C, and 1000°C– the comparison of phase percentage (p, %), lattice parameter (a, Å), average scattering length ($\langle b \rangle$, fm), and the atomic displacement parameters (B, Å^2) of tetrahedral cation, octahedral cation, and oxygen sites extracted from refinement with 30 Å PDF data range with one-spinel phase (1-phase) model (left column) and two-spinel phase (2-phase) model (right column), respectively. . 244

S6.5 Rietveld refinement fits to data for the sample annealed at 800°C indicates a major spinel phase along with the presence of impurities: tenorite (CuO) and rocksalt (MgO). The refinement of the sample annealed at 1000°C indicates the same impurities, along with the emergence of a second (minor) spinel phase. 245

S6.6 The magnetic hard phase fraction obtained from 5 K FORC measurements for all four samples, assuming the sample calcined at 400°C as predominantly soft phase, and the 1000°C annealed sample as hard phase. 245

S6.7 PDF data comparison over 1-50 Å for the samples that were calcined at 400°C, and post-annealed at 600°C, 800°C, and 1000°C. 246

Chapter 1

Introduction

Functional ceramics, broadly defined as nonmetallic inorganic materials designed to provide electronic, magnetic, catalytic, or other functions, comprise an expansive array of materials, both basic and complex. In this context, complex functional ceramics (CFCs) encompass compounds with two or more distinct cation (and/or anion) species. CFCs attract great attention owing to the rich possibilities of obtaining unique physicochemical properties via fine tailoring of their chemical compositions and their atomic structures– there have been wide investigations into the structure-property relationships of such systems. Efforts have predominately been focused on the average (long-range) structure, though, leaving the influence of chemical short range order (CSRO) of cations (or anions) under-explored. In fact, the CSRO, rooted in the atomic disorder and related lattice distortions of CFC crystal structures, may play special roles in directing the key structure-property trends. Therefore, in this study, CSRO was explored in several representative CFC systems (oxynitride perovskites, high entropy oxide (HEO) ferrites, and a large family of nano compositionally complex oxide (CCO) spinels). In the latter case, new families of materials were prepared for the purpose of systematically tuning CSRO to impact their catalytic and magnetic properties.

1.1 Background and Motivation

Guided by Goldschmidt's rules, atomic substitution has long been used to tune the properties of ceramics by changing elemental composition. Both anion substitution and cation substitution offer rich variation within given structural families. Within the last decade, this exploration has leaped into a new realm with the development of 'High Entropy Oxides (HEOs).' These materials involve high levels of cation substitutions, popularly defined as having five or more cation species (in equiatomic or near equiatomic ratios) sharing a specific sublattice site in a single phase material, and more exactly defined as having configurational entropies (S_{config}) being equal to or larger than 1.5R (where R is the universal gas constant)[282, 189]. A more expansive classification includes the 'compositionally complex oxides (CCOs)' which include lower entropy and non-equimolar oxides[259].

In the domain of these high/medium entropy CFCs, achieving homogeneity across multiple scales is a critical yet often overlooked aspect. A thorough comprehension of these materials requires a deep investigation of the interplay of cations/anions at various scales, as it is essential for defining and customizing the distinct properties of CFCs. It is crucial to uncover the homogeneity/heterogeneity at various levels to fully harness the tailorable nature of these CFCs. In the following section, we introduce three classes of CFCs that will be explored in this thesis: (1) Ta perovskite oxynitride dielectrics; (2) Fe-based compositionally complex ferrimagnetic spinel oxides; and (3) nanoscale Co-based compositionally complex electrocatalytic and ferrimagnetic spinel oxides.

1.1.1 Cation and anion substitution in Ta perovskite oxynitrides

For simple ceramic oxides, like metal titanates ($BaTiO_3$, $SrTiO_3$ and $CaTiO_3$[223, 241, 192, 134, 119, 305, 156]), their dielectric constants (κ) are high but Curie

temperatures (T_C) are very low. This limits their useful temperature range and therefore their practical application in devices[103]. In order to obtain dielectric materials that have high κ over a broad temperature range, Kim *et al.* [103] explored Ta perovskite oxynitrides, complex ceramics, to enhance dielectric polarizability. The individually reduced electronegativities of Ta^{5+} and N^{3-} compared to Ti^{4+} and O^{2-}, respectively, introduce displacements of Ta^{5+} and further causes an increase of dielectric permittivity. It turns out that $BaTaO_2N$ and $SrTaO_2N$ have high bulk permittivity, approximately 4900 (with a moderate temperature coefficient of 1140 ppm/K) and 2900 (with -730 ppm/K) near room temperature, respectively. Their dielectric properties are unusual and they show a weak dependence on temperature. Interestingly, these compounds present with centrosymmetric crystal structures. It is difficult to explain these observed high κ values, inferring permanent nonzero dipole moments, if all local dipoles are counteracted in the structures. This infers the existence of local ordering in such systems. Indeed, previous local structure studies of $BaTaO_2N$[172] and $SrTaO_2N$[281] proved CSRO– *cis* configuration of N-Ta-N bonding are preferred in the TaO_4N_2 octahedra.

Particularly noteworthy is the dielectric constant of $CaTaO_2N$ – it is lower than those of $BaTaO_2N$ and $SrTaO_2N$ by ∼2 orders of magnitude, and the electrical conductivity by ∼3 orders of magnitude. The origin of this large difference of dielectric permittivities among the $ATaO_2N$ (A=Ba, Sr, Ca) series is therefore of interest. Uncovering the relationship between A cation size and structure-property trends in this series of materials through a detailed look at their respective local and long-range atomic structures will provide new insights into the rules of design for complex ceramic dielectrics.

1.1.2 High entropy ferrites made by special cation substitution

Since the first HEO structure (rocksalt $(Mg_{0.2}Ni_{0.2}Co_{0.2}Cu_{0.2}Zn_{0.2})O$) was reported[189], additional families of HEOs have been made within the perovskite, fluorite, spinel

and pyrochlore structure types, to name a few[88, 254, 255, 233, 224, 199, 118, 292, 127, 158, 171, 6, 221, 267, 193, 195, 6, 57, 149], due to their promising tunability in regards to various physicochemical properties. The first HEO spinel, $(Cr_{0.2}Mn_{0.2}Fe_{0.2}Co_{0.2}Ni_{0.2})_3O_4$, was synthesized successfully by Dąbrowa *et al.* [47] with solid state synthesis (SSS) methods. This HEO spinel's magnetic properties were then investigated by Mao *et. al*, utilizing samples synthesized with a different method – solution combustion synthesis (SCS)[139]. The exploration of magnetic properties in such systems is a trending direction but has so far been limited in scope due to the complex nuclear and spin coupled environments that can range from local to long-range. In the same year, Musicó *et al.* [157] introduced nine single-phase HEO spinels, (Mg, Cr, Mn, Co, Fe, Ni, Cu, and/or Zn)(Cr, Fe or Al)$_2$O$_4$, with SSS. Within this set, four ferrimagnetic HEO spinel ferrites, featuring combinations of Mg, Fe, Co, Ni, Cu, Mn, and Zn cations, displayed interesting magnetic properties. For example, the system containing Zn and Mg (two non-magnetic cations) had the largest magnetic moment and lowest Néel temperature (T_N), in keeping with the tetrahedral site preferences of the smaller cations. Likewise, the systems containing only Mg show the second-largest saturation moment and a higher T_N. However, the system without Mg and Zn, with the smallest magnetic moment, had an intermediate T_N. These observations indicate that non-random cation distributions are likely to exist and vary across the family. Additionally, two of the spinel ferrites show peculiar magnetic behavior–field warming magnetization dips below the field cooling magnetization at low-to-intermediate temperatures, indicating an increase in magnetization as the temperature increases. This is possibly related to antiferromagnetic coupling between neighboring atoms in the cation sublattice. These two indications suggest that while the SSS approach results in a single-phase HEO spinel it fails to completely overcome the site preferences of the individual cations to create an exact random structure. Therefore, exploring the local structure in this family of HEO spinel ferrites will provide further context and understanding of the unique properties and potential tunabilities of magnetic HEOs/CCOs.

1.1.3 Special cation substitution in nano compositionally complex cobalt oxides

Nanomaterials offer unique physicochemical properties across diverse applications, such as energy storage, sensors, catalysis, and biomedical therapies and diagnostics. Specifically in the context of HEOs/CCOs, the nano-size effect may offer increased stability and increased structure-property tunability. However, there is only limited work in nano-HEOs to date with laser scanning ablation[234], ball-milling, chemical co-precipitation, and polymeric steric entrapment[93] being a few demonstrated synthesis pathways. Spinel Co_3O_4 is considered a favorable low-temperature economical catalyst for formaldehyde oxidation, and chemically related variations are used in many other catalytic and electrochemical reactions[120]. The family represents some of the best heterogeneous oxygen evolution reaction (OER) electrocatalysts[1] and improves both OER and oxygen reduction reaction (ORR) in 1 M NaOH electrolyte[218]. Being one of the ferromagnetic metals (iron, nickel, and cobalt) in nature, cobalt (Co) is essential to the development of hard magnetic materials due to its high saturation magnetization (M_S), high Curie temperature (T_C) and high magnetocrystalline anisotropy[153]. Most end-member transition metal cobalt oxide spinels (with formula ACo_2O_4) are earth-abundant ferrimagnetic phases[19, 16, 95, 159]. These transition metal cobalt oxide spinels are also well known to provide catalytic and electrochemical characteristics[205, 66, 265]. Compositionally complex variants are therefore ripe for exploration. Here, we propose to make a large family of nano compositionally complex versions of transition metal cobalt oxides. The variation in entropic (configurational mixing) contributions arising from the type and number of cations selected and the thermal processing history are anticipated to impact local lattice distortions, cation site preferences, and other CSRO effects. Meanwhile, the influence of such a complex interplay upon phase formation/stability and tunability of physicochemical properties will be investigated systematically.

The complex structure-property relationships anticipated across the three families of compounds introduced above illustrate rich opportunities for crystal chemical design and unique property combinations among CFCs. In each, the specific local ordering motif of participating ions within/among crystallographic lattice sites is of special interest. In practice, however, evaluating the anion or cation distributions in bulk polyanionic compounds, HEOs and CCOs is challenging; it is an even greater challenge at the nanoscale. The characterization and analysis scheme for this work will be presented in the next section, involving total scattering and density functional theory (DFT) simulation.

1.1.4 Chemical short range order characterization and simulation

Total Scattering In real materials, atoms are not perfectly fixed in their crystallographic positions but rather disorder is a ubiquitous phenomenon. Such disorder, coming in various forms, such as thermal motion and internal degree of freedom, in some cases, is random, but more often, it is correlated. Chemical short range order (CSRO), describing the local ordering preference of elements within a few nearest neighbor distances, is one of the essential aspects of disorder. The more general term short range order (SRO) extends the concept to correlations beyond the nearest neighbors, essentially encompassing any atomic ordering motif that departs from the average (unit cell-based) description of the long-range order. Early qualitative studies of SRO performed on single crystals can be traced back to the 1940s even before the computer was born. The investigations were restricted to simple 1D stacking faults, based on experimental diffuse scattering signal. Atomic size-effect distortions and point defect introduced relaxations were taken into consideration in the 1950s, having impacts on Bragg peak shapes[251]. The 1960s and 1970s saw growth in the use of the Pair Distribution Function (PDF) method to study the SRO through powder diffraction experiments – heralded in part by the development of computers which

make the Fourier transform less formidable. However, obtaining high-resolution PDF patterns for quantitative SRO studies requires the scattering data to be collected to a high reciprocal space (Q-space) region with high data quality (i.e., high signal-to-noise ratio). The advent and development of synchrotron X-ray sources and spallation neutron sources over the past 30 years provided these characteristics. The PDF method has since been applied to study disorder in many crystalline materials.

The conventional method for analyzing diffraction data involves extracting information from the location, intensity, and shape of Bragg peaks. Order and disorder phenomena can be studied from the average structure perspective with the Rietveld refinement method[186]. With the total scattering technique, diffraction data is very carefully reduced to guarantee that the diffuse scattering signal, corresponding to local correlations within the sample, is preserved. The combination of diffuse scattering and Bragg peaks comprises the overall total scattering pattern, in reciprocal space. Through a Sine Fourier transform, the pair distribution function (PDF) is produced[56, 97, 168, 294]. The reciprocal space total scattering function is given as,

$$S(\mathbf{Q}) = \frac{\frac{1}{N}\sum_{v,\mu} b_v b_\mu e^{i\mathbf{Q}(\mathbf{R}_v - \mathbf{R}_\mu)} + \langle b\rangle^2 - \langle b^2\rangle}{\langle b\rangle^2}, \tag{1.1}$$

where $\mathbf{Q}$ is the scattering vector, N is the numbers of atoms, $\mathbf{R}_v$ ($\mathbf{R}_\mu$) is the vth (μth) atom position and b_v (b_μ) is the scattering length of the atom v (μ); $(\langle b\rangle^2 - \langle b^2\rangle)/\langle b\rangle^2$ together is termed as the normalized Laue monotonic scattering. In general cases for powder samples, the polycrystals are assumed to be randomly and uniformly oriented and therefore the direction dependent term in Eqn. 1.1 is averaged according to the isotropic approximation, to give,

$$S(Q) = \frac{1}{N\langle b\rangle^2}\sum_{\nu}^{N}\sum_{\mu}^{N} b_\nu b_\mu \frac{sin(Qr_{\nu\mu})}{Qr_{\nu\mu}} + \frac{\langle b\rangle^2 - \langle b^2\rangle}{\langle b\rangle^2} \tag{1.2}$$

Applying the Sine-Fourier transform to the reciprocal space pattern following the equation below, the PDF is produced in $G(r)$ form, yielding,

$$G(r) = \frac{2}{\pi} \int_0^\infty Q[S(Q) - 1] sin(Qr)\, dQ \tag{1.3}$$

To link the atomic configuration with the experimentally obtained $G(r)$ pattern, one has,

$$G(r) = \sum_{\nu,\mu=1}^{n} c_\nu c_\mu b_\nu b_\mu [g_{\nu\mu}(r) - 1] \tag{1.4}$$

where b_ν and b_μ carry the same meaning as in Eqn. 1.1. c_ν and c_μ refer to the concentration of atoms of type ν and μ, respectively. The $g_{\nu\mu}(r)$ function can be computed from any atomic configuration, following,

$$g_{\nu\mu}(r) = \frac{n_{\nu\mu}(r)}{4\pi r^2 dr \rho_\mu} \tag{1.5}$$

where $n_{\nu\mu}(r)$ is the number of particles of type μ between distances r and $r + dr$ from a particle of type ν and $\rho_\mu = c_\mu \rho_0$ (ρ_0 is the overall number density of the material, in atoms/Å^3).

X-ray and Neutron Source Comparison Depending on the system being studied, X-ray or neutron diffraction may be selected or both applied due to their complementary strengths and weaknesses. Since the scattering mechanisms for X-ray and neutron sources are different, the information they provide is different. X-rays are scattered by the electrons of atoms and provide information about the electron density of the scattering material. Neutrons are scattered by atomic nuclei and provide information about the nuclei positions in the scattering material. Since neutrons have magnetic dipole moments, in magnetic materials, neutrons can also be scattered by the atomic magnetic moments which arise from the alignment of the spins of the electrons that are in the partially filled energy levels.

Due to the strong interaction between X-rays and electrons, the X-ray scattering process is a stronger process than neutron scattering. Coupled with the fact that X-ray beams are much more intense than neutron beams, the requirement for sample amounts in an X-ray experiment (on the level of mm^3) is usually much less than that for a neutron experiment (on the level of cm^3). One of the downsides associated with the fact that X-rays are scattered by electrons is that atomic scattering strength of X-rays is Q-dependent. Mathematically, the X-ray form factor is the Fourier transform of the electron density. The distribution of the electron density in real space then corresponds to the finite range of the form factor in Q-space, i.e., the form factor for X-ray is intrinsically dampened as Q increases. In contrast, since neutrons interact with atomic nuclei, the much smaller size of the nuclei, when Fourier transformed, gives nearly no dampening of the scattering strength in Q-space. In practice, the neutron scattering strength (i.e., the scattering length) is treated as constant, i.e., independent of Q. Therefore, concerning the total scattering studies that require large Q-space coverage, the neutron has an intrinsic advantage over X-rays in this regard. Another feature of X-rays being scattered by electrons is that the scattering strength is proportional to the number of electrons and therefore, heavy atoms scatter much more strongly than light atoms. This can be beneficial if you are seeking to emphasize the presence and visibility of heavy atoms. Neutrons, however, do not have such dependence of scattering strength upon element and therefore are preferably chosen for studying light elements, such as Li, O, etc.

Here, a typical example (the CCO nano-$(Mn_{0.2}Fe_{0.2}Cu_{0.2}Zn_{0.2}Mg_{0.2})Co_2O_4$) from our studies is presented to showcase the comparison of experimental X-ray and neutron PDFs. As shown in Figure 1.1, the neutron PDFs for the three different samples show more obvious distinction as compared to X-ray PDFs. Therefore, neutron PDFs in this specific situation would provide richer structural information as compared to X-ray. In practice, neutron and X-ray PDFs are often complementary and can be pursued together to provide sensitivity to different aspects of a given material structure.

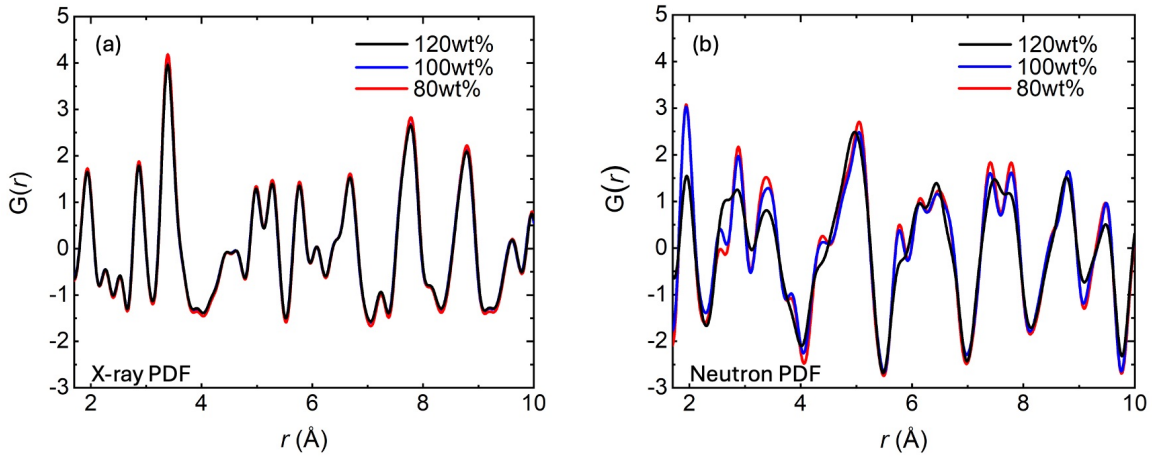


Figure 1.1: (a) X-ray PDF and (b) neutron PDF comparison of three different samples with the composition $(Mn_{0.2}Fe_{0.2}Cu_{0.2}Zn_{0.2}Mg_{0.2})Co_2O_4$, each synthesized with a different weight percentage of polymer reactant and calcined at 400°C. Neutrons reveal local structure variations that are not distinguished with X-rays.

Other Techniques Comprehensive characterization of material structure often requires a combination of complementary techniques. This is especially the case in our studies of the CSRO in complex functional ceramics, considering the complexity introduced by multiple factors such as chemical composition, spin-lattice coupling, local lattice distortion, etc. A comparison of experimental techniques that can be used to probe various features of local atomic structure is briefly summarized in Table 1.1, highlighting several merits and limitations of each. The probes include neutron and X-ray total scattering (NTS and XTS), Nuclear magnetic resonance spectroscopy (NMR), Extended X-ray Absorption Fine Structure (EXAFS), X-ray absorption near-edge structure (XANES), Raman spectroscopy (RS), and Mössbauer spectroscopy (MS).

Theoretical Calculation with Density Functional Theory In addition to the experimental techniques for local structure studies, theoretical calculations with Density Functional Theory (DFT) are employed to study the ground state configurations and energies of CFCs in this work. A brief introduction to the DFT method is recast here[146, 96, 207]. Starting from the stationary Schrödinger equation,

$$\hat{H}\Psi = E\Psi, \tag{1.6}$$

the system energy can be written as

$$E = \frac{\langle\Psi|\hat{H}|\Psi\rangle}{\langle\Psi|\Psi\rangle}. \tag{1.7}$$

Based on the variational theorem, it can be derived that a change in wave function will lead to a second-order change in the energy, which therefore demonstrates that the best wave function is that for which the energy is a minimum[44]. The importance of such a principle is that it makes it possible to propose a trial form for the wave function with a certain number of adjustable parameters. Those parameters could

Table 1.1: A brief summary of several merits and limitations of different local structure characterization techniques (Tech), including neutron and X-ray total scattering (NTS and XTS, respectively), Nuclear magnetic resonance spectroscopy (NMR), Extended X-ray Absorption Fine Structure (EXAFS[71]), X-ray absorption near-edge structure (XANES), Raman spectroscopy (RS), and Mössbauer spectroscopy (MS).

Tech	Merits	Limitations
NTS	distinguishes isotopes	low flux
	sensitive to light elements	large amount of sample needed
	characterizes magnetic moments	longer measurement times
	probes local structure beyond the first few neighbors	
XTS	small sample amounts	low sensitivity to light elements
	fast measurements	
	probes local structure beyond the first few neighbors	
NMR	non-destructive	low sensitivity
		large amount of sample needed
EXAFS/ XANES	element specific local bonding	limited length scale
	oxidation state sensitive	reference samples often needed
	sensitive to low concentrations	
RS	non-destructive	weak Raman effect
	fast measurement	strong fluorescence effect
MS	quantitative determination of the valence state	large amount of sample needed
		only available for a few elements

then be optimized to give the lowest energy, in which case the optimized wave function is expected to resemble the true wave function (i.e., the ground state). Based on the density functional theory and owing to the groundbreaking work by Kohn and Sham, the variational principle can be put into practice for solving the ground state of systems. With density functional theory, the system potential can be given as the functionals of the electron density which is further given by the system wave function. The Kohn-Sham approach then turns the interacting system into a non-interacting one which would yield the same electron density as the interacting system. In the Kohn-Sham framework, the system energy is given as,

$$E_{KS} = \frac{1}{2}\sum_{\sigma}\sum_{i=1}|\nabla\Psi_i^{\sigma}|^2 + \int d\mathbf{r}V_{ext}(\mathbf{r})n(\mathbf{r}) + E_{Hartree}[n] + E_{II} + E_{xc}[n] \qquad (1.8)$$

where $n(\mathbf{r})$ refers to the electron density function. The first term defines the kinetic energy of independent particles. The second term is corresponding to the electron-nuclei interaction, $E_{Hartree}$ is the self-interaction energy of the classical charge density, E_{II} is the interaction energy of the positive nuclei. The first four terms can be conveniently constructed from the electron density and the only unknown term is the last one – the E_{xc} term for exchange-correlation interaction which requires certain approximations. The exchange interaction is generated by the Pauli exclusion principle and the electronic correlation corresponds to the Coulomb repulsion. There are two mainly used approximations to give the exchange-correlation functional – the local density approximation (LDA) and the semi-local generalized gradient approximation (GGA). The choice of different approximations and different forms of the exchange-correlation function is usually system-dependent. With LDA, the covalent, metallic, and ionic bonds are generally well described. However, LDA is not adequate to solve problems involving hydrogen bonds, and meanwhile, since it was generated by the approximation on a homogeneous electron gas, it will be hard to

solve the self-interaction problem. GGA is typically more accurate than LDA owing to the introduction of the derivative of the charge density.

In practice, the wave function is represented as the combination of a certain set of basis functions and the optimization focuses on those combination coefficients. Alternative basis function sets involve the plane wave set (and its variation such as linearized augmented plane wave, LAPW), the local basis such as Gaussian orbitals, etc. Concerning computational efficiency, the so-called pseudopotential method is often employed – the electrons lying close to the core of the atoms are treated separately and replaced by an effective potential energy function that closely approximates the effect of the inner electrons on the outer electrons. Generalization of such a framework also exists to further boost the computational efficiency; for example, the projector augmented wave method (PAW) is a generalization of the pseudopotential and linear augmented-plane-wave methods. By transforming the rapidly oscillating wave functions (near the ion cores) into smooth wave functions, the PAW method[17] can provide greater computational efficiency.

Chapter 2 of this dissertation employed DFT simulations to compare the relaxed configurations and relative energies of $ATaO_2N$ (where A = Ba, Sr, Ca) with various candidate configurations of ions decorating the lattices. This analysis aimed to investigate the presence of distinct CSRO patterns and assess their prevalence across the entire family of structures.

1.2 Objectives of the Study

The overarching theme of this study is uncovering the special role of local structure in directing physicochemical properties in several families of CFCs. The central hypothesis emerges that materials with high compositional complexity offer added flexibility and (perhaps) opportunities for fine control of experimental 'knobs' to achieve specific structure-property aims. We have focused on the specific aim of achieving an understanding of the impact of synthesis variations on cation

heterogeneity and corresponding catalytic and magnetic property trends in nano spinel CCOs, expanding design strategies for novel nanostructured materials.

1.3 Scope of the Dissertation

The proposal comprises 7 chapters, namely;

Chapter 1 describes the background and motivation of the proposal. The fundamental concepts along with the aims and objectives as well as context of the thesis are narrated. An account of the research hypothesis is given in this chapter with a breakdown of the methodological approaches used in the investigation.

Chapter 2 explores the relationship between local structure and the electronic properties in a family of Ta oxynitrides. This work was published as the paper - *Influence of Cation Size on the Local Atomic Structure and Electronic Properties of Ta Perovskite Oxynitrides* (Reprinted (adapted) with permission from *Inorg. Chem.* 2021, 60, 14190–14201. Copyright 2021 American Chemical Society. DOI: 10.1021/acs.inorgchem.1c01594 [243]).

Chapter 3 is centered on understanding the magnetic behavior reported for "high-entropy spinel ferrites," exhibiting differing degrees of chemical short-range order. The work was published as the paper - *Local Cation Order and Ferrimagnetism in Compositionally Complex Spinel Ferrites* (Reproduced from *APL Materials* 2022, 10, 121102.), with the permission of AIP Publishing. DOI: 10.1063/5.0123728 [246]).

Chapter 4 presents the observation of temperature-activated compositional heterogeneity and discusses the competition between entropy and cation selection towards phase stability and complex thermodynamics in a large compositionally complex nano family $(n\mathrm{A}_{1/n})\mathrm{Co}_2\mathrm{O}_4$ (n= 1 to 7) that has been made for the first time. This work was published as the paper - *Phase Selectivity and Stability in Compositionally Complex Nano* $(nA_{1/n})Co_2O_4$ (Reprinted (adapted) with permission from *Chem. Mater.* 2023, 35, 7283–7291. Copyright 2023 American Chemical Society. DOI: 10.1021/acs.chemmater.3c01647 [245]).

Chapter 5 investigates the bifunctional oxygen evolution reaction (OER) and oxygen reduction reaction (ORR) electrocatalytic properties in a family of nano CCO $(5A_{1/5})Co_2O_4$. The work was published as the paper - *Excellent Bifunctional Oxygen Evolution and Reduction Electrocatalysts* $(5A_{1/5})Co_2O_4$ *and Their Tunability* (Reprinted (adapted) with permission from *ACS Mater. Au* 2024, *in press*. Copyright 2024 American Chemical Society. DOI: 10.1021/acsmaterialsau.3c00088 [247])

Chapter 6 explores the sensitivity of magnetic properties to the thermal history of the compositionally complex oxide $(Mg_{0.2}Mn_{0.2}Fe_{0.2}Cu_{0.2}Zn_{0.2})Co_2O_4$, a nanostructured CCO. A summary of the work is currently under preparation as a journal article.

Chapter 7 summarizes the work that has been conducted in this dissertation, offers recommendations for the high entropy community, evaluates the limitations of the work, proposes strategies for expanding the work, and highlights the significant contributions of this dissertation to the high entropy and wider CFC fields.

Chapter 2

Influence of Cation Size on the Local Atomic Structure and Electronic Properties of Ta Perovskite Oxynitrides

It was introduced in Section 1.1.1 that higher and more temperature stable dielectric constants can be obtained in Ta perovskite oxynitrides relative to simpler Ti perovskite oxides by virtue of simultaneous substitutions on cation and anion sites. However, the effectiveness of this strategy is seen to decrease in moving from compounds featuring the larger cation Ba to the smaller cation Ca in the family of perovskite tantalum oxynitrides - $ATaO_2N$ (A= Ba, Sr, Ca). CSRO was identified as an important factor in the properties of $BaTaO_2N$ and $SrTaO_2N$ previously, so a natural question is whether the same type of local ordering also exists in $CaTaO_2N$. Additionally, the complex interplay between electronic properties and the A cation size, nature of Ta displacement, octahedral tilting, and the local anion ordering remains vague. In this chapter, these two aspects are explored with a combination of neutron total scattering, density functional theory (DFT), and *ab initio* molecular

dynamics (AIMD) simulations. Specifically, we present the first experimental study of chemical short range order (CSRO) in $CaTaO_2N$, confirming local *cis* N ordering of the anion sub-lattice. Our systematic exploration of local structure across the A cation size series (from the larger Ba to the smaller Ca), reveals a perovskite motif increasingly distorted with respect to long-range average structures. DFT and AIMD simulations support the observed trends. Overall, structures with *cis* ordering of the nitrogen anions in each TaO_4N_2 octahedron are favored over those with *trans* ordering. With diminishing A cation size, local *cis* ordering and Ta off-centering play decreasing roles in overall lattice stability, overshadowed by the stabilizing effects of octahedral tilting. The influence of these factors on local dipole formation and frustrated dipole ordering is discussed.

Chapter 2– *Influence of Cation Size on the Local Atomic Structure and Electronic Properties of Ta Perovskite Oxynitrides*– is reprinted (adapted) with permission from *Inorg. Chem.* 2021, 60, 14190–14201. Copyright 2021 American Chemical Society. DOI: 10.1021/acs.inorgchem.1c01594 [243] The authors of the work are Xin Wang, Bo Jiang, Yuanpeng Zhang, Young-Il Kim, and Katharine Page.

2.1 Introduction

Since first reported [142] transition metal oxynitride perovskites and related phases have received considerable interest for their potential use as non-toxic replacements for inorganic pigments and photocatalysts. [87, 2, 100, 94, 81, 278, 32, 154, 137, 78, 167] Specifically, the rather unusual dielectric and magnetoresistive behavior of AMO_2N compounds (A=alkaline earth and M=transition metal)[102, 298, 83, 92] have garnered attention since Kim *et al.* [103] reported their dielectric properties. It has been observed that the dielectric polarizability of parent perovskite oxides is enhanced in these compounds when more polarizable ions are aliovalently substituted into the lattice [202]. At the same time, the reduced electronegativity of the nitride ion increases the covalency of the cation-anion bonds, increasing the probability of a

second-order Jahn-Teller distortion involving the d^0 cation. [73, 15, 21] Finally, local ordering of O and N affect the electronic properties of these materials, including a tendency for Ta off-centering and thus increased polarizability[172, 281, 297, 170, 276].

Distortions of the perovskite structure occur when a size mismatch of the constituent atoms is present. The Goldschmidt tolerance factor[65] τ gives an indication of how well the sizes of the ions match with each other, defined as:

$$\tau = \frac{(r_A + r_X)}{\sqrt{2}(r_{Ta} + r_X)} \tag{2.1}$$

where r_A, r_{Ta}, and r_X are the radii of the A, Ta, and X=O/N ions respectively (r_X being a weighted average of the oxygen and nitrogen anion radii). An ideal perovskite has a tolerance factor of unity. As τ increases beyond 1, the cubic structure becomes increasingly less stable relative to structures of lower symmetry and ion displacements occur to attain maximized electronic stabilization. When smaller than ideal A-site cations are present, τ is below 1 and the octahedra tilt, also resulting in a structure of lower symmetry. $BaTaO_2N$, $SrTaO_2N$ and $CaTaO_2N$ have been reported as cubic $Pm\bar{3}m$, tetragonal $I4/mcm$, and orthorhombic $Pnma$ at room temperature, respectively.[103] The average crystal structures, tolerance factors and perovskite tilt systems for the series are listed in Table 2.1, and the crystallographic unit cells are depicted in Figure 2.1. $BaTaO_2N$ has a tolerance factor of 1.043, Ta has been observed to exhibit local Ta off-centering, increasing electronic stability[172, 184]. The tolerance factor of 0.985 in $SrTaO_2N$ suggests octahedral tilting plays a larger role in the overall lattice energy compared to $BaTaO_2N$. $CaTaO_2N$ has a tolerance factor of 0.937, indicating an octahedral tilting distortion is certain to be present.

In the classification proposed by Glazer[64] and refined by Woodward[257, 258], and Howard and Stokes[84, 85], $SrTaO_2N$ takes on the $a^0a^0c^-$ structure, where octahedra tilt about the c-axis and adjacent ab-layers rotate in opposite directions (out of phase). In this tetragonal cell, Ta does not displace from the center of octahedra, but the two apical anions are positioned slightly closer to Ta than the

Table 2.1: Average structures, tolerance factors and tilt systems for $ATaO_2N$ (A= Ba, Sr, Ca).

	τ	Crystal System	Space Group	Tilt System
$BaTaO_2N$	1.043	Cubic	$Pm\bar{3}m$	$a^0a^0a^0$
$SrTaO_2N$	0.985	Tetragonal	$I4/mcm$	$a^0a^0c^-$
$CaTaO_2N$	0.937	Orthorhombic	$Pnma$	$a^-b^+a^-$

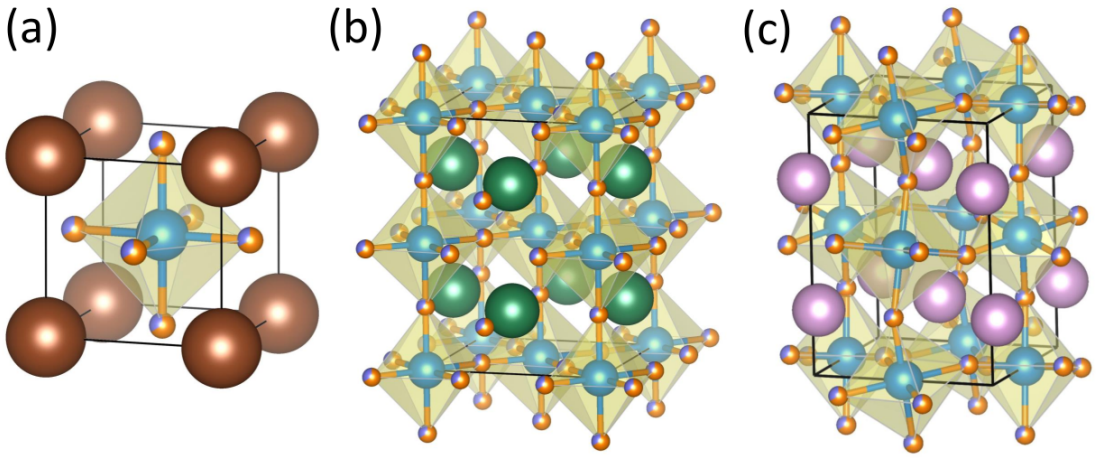


Figure 2.1: Average crystal structures of $ATaO_2N$ (A= Ba, Sr, Ca): (a) $BaTaO_2N$, $Pm\bar{3}m$, viewed almost along a-axis; (b) $SrTaO_2N$, $I4/mcm$, viewed almost along a-axis; and (c) $CaTaO_2N$, $Pnma$, viewed almost along c-axis. $Ta(O/N)_6$ octahedra are shown as yellow. Ba, Sr, and Ca are shown as brown, green, and mauve spheres, respectively. The blue spheres represent Ta, and the orange-purple mixed spheres represent the 2/3 and 1/3 partially O and N occupied anion sites.

four equatorial anions. The tilting along the c-axis leads to a modified coordination environment around the Sr cation. $CaTaO_2N$ takes on the $a^-b^+a^-$ structure, with in phase tilting along the b-axis and out of phase tilting about the a and c axes. Thus the coordination environments of the cations are strongly impacted.

Typically, O and N are reported as disordered using average techniques, notably neutron diffraction, on the anion sublattice sites in the $ATaO_2N$ series, as depicted in Figure 2.1. To preface: with respect to anion order in AMO_2N compounds, *cis* models are those where the 2 N on corners of the TaO_4N_2 octahedron share a common edge and *trans* models are those where the 2 N occupy positions on either side of an octahedron, forming linear N-Ta-N bonds. Local, intermediate, or long-range order of N anions has been observed in the $ATaO_2N$ series of compounds. Anion sublattice order is a known strategy for inducing chiral or polar atomic arrangements[74], and thus is of great interest in understanding electronic, magnetic, and other functional properties.

In the family of tantalum oxynitrides $ATaO_2N$ (A= Ba, Sr, Ca), polycrystalline $BaTaO_2N$ and $SrTaO_2N$ have high bulk permittivity, approximately 4900 (with a moderate temperature coefficient of 1140 ppm/K) and 2900 (with -730 ppm/K) near room temperature, respectively.[103] It has been discussed that these very high bulk permittivity values are likely not intrinsic values, as factors such as ceramic porosity, grain boundary effects, and nitrogen vacancies are known to affect dielectric responses, conductivity, and other electronic properties.[102, 83, 220, 275, 276] Nonetheless, later studies on dense $BaTaO_2N$ ceramics, formed via sintering with additives and post-treatment with ammonolysis, report relatively high permittivities (620 at 10^2 Hz and 320 at 10^8 Hz),[83] significantly higher than the values reported for similarly prepared $SrTaO_2N$ in the same frequency range[220]. In addition, similar trends are observed in thin films: highly crystalline $BaTaO_2N$ thin films have been reported to have a dielectric constant of 220,[102] and $SrTaO_2N$ thin films a dielectric constant of 80.[308] While the electronic properties of thin films may be influenced by their own extrinsic effects, such as interfacial bonding or epitaxial stress of substrates, experimental

studies across sample types consistently indicate high/moderately high dielectric constants and near temperature/frequency independent dielectric permittivity in $BaTaO_2N$ and (to a lesser extent) $SrTaO_2N$. In contrast to other high-permittivity materials, such as a material near a ferroelectric transition, like $Ba(Ti,Sn)O_3$ [59], no evidence of the phase transition was detected in these materials on cooling from room temperature. Materials possessing high permittivities are typically associated with polar behavior and often display phase transitions to lower symmetry structures. These displacements are the origin of ferroelectricity.

We have previously examined the local structure of $BaTaO_2N$ using pair distribution function (PDF) analysis of neutron total scattering data and DFT simulations [172]. While the average structure was found to be cubic, with fully disordered O and N occupancy on the perovskite anion sites, the local structure favored a *cis* configuration of N-Ta-N bonding within octahedra and small Ta displacements towards the N atoms[172]. Kim et al. later uncovered frustrated one-dimensional polar nanoregions in $BaTaO_2N$ through analysis of electron diffraction diffuse scattering intensities, and suggested they are intrinsic to the fundamental underlying crystal chemistry of the material. Though local chemical O/N ordering was thus not reasoned to be directly responsible for the material's dielectricity, the authors suggested that associated local strain distortions may inhibit long-range ordered ferroelectric states in the material.[253] Since then, anion order was also examined with electron diffraction and variable temperature neutron diffraction in $SrTaO_2N$ [281]. A variety of reports have observed and often linked the presence of local-to-intermediate length-scale *cis* ordering of N to specific short-range structural features such as tilting of octahedra and off-centering of Ta cations. The local order is sometimes seen to give rise to zig-zag, chain, or other cooperative ordering motifs of cations in the perovskite lattice. Local atomic *cis* configuration with concomitant octahedral tilting around the c-axis was observed with neutron diffraction [297]. Subsequently, a lower symmetry orthorhombic $Fmmm$ supercell, allowing for effects of both tilting and local *cis* anion order was reported. This model introduces a

change from $a^0a^0c^-$ to $a^0b^0c^-$ tilting modification in Glazer notation, allowing for the chemical inequivalence between O and $O_{0.5}N_{0.5}$ anion sites in the ab-plane.[34] A second-order phase transition consequent upon the loss of the R_5^- (a,0,0) (rotation about the c axis) mode of $SrTaO_2N$ was observed at 400-450 K with time-of-flight (TOF) powder neutron diffraction[235]. Local *cis* ordering has been seen to give rise to disordered zig-zag A-Ta (A= Ba, Sr) chains with the perovskite lattice.[281, 22, 12, 170, 169, 91, 58] This includes observation of a crossover from two to three-dimensional local chain order in Ba-Sr perovskite oxynitride solid solutions[91]. All these cases give rise to local cation displacements and thus potential local/disordered dipoles within the systems. Electronic-structure DFT simulations applied to investigate the anion order in $ATaO_2N$ (A= Ba, Sr) [79] agree well with neutron diffraction structural analysis for the stability of *cis*-TaO_4N_2. In striking contrast, the electronic properties of $CaTaO_2N$ are similar to those of the insulating perovskite oxides. In brief, the dielectric constant of $CaTaO_2N$ is lower than those of $BaTaO_2N$ and $SrTaO_2N$ by $\approx$ 2 orders of magnitude, and the electrical conductivity by $\approx$ 3 orders of magnitude (Supplementary Information, SI, Figure S2.1). As discussed above, these very high values are likely influenced by porosity or other extrinsic effects; yet the observed relative property trends in the $ATaO_2N$ family persist under densification/sintering studies and for thin films. Although the electronic properties of $CaTaO_2N$ have been studied by experiments [13] and calculations[82], and the local anion order has been investigated with first-principles approaches [256, 108, 276], the origin of the large difference of bulk dielectric permittivities among the $ATaO_2N$ series is still unknown. Recent theoretical studies incorporating anion configuration effects successfully capture the trend in decreasing dielectric constant in $BaTaO_2N$, $SrTaO_2N$ and $CaTaO_2N$, but the calculated values are severely underestimated for $BaTaO_2N$ and overestimated for $CaTaO_2N$, relative to experimentally observed values.[276] Herein we examine the average and local crystal structures of $ATaO_2N$ (A=Ba, Sr, Ca) compounds with neutron total scattering, DFT and AIMD simulations, to give insight into the factors that may influence dipole

formation and frustration within the functional materials family. We present for the first time the experimental analysis of local ordering in $CaTaO_2N$, evaluated in the context of the family of $ATaO_2N$ perovskites with decreasing A (A=Ba, Sr, Ca) cation size. Our experimental analyses of $BaTaO_2N$ and $SrTaO_2N$ support previous studies, while our combined experimental and theoretical approach uncovers key relationships between A cation size and structure-property trends involving Ta off-centering, octahedral tilting and local anion ordering in the series.

2.2 Experimental and Computational Details

2.2.1 Materials synthesis

$ATaO_2N$ (A=Ba, Sr, Ca) compositions were prepared by ammonolysis reaction as reported by Kim *et al.*.[103] The syntheses of $BaTaO_2N$ and $SrTaO_2N$ were conducted as follows; briefly, $BaCO_3$(J.T. Baker, 99.8 %)/$SrCO_3$(Aldrich 99.9 %) and Ta_2O_5 (Cerac, 99.5%) were stoichiometrically mixed, pressed in a pellet, and heated in flowing anhydrous ammonia (99.99%, $\approx$ 0.5mL/sec) to 1223 K - 1273 K at a rate of 5 K/min. After holding for 80 h, the product was cooled at 10 K/min. The preparation of $CaTaO_2N$ was similar (using $CaCO_3$ (Mallinckrodt, 99.9+%) as precursor). However, in this case, it was necessary to react an intermediate pyrochlore phase ($Ca_2Ta_2O_7$) in a 50/50 wt% NaCl/KCl flux for 80 h to produce stoichiometric $CaTaO_2N$ without impurity phases. As previously reported, the resulting color of $BaTaO_2N$ powder is red-brown, the $SrTaO_2N$ powder is orange-red in color, and the $CaTaO_2N$ powder is yellow in color.

2.2.2 Neutron total scattering and data analysis

TOF neutron powder diffraction data were collected on the Neutron Powder Diffractometer (NPDF) instrument at the Los Alamos National Laboratory Lujan Neutron Scattering Center [181] at room temperature. The high reciprocal space

scattering vector magnitude, $Q = 4\pi \sin\theta/\lambda$, moderate-to-high resolution, and low background intensities of diffraction measurements obtained at this instrument lend it to high quality PDF studies. Approximately 2 g of powder were loaded into a vanadium can for the experiment, and data were collected for 12 h for each sample. The diffraction data were analyzed with the Rietveld method as embodied in the TOPAS-V7 [36] program. Models with disordered anion sites (2/3 O and 1/3 N occupy all anion sites), occupancy refined anion sites (distributions on sites are refined, constrained to sum to the 2/3 O and 1/3 N average occupancy), fixed *trans* ordered anion sites (with N occupying axial anion positions and O occupying equatorial anion positions), and fixed '50/50-75/25' anion sites[297] (occupancies of O/N are 50/50 at 4*a* site for $SrTaO_2N$ and at 4*c* site for $CaTaO_2N$, and 75/25 at 8*h* site for $SrTaO_2N$ and at 8*d* site for $CaTaO_2N$) were constructed (see details in SI Table S2.1), based on parent $I4/mcm$ symmetry for $SrTaO_2N$ [103, 281, 298] and $Pnma$ symmetry for $CaTaO_2N$ [103]. In addition to the anion occupancy parameters identified for the specific above models, background parameters, scale factors, lattice parameters, isotropic atomic displacement parameters, profile parameters, and atom positions were refined. Anisotropic atomic displacement parameters were additionally refined for the best fitting Rietveld refinement models. The pattern weighted residual (R_{wp})[42] value, defined by

$$R_{wp} = \sqrt{\frac{\sum_t \omega_t (y_t^o - K y_t^c)^2}{\sum_t \omega_t (y_t^o)^2}} \tag{2.2}$$

where y_t^o and y_t^c are, respectively, the observed and calculated counts corresponding to the tth point in the powder diffraction profile, K is a scale factor and ω_t is a weighting factor (approximated as a Poisson distribution in the counting statistics, ω_t=$1/y_t^o$), was used to evaluate the quality of refinements.

To probe the local structure in real space, the program PDFGetN [177] was used to extract the experimental PDF from the total scattering data. Background and container contributions were subtracted and the data were corrected for detector

deadtime, absorption, multiple scattering, and were normalized by the incident flux and total sample scattering cross-section. The maximum Q vector used for the experiment was 30 Å^{-1}. 'Small-box' PDF refinements were carried out in the program PDFgui [50], beginning with the structure models determined from Rietveld analysis. Anion-ordered unit cell variants of the respective crystal symmetries were tried as real-space models (all high symmetry anion ordered substructures, as determined in the Bilbao Crystallographic Server[11] program). Refinements included the scale factor, lattice parameters, quadratic peak sharpening parameter for correlated atomic motion, and isotropic atomic displacement factors. Instrument parameters for real-space dampening and broadening were fixed to values determined through refinement of a crystalline standard material. Weighted residual (R_{wp})[48], similar to the Rietveld value, defined as

$$R_{wp} = \sqrt{\frac{\sum_{i=1}^{N} \omega(r_i)[G_{obs}(r_i) - G_{calc}(r_i)]^2}{\sum_{i=1}^{N} \omega(r_i) G_{obs}^2(r_i)}} \tag{2.3}$$

where G_{obs} is the observed PDF, G_{calc} is the calculated model PDF, and ω is the associated weighting factor, was used to assess the refinement quality.

'Large-box' fitting of neutron total scattering data was carried out with the Reverse Monte Carlo (RMC) approach using the RMCProfile[226, 294] package. Three types of starting structures were applied to explore the local structure of $ATaO_2N$. In the first series, the starting atomic configurations were derived on the basis of the respective average atomic structures ($Pm\bar{3}m$ for $BaTaO_2N$, $I4/mcm$ for $SrTaO_2N$, $Pnma$ for $CaTaO_2N$). The starting atomic configurations contained $10 \times 10 \times 10$ unit cells of $ATaO_2N$ (A=Ba, Sr, Ca), resulting in a total of 5000 atoms for $BaTaO_2N$, 20000 atoms for $SrTaO_2N$, and 20000 atoms for $CaTaO_2N$. RMC refinements involved the simultaneous fitting of neutron PDF, normalized neutron total scattering structure factor data, and neutron Bragg data. Whole configuration-based bond valence sum (BVS) constraints were applied and site-swapping of O and N atoms in the lattice was allowed. The number of moves generated per atom are

$\approx$ 2613 for $BaTaO_2N$, $\approx$ 450 for $SrTaO_2N$, and $\approx$ 371 for $CaTaO_2N$. The number of moves accepted per atom are $\approx$ 187 for $BaTaO_2N$, $\approx$ 40 for $SrTaO_2N$, and $\approx$ 43 for $CaTaO_2N$. In the second series, anion atoms were ordered (fixed) to occupy distinct *cis* or *trans* positions within the anion sublattices (*trans*-$P4/mmm$ and *cis*-$Pbmm$ for $BaTaO_2N$, *trans*-$I4/mcm$ and *cis*-$Ima2$ for $SrTaO_2N$, *trans*-$Pnma$ and *cis*-$Pmn2_1$ for $CaTaO_2N$). Atomic structures contained $10 \times 10 \times 10$ unit cells of $ATaO_2N$ with a total of 10000(*cis*)/5000(*trans*) atoms for $BaTaO_2N$, 20000 atoms for $SrTaO_2N$, and 20000 atoms for $CaTaO_2N$. The number of moves generated per atom are $\approx$ 516(*cis*)/1821(*trans*) for $BaTaO_2N$, $\approx$ 383(*cis*)/243(*trans*) for $SrTaO_2N$, and $\approx$ 387(*cis*)/387(*trans*) for $CaTaO_2N$. The number of moves accepted per atom are $\approx$ 41(*cis*)/121(*trans*) for $BaTaO_2N$, $\approx$ 31(*cis*)/32(*trans*) for $SrTaO_2N$, and $\approx$ 40(*cis*)/43(*trans*) for $CaTaO_2N$. For the third series, anions were arranged to occupy *cis* positions within individual octahedra, but were patterned within a supercell to feature '90-deg' configurations of each pair of *cis*-TaO_4N_2 octahedra sharing an axial N, forming two similar 3D distribution of the -Ta-N-Ta-N *cis*-chains motifs, as proposed by Hinuma [79] (resulting in $P2$ symmetry for $BaTaO_2N$ and $SrTaO_2N$). These atomic structures contained $8 \times 4 \times 8$ unit cells of $BaTaO_2N$ with a total of 20480 atoms, $4 \times 8 \times 8$ unit cells of $SrTaO_2N$ with 20480 atoms, and $11 \times 4 \times 11$ unit cells of $CaTaO_2N$ with 19360 atoms (created with $P1$ symmetry). The number of moves generated per atom are $\approx$ 365 for $BaTaO_2N$, $\approx$ 242 for $SrTaO_2N$, and $\approx$ 443 for $CaTaO_2N$. The number of moves accepted per atom are $\approx$ 33 for $BaTaO_2N$, $\approx$ 26 for $SrTaO_2N$, and $\approx$ 46 for $CaTaO_2N$. For the second and third series refinements (featuring fixed anion site order) the neutron PDF and normalized neutron total scattering structure factor data were fit, no BVS constraints were applied, and no atomic site swapping was allowed.

2.2.3 Computational details

DFT simulations were conducted within the Vienna *ab initio* simulation package (VASP) [106] using the PBEsol functional [176, 175]. The standard projector augmented wave (PAW) method [107] was used with the Ba_sv ($5s^2 5p^6 6s^2$), Sr_sv ($4s^2 4p^6 5s^2$), Ca_sv ($3s^2 3p^6 4s^2$), Ta_pv ($5p^6 5d^3 6s^2$), O ($2s^2 2p^4$) and N ($2s^2 2p^3$) potentials supplied with VASP. Electron wave functions were expanded in plane waves up to a cutoff energy of 500 eV and the forces on the ions were relaxed below 0.001 eV/Å. The Brillouin zone was sampled with a $9 \times 9 \times 9$ Γ-centered k-point mesh for the smallest tetragonal unit cell used in this work and a similar mesh density was used for other supercell calculations. Hubbard U values of 5 eV were applied to Ta 5d for partial density of states (PDOS) calculations. The energy convergences were tested to ensure reasonable results. AIMD simulations using the NVT ensemble [252] were carried out via the algorithm of Nosé [166] to control the temperature oscillations during the DFT simulations. Brillouin zone integration was done on a single Γ-centred k-point and the cutoff energy was reduced to 420 eV for all AIMD simulations. We used the anion ordered supercells with '90-deg' configuration of each pair of *cis*-TaO_4N_2 octahedra sharing an axial N, as proposed by Hinuma [79]. Each AIMD simulation ran for 2500 steps with a time-step of 1 fs. The last 2000 steps were used to generate the time averaged structure at each temperature.

2.3 Results and Discussion

2.3.1 Average structure from neutron diffraction

Figure 2.2 and Table 2.2 display the results of neutron diffraction Rietveld analysis for $SrTaO_2N$ and $CaTaO_2N$ datasets (results are reported for $BaTaO_2N$ as cubic perovskite $Pm\bar{3}m$ with 2/3 O and 1/3 N occupancy on the anion site in Page et al. [172]). A summary of the Rietveld refinement results based on the four types of anion site occupancy models applied are shown in SI Table S2.1 for comparison. It is

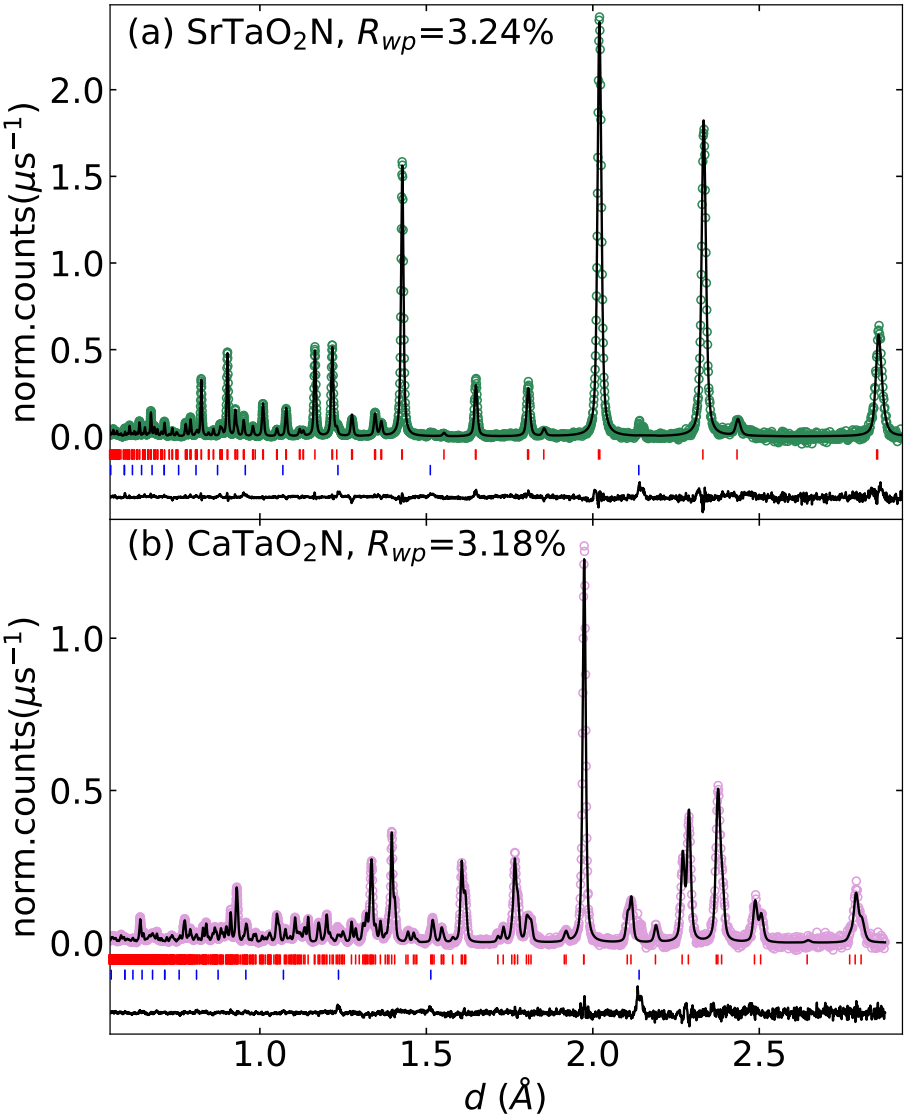


Figure 2.2: (a) $SrTaO_2N$ and (b) $CaTaO_2N$ Rietveld refinement results for the NPD data (119° detector bank) with anion site fixed 50/50-75/25 and disordered O/N anion models, respectively. Data are given as green ($SrTaO_2N$) and mauve ($CaTaO_2N$) circles and the solid lines through the data are fits using the $I4/mcm$ and *Pnma* structures, respectively. The black difference curves are displayed below the data and fits. Phase markers are displayed as vertical lines between the fit and difference curves (red markers correspond to the hkl indices of the refined perovskite phase, while blue markers correspond to those of a parasitic vanadium phase resulting from incomplete container scattering subtraction). The vanadium phase markers are shown for reference only; the phase was not included in the Rietveld refinements.

Table 2.2: Lattice parameters, atomic positions, and isotropic atomic displacement parameters resulting from Rietveld refinement of neutron powder diffraction (NPD) data for $SrTaO_2N$ and $CaTaO_2N$ with anion site fixed 50/50-75/25 model and disordered O/N anion model, respectively.

atom	Wyck.	x	y	z	U_{iso} (Å^2)	Frac.
$SrTaO_2N$ in $I4/mcm$: a=b=5.7052(0)Å, c=8.0836(2)Å, R_{wp}=3.24%						
Sr	4*b*	0	0.5	0.25	0.0114(2)	1
Ta	4*c*	0	0	0	0.0081(2)	1
O1/N1	4*a*	0	0	0.25	0.0171(7)	0.5/0.5
O2/N2	8*h*	0.2690(1)	0.7690(1)	0	0.0185(4)	0.75/0.25
$CaTaO_2N$ in $Pnma$: a=5.6229(2)Å, b=7.9000(3)Å, c=5.5539(2)Å, R_{wp}=3.18%						
Ca	4*c*	0.0311(5)	0.25	0.9910(7)	0.0199(5)	1
Ta	4*b*	0.5	0	0	0.0067(2)	1
O1/N1	4*c*	0.4806(4)	0.25	0.0762(3)	0.0168(5)	0.6667/0.3333
O2/N2	8*d*	0.2906(2)	0.0406(2)	0.7090(2)	0.0141(3)	0.6667/0.3333

noted that the anion distribution is found to be correlated with the refined atomic displacement parameters, and we have favored models with fewer parameters and lower isotropic atomic displacement parameters when presenting overall results in Figure 2.2 and Table 2.2.

In the case of $SrTaO_2N$, the $I4/mcm$ model with anion site occupancy fixed 50/50-75/25 resulted in an overall R_{wp} of 3.24% (shown in Figure 2.2 (a)). Fitting that allows O/N occupancy of anion positions to be refined results in a minimal improvement in quality of refinement, with a R_{wp} value of 3.23%; a disordered anion site model provides a slightly worse fit, with R_{wp} of 3.26%; while the fixed *trans* anion site model results in significantly worse agreements, with an R_{wp} value of 3.35%. Our designation of the average structure model with occupancies of O/N as 50/50 at the $4a$ site and as 75/25 at the $8h$ site is consistent with several previous reports[297, 35].

In the case of $CaTaO_2N$ data, within the $Pnma$ perovskite structure, a model with disordered anions (with 2/3 O and 1/3 N) in each of the $4c$ (axial) and $8d$ (equatorial) anion positions provides the same quality of fit as a model with an additional parameter for refinement of anion occupancies (R_{wp} of 3.18%). The refined site occupancy values are very close to the 2/3 O and 1/3 N average occupancy values. The anion model with O/N occupancy of 50/50 at the $4c$ site and 75/25 at the $8d$ site in $CaTaO_2N$ provides a slightly worse refinement result in our analysis (with an overall R_{wp} of 3.22%). The small increase in R_{wp} is accompanied by a factor of 1.5 difference in the anion site U_{iso}s, suggesting that the $4c$ site wants less N and the $8d$ site more N, in line with the lower R_{wp} and more-or-less equal U_{iso}s for the disordered or occupancy refined models. The model with fixed *trans* anion sites results in a significantly worse agreement, with a R_{wp} value of 3.68%. Thus the disordered anion site model is presented here (shown in Figure 2.2 (b)) as the determined average crystallographic structure of $CaTaO_2N$.

Anisotropic displacement parameters were also applied to our best fitting models for $SrTaO_2N$ and $CaTaO_2N$. For $SrTaO_2N$, the R_{wp} value was improved by 0.08%, while for $CaTaO_2N$ the value improved only 0.01%. The resulting parameters

are reported in SI Table S2.2, along with corresponding structure models shown with 99% probability thermal ellipsoids in Figure S2.2. Values for $SrTaO_2N$ were found to be similar to those previously reported in the literature[297], featuring pancake-like displacement ellipsoids for equatorial anions and ellipsoids significantly elongated along [001] for Sr. Due to the overall similar refinement quality, the models with isotropic atomic displacement parameters (which involve fewer parameters) are presented in this paper.

The average structure results for $SrTaO_2$ in this study are consistent with other reports favoring anion site fixed 50/50-75/25 models [297, 35]; however, fully *trans* N ordered $I4/mcm$ $SrTaO_2N$ (with N occupying axial anion positions and O occupying equatorial anion positions)[70], as well as occupancy refined $I4/mcm$ $SrTaO_2N$ [281, 297] and $Pnma$ $CaTaO_2N$ [70] have been reported. It has been observed that anion ordering in these crystal structures can be strongly impacted by variation in sample preparation. Particularly, results suggest complete disorder is favored in perovskite structures when materials are prepared by nitridation of pure oxide precursor at 900 to 1000 °C, or by reacting alkaline earth oxide with TaON at 1500 °C under nitrogen. Full ordering has been observed when a mineralizer is used in nitridation[35]. These assertions have not been systematically studied, and we must assert that our experimental results may be unique only to the samples we have studied[103]. Nonetheless, we expect the observed trends across the series to be meaningful.

Interestingly, there are several features of the Rietveld results (Table 2.2) suggesting possible atomic distortions, chemical short-range order (CSRO), or other potential disorder effects in the two systems. First, significant anisotropic atomic displacement ellipsoids for Sr and O/N are found to improve the $SrTaO_2N$ model fits (See SI Figure S2.2). Second, the isotropic atomic displacement parameters for Ca are higher than typically observed, particularly in comparison to the O/N atomic displacement parameters. In general, for a well ordered crystalline material, the displacement factors refined for lighter elements are higher than those refined

for heavier elements. In a previous neutron diffraction study of $BaTaO_2N$, a large atomic displacement parameter was observed for Ta, but not for Ba nor N/O[101]. The distinct atomic displacement parameter features of $ATaO_2N$ imply that their stabilities are achieved by different structural relaxations, depending on the type of A (A=Ba, Sr, Ca) involved. To examine the nature of CSRO and local atomic displacements thought to be key to the functional properties of the $ATaO_2N$ family, the local structures of $SrTaO_2N$ and $CaTaO_2N$ must be considered (as discussed, partial results for $BaTaO_2N$ were reported previously[172]).

2.3.2 Local and intermediate range structure

Real-space refinements using the models determined by Rietveld analysis for the average structures ($I4/mcm$ fixed 50/50-75/25 model for $SrTaO_2N$ and $Pnma$ disordered anion model for $CaTaO_2N$) were applied to two different pair distribution function (PDF) length scales: a local structure range from 1.5 to 6 Å in r; and an intermediate range from 6 to 50 Å in r. The results are shown in Figure 2.3. It can be seen that the models provide a good fit to the whole PDF range (both 1.5 to 6 Å, R_{wp} of 11.03% and 6 to 50 Å, R_{wp} of 11.07%) for $SrTaO_2N$. In the case of $CaTaO_2N$, the average structure describes the intermediate range well (6 to 50 Å, R_{wp} of 14.43%), but fails to model all features of the local range (1.5 to 6 Å, R_{wp} of 15.70%). The nearest-neighbor Ta-O correlation is particularly poorly fit. The corresponding model parameters are given in Table 2.3 for 1.5 to 6 Å refinement and in Table 2.4 for 6 to 50 Å refinement. An $I4/mcm$ disordered anion model was additionally tried in the case of $SrTaO_2N$, and a $Pnma$ fixed 50/50-75/25 model was additionally tried in the case of $CaTaO_2N$. The results applying a disordered anion model for $SrTaO_2N$ are slightly worse (1.5 to 6 Å, R_{wp} of 11.31% and 6 to 50 Å, R_{wp} of 11.12%). Applying a $Pnma$ fixed 50/50-75/25 model for $CaTaO_2N$ results in a slightly improved fit in the low-r range (1.5 to 6 Å, R_{wp} of 15.50%), but not in the high-r range (6 to 50 Å, R_{wp} of 14.52%) comparing to the average model results. Also, the nearest neighbor

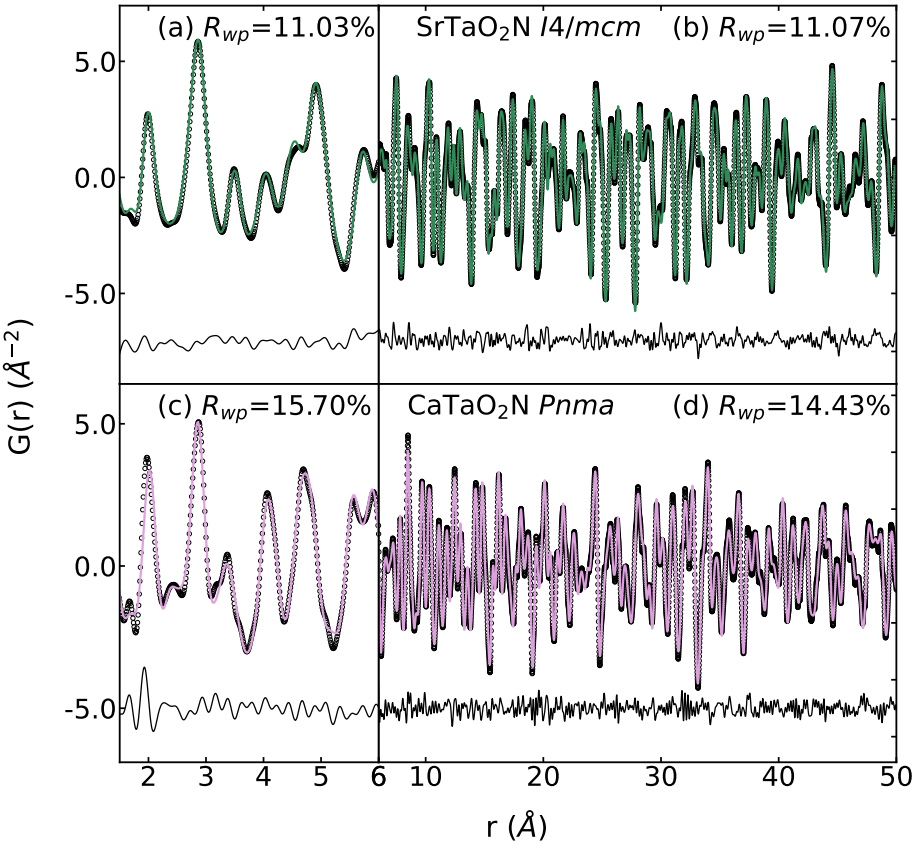


Figure 2.3: Real space PDF refinement results for $SrTaO_2N$ using the $I4/mcm$ fixed 50/50-75/25 model, displaying: (a) 1.5 to 6 Å local PDF fit and (b) 6 to 50 Å intermediate length-scale PDF fit; and for $CaTaO_2N$ using the *Pnma* disordered anion occupancy model, displaying (c) 1.5 to 6 Å local PDF fit and (d) 6 to 50 Å intermediate length-scale PDF fit. Experimental PDF data are shown as black circles for both $SrTaO_2N$ and $CaTaO_2N$. The fits are shown as green and mauve lines through the data for $SrTaO_2N$ and $CaTaO_2N$, respectively. The black difference curves are shown at the bottom of each panel and the fit quality values are noted at the top right of each sub figure for each fitted region.

Table 2.3: Refined lattice parameters, atomic positions, atomic displacement parameters and fixed O/N fractional site occupancies from $SrTaO_2N$ and $CaTaO_2N$ local PDF refinements (from 1.5 to 6 Å) with anion site fixed 50/50-75/25 model and disordered O/N anion model, respectively.

atom	Wyck.	x	y	z	U_{iso} (Å^2)	Frac.
$SrTaO_2N$ in $I4/mcm$: a=b=5.7690(13)Å, c=7.9258(33)Å, R_{wp}=11.03%						
Sr	4*b*	0	0.5	0.25	0.0048(2)	1
Ta	4*c*	0	0	0	0.0087(2)	1
O1/N1	4*a*	0	0	0.25	0.0080(2)	0.5/0.5
O2/N2	8*h*	0.2682(4)	0.7682(4)	0	0.0233(5)	0.75/0.25
$CaTaO_2N$ in $Pnma$: a=5.5893(63)Å, b=7.9488(68)Å, c=5.5404(56)Å, R_{wp}=15.70%						
Ca	4*c*	0.0302(9)	0.25	0.9835(13)	0.0059(6)	1
Ta	4*b*	0.5	0	0	0.0107(5)	1
O1/N1	4*c*	0.4814(16)	0.25	0.0790(10)	0.0079(6)	0.6667/0.3333
O2/N2	8*d*	0.2854(13)	0.0455(3)	0.7140(10)	0.0068(3)	0.6667/0.3333

Table 2.4: Refined lattice parameters, atomic positions, atomic displacement parameters and fixed O/N fractional site occupancies from $SrTaO_2N$ and $CaTaO_2N$ PDF refinements over an intermediate range from 6 to 50 Å with anion site fixed 50/50-75/25 model and disordered O/N anion model, respectively.

atom	Wyck.	x	y	z	U_{iso} (Å^2)	Frac.
$SrTaO_2N$ in $I4/mcm$: a=b=5.6978(1)Å, c=8.0771(4)Å, R_{wp}=11.07%						
Sr	4*b*	0	0.5	0.25	0.00796(3)	1
Ta	4*c*	0	0	0	0.00553(3)	1
O1/N1	4*a*	0	0	0.25	0.0171(2)	0.5/0.5
O2/N2	8*h*	0.2690(1)	0.7690(1)	0	0.0103(1)	0.75/0.25
$CaTaO_2N$ in $Pnma$: a=5.6206(3)Å, b=7.8975(4)Å, c=5.5506(2)Å, R_{wp}=14.43%						
Ca	4*c*	0.0331(2)	0.25	0.9935(5)	0.0095(1)	1
Ta	4*b*	0.5	0	0	0.0059(1)	1
O1/N1	4*c*	0.4800(2)	0.25	0.0770(2)	0.0088(2)	0.6667/0.3333
O2/N2	8*d*	0.2920(2)	0.0403(1)	0.7091(2)	0.0084(1)	0.6667/0.3333

Ta-O correlation remains poorly fit. These results confirm the selection of the average structures for $SrTaO_2N$ and $CaTaO_2N$ and indicate the existence of local ordering. It is noted there are sizable discrepancies in the magnitudes of the isotropic atomic displacement parameters (U_{iso}s) refined for specific atomic positions in the $SrTaO_2N$ and $CaTaO_2N$ models resulting from Rietveld, intermediate PDF, and local PDF fits. For example, the refined U_{iso} values for the Sr and O1/N1 positions in $SrTaO_2N$ are approximately 50% smaller for the low-r range (1.5 to 6 Å) PDF fit, relative to those for the intermediate PDF and Rietveld fits. Such observations are overall consistent with an order/disorder motif in the local to long-range structure. However, it is difficult to draw specific conclusions given the variation in trends observed across atomic positions and refinement length scales, and especially given the relatively poor quality of fit achieved in the $CaTaO_2N$ case.

To model the observed discrepancies between experimental PDFs and the fits from long-range (average) model structures we next considered structural variations resulting from specific octahedral tilting and CSRO patterns of nitrogen and oxygen in the average parent lattices. In the case of $SrTaO_2N$, modification of the $I4/mcm$ parent structure resulted in sub-space groups with variation of *cis* N ordering ($Ima2$), and sub-space groups with *trans* N ordering ($I\bar{4}2m$, $I422$, $I4m$, $I\bar{4}$, and $Ibam$). In the case of $CaTaO_2N$, modification of the $Pnma$ parent structure resulted in sub-space groups with *cis* N ordering (including $Pmn2_1$, $P2_12_12_1$, $Pna2_1$, and $Pmc2_1$), as well as sub-space groups with *trans* N ordering ($P2_1/c$, $P2_1/m$). The model structures explored are displayed in Figure 2.4 along with corresponding PDF fits. The best resulting fits to the local structure are shown in Figure 2.4 (f) and (i), corresponding to R_{wp} values of 9.17% and 7.78% for $SrTaO_2N$ and $CaTaO_2N$, respectively. The fits were obtained with the $Ima2$ model for $SrTaO_2N$ and $Pmn2_1$ model for $CaTaO_2N$, both exhibiting *cis* N ordering, matching the previously discussed experimental results (for Sr) and theoretical predictions (for Sr and Ca) in the literature.

To understand the effect of various model parameters on calculated PDFs, we completed sensitivity tests for *cis*, *trans*, and random site occupancy variants of

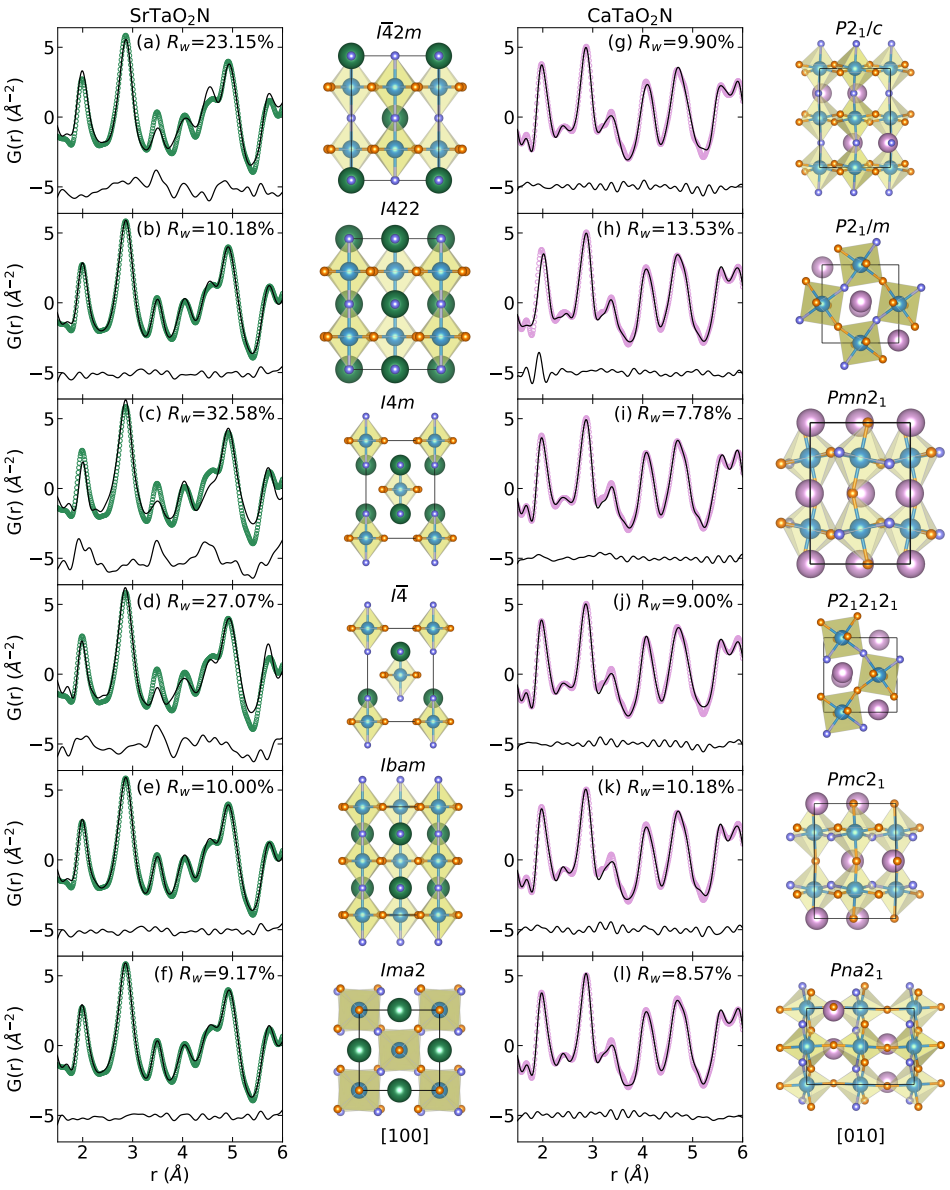


Figure 2.4: Real space PDF refinement results for $SrTaO_2N$ sub-space groups with *trans* N ordering ((a) $I\bar{4}2m$, (b) $I422$, (c) $I4m$, (d) $I\bar{4}$, and (e) $Ibam$) and *cis* N ordering (f) $Ima2$, with corresponding structures displayed beside them. Refinement results for $CaTaO_2N$, derived from the $Pnma$ parent structure, include sub-space group models with *trans* ordering ((g) $P2_1c$, (h) $P2_1m$), as well as sub-space groups with *cis* N ordering (including (i) $Pmn2_1$ (j) $P2_12_12_1$, (k) $Pmc2_1$, and (l) $Pna2_1$). Green and mauve circles correspond to the experimental PDF data for $SrTaO_2N$ and $CaTaO_2N$, respectively. Model fits are shown as black lines through the data. The difference curves are shown at the bottom of each panel and the fit quality values are noted at the top right (The best results for $SrTaO_2N$ and $CaTaO_2N$ are (f) and (i), respectively).

$CaTaO_2N$ and $SrTaO_2N$ structures, included asSI Figure S2.3. We note there is a weak real-space dependence on the various models when anion order is considered alone. On the other hand, the PDF is strongly sensitive to local atomic features such as octahedral tilting and Ta off-centering, which may possibly be related to specific local/intermediate length-scale metal-anion bonding patterns, as found for the local Ta off-centering towards N-N octahedral edges reported for $BaTaO_2N$[172], and the zig-zag chains found in other references.[281, 22, 12, 170, 169, 91, 58] Figure 2.4 shows that lower symmetry models (with increased degrees of freedom) are needed to capture the type of tilting and off-centering distortions present in $SrTaO_2N$ and $CaTaO_2N$. SI Table S2.3 summarizes the numbers of refined atomic coordinate parameters involved in the local structure model fits of Figure 2.4. It is the increased degrees of freedom which are principally responsible for improved local PDF fits (not the selection of *cis* or *trans* variants). The local structure models highlight the need for accompanying theoretical work to understand the relative importance of CSRO, octahedral tilting, and Ta off-centering in the series.

2.3.3 Reverse Monte Carlo modeling, AIMD and DFT analysis

RMC and AIMD analyses are experimental and theoretical 'large-box' modeling approaches that can produce a statistical ensemble reconciling local and long-range (average) structure configurations in disordered material systems. They are often valuable in providing additional detail regarding the extent and/or length-scale of local chemical ordering or local atomic displacements; thus being more representative of atomic configurations in real materials. The first series of RMC refinements were completed by fitting the Bragg diffraction data, PDF data, and normalized structure factor data, allowing N and O atoms to swap freely, and applying global BVS constraints. The modeling resulted in high fit quality, however, the models featured a large percentage ($\approx 65\%$) of $Ta(O/N)_6$ octahedra without the exactly 2

N and 4 O required for local charge balancing. This nonphysical anion order was accompanied by large atomic displacements, and it was therefore determined the models were inadequately constrained during refinement. Partial results and point clouds for this series of models are presented in Figure S2.4.

The RMCProfile program does not allow local bond valence constraints and atom site swapping to be applied simultaneously, thus it was found necessary to fix the ratio of O/N to 4/2 for each Ta environment in further modeling. Alternate symmetry elements are required in order to explore anion order within the unit cells or within unit cell superlattices which would create conditions for additional Bragg scattering peaks. Therefore, fitting to the Bragg profile was abandoned in subsequent RMC analysis trials. RMC refinement trials conducted beginning with fixed anion sublattice order again resulted in high fit quality, but featured nonphysically large variations in the statistical distribution of atomic site positions. Partial results and point clouds for this second series of models are presented in Figure S2.5 and S2.6. The starting atomic configurations were therefore judged to be too regular to successfully model the local to intermediate structure with RMC analysis. Overall, models with fixed *cis* N order in each octahedron resulted in more ordered configurations than those with fixed *trans* N order in each octahedron. For these reasons, and since the 'small-box' PDF models support local *cis* anion ordering, *cis* N ordered supercell models were selected as final starting atomic configurations in the RMC analysis.

The final RMC refinement results based on identified 3D distribution of the -Ta-N-Ta-N- *cis*-chains supercells are displayed in Figure S2.7, S2.8 and S2.9 for all $ATaO_2N$ data. It can be seen that the experimental data and the RMC simulations agree well. Atomic point clouds resulting from folding the final 'large-box' RMC configurations into a single unit cell volume are illustrated alongside conventional unit cell depictions in Figure 2.5 (a-c). Partial pair distribution functions g(r) resulting from RMC and AIMD analysis are shown in Figure 2.6 (RMC (a, b, c, d), AIMD (e, f, g, h)), with the results for the respective A cation types aligned. Several observations reveal a number of important trends in the structural series. First, RMC and AIMD

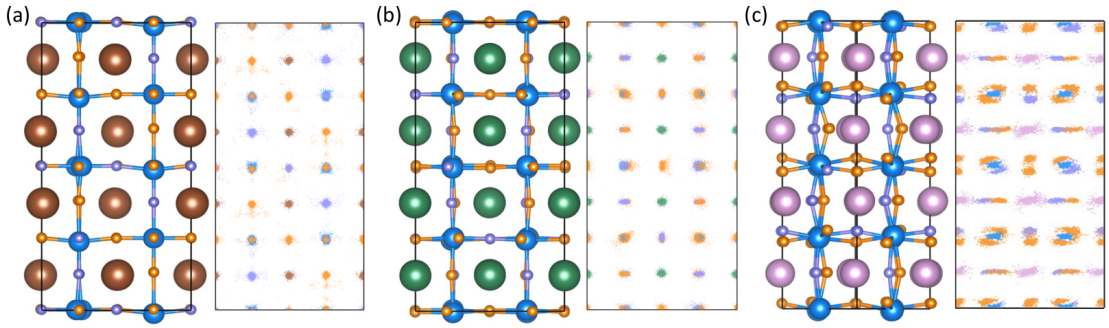


Figure 2.5: *cis* N ordered supercell structures (left) used in constructing RMC simulations and resulting point clouds of RMC simulations (right) of (a) $BaTaO_2N$, orthogonal to {001} (b) $SrTaO_2N$, orthogonal to {001} and (c) $CaTaO_2N$, orthogonal to $\{10\bar{1}\}$. The blue spheres represent Ta, the small orange spheres O, and the small purple spheres N. Ba, Sr, and Ca atoms are shown as brown, green, and mauve spheres, respectively.

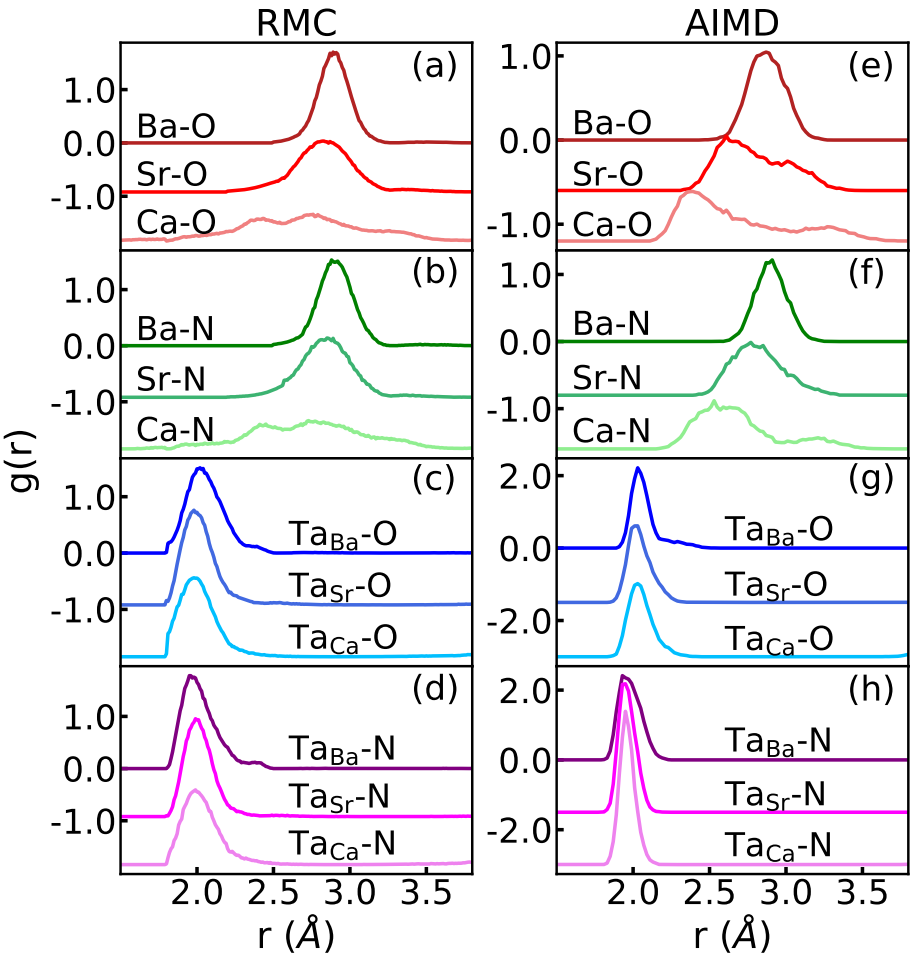


Figure 2.6: The $ATaO_2N$ (A=Ba, Sr, Ca) partial pair distribution functions (pPDF) from RMCProfile (RMC) for (a) A-O, (b) A-N, (c) Ta_A-O, (d) Ta_A-N and radial distribution functions (RDF) from AIMD simulations for (e) A-O, (f) A-N, (g) Ta_A-O, and (h) Ta_A-N. The supercells used in RMC and AIMD feature *cis* N in TaO_4N_2 octahedra with '90-deg' configuration at axial N as proposed by Hinuma[79]. $BaTaO_2N$, $SrTaO_2N$, and $CaTaO_2N$ correlations are depicted in each panel in darkest (Ba) to lightest (Ca) hues, respectively).

indicate that A-O (Figure 2.6 (a, e)) and A-N (Figure 2.6 (b, f)) distributions become shorter and broaden as A cation size (and perovskite tolerance factor) decreases. This is entirely consistent with the increasing degrees of octahedral tilting found traversing the series. This is manifest in the small and nearly spherical atomic point clouds for Ba in Figure 2.5 (a), the larger but mostly spherical point clouds for Sr in Figure 2.5 (b), and the widely distributed displacements in $CaTaO_2N$ preferring directions orthogonal to $\{10\bar{1}\}$ in Figure 2.5 (c). The agreement between RMC and AIMD models shown in this work strongly supports that the displacement of A-O (A=Ba, Sr, Ca) driven by radius/tolerance effects is characteristic of this compositional series.

The case is a little more interesting when it comes to Ta-O/N distributions. At first glance, the bonding within TaO_4N_2 octahedra appear strikingly similar across the A cation series. It can be seen that RMC analysis shows a distinct shorter Ta-N correlation than Ta-O correlation in $BaTaO_2N$. This is again found to agree with AIMD. Indeed, upon close inspection, Figure 2.5 (a) reveals Ta displacing towards N-N edges in TaO_4N_2 octahedra, in keeping with the previously reported *Pbmm* local structure model.[172]. This asymmetric TaO_4N_2 octahedra across the series provides a means for point-charge dipole formation and potential electronic domain fields. The off-centering of Ta in $BaTaO_2N$ relieves the strain field through cooperative displacements tied to observed *cis* N-N CSRO, while for $CaTaO_2N$, the strain is primarily relieved by octahedral tilting, accompanied by an apparently large degree of positional site disorder. The distortions lead to less cooperative (shorter length-scale) dipole correlations and thus a dielectric constant that is approximately two orders of magnitude lower and a bulk electronic conductivity that is approximately three orders of magnitude lower than those of $BaTaO_2N$ (SI Figure S2.1). It appears that the nature of local order in $SrTaO_2N$ lies somewhere in between, in keeping with the observed electronic property trends across the series.

AIMD also indicates that the Ta-O and Ta-N nearest neighbor correlations in $SrTaO_2N$ and $CaTaO_2N$ are distinct, with shorter Ta-N than Ta-O bonds (as one may expect according to the increased bond order of Ta-N). On the other hand, RMC

analysis of Sr and Ca compounds indicate similar average bond length distributions for Ta-N and Ta-O. It is not possible to distinguish with these results alone if this is a model/method limitation, or if this reflects true atomic structure. Regardless, the overall results indicate a propensity for local *cis* N order in all compounds, and increasing octahedral tilting and positional disorder as A cation size decreases.

It is advantageous to study these short range structures computationally as calculations can predict which configurations are energetically favorable and provide evidence of mixed phases or nanoscale domains based upon similar energies of competing structures. Various *trans* N and *cis* N ordered structures explored via DFT are depicted in Figure 2.7 (a) and (b), respectively. Briefly, the *cis* and *trans* variants of the models in each column (left to right) are constructed to be metrically identical. The *cis* N ordered models of $Pbmm$, $Ima2$ and $Pmn2_1$ correspond to the structures describing the best local fit for $BaTaO_2N$, $SrTaO_2N$ and $CaTaO_2N$, respectively (naturally corresponding to increasing degrees of freedom for octahedral tilting across the series). An additional *cis* ordered $Pbmm\_Ta_{fix}$ model is included that is metrically identical to the $Pbmm$ model, but fixes the location of the Ta atom to the center of the TaO_4N_2 octahedra (denoted with the subscript 'fix'). The *trans* models of $P4/mmm\_O_{fix}$, $P4mm$ and $Pnma$ are derived from the same lattice structures, with nitrogen positions transferred from *cis* ordering to *trans* ordering. A model with Ta fixed at the center of the TaO_4N_2 octahedra is also included here, labeled as $P4/mmm$. The electronic total and partial density of state (DOS and PDOS) and corresponding band gaps of $BaTaO_2N$, $SrTaO_2N$ and $CaTaO_2N$ (*cis* and *trans*) are shown in Figure S2.10 and Table S2.4. The PDOS of all three compounds exhibit similar features with increasing band gap ('band gap' refers to the energy difference between the upper part of the valence band (Fermi level) and the bottom of the conduction band), corresponding to the observed lower electrical conductivity and change in color as cation size is decreased across the series (the $BaTaO_2N$ powder is red-brown, the $SrTaO_2N$ powder is orange-red, and the $CaTaO_2N$ powder is yellow). The top of the valence band (below Fermi level = 0 eV) is mainly composed of N-2p

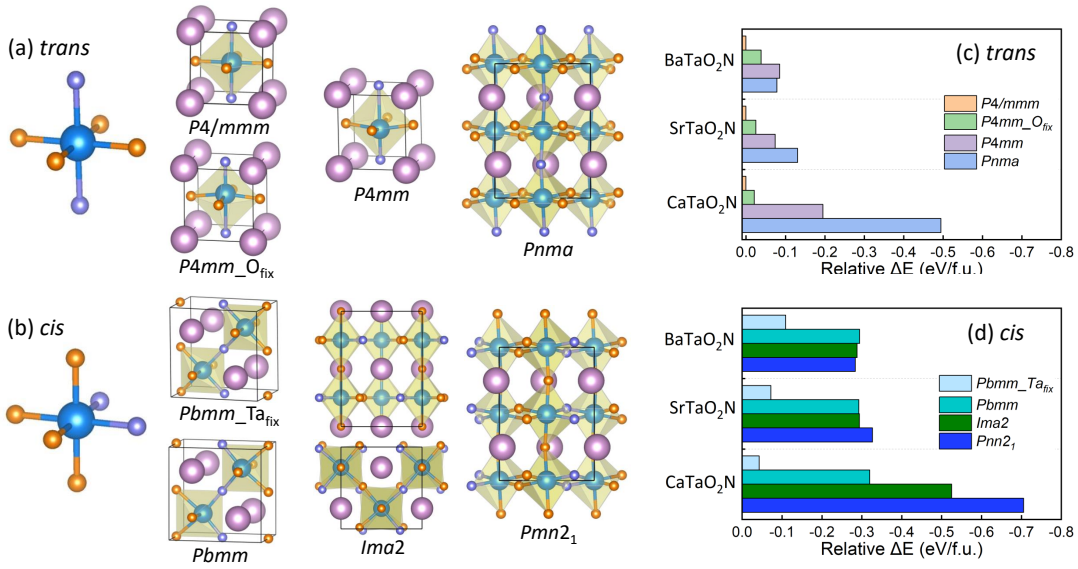


Figure 2.7: (a,b) Illustration of the *cis* and *trans* N ordered configurations of $ATaO_2N$ (M=Ba, Sr, Ca) examined with DFT analysis. $P4/mmm$ and $Pbmm\_Ta_{fix}$ models entail metrically cubic symmetry (equivalent to $Pm\bar{3}m$ lattice, with *cis* and *trans* sublattice order lowering the symmetry, respectively). For the energetics of the cubic $P4/mmm$ and $Pbmm\_Ta_{fix}$ structures, only the structure volume and shape were allowed to relax (atomic positions were fixed). In the $P4mm\_O_{fix}$ and $Pbmm$ variants, anion positions are fixed, but Ta is allowed to displace, according to the $P4mm$ and $Pbmm$ lattice symmetry. (c,d) Relative energies for relaxed *cis* and *trans* configurations of $BaTaO_2N$, $SrTaO_2N$ and $CaTaO_2N$ with corresponding ordered phase indicated. The calculated energy level is shown relative to the energy of the $P4/mmm$ structure, which has the highest energy.

and O-2p orbitals. The *cis* N ordered structures exhibit comparatively flat peaks, indicating greater energy stability relative to *trans* N ordered counterparts. The relative energies of *cis* and *trans* configurations of $BaTaO_2N$, $SrTaO_2N$ and $CaTaO_2N$ with different ordering schemes and lattice symmetries are shown in Figure 2.7(c) and 2.7(d). Here, the highest resulting energy, that of the $P4/mmm$ structure, is set as a baseline from which to compare relative sources of energy minimization. Closer inspection of the final energy differences from DFT simulations reveal a strong preference for *cis* ordering (greater energy minimization) for all three compounds. Within Figure 2.7 (c) and (d) the bars from top to bottom in each group correspond to the relative energy minimization attained by introducing lower symmetry (additional free parameters) for each compound.

In Figure 2.7 (d), the energy gain of all three compounds compared to the $Pbmm\_Ta_{fix}$ model stems primarily from Ta cation displacement, which introduces octahedral distortion due to short Ta-N and long Ta-O bonds, in agreement with the AIMD results and the RMC results for $BaTaO_2N$. In the case of $BaTaO_2N$, the $Pbmm$ model is the most favored, in agreement with our previous local structure work,[172] suggesting oxygen/nitrogen octahedral tilting does not provide additional stability to the structure. In contrast, $SrTaO_2N$ and $CaTaO_2N$ gain stability when the symmetry is lowered from $Pbmm$ to $Ima2$ and $Pmn2_1$, corresponding to increasing degrees of O/N octahedral tilting, especially in the $CaTaO_2N$ system (further DFT analysis comparing the impact of tilting modifications on distinct *cis* configurations in $CaTaO_2N$ are provided in SI Figure S2.11). This result is consistent with the analysis of PDF data in Figure 2.6 RMC (a, b) and AIMD (e, f) where the partial PDFs of A-O/N are significantly broadened traversing the A cation series. Crystalline solids maximize phase stability through structural relaxation. Particularly, the equilibrium structure of $ATaO_2N$ is decided by the interplay between the geometric preferences of the octahedral framework and the A cation, usually in such a way that the $Ta(O, N)_6$ octahedra tolerate the distorted environment imposed by the A cation. In $BaTaO_2N$, the larger-than-ideal Ba^{2+} maintains a cubic lattice

symmetry,[184] where the Ta(O, N)$_6$ are expanded to accommodate the large cation size. However, in $CaTaO_2N$, the smaller Ca^{2+} incurs octahedral tilting towards the optimum coordination environment. Noteworthy from the above DFT examination is that these distinct octahedral relaxations can lead to dissimilar energetics around the ground state. The lowest-level configuration of $CaTaO_2N$ is well separated from the others (Figure 2.7 (d)), which is not the case for $BaTaO_2N$ or $SrTaO_2N$. Certainly, the presence of a deeper energy minimum can provide a substantial inhibiting factor in the formation of atomic displacements and lattice polarization.

2.4 Conclusion

The local anion ordering and atomic distortions of tantalum oxynitride perovskites were investigated by combined neutron total scattering and computational analysis methods. It was found that *cis* N ordering models were favored over *trans* N ordering models in $ATaO_2N$ (A=Ba, Sr, Ca); we have confirmed this for the first time in $CaTaO_2N$ by neutron PDF modeling. In $BaTaO_2N$, Ta displacements significantly stabilize structures, and TaO_4N_2 tilting is minor. $SrTaO_2N$ was found to also be stabilized by Ta displacements; however, octahedral tilting played a more prominent role. In $CaTaO_2N$ calculations, structures were found to be dramatically stabilized by octahedral tilting. In general, it was observed that in systems with significant octahedral tilting, *cis* N ordering and associated Ta displacements had minimal effect on the overall energy. It appears these effects cooperate to stabilize local point-charge dipole correlations among TaO_4N_2 octahedra in $BaTaO_2N$, while this driving force is diminished progressively in the Sr and Ca cases. These results suggest that anion sublattice order as a materials design parameter may have a bigger impact on local dipoles and dipole ordering in perovskite systems with high tolerance factors (those with larger A-to-B site radius ratios). This work highlights the benefit of consistently employing combined theoretical and experimental approaches across a

materials family, providing insight into the roles various structural and chemical parameters play in directing structure-property trends.

Chapter 3

Local Cation Order and Ferrimagnetism in Compositionally Complex Spinel Ferrites

In this chapter, the exploration of a family of compositionally complex cubic spinel ferrites featuring combinations of Mg, Fe, Co, Ni, Cu, Mn, and Zn cations is presented. These materials are introduced as HEO spinel ferrites in Chapter 1, Section 1.1.2. Herein, the average and local atomic structure, chemical short-range order, magnetic spin configurations, and magnetic properties of the compounds are systematically investigated. All compositions result in ferrimagnetic average structures with extremely similar local bonding environments, however, the samples display varying degrees of cation inversion and therefore differing apparent bulk magnetization. Additionally, first-order reversal curve (FORC) analysis of the magnetic reversal behavior indicates varying degrees of magnetic ordering and interactions, potentially including local frustration. Reverse Monte Carlo (RMC) modeling of the spin orientation demonstrates a relationship between the degree of cation inversion and the spin collinearity. Collectively, these observations correlate with differences in synthesis procedures. This work provides a framework for understanding magnetic behavior

reported for "high-entropy spinels," revealing many are likely compositionally complex oxides (CCOs) with differing degrees of chemical short-range order– not meeting the community established criteria for high or medium entropy compounds. Moreover, this work highlights the importance of reporting complete sample processing histories and investigating local to long-range atomic arrangements when evaluating potential entropic mixing effects and assumed property correlations in high entropy and related materials.

Chapter 3– *Local Cation Order and Ferrimagnetism in Compositionally Complex Spinel Ferrites*– is reproduced from *APL Materials* 2022, 10, 121102, with the permission of AIP Publishing: DOI: 10.1063/5.0123728 [246]. The authors of the work are Xin Wang, Brianna L. Musicó, Corisa Kons, Peter C. Metz, Veerle Keppens, Dustin A. Gilbert, Yuanpeng Zhang, and Katharine Page.

3.1 Introduction

High entropy oxides (HEOs) are being increasingly reported in various oxide crystal structures, including in the perovskite, fluorite, spinel and pyrochlore structure motifs [88, 254, 255, 233, 224, 199, 118, 292, 127, 158, 171, 6, 221, 267, 193, 195, 6, 57, 149]. HEOs are generally described as single phase solid solution systems exhibiting five or more homogeneously distributed cations in equimolar or near-equimolar ratios on a single crystallographic site. When a positive entropy of formation (ΔS_f) overcomes a positive enthalpy of formation (ΔH_f), the Gibbs free energy of formation ($\Delta G_f = \Delta H_f - T\Delta S_f$) will be negative, making the system an entropy stabilized oxide (ESO). The ESO, a five component oxide $(Mg_{0.2}Ni_{0.2}Co_{0.2}Cu_{0.2}Zn_{0.2})O$, exhibiting a single rock salt phase, was first introduced by Rost *et al.* in 2015 [189]. HEOs/ESOs draw interest due to inherent opportunities to tailor and combine materials properties. The extent to which their enhanced compositional and configurational complexity impart additional stability, synergistic effects, and emergent/tunable properties to HEO archetypes is an active area of exploration. The magnetic properties of HEOs

represent one of the fastest growing research directions in this scientific community. From the perspective of magnetic behavior, the complexity of the local and long-range nuclear and spin structures found in HEOs gives rise to an unusually large number of metal-oxygen-metal interactions[198]. The inherent variation in coordination geometry, valence state, spin state, number of cations and metal cation type each HEO lattice can accommodate presents a rich pallet for exploring the tunability of the structure-property effects in the class. However, relatively few compositions have been studied in detail[198], no doubt due in part to the complex cation and spin order likely to be present.

Spinels crystallizing in cubic space group $Fd\bar{3}m$, with nominal formula AB_2O_4, feature a close-packed oxygen substructure with two thirds of cations occupying octahedral interstices and one third occupying tetrahedral ones. The spinel compounds in this work involve A and B cations in the cation charge state combination of +2 and +3 (charge-balanced spinel oxide families with +2 and +1, and +6 and +1 cation combinations are also known to exist). Spinels are typically classified according to which cations occupy the respective coordination environments, with a degree of inversion, γ, denoting the fraction of A ions occupying the octahedral sites, $[A_{1-\gamma}B_{\gamma}]_{tet}[A_{\gamma}B_{2-\gamma}]_{oct}O_4$. In the "normal" spinel structure ($\gamma = 0$, $[A]_{tet}[B_2]_{oct}O_4$), B^{3+} fully occupies the spinel octahedral site, while A^{2+} fully occupies the tetrahedral site. In the "inverse" spinel structure ($\gamma = 1$, $[B]_{tet}[AB]_{oct}O_4$), half of the B^{3+} cations fully occupy the tetrahedral site, leaving an equal amount of A^{2+} and B^{3+} atoms occupying the octahedral site. In a "random" spinel structure ($\gamma = 2/3$, $[A_{1/3}B_{2/3}]_{tet}[A_{2/3}B_{4/3}]_{oct}O_4$), A^{2+} and B^{3+} atoms take up residence on both sites according to their overall molar ratio, with 1/3 and 2/3 distribution, respectively. Arbitrary intermediate states between the normal and inverse spinels are possible (γ value between 0 and 1). Figure 3.1 provides a depiction of high entropy spinel AB_2O_4

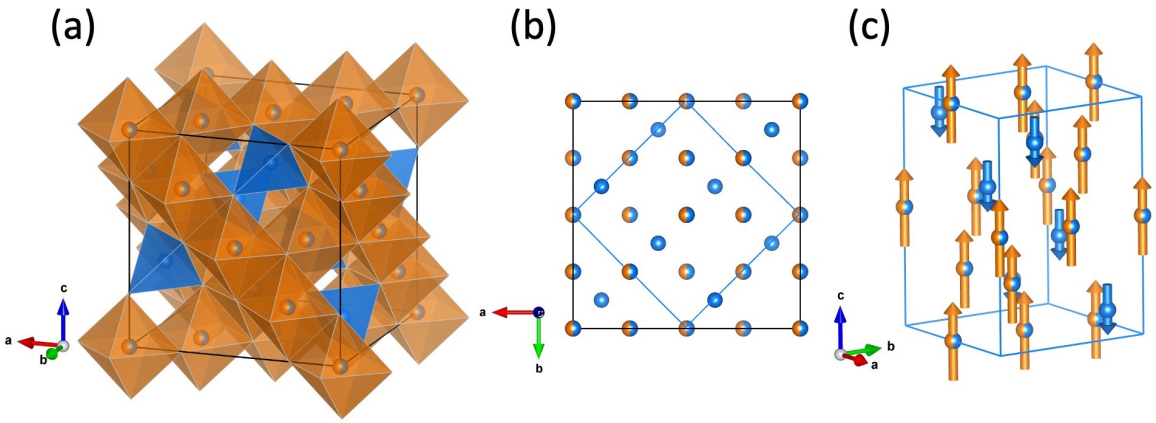


Figure 3.1: Schematic view of (a) the inverse spinel unit cell with blue tetrahedra (A-sites) and orange octahedra (B-sites). Cations on the octahedral site are drawn half blue and half orange to represent site mixing. Oxygen atoms sitting on polyhedral vertices are omitted for clarity. (b) The [0 0 1] projection of the cation substructure in the unit cell (black square) overlaid with the unit cell of the magnetic structure (blue frame). (c) The room-temperature zero-field magnetic spin structure composed of magnetic moments on the tetrahetral site (blue vectors pointing down) and octahedral site (orange vectors pointing up).

(with A = 5 equimolar cations and B = a single metal cation), shown for the case of the inverse spinel ferrite structure. Specific (not random) cation site preferences of the crystal chemistry in spinel oxides are well documented in the literature[163, 162], going back to early reports[231, 67] linking cation site distribution and magnetic properties in spinel ferrites. There has been ample research into the magnetic properties of spinel AFe_2O_4 since. AFe_2O_4 (A = Fe^{2+}[49, 10], Ni^{2+}[20], Cu^{2+}[200], Mg^{2+}[18], or Co^{2+}[10, 203, 230]) spinels have a variety of important applications in magnetic technologies[67, 219, 160]. They all have an inverse (either partially or completely) spinel structure. Previous works have shown that, in spinel ferrites, Zn^{2+} prefers to occupy the tetrahedral site while Mg^{2+}, Mn^{2+}, Mn^{3+}, Fe^{2+}, Fe^{3+}, Ni^{2+}, Cu^{2+}, and Co^{2+} tend to occupy the octahedral site in spinel ferrites[67]. It remains to be seen whether high entropy spinels will follow the trends in site preference observed among the ternary spinel ferrite systems, or if the potential for increased configurational entropy will lead to more random cation distributions.

High entropy spinels have been synthesized by solid state[47, 157, 69, 236, 33, 126, 144, 145, 217, 53, 123, 232, 296, 29, 27, 135], co-precipitation[183, 204], solution combustion synthesis (SCS)[139, 37, 140, 141, 269, 306, 152, 268], sol-gel method[173, 238], solvothermal synthesis[237], reverse co-precipitation[227], flame spray pyrolysis[178], hydrothermal method[165], polymerized complex method[80] and glycine-combustion method[38] among other techniques. Examples of reported high-entropy ferrite powders are summarized in Table 3.1.

Research into the magnetic properties and cation site ordering among high entropy spinels is still in its infancy. There is one recent report[197] demonstrating that the site ordering $(Co_{0.6}Fe_{0.4})(Cr_{0.3}Fe_{0.1}Mn_{0.3}Ni_{0.3})_2O_4$ in A_3O_4 spinel is governed by maximization of the crystal field stabilization energy (CFSE) of the constituent ions through site selectivity rather than by maximization of the configurational entropy (S_{config}) through random and homogenous cation disorder[197]. It is not known whether this generalizes to other high entropy spinel compositions, including compositional variations of the technologically important spinel ferrite (AFe_2O_4).

Table 3.1: A summary of powder sample high entropy spinel ferrite compositions appearing in the literature, including year reported (Year), chemical composition (Chem.), magnetic ground state (GS) (where FIM denotes ferrimagnetic), and the reference (Ref.).

Year	Chem.	GS	Ref.
Solid State Method + Sintering			
2019	$(Mg_{0.2}M_{0.2}Co_{0.2}Ni_{0.2}Cu_{0.2})Fe_2O_4$, M=Zn,Mn,Fe	FIM	[157]
2019	$(Mn_{0.2}Fe_{0.2}Co_{0.2}Ni_{0.2}Cu_{0.2})Fe_2O_4$	FIM	[157]
2020	$(Co_{0.2}Mn_{0.2}Ni_{0.2}Fe_{0.2}Zn_{0.2})Fe_2O_4$ (no sintering)	N/A	[296]
2022	$(Mg_{0.2}Fe_{0.2}Co_{0.2}Ni_{0.2}M_{0.2})Fe_2O_4$, M=Mn,Cu,Zn	FIM	[135]
Co-Precipitation + Annealing			
2019	$(Zn_{0.2}Mg_{0.2}Ni_{0.2}Fe_{0.2}Cd_{0.2})Fe_2O_4$	N/A	[183]
Sol-Gel Method			
2020	$(Co_{0.2}Cr_{0.2}Fe_{0.2}Mn_{0.2}Ni_{0.2})Fe_2O_4$	FIM	[173]
Solution Combustion Synthesis (SCS)			
2021	$(MnNiCuZn)_{1-x}Co_xFe_2O_4$ (x=0.05,0.1,0.2,0.3)	FIM	[152]
Glycine-Combustion Method			
2022	$(M_{0.2}Zn_{0.2}Co_{0.2}Ni_{0.2}Cu_{0.2})Fe_2O_4$, M=Mn,Fe	N/A	[38]
2022	$(Mn_{0.2}Fe_{0.2}Co_{0.2}Ni_{0.2}Cu_{0.2})Fe_2O_4$	N/A	[38]

The magnetic properties of spinel ferrites are highly sensitive to the distribution of cations (the degree of inversion, γ) across the tetrahedral and octahedral sublattices [67, 194]. For example, this phenomena has been well explored by mixing of Zn-ferrite (a normal spinel) with Co-ferrite (an inverse spinel), resulting in non-magnetic Zn^{2+} swapping for magnetic Fe^{3+} on octahedral sites and increasing the overall magnetization[25, 110]. Similar effects may arise in compositionally complex spinel samples, potentially with greater sublattice disorder and/or expanded substitution limits for specific cations. Research into the magnetic properties and cation site ordering among high entropy spinels is still in its infancy. There is one recent report[197] demonstrating that the site ordering $(Co_{0.6}Fe_{0.4})(Cr_{0.3}Fe_{0.1}Mn_{0.3}Ni_{0.3})_2O_4$ in A_3O_4 spinel is governed by maximization of the crystal field stabilization energy (CFSE) of the constituent ions through site selectivity rather than by maximization of the configurational entropy (S_{config}) through random and homogenous cation disorder[197]. It is not known whether this generalizes to other high entropy spinel compositions, including compositional variations of the technologically important spinel ferrite (AFe_2O_4). The magnetic properties of spinel ferrites are highly sensitive to the distribution of cations (the degree of inversion, γ) across the tetrahedral and octahedral sublattices [67, 194]. For example, this phenomena has been well explored by mixing of Zn-ferrite (a normal spinel) with Co-ferrite (an inverse spinel), resulting in non-magnetic Zn^{2+} swapping for magnetic Fe^{3+} on octahedral sites and increasing the overall magnetization[25, 110]. Similar effects may arise in compositionally complex spinel samples, potentially with greater sublattice disorder and/or expanded substitution limits for specific cations.

In 2019, Musicó et al. [157] reported on the magnetic properties and trends amongst a series of high entropy spinel ferrites (compositions AFe_2O_4) and chromates (compositions ACr_2O_4). All reported high entropy spinel ferrites were shown to be room temperature ferrimagnets and like several other HEO magnetic phases, were reported to generally follow trends found in the majority of the simpler ternary systems involving groups of the constituent cations. For example, the high entropy

system including Zn and Mg (the two non-magnetic cations) had the largest magnetic moment and lowest Néel temperature (T_N) relative to other high entropy spinels. On the other hand, several other HEO ferrites ($(Mg_{0.2}Fe_{0.2}Co_{0.2}Ni_{0.2}Cu_{0.2})Fe_2O_4$ and $(Mg_{0.2}Mn_{0.2}Co_{0.2}Ni_{0.2}Cu_{0.2})Fe_2O_4$) were noted to show peculiar magnetic behavior. For example, the low temperature field warming magnetization dips below the field cooling magnetization and for intermediate temperatures indicates an increase in magnetization as temperature is raised. A possible explanation for this peculiar thermal hysteresis is the antiferromagnetic coupling between neighboring elemental components in the cation sublattice. This leads to a key question of whether the reported high entropy spinels contain cation short-range order and small locally ordered magnetic clusters or chemically homogeneous distributions with more dilute clusters, and whether the substructures can be tuned.

The extent to which high entropy spinels will exhibit cation distributions different from bulk ternary spinels that influence their properties remains to be determined. In this work, we explore the influence of local cation ordering upon magnetic properties in a family of AFe_2O_4 high entropy spinels using magnetometry, neutron powder diffraction, neutron atomic pair distribution function (PDF) studies, and reverse Monte Carlo modeling of spin correlations. We draw several connections between observed magnetic properties, the average and local atomic and magnetic structures, and the influence of material processing history in the series.

3.2 Methods

3.2.1 Materials synthesis

In this work, the four phase-pure spinel ferrites originally reported by Musicó *et al.*[157] were synthesized by solid state reaction using identical starting materials and processing conditions. We have elected to use the same naming convention as in the original work, with samples labelled F1, F3, F4, and F5, as noted in Table 3.2.

Table 3.2: High entropy spinels in this study, with firing temperatures and number of hours noted. Sample names correspond with those reported by Musicó *et al.*[157].

Name	Composition	Heat treatment	
		No.1	No.2
F1	$(Mg_{0.2}Fe_{0.2}Co_{0.2}Ni_{0.2}Cu_{0.2})Fe_2O_4$	1250°C, 10h	1250°C, 10h
F3	$(Mg_{0.2}Co_{0.2}Ni_{0.2}Cu_{0.2}Zn_{0.2})Fe_2O_4$	1250°C, 10h	1250°C, 10h
F4	$(Mg_{0.2}Mn_{0.2}Co_{0.2}Ni_{0.2}Cu_{0.2})Fe_2O_4$	950°C, 10h	1250°C, 10h
F5	$(Mn_{0.2}Fe_{0.2}Co_{0.2}Ni_{0.2}Cu_{0.2})Fe_2O_4$	950°C, 10h	1250°C, 10h

Briefly, all the samples were prepared in 5-gram batches using mixtures of stoichiometric proportions of dried precursor oxide powders (MgO, NiO, CoO, CuO, ZnO, MnO_2, and Fe_2O_3). The mixtures were ball milled, pressed into pellets, and heat treated according to the details in Table 3.2. Mixtures for samples F1 and F3 were initially heated at 1250°C for 10 hours. Samples F4 and F5 (both containing Mn) were obtained by first heating the mixed powder at 950°C in order to convert the MnO_2 precursor to Mn_3O_4. After the first heating step, all samples were ground, repressed, and sintered a second time at 1250°C for 10 hours. The heat treatment protocols are the same used for the compositions reported in Musicó *et al.*[157], though the heat treatment temperatures and times were not included in the original work.

3.2.2 Magnetic measurement

Magnetometry measurements were performed using a vibrating sample magnetometer (VSM) as part of a Quantum Design PPMS DynaCool system. Temperature-dependent magnetometry (M vs T) was performed using field cooled (FC) and zero field cooling (ZFC) methods. For each sample, a ZFC measurement was first performed by cooling the powder sample to 2 K in the absence of a magnetic field, then applying a 10 mT field and measuring the magnetic moment as the temperature was increased from 2 K to 400 K. After the ZFC measurement, the applied field was kept at 10 mT while measuring the magnetization as the temperature was reduced from 400 K to 2 K for the FC curve. Magnetic hysteresis (M_H) loops between ± 2 T were also measured at temperatures ranging from 2 K and in 25 K steps up to 400 K. All measurements have been normalized to the sample mass.

First order reversal curve (FORC) measurements were performed to evaluate the distribution of magnetic phases and interactions within the samples[179, 187, 63]. Following previously published procedures, FORC measurements were performed by first positively saturating the sample, then reducing the magnetic field to a reversal field (H_R). Next, the magnetization is measured as the applied field (H) is increased

from H_R back to positive saturation. This sequence was repeated at H_R between the positive and negative saturation. The FORC distribution (ρ) is calculated by applying a mixed second order derivative to the dataset:

$$\rho(H, H_R) = \frac{-1}{2M_S} \frac{\partial^2 M(H, H_R)}{\partial H \partial H_R} \tag{3.1}$$

where M_S is the saturation magnetization of the sample. FORC measurements were completed at 2 K and 300 K for each sample. While H and H_R separately probe up and down-switching events, respectively, FORC distributions are commonly presented with a change of coordinates from (H, H_R) to:

$$H_C = \frac{H - H_R}{2}, \quad \text{and} \quad H_B = \frac{H + H_R}{2} \tag{3.2}$$

where H_C and H_B represent the local coercive and bias (interaction) fields, respectively. As all samples show features prominent along axes in both coordinate systems, FORC distributions are presented in (H, H_R) while also indicating the (H_C, H_B) axes. The FORC distributions also include significant reversible components, which are captured using a constant extension mechanism[62].

3.2.3 Neutron total scattering

Time of flight (TOF) neutron powder diffraction (NPD) data was collected at 300 K on the Nanoscale Ordered Materials Diffractometer (NOMAD) at the Spallation Neutron Source (SNS) at Oak Ridge National Laboratory (ORNL)[164]. For each sample, approximately 0.3 g of powder was loaded into a 3 mm diameter quartz capillary, placed in a temperature controlled Ar cryostream, and data was collected for 1 h. Data reduction was completed with the Advanced Diffraction Environment (ADDIE) suite[150]. The instrument background and sample container contributions were subtracted, data were corrected for detector deadtime, absorption, and multiple scattering effects, and were normalized by the incident flux and total sample scattering

cross section. The maximum value of Q vector used for generation of the PDF was 40 Å^{-1}. The coherent neutron scattering lengths vary considerably among the cations in the sample series, with (in order from smallest to largest) b_{Mn}= -3.73 fm, b_{Co}= 2.49 fm, b_{Cr} = 3.635 fm, b_{Mg}= 5.375 fm, b_{Zn}= 5.68 fm, b_{Cu}=7.718 fm, b_{Fe} = 9.45 fm, and b_{Ni}= 10.3 fm. The neutron scattering length of oxygen is b_O= 5.803 fm.

The experimental diffraction data (31° 2θ detector bank) were analyzed with the Rietveld method as embodied in the TOPAS-V7[36] program. Analysis was completed for each dataset fixing the cation site occupancy according to a normal ($[\text{A}]_{tet}[\text{Fe}_2]_{oct}\text{O}_4$), an inverse ($[\text{Fe}]_{tet}[\text{A,Fe}]_{oct}\text{O}_4$) (Shown in Figure 3.1(a)), and a random ($[\text{A}_{1/3}\text{Fe}_{2/3}]_{tet}[\text{A}_{2/3}\text{Fe}_{4/3}]_{oct}\text{O}_4$) spinel structure model ($\text{F}d\bar{3}m$). In all fits, the magnetic scattering was modelled using a magnetic structure model with an $\text{I}4_1/am'd'$ structure featuring one constrained magnetic moment for all tetrahedral sites and one constrained magnetic moment oriented in opposite direction for all octahedral sites (shown in Figure 3.1(c)). Background parameters, scale factors, cubic lattice parameters a_{nuc}, isotropic atomic displacement parameters (ADPs) (one for oxygen atoms, one for all cations on the tetrahedral site, and one for all atoms on the octahedral site), instrument profile parameters, and the oxygen atom position (u) were refined for the nuclear structure models. For the refinement of magnetic structure, the isotropic ADPs were constrained to be equivalent to those in the nuclear structure, while the lattice parameters a_{mag}=b_{mag} were constrained to equal $\sqrt{2}a_{nuc}/2$ and the lattice parameter c_{mag} was constrained to equal a_{nuc} (according to geometry, Figure 3.1(b)). The scale factor of the magnetic phase was constrained to one half that of the nuclear phase (since $\text{V}_{mag}/\text{V}_{nuc}$=1/2). Magnetic moments were refined along the z direction for the magnetic elements sitting on the respective tetrahedral and octahedral sites (constrained as one unique value per lattice site).

PDF refinements and model simulations were completed using normal, inverse spinel and the random solution models in the PDFgui[50] program, and included a scale factor, lattice parameters, quadratic peak sharpening parameters for correlated atomic motion, and isotropic ADPs. Instrument parameters for real-space dampening

and broadening were fixed to values determined through refinement of a silicon crystalline standard reference material.

3.2.4 Reverse Monte Carlo modeling

RMC modeling involving both total scattering and Bragg data was conducted using the RMCProfile package [226]. Fits for both neutron $F(Q)$ and neutron Bragg data were completed. $F(Q)$ is defined by

$$F(Q) = (\sum_{i=1}^{n} c_i \bar{b}_i)^2 \left(S(Q) - 1\right), \tag{3.3}$$

where $Q = k - k'$ is the scattering vector of length $4\pi sin\theta/\lambda$ for a neutron of wavelength λ scattered at an angle 2θ, and k and k' are the initial and final wavevectors of the scattered neutron, respectively. $S(Q)$ is the normalized total-scattering structure factor. $\bar{b}_i$ is the coherent bound neutron scattering length of species i, averaged over the different isotopes and nuclear spin states of i. c_i is the portion of species i in the material[97]. A 10×10×10 supercell was first built, based on the unit cell model obtained via Rietveld refinement for each sample. The supercell structural configuration was then optimized in a data-driven manner, following the Metropolis approach. Two sets of RMC modeling was completed for each sample, assuming either inverse or random site occupancy (the normal model was excluded because of the poor agreement demonstrated by Rietveld refinements). No atomic position swapping was allowed between tetrahedral and octahedral sites. In the original report by Musicó et al., multiple valence states for Fe and Mn were detected among high entropy spinels via X-ray absorption spectroscopy. Thus, RMC trials were performed for several samples assuming various valence states for Fe and Mn atoms (since valence determines the magnetic form factors assigned). Here, it should be pointed out that the magnetic moment vectors in RMC configurations are unit vectors with magnetic moment magnitude specified (fixed) according to each cation

involved. The bond valence sum (BVS) constraint in RMC fitting is implemented in such a way that it effectively constrains the net valence of the whole system to be 0. The findings discussed in this report were found to be independent of the valence settings in RMCProfile. The final configurations were initiated assuming a +2 valence state for all A cations in the AFe_2O_4 compositional series, and a +3 valence state for the remaining two Fe cations.

Neutron total scattering structure factor data, F(Q), and Bragg data were used for RMC modeling, since the calculation for magnetic diffuse scattering is performed only in Q-space in RMCProfile. For the inclusion of Bragg data in RMC modeling, peak profiles and background were extracted from Topas refinement and tabulated for RMCProfile to read in – hence the RMC engine only calculates peak intensities. In addition to the experimental data, a minimum distance for each single pair of atoms and an overall bond valence sum were added as model constraints. Given multiple constraints exerted upon the structural model, an automatic weight assigning scheme[294] was used.

A kernel density estimation (KDE) and the Henze-Zirkler (HZ) statistic were utilized to interpret variation in the distribution of atom sites and magnetic spin correlations resulting from RMC model fits to neutron total scattering data. KDE is a commonly used method for estimating the underlying probability distribution function in a collection of data points with a non-parameterized approach. Here, the standard normal function is used as the kernel and in practice that means one would have a standard normal distribution function with the center at each of the data points. The overall distribution function is then composed of all those kernels, while being normalized to give the overall distribution probability of 1. The HZ parameter[77, 51, 52, 225] is a parameter characterizing the normality of a distribution and the closer its value gets to 1, the closer that underlying distribution is to a Gaussian distribution. The following equation defines the HZ parameter:

$$HZ = [\frac{1}{n}\sum_{i=1}^{n}\sum_{j=1}^{n} e^{-\frac{\beta^2}{2}D_{ij}}] - [2(1+\beta^2)^{-\frac{d}{2}}\sum_{i=1}^{n} e^{-\frac{\beta^2}{2(1+\beta^2)}D_i}] + [n(1+2\beta^2)^{-\frac{d}{2}}], \quad (3.4)$$

where D_i is the squared Mahalanobis distance of the i^{th} observation to the centroid and D_{ij} gives the squared Mahalanobis distance between i^{th} and j^{th} observations:

$$D_i = (\overrightarrow{x}_i - \overrightarrow{\bar{x}})^T S^{-1} (\overrightarrow{x}_i - \overrightarrow{\bar{x}}), \quad (3.5)$$

$$D_{ij} = (\overrightarrow{x}_i - \overrightarrow{x}_j)^T S^{-1} (\overrightarrow{x}_i - \overrightarrow{x}_j), \quad (3.6)$$

β is given by

$$\beta = \frac{1}{\sqrt{2}}(\frac{n(2d+1)}{4})^{\frac{1}{d+4}}, \quad (3.7)$$

which includes the particle sample size n_p and sample dimensions d.

3.3 Results and Discussion

3.3.1 Entropy, energy, and predicted site preference

The cation distribution in high entropy spinels will be impacted by a number of thermodynamic and crystal-chemical factors. The CFSE of the oxygen ligand field and the S_{config} resulting from the number of participating cations are two important factors. The electron configuration energy difference between the ligand field and isotropic field is defined as CFSE,

$$CFSE = \Delta E = E_{ligand\,field} - E_{isotropic\,field}. \quad (3.8)$$

The CFSE can be straightforwardly calculated for each participating cation assuming a specific charge state and either an octahedral or tetrahedral geometry, and the net CFSE can be compared for specific distributions of cations to evaluate potential site preferences.

The CFSE for the four compositions in the AFe_2O_4 series are shown in Figure 3.2 (a), assuming a +2 valence state for all five cations on the A-site, and a +3 valence state for the remaining two Fe cations. Regardless of the oxidation state used in calculations, the CFSE of the inverse structure model is the lowest among the model spinel structures while the CFSE of the normal structure model is the highest.

The entropy contribution made by the compositional mixture on the tetrahedral and octahedral lattice sites will differ for normal, inverse, and random spinels. The ideal S_{config} per cation for HEOs with multiple cations occupying different sublattice sites can be calculated[197] by

$$\frac{S_{config}}{cation} = -R\frac{\sum_{x=1}^{x} a^x \sum_{N=1}^{N}(f_i^x ln f_i^x)}{cation}, \tag{3.9}$$

where R is the universal gas constant, a^x is the number of sites on the x sublattice, f_i^x is the fraction of elemental species occupied on the respective sublattice, and N is the number of elements in a given sublattice. For example, for the normal spinel AFe_2O_4, Eqn. 3.9 can be evaluated as

$$\frac{S_{config}}{cation} = \frac{S_{config}}{3} = -R\frac{1*(5*0.2ln0.2)+2*1ln1+4*1ln1}{3} \approx 0.54R. \tag{3.10}$$

As shown in Figure 3.2(b) the random spinel offers the highest entropy contribution, regardless of the number N of cations on the A sublattice site of AFe_2O_4 (from 1 to 8, with Fe not included), followed by the inverse and normal spinel configurations. The S_{config} calculations for N from 1 to 8 with Fe from the B site included are also completed in Figure S3.1. Since F3 and F4 do not have Fe on the A-site their S_{config}s are larger than those of F1 and F5 when random and inverse spinel models

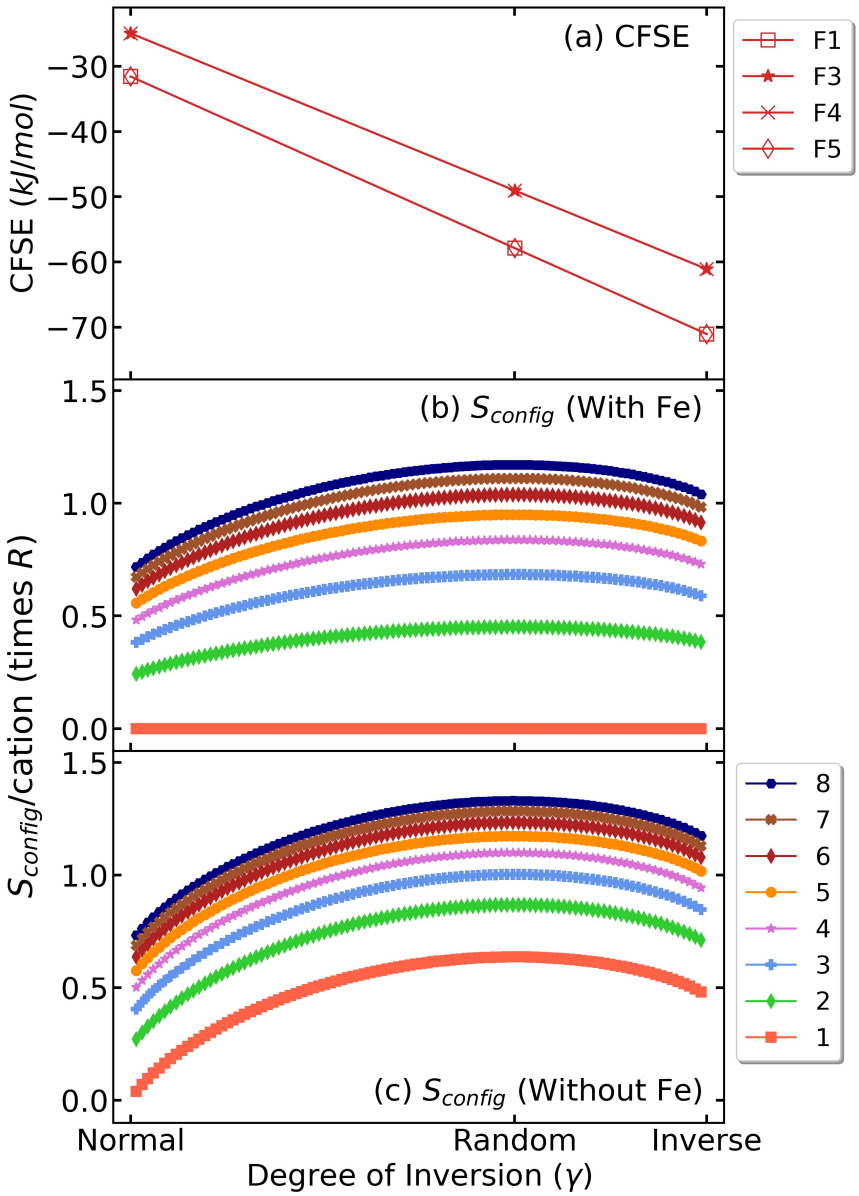


Figure 3.2: (a) The CFSE calculations for F1 (□), F3 (★), F4 (×), and F5 (◊) with normal spinel, random solution, and inverse spinel structure models assumed (with a +2 valence state for all A cations in the AFe_2O_4 compositional series, and a +3 valence state for the remaining two Fe cations). (b) The calculated S_{config} of AFe_2O_4 high entropy spinels with the degree of inversion (γ) changing from 0 to 1 and the assumption that there are N (from 1 to 8, Fe is not included) cations occupying the A-site (the γ values 0, 2/3, and 1 were labeled according to the corresponding normal, random solution, and inverse spinel structure configurations).

are considered, respectively. It is worth noting that the S_{config}s for the compositions in the series are all smaller than $1.5R$, meaning the spinels do not meet the classic definition of a high entropy oxide (or even medium entropy oxide). In thermodynamic terms, these compositions are more accurately classified as compositionally complex oxides (CCOs).

To summarize, the CFSE and S_{config} terms for AFe_2O_4 spinels provide competing drivers for cation site selectivity, favoring inverse versus random cation configurations, respectively. Observed cation distributions could very well be influenced by the sample-specific processing procedures.

3.3.2 Magnetic measurements

Results of temperature- and field-dependent magnetometry for the samples in our study are shown in Figure 3.3 and Figure 3.4 (a), respectively. For all of the samples, the black, dashed ZFC curve shows a continuous increase with increasing temperature, indicating the enhanced role of thermal fluctuations by reorienting the magnetization with the magnetic field. Also, the ZFC curve is well separated from the FC curve, with no apparent inflection, and the FC curve is smooth and persistently non-zero, indicating the system does not have a blocking temperature and is not superparamagnetic in this temperature range. This is consistent with the previous work by Musicó et al.[157], which identified the Néel temperature (T_N) of $>$ 400K; the Néel temperature of other spinel ferrites includes 858K for Fe_3O_4 and 725K for $CoFe_2O_4$. These conclusions are also consistent with the M_H loops, shown in Figure 3.4 (a), which show that every sample has a very small, but non-zero, coercivity ($\approx$ 2-5 mT) at 300 K.

The field-dependent magnetometry measurements of F1, F3, F4, and F5 samples in this study are shown in Figure 3.4 (a), the measurements completed by Musicó et al.[157] are reproduced in Figure 3.4 (b) for comparison. This comparison shows significant differences in the M_H loops, with the samples in this work having a nearly

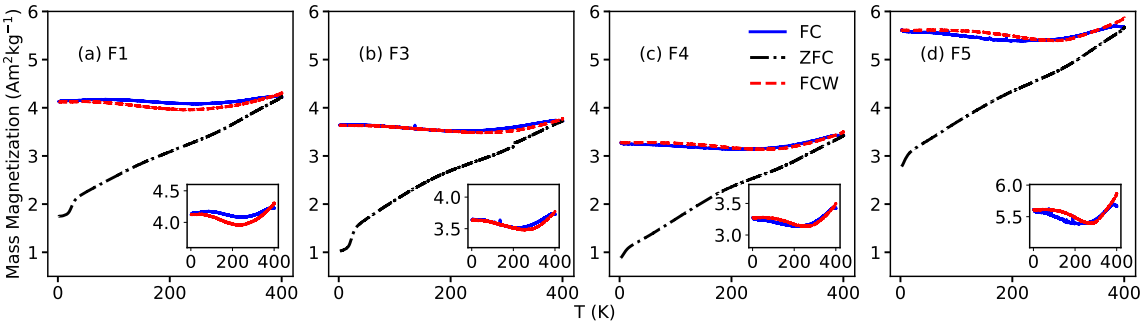


Figure 3.3: The comparison of field-cooled (FC), zero-field-cooled (ZFC), and zero-field-warming (FCW) for all ferrite samples measured from 2K to 400K with an applied field of 10 mT: (a) F1, (b) F3, (c) F4, and (d) F5. The legend in (c) applies to all subplots. The insets are displayed in order to emphasize the cross-over and hysteresis in the FC and FCW curves.

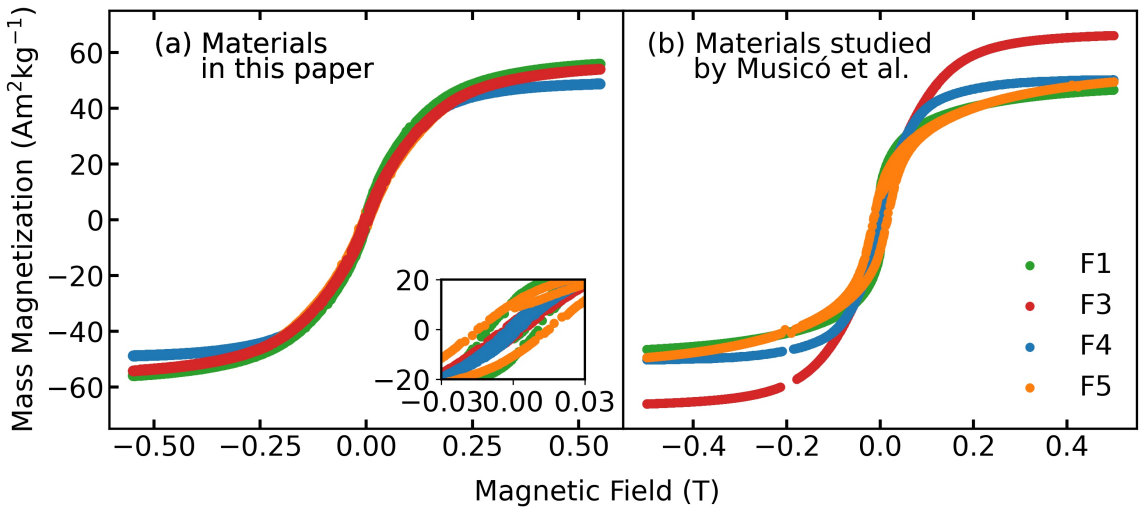


Figure 3.4: The comparison of magnetic hysteresis loop data for ferrite compositions (F1,F3,F4,F5) measured at 300K with a ± 0.5 T range for (a) materials in this paper, measured with a 10 mT cooling; and (b) materials studied by Musicó et al., measured with a 100 mT cooling. The legend in (b) applies to both subplots.

constant (compositionally independent) magnetic saturation (M_S) and an exceedingly small coercivity in all of the samples. By comparison, the samples from Musicó et al.[157] shows a variable M_S between the different samples, with F3 being particularly large, while the others are similar to the current work. Also the coercivity in Ref. [157] is generally larger than the current work, especially F5. The two batches of samples were synthesized in the same laboratory, by the same researcher, using the same batch size, grinding and sintering procedure, and precursors from the same supplier. The only known change in sample preparation involved a replaced heating element for the furnace used. Additionally, the magnetometry measurements of samples prepared for Musicó et al.[157] were completed soon after synthesis, whereas and mangetometry measurements of samples prepared in the present work was completed two years after synthesis. The observed difference in magnetic behavior among samples of the same composition suggests a potential high sensitivity to synthesis and processing conditions, and/or ageing, in high entropy spinels, and deserves further investigation. For consistency, it is important to note that the M_H loops in this work were field cooled in 10 mT, while Ref. [157] uses 100 mT. This difference would manifest if the system has an antiferromagnetic phase coupled to the ferromagnetic phase or high anisotropy phase with a saturation field larger than the 2 T applied here. In these cases, the hysteresis loop would be vertically and horizontally shifted in Figure 3.4 due to the exchange bias effect. The absence of these features suggests that the cooling field is not responsible for the observed differences.

3.3.3 Distinct small magnetic clusters

The differences in the M_H plots maybe the result of a strong sensitivity to local compositional distributions and microstructure. This sensitivity would manifest in the magnetic reversal behavior of the sample, which can be probed using the FORC technique. The calculated FORC distributions are shown in Figure 3.5 at 2 K (a,c,e,g) and 300 K (b, d, f, h) for all samples.

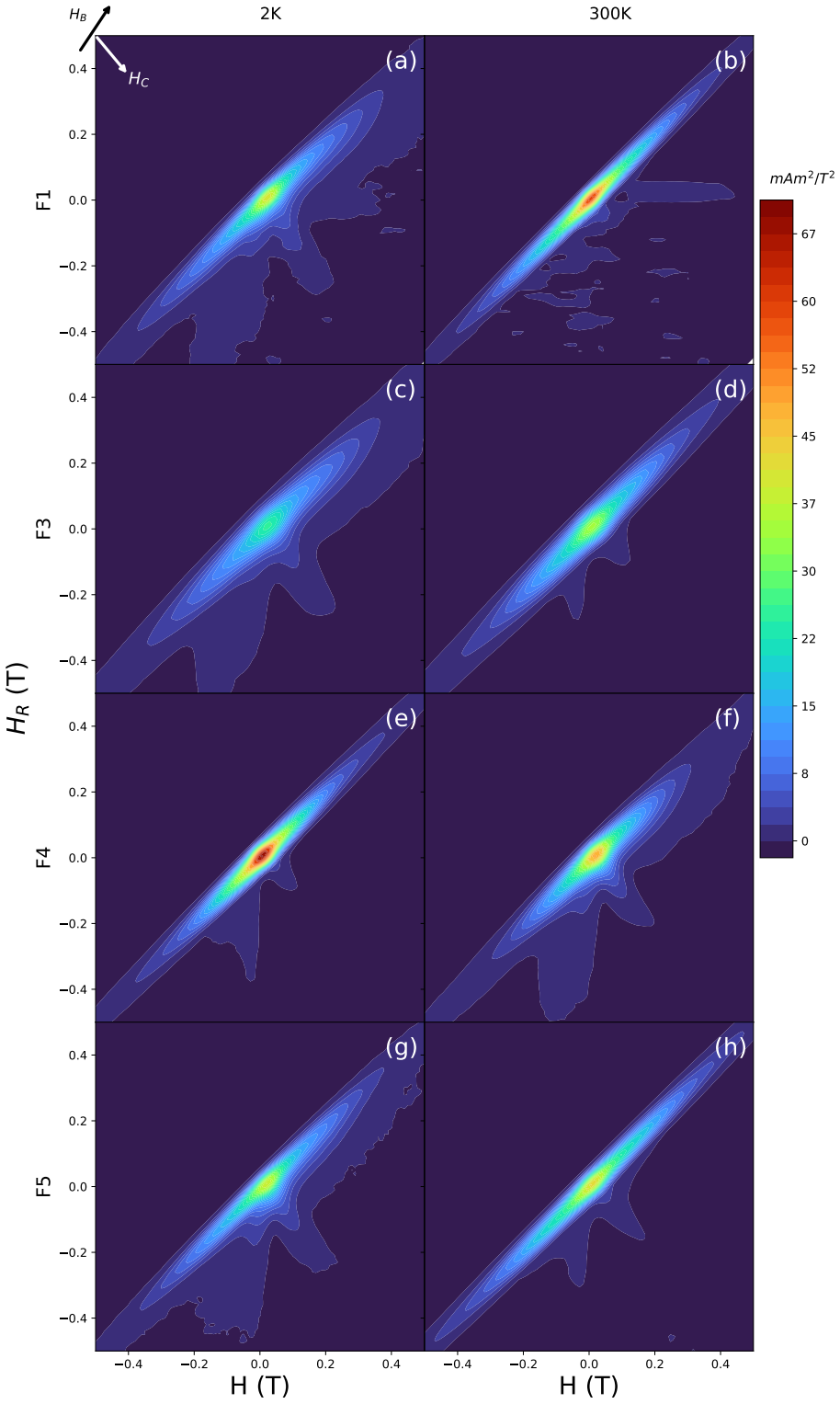


Figure 3.5: The comparison of FORC measurements at 2 K and 300 K for sample F1 (a,b), F3 (c.d), F4 (e,f), and F5 (g,h), respectively. The directions of H_B and H_C are plotted for clarification and the scale bar indicates the rate at which the magnetic reversal speed changes for different H_R.

The FORC distributions all show their primary feature aligned along the H_B axis with a small feature in the H_C direction which is more prominent at low temperatures. A small bump in the H_R direction is also seen at 2 K but is absent at room temperature. While these features are present for all of the samples, they vary in intensity and prominence, with the attributes being lowest for sample F3.

The FORC distribution encodes a map of the switching events within a particular hysteretic system. The bias-field axis identifies the shift from $H = 0$ of a particular set of switching events. For a system without exchange bias, this shift can be attributed to interactions within the sample. The FORC distribution shown here has a wide spread in H_B, indicating strong demagnetizing interactions, e.g. interactions which drive the system away from a saturated configuration[63, 180]. These interactions can be the result of dipolar coupling or exchange-motivated frustration. The presence of long-range ferrimagnetic magnetic ordering without a blocking temperature, and with only a very small coercivity, suggests the interactions are likely due to frustration. At low temperatures, the protrusion along the H_C axis suggests the intrinsic anisotropy has increased compared to the room temperature measurements. The protrusion along the H/H_R axes indicate some of the sample reverses by a domain nucleation/propagation mechanism[39]. The appearance of the domain reversal mechanism indicates that large areas of the sample have become magnetically coupled and can support domain growth through their boundaries. Complementary to this, the higher temperature samples may consist of magnetic islands, or regions which are coupled by non-magnetic or antiferromagnetic phases.

3.3.4 Average structure

The neutron diffraction patterns of all four samples appear visually similar (Figure 3.6 (a)) and can be indexed to a cubic spinel $Fd\bar{3}m$ structure model with corresponding $I4_1/a'd'$ ferrimagnetic ordering model, with no detected secondary phases. Distinguishing cation order is challenging with Bragg diffraction data. The scattering

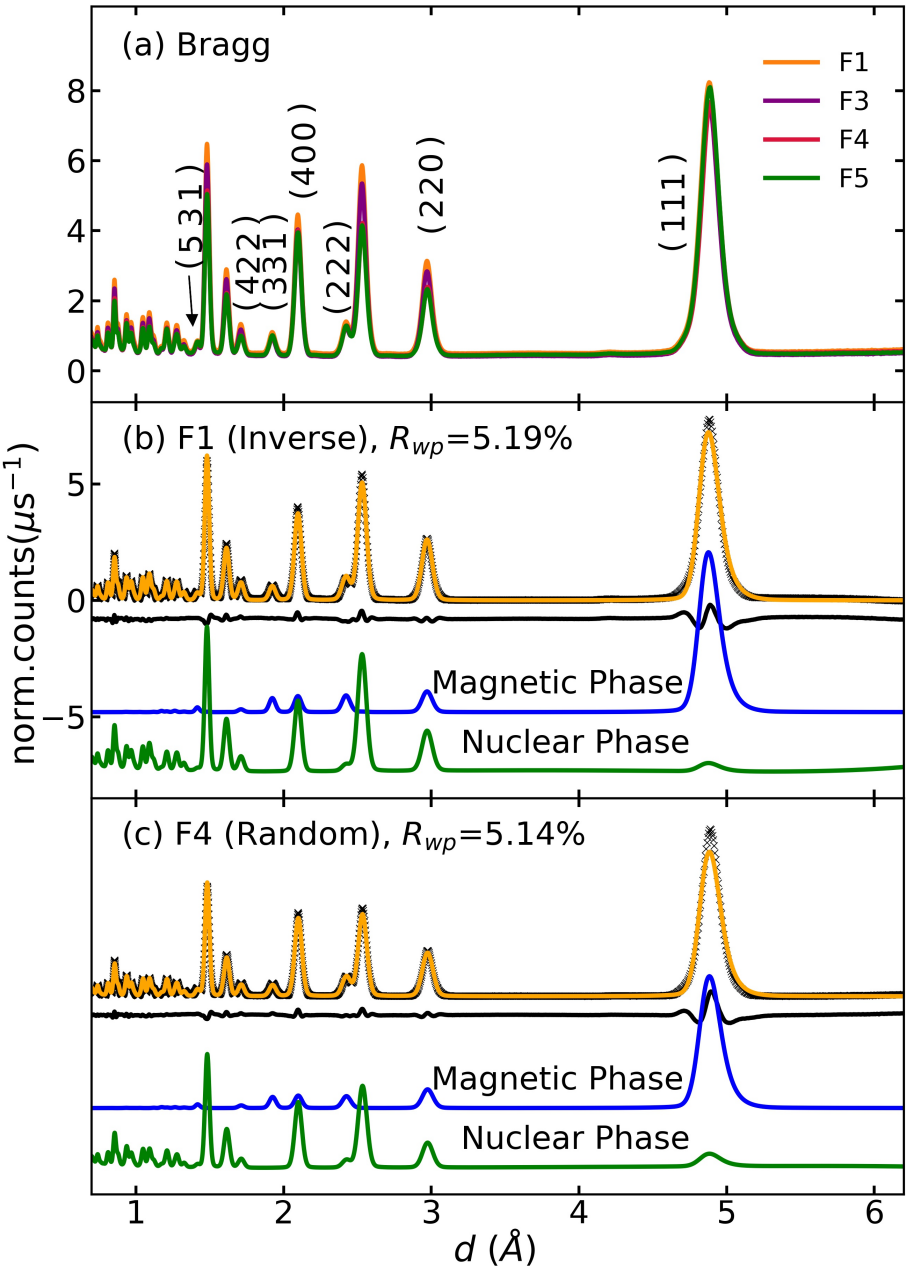


Figure 3.6: (a) The comparison of neutron Bragg data (31° detector bank) from F1 (orange line), F3 (purple line), F4 (red line), and F5 (green line) samples. Several hkl peaks featuring ferrimagnetic contributions are labeled. Best-fit Reitveld refinement of (a) F1 data using inverse spinel and ferrimagnetic spin order model and (c) F4 data using random solution spinel and ferrimagnetic spin order model. In (b) and (c) data are shown as black "x"s, fits are shown as solid orange lines, and difference curves fall below the data and fits in black lines. The blue and green solid curves displayed below the refinement results display the magnetic and nuclear contributions to the fits, respectively.

length of involved elements, the degree of cation inversion, and the magnetic order on the cation sublattice may all contribute to observed variation in peak intensities. As a demonstration, the calculated neutron diffraction patterns for nuclear and magnetic scattering assuming inverse, random, and normal spinel structure models with assumed ferrimagnetic spin order for each sample are shown in Figure S3.2. It can be seen in Figure 3.6(a) that the nuclear Bragg peak intensities are higher for F1 and F3 samples relative to F4 and F5 samples. The intensities of dominant magnetic peaks (for example, the (331) and (111) reflections) appear similar for all compositions.

Separate Rietveld refinements assuming normal, random, and inverse spinel models were completed for each sample (Table S3.1 for F1, Table S3.2 for F3, Table S3.3 for F4, Table S3.4 for F5), each incorporating the ferrimagnetic structure shown in Figure 3.1 (c). A summary of Rietveld refinement results is presented in Table 3.3. The Rietveld refinement results reveal distinct preference in cation site ordering. For all samples, the normal spinel structure model resulted in poor agreement and nonsensical magnetic moments. The combination of inverse spinel and ferrimagnetic model fits the data better than those of random and normal spinel models for F1 and F3 samples (the F1 result is shown in Figure 3.6(b)), while the combination of random solution spinel and ferrimagnetic model fits the data better than normal and inverse models for F4 and F5 samples (the F4 result is shown in Figure 3.6(c)). The ferrimagnetic scattering contributes 100% to the hkl peak (331), a large portion to the peaks (531), (222), (111), and some percentage to the (422), (400), and (220) peaks. The intensity of peaks with combination contributions from nuclear and magnetic structures are not precisely fit with either random or inverse structure; the average structures may lie somewhere in between. Since the nuclear Bragg peaks are overlapped with the magnetic Bragg peaks and there are a high number of participating cations, Bragg diffraction data alone is not enough to determine the detailed structure and cation site preferences of the high entropy spinels.

Table 3.3: Parameters for the best fitting model results among the normal, inverse and random solution F$d\bar{3}m$ spinel models applied for F1, F3, F4, and F5 Rietveld refinements. The table includes the refined magnetic moment (M), lattice parameter (a), oxygen position (u), isotropic atomic displacement parameters (U_{iso}) for the 8b, 16c, and 32e sites, and the resulting refinement goodness-of-fit, R_{wp}.

Sample	F1	F3	F4	F5
Best Model	Inverse	Inverse	Random	Random
M(μ_B/Å)	0.406	0.215	1.162	0.532
a (Å)	8.3796(1)	8.3793(1)	8.3894(1)	8.3839(1)
u (frac.)	0.2440(0)	0.2438(0)	0.2433(0)	0.2436(0)
$U_{iso,8b}$ (Å^2)	0.0057(1)	0.0066(1)	0.0054(1)	0.0069(1)
$U_{iso,16c}$ (Å^2)	0.0040(1)	0.0035(1)	0.0047(1)	0.0069(1)
$U_{iso,32e}$ (Å^2)	0.0079(1)	0.0088(1)	0.0085(1)	0.0084(1)
R_{wp}	5.19	5.28	5.14	4.54

3.3.5 Chemical short range order

A comparison of the neutron PDFs for the high entropy spinels is provided in Figure 3.7(a), displayed between 1.7 Å and 10 Å. All pair correlations have been numbered and identified by category with a color key to aid discussion. First, it is immediately apparent that the local atomic configurations of the high entropy spinels in the present study are similar; in particular, the location and peak shapes of nearest-neighbour and nex-nearest neighbor pair correlations are coincident across the four compositions. This immediately rules out significant local distortion of specific A-site cations. Next, there are specific sets of peaks in the data that vary systematically from sample to sample at low r: the peaks highlighted by magenta (peak 1, 5, 9, 12, 15, 17), green (peak 2, 6, 10, 13), red (peak 4), and pink (peak 8) dashed lines representing A-O, A_{oct}-A_{oct}/O-O, O-O, and A_{oct}-A_{oct}/A_{tet}-A_{tet}/A-O correlations, respectively, are matched in amplitude; the peaks highlighted by sky blue (peak 3, 11, 16) and orange (peak 7, 14), representing A_{oct}-A_{tet}/A_{tet}-A_{tet}/A-O and A_{oct}-A_{tet}/A_{tet}-O correlations, respectively, differ in amplitude. Inspection reveals that samples F1 and F3 exhibit similar and higher amplitudes of specific correlations relative to samples F4 and F5. PDF data comparisons for every 10Å across the whole range (1.7-50 Å) are shown in Figure S3.3.

Neutron PDF refinements in Figure 3.7 (b) and (c) show the effect of changing the cation ordering model (inverse, normal, random configuration models) for F1 and F4 samples, respectively. Fits for F3 and F5 are shown in Supporting Information Figure S3.4, and provide similar results to F1 and F4, respectively. It is highly likely the unfit residual is in part due to magnetic spin correlations that are unaccounted for in the models[55, 54]. At present there are no PDF data refinement programs that allow for shared site occupancy and magnetic PDF refinement, thus we have elected to present the nuclear structure fits alone here and address magnetic spin correlations separately. The 15^{th} pair amplitude (an A-O correlation at approximately 8.75Å) is shown to be sensitive to the degree of inversion in spinel ferrite models. Overall, for

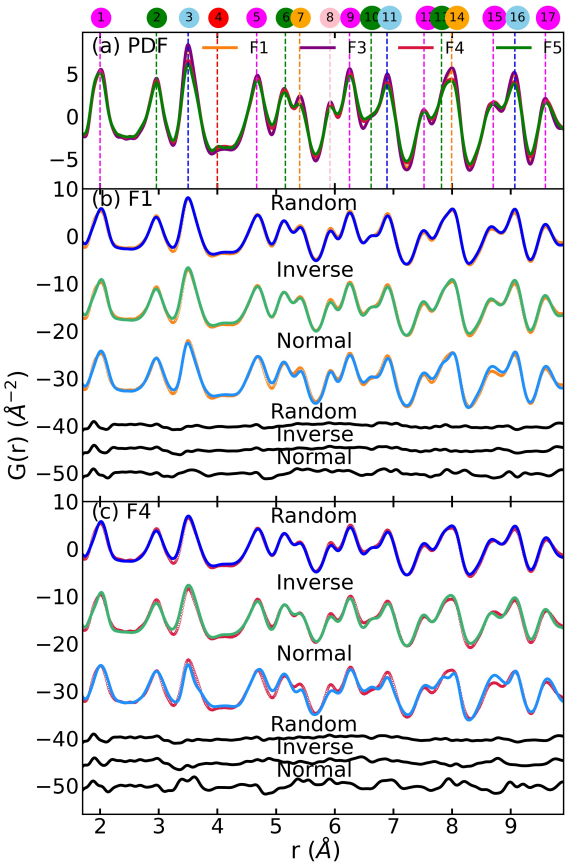


Figure 3.7: (a) The PDF data comparison of F1 (orange line), F3 (purple line), F4 (red line), F5 (green line). The 6 peaks (1, 5, 9, 12, 15, 17) highlighted with magenta dashed lines correspond to A-O pairs. The 4 peaks (2, 6, 10, 13) indicated with green dashed lines arise from A_{oct}-A_{oct} and O-O pair correlations. The 3 peaks (3, 11, 16) contributed by A_{oct}-A_{tet},A_{tet}-A_{tet} and A-O are identified in sky blue dashed lines. The peak (4) around 4 Å highlighted in a red dashed line corresponds to an O-O correlation. The combination of A_{oct}-A_{tet} and A_{tet}-O pair correlations contribute the 2 peaks (7, 14) indicated by orange dashed lines. The peak (8) highlighted by a pink dashed line arises from A_{oct}-A_{oct},A_{tet}-A_{tet} and A-O pair correlations. A comparison of the PDF refinements for (b) F1 sample data and (c) F4 sample data using different structure models (random, inverse, and normal spinel ferrite models). PDF data for F1 and F4 samples are shown in orange and red dots, respectively. The blue, lemon green and sky blue solid curves present fits to the data completed with the random solution spinel structure, inverse spinel structure and normal spinel structure model, respectively. The fit difference curves displayed below the data and fits are represented as black solid curves.

F1 and F3, the random model and inverse model provide a very similar fit quality and cannot be easily distinguished with PDF refinement. For sample F4 and F5, the fit quality for a random model is superior to that for an inverse model. These results correlate well to conclusions drawn from Rietveld refinement. However, no further conclusion can be made from PDF refinement due to the high numbers of cations present per site and the limitation of existing software for exploring local nuclear and magnetic cation ordering together.

3.3.6 Large box reverse Monte Carlo (RMC) modeling

As noted above, quantitative real-space refinement of the series of data is complicated by the presence of magnetic spin correlations and the large number of cations involved on the spinel tetrahedral and octahedral sublattices. Large box modeling of PDF data with nuclear and magnetic spin correlations was pursued to provide additional insight into structure-property characteristics in the series. Combined fits of $F(Q)$ (Figure S3.5, Figure S3.6) and Bragg (Figure S3.7, Figure S3.8) intensities were completed for all samples assuming an inverse spinel model and a random solution spinel model (trials with a normal spinel model were not tried as they were ruled out conclusively by Rietveld analysis and small box PDF modeling). The agreement of fits to experimental data is high for both model types for all four samples. Table S3.5 (for F1 and F3) and Table S3.6 (for F4 and F5) list the resulting anisotropic atomic displacement parameters (ADPs) on cation tetrahedral sites, cation octahedral sites, and oxygen sites of each RMC refinement for F1, F3, F4 and F5. For F4 and F5 samples, resulting ADP values for the tetrahedral sites and for oxygen positions in the random solution spinel model fits are found to be nearly half those found for inverse spinel model fits. Such an anomaly, combined with Rietveld refinement results, indicate a strong preference for a random model over an inverse one for F4 and F5 samples. Thus the following discussion is based on analysis of the model

configurations obtained from an inverse spinel model for samples F1 and F3 and a random solution spinel model for samples F4 and F5.

With the magnetic spin configuration obtained via RMC modeling for all samples, all magnetic moment vectors contained in the supercell were mapped into a single unit cell and then projected onto the XY plane. Results are shown visually in Supporting Information Figure S3.9 and Figure S3.10, the magnetic spin distribution of F1 and F3 samples are more disperse on both tetrahedral and octahedral sites than F4 and F5. In all samples, the magnetic spin distributions of octahedral sites are more disperse than those found on tetrahedral sites. Overall, less collinear spin order and stronger displacements from atom sites are observed for F1 and F3 samples. Two types of statistical analyses were completed to quantify the findings. First, a KDE analysis was conducted, capturing the proportion of magnetic moments found within a specified radius (with the variation ranging from 0 to 1). In principle, the faster such a proportion approaches 1, the stronger the collinearity in magnetic ordering. The results are presented in Figure 3.8 (a) for the tetrahedral site magnetic vector distribution and (b) for the octahedral site magnetic vector distribution, indicating a significantly more collinear spin arrangement in F4 and F5 samples than in F1 and F3 samples. This result is consistent with the smaller net magnetic moment in F1 and F3 samples - see Table S3.7 in the SI. Additionally, in all samples, tetrahedral site spin correlations are found more collinear than octahedral site spin correlations.

Second, the HZ statistic was calculated to quantify the non-Gaussian behavior of the oxygen coordinate distributions and magnetic moment vectors within the XY plane. Different starting cation distribution configurations are found to influence the HZ statistic values for F1 and F3 samples; however, values determined for F1 and F3 are generally larger than those found for F4 and F5. Overall, in Figure 3.9(a) and Figure 3.9 (c)., it can be observed that F1 and F3 samples exhibit a more non-Gaussian behavior in oxygen atom distributions and in magnetic moment vector distributions on the octahedral site than F4 and F5 samples. (HZ parameters for F4 and F5 samples are much closer to 1, i.e., no obvious non-Gaussian distortion could

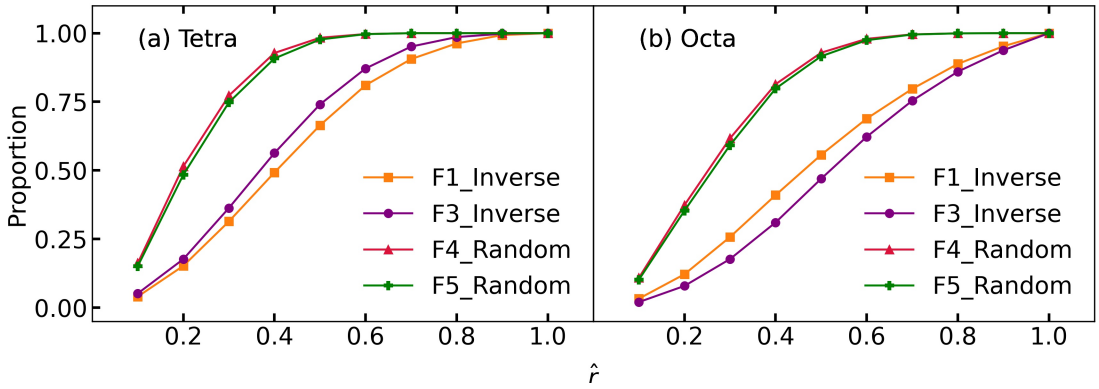


Figure 3.8: The proportion of magnetic moment vectors with projection on the XY plane for samples F1, F3, F4 and F5 falling into specified radii, relative to atoms of (a) tetrahedral (Tetra) and (b) octahedral (Octa) sites that the corresponding magnetic moments belong to. Results presented correspond to an inverse spinel structure model for F1 and F3 sample data and a random solution spinel model for F4 and F5 sample data. It is noted that similar results are obtained when the alternate models are used (inverse spinel model for F1 and F3 sample data and random solution spinel model for F4 and F5 samples).

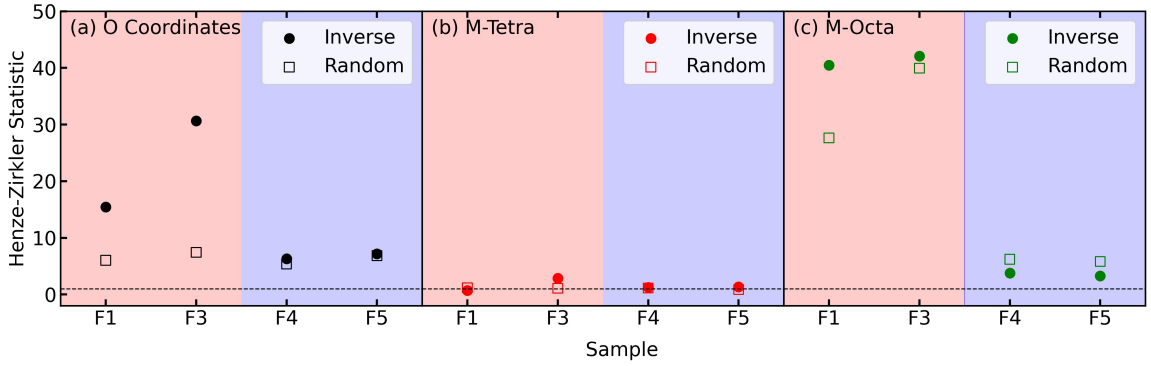


Figure 3.9: The HZ statistic for the distribution of (a) oxygen atom (O) coordinates and magnetic moment vectors (M) on (b) tetrahedral sites (Tetra) and (c) octahedral sites (Octa), for F1, F3, F4, and F5 samples. The horizontal dashed lines indicate a Gaussian distribution.

be observed). Meanwhile, if focusing on magnetic moment vector distributionson the tetrahedral site (Figure 3.9 (b)), all four samples show HZ parameter values close to 1, indicating a nearly Gaussian distribution. These comprehensive results here suggest strong coupling between non-collinear magnetic correlations originating primarily from octahedral site spins and oxygen site displacements, especially in F1 and F3 samples. Variation in the level of spin-lattice coupling among high entropy spinels of similar composition demonstrates a potentially tunable interaction in the more extended family.

3.4 Conclusion

We have determined the average ferrimagnetic structure in a family of AFe_2O_4 high entropy spinels with neutron Bragg diffraction analysis and found evidence for a variation in the tetrahedral and octahedral site occupancies of A-site cations with local structure analysis of neutron total scattering data. These high entropy spinels are not found to have strictly random cation configuration structures (highest S_{config}), but rather, F1/F3 samples in this study were found to have configurations closer to an inverse spinel. The distinct populations of Fe and other magnetic cations on tetrahedral and octahedral sites in the samples manifests in variation in the prevalence and propagation of local spin clusters, as revealed by FORC analysis of magnetometry data. RMC modeling reveals spin non-collinearity in all four samples, enhanced in cases presenting a larger degree of cation inversion.

While identifying the cause for the variation in cation disorder among similar compositions falls outside the scope of the present study, we bring attention to a potential competition between crystal field stabilization effects (which promotes inverse spinel ferrite configurations for the compositions studied) and the entropy stabilization present in truly random spinel ferrite configurations. How much the relative effects of these phenomena are influenced by sample synthesis conditions or other factors, potentially creating samples in one of many different metastable

states, remains unknown. Overall, this work highlights that it may prove extremely challenging to achieve a true solid solution with ideal/homogeneous cation mixing in compositionally complex ceramics with complex energy landscapes. We suggest great care be taken in this community to precisely describe reaction conditions, etc. when reporting HEO properties and drawing conclusions regarding the effects of configurational entropy on resultant products. Additionally, experimental characterization of the local to long-range crystal-chemical structure in HEOs may be key to determining and understanding their physical properties. The limitations of the characterization methods explored herein indicate future efforts are needed towards combined experimental probes and advanced data modeling. Hard and soft X-ray absorption near edge spectroscopy (XANES), soft X-ray magnetic circular dichroism (XMCD) and ^{57}Fe Mössbaruer spectroscopy (with and without external magnetic field) are examples of techniques that may provide additional insights.

Chapter 4

Phase Selectivity and Stability in Compositionally Complex Nano $(n\mathrm{A}_{1/n})\mathrm{Co}_2\mathrm{O}_4$

The previous chapter explored the intriguing structure-property trends in a family of compositionally complex spinel ferrites, revealing their processing history and resulting chemical short-range order can strongly influence magnetic behavior. As discussed in Chapter 1, Section 1.1.3, nano-compositionally complex oxides (CCOs) are expected to offer further structure-property tunability through the introduction of nano-size effects. In this chapter, a family of compositionally complex spinels with the formula of $(n\mathrm{A}_{1/n})\mathrm{Co}_2\mathrm{O}_4$ (A = combinations of Mg, Cr, Mn, Fe, Co, Ni, Cu, and Zn) was synthesized using a low-temperature soft-templating method. The phase selectivity and the temperature stability window for the series were found to depend strongly upon A-site composition and only modestly on the number of elements (n) present on the A-site. Select control reactions and in situ high temperature X-ray diffraction (XRD) uncovered a propensity for temperature-activated de-mixing for compositions containing Mg, Ni, Mn, and Fe. The A-site cations exhibit spatially heterogeneous distributions in the *as-formed* spinels, which diminishes

with intermediate thermal annealing, as shown by scanning transmission electron microscopy (STEM)/energy dispersive spectroscopy (EDS) and X-ray line profile analysis. The single spinel phases obtained are metastable, separating into a mix of impurity phases and multiple spinel phases with higher temperature annealing. Furthermore, we demonstrate a 'continuous lattice' parameterization of the CCO structure provides a rapid means by which to examine the heterogeneity of the cation distribution through full profile refinement. The demonstrated tunability of the cation distribution or clustering in these compositionally complex spinels via thermodynamic levers affords interesting opportunities for rational design of functional materials.

Chapter 4– *Phase Selectivity and Stability in Compositionally Complex Nano* $(nA_{1/n})Co_2O_4$– is reprinted (adapted) with permission from *Chem. Mater.* 2023, 35, 7283–7291, DOI: 10.1021/acs.chemmater.3c01647 [245]. Copyright 2023 American Chemical Society. The authors of the work are Xin Wang, Peter C. Metz, Eleonora Calì, Palani Raja Jothi, Eric A. Lass, and Katharine Page.

4.1 Introduction

Nanostructured materials offer promising physicochemical properties across diverse applications in energy storage, sensing, catalysis, biomedicine, and more. Nano high entropy oxides (HEOs) and the more general class of compositionally complex oxides (CCOs) are expected to offer enhanced structure-property tunability by virtue of their large numbers of participating cations, their combined entropic disorder, and their intrinsic nano-size effects. HEOs are widely described as single-phase oxides that have five or more metal cations sharing a specific crystallographic lattice site in a random fashion. More stringent definitions add a criterion for configurational entropy (S_{config}) equal to or higher than $1.5R$ per mole of metals/cations, where R is the universal gas constant. In principle, the configurational entropy S_{config} can be tuned to achieve maximum site mixing at an equimolar ratio among the site sharing cations, allowing the entropic contribution (ΔS_{mix}) to the system energy to

overcome competing enthalpic driving forces (ΔH_{mix}) with an increase in system temperature (T). According to the Gibbs free energy (ΔG_{mix}) formulation, $\Delta G_{mix} = \Delta H_{mix} - T\Delta S_{mix}$, a larger entropic term at higher temperature stabilizes the structure in a high entropy state, and the system is then termed an entropy stabilized oxide (ESO). However, in practice, depending on the system, the maximized configurational entropy may not overcome the enthalpic energy with respect to alternate phase formation. Multiple factors in real systems contribute to the enthalpic term, including the specific cations incorporated, the preferred structural configuration (defects, distortions, specific patterns of chemical short-range order) associated with certain cations, the surface/interfacial energy, etc. [215, 199, 195, 149] Many materials currently reported as HEOs and ESOs, some with novel and exceptional physical properties, do not meet the above thermodynamic criteria and likely feature cation configurations that are far from homogeneous and completely mixed.

Intentional efforts in designing and exploiting the wider class of CCOs can be embraced, including medium-entropy and non-equimolar composition oxides,[259] with the recognition that they provide even wider highly tunable phase space. For example, a number of recent works have highlighted the inherent flexibility and potential promise of exploring CCOs [259] by achieving low thermal conductivity and high stiffness among fluorite[261, 263], pyrochlore[262, 182, 260, 286, 287], weberite, fergusonite[182], and bixbyite[229] systems. A number of perovskite CCOs have shown promise as stable and high performing materials for energy storage/transformation applications[104, 288, 289]. These studies uncovered instances of property or structure tuning,[263, 262, 182, 104, 288] specific short-range order motifs,[263] order-disorder transformations,[260, 286] multi-phase regions,[229] and other crystal-chemical phenomena.

Nano-size effects ubiquitous in nanosystems arise due to high surface area to volume ratios, non-equilibrium surface structures, unique shape/morphology, high interfacial energy, and more, offering further opportunities to explore phase space within the HEO/CCO paradigm. Limited work has been reported on nano-HEOs to

date. Wang *et al.*[234] reported a nano-HEO material (Cu-Cr-Fe-Co-Ni-O) obtained via laser scanning ablation. Preparation of nano-fluorite HEO materials with ball-milling, chemical co-precipitation, and polymeric steric entrapment was reported by Jothi *et al.*[93]. Nebulised spray pyrolysis, flame spray pyrolysis and reverse co-precipitation techniques were employed by Sarkar *et al.* to synthesize nanocrystalline rock salt structure HEOs[196, 292]. Low-temperature solvothermal synthesis with pyrolysis at 400 °C was developed for obtaining nano-spinel structure HEOs by D. Wang *et al.* [237], and the sol-gel method was used by G. Wang *et al.* to fabricate nano spherical mesoporous spinel HEO particles.[238] We note materials in these works have been reported as nano-HEOs (not nano-CCOs), though most do not explore/discuss specific thermodynamic criteria distinguishing them one way or the other.

The spinel structure offers a highly flexible phase space where competing thermodynamic factors can be exploited. This work explores CCO compositions related to spinel cobalt oxide, Co_3O_4. Spinel Co_3O_4 is considered a favorable low temperature economical catalyst for formaldehyde oxidation, and variations are used in many other catalytic and electrochemical reactions[120, 205, 66, 265]. For example, Co_3O_4 nanocrystals grown on reduced graphene oxide are high-performance bi-functional catalysts for the oxygen reduction reaction (ORR) (with reported overpotential of 310 mV) and oxygen evolution reaction (OER) (with reported onset potential of 0.82 V)[125]. Furthermore, as one of the ferromagnetic metals (iron, nickel and cobalt) in nature, cobalt (Co) is essential to the development of hard magnetic materials due to its high saturation magnetization (M_S), high Curie temperature (T_C) and high magnetocrystalline anisotropy[153]. Most binary transition metal cobalt oxide spinels are earth abundant ferrimagnetic phases[19, 16, 95, 159, 277].

In this work, a family of nano-$(nA_{1/n})Co_2O_4$ is synthesized by a low-temperature soft-templating (LTST) reaction route, where A includes n different equiatomic ratio $(1/n)$ combinations of 1 to 7 transition metal cations. Trends in phase selectivity and temperature stability are examined. The configurational entropy per mole of

metals/cations (S_{config}) is smaller than $1.5R$ even if seven cations are sitting on the A-site and all possible spinel configurations are assumed[246]. For example, the configurational entropies calculated for a normal spinel with formula ACo_2O_4 are 0.54R, 0.60R, and 0.65R for n=5, 6, and 7, respectively. The size/morphology, distribution of cations, and crystal structure within the nanostructures is examined via XRD, high resolution scanning transmission electron microscopy (STEM)/energy dispersive spectroscopy (EDS), and thermogravimetric analysis/differential scanning calorimetry (TGA/DSC) analysis. A new approach for obtaining nano/bulk structure information from CCOs with a 'continuous lattice' (CL) Rietveld refinement is also explored for the first time.

4.2 Methods

4.2.1 Materials synthesis

The LTST synthesis procedure used in this work is illustrated in Figure 4.1. The structuring agent [3.2 g of Pluronic P123, a symmetric triblock copolymer comprising poly(ethylene oxide) (PEO) and poly(propylene oxide) (PPO) in an alternating linear fashion, PEO-PPO-PEO, ALDRICH Chemistry] was mixed in 20 mL Ethyl Alcohol (absolute, 200 Proof, 99.5+%, ACROS Organics). 0.5 mL Hydrochloric acid (HCl, Fisher Chemical) was added, and the mixture was stirred with a magnetic stir bar until Pluronic P123 was completely dissolved. Finally, a stoichiometric amount (1 g $(nA_{1/n})Co_2O_4$ as the target) of inorganic nitrate hydrate precursor solutions in wt.% of metal were added into the solution. The nitrate hydrate sources are manganese nitrate tetrahydrate [$Mn(NO_3)_2{\cdot}4H_2O$, ACROS Organics], iron chloride tetrahydrate ($FeCl_2{\cdot}4H_2O$, 99+%, ACROS Organics), nickel nitrate hexahydrate [$Ni(NO_3)_2{\cdot}6H_2O$, 98%, Alfa Aesar], zinc nitrate hexahydrate [$Zn(NO_3)_2{\cdot}6H_2O$, 99%, metal basis, Alfa Aesar], magnesium nitrate hexahydrate [$Mg(NO_3)_2{\cdot}6H_2O$, 99+%, ACROS Organics], cobalt nitrate hexahydrate [$Co(NO_3)_2{\cdot}6H_2O$, 99%, pure, ACROS Organics], and

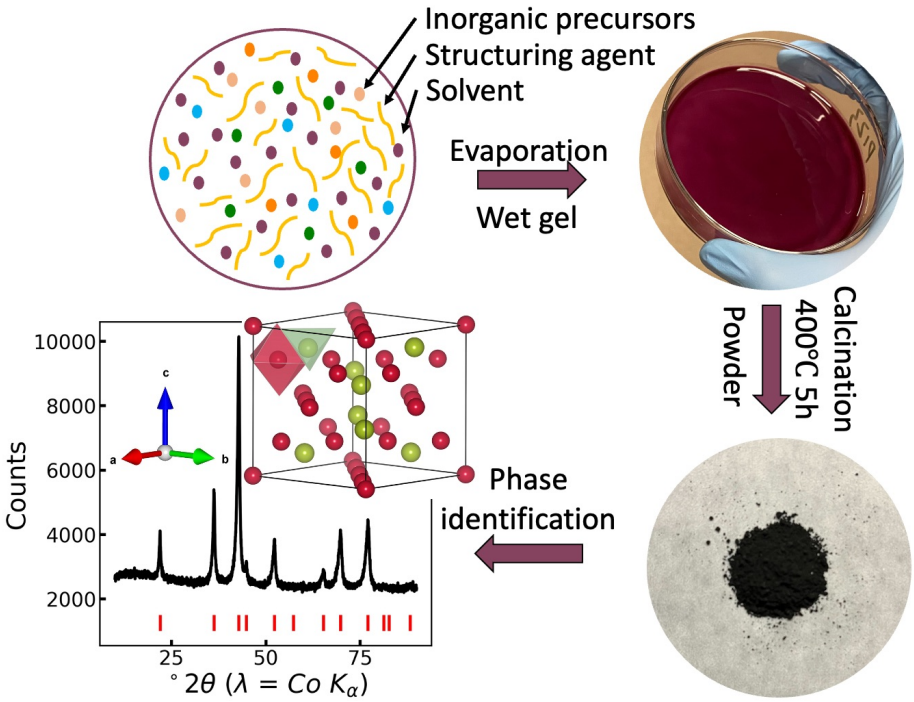


Figure 4.1: Schematic diagram of the LTST method used to synthesize a large family of compositionally complex cobalt-based nano spinels, $(n\mathrm{A}_{1/n})\mathrm{Co}_2\mathrm{O}_4$. First, a solution of inorganic precursors, structuring agent, and solvent is stirred for 30 mins. A wet gel is obtained after 24 h evaporation and a black powder is formed after calcination at 400 °C for 5 h (the *as-formed* (AF) sample). Finally, a spinel phase structure with 8 tetrahedral (green) sites and 16 octahedral (red) sites in the unit cell is identified by XRD (oxygen atoms are not shown in the image).

chromium nitrate nonahydrate [$Cr(NO_3)_3 \cdot 9H_2O$, 99%, ACROS Organics]. The entire mixed solution was stirred for 30 mins with a magnetic stirrer. The mixed solution was poured into a petri dish and evaporated under a fume hood for 24 h to obtain a wet gel. After evaporation, the gel was transferred to a furnace and calcined at 400°C for 5 h with a ramp rate of 1°C/min. The powder samples obtained via such steps without any further treatment are hereafter referred to as the *as-formed* (AF) samples. The majority of AF compositions in this work result in a spinel structure (SG 227, $Fd\bar{3}m$), as identified by XRD analysis (more details in Results section). Pellets of the AF samples were then made using a MP24A desktop pellet press and placed into the furnace for post-annealing heat treatment (*post-treatment*, PT) (at 600 °C (PT6), 800 °C (PT8), or 1000 °C (PT10) for 5 h and with a slow ramp rate of 2 °C/min, 3 °C/min, and 3 °C/min, respectively). Sample compositions explored in this work with n of 5 or more are listed in Table 4.1, with corresponding XRD data shown in supplemental information (SI) Figure S4.1. Additional sample compositions are listed in SI: Table S4.1. Corresponding XRD data are shown in SI Figure S4.2. Sample names nCN reflect the number of n cations targeted (first character) and a specific Composition Number (CN), as summarized in Tables 4.1 and Table S4.1.

4.2.2 Characterization

X-ray Diffraction (XRD) Ambient XRD and high temperature XRD (HTXRD) data were measured using a PANalytical Empyrean diffractometer equipped with a Co X-ray source. Ambient XRD patterns were measured between 10° and 90° 2θ with a step size of 0.026°. HTXRD patterns were measured between 18° and 56° 2θ with a step size of 0.026° and acquisition time of 316 s at 11 °C intervals from room temperature to 1000 °C. The use of Co Kα radiation was essential to minimize fluorescence and uncover minor impurity phases.

Scanning Electron Microscopy/Energy Dispersive X-Ray Spectroscopy (SEM/EDS) Specimens for scanning electron microscopy (SEM) and energy

Table 4.1: Compositions $(n\mathrm{A}_{1/n})\mathrm{Co}_2\mathrm{O}_4$ with $n \geq 5$ explored within this work, separated into groups (see main text for details). Samples are observed after calcination (*as formed* 400°C, AF4) and following post-annealing heat treatment (*post-treatment* 600°C, PT6, etc.). Check marks indicate the presence of specific elements in each composition. Conditions resulting in X-ray pure phases are colored green and conditions resulting in phase mixtures are colored purple. Impurities are coded: CuO ("c"); rock salt ("r"); secondary spinel ("s"); and $\mathrm{CoCl_2{\cdot}2H_2O}$ ("h").

Name	n	Mg	Cr	Mn	Fe	Co	Ni	Cu	Zn	AF4	PT6	PT8	PT10
Group 1: n=5 cation combinations													
5C1	5	✓		✓	✓			✓	✓			r	r+s
5C2	5			✓	✓		✓	✓	✓	h		c	c+r+s
5C3	5	✓		✓	✓		✓		✓			r	r+s
5C4	5	✓		✓			✓	✓	✓	r	r	r	r+s
5C5	5	✓			✓		✓	✓	✓	c+r	c+r	c+r	c+r
5C6	5	✓		✓	✓		✓	✓				r	r+s
Group 2: Increased number of cations (with Mg included)													
5C1	5	✓		✓	✓			✓	✓			r	r+s
6C1	6	✓		✓	✓		✓	✓	✓			r	r+s
7C1	7	✓	✓	✓	✓		✓	✓	✓			r	r+s
Group 3: Increased number of cations (without Mg included)													
5C2	5			✓	✓		✓	✓	✓	h		c	c+r+s
6C2	6			✓	✓	✓	✓	✓	✓				r+s
6C3	6		✓	✓	✓		✓	✓	✓				r+s
Group 4: n=5 cation combinations without Ni or Mg													
5C7	5			✓	✓	✓		✓	✓				c+s
5C8	5		✓	✓	✓			✓	✓				c+s

dispersive spectroscopy (EDS) were prepared by gently dispersing the ground powders onto a standard carbon tape. Zeiss Auriga high resolution SEM was used to characterize the morphologies of the specimens. Elemental analysis was carried out with a Zeiss EVO SEM.

Scanning Transmission Electron Microscopy (STEM)/Energy Dispersive Spectroscopy (EDS) The morphology of the samples was investigated at the nanoscale by STEM imaging using a JEOL JEM-2100F microscope operated at 200 kV. The chemical composition and elemental distribution of the samples were analyzed by energy dispersive X-ray spectroscopy (EDS) operated in scanning transmission electron microscopy (STEM) mode (EDS 80 mm X-Max detector, Oxford Instruments). The STEM-EDS specimen preparation was carried out by sonication of powder samples in high purity propan-2-ol then drop-casted on copper grids coated with a holey carbon film (3.05 mm diam. 300 mesh, TAAB).

Thermogravimetric Analysis (TGA) and Differential Scanning Calorimetry (DSC) The simultaneous measurement of weight change (TGA) and true differential heat flow (DSC) were examined by TA instuments SDT Q600 from ambient to 1000 °C with a 5 °C/min ramp rate in air.

4.3 Results and Discussion

4.3.1 Composition and heat treatment effects

Naively assuming a normal spinel structure, the tetrahedal site is occupied by the equimolar A^{2+} cations while the octahedral site is soley occupied by Co^{3+}. Figure 4.2 displays the calculated tolerance factor (top) and average ionic radii of tetrahedral site cations (bottom) resulting from these assumptions. Experimental conditions resulting in single phase spinel samples are indicated in green coloring while conditions

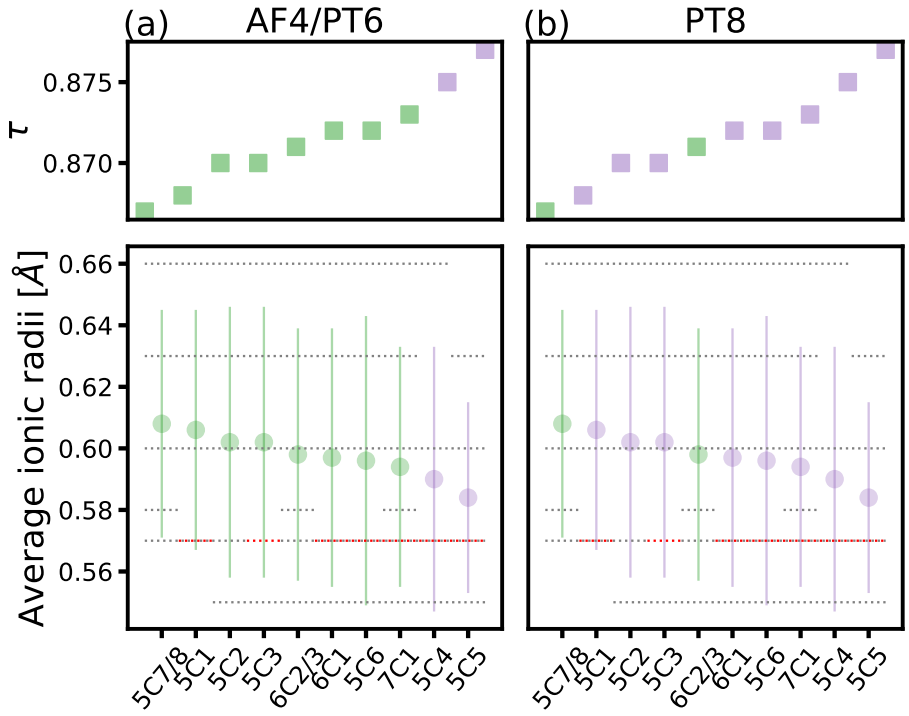


Figure 4.2: Spinel tolerance factore (τ) (top panels) and average ionic radii of tetrahedral site cations (bottom panels), assuming a normal spinel configuration, for (a) AF4 and PT6 samples, and (b) PT8 samples for each composition. Vertical lines in the bottom panels represent the calculated standard deviation of participating radii. The red dotted lines indicate the presence of "Mg" in a sample while black dotted lines indicate the presence of all other elements in the sample. Markers colored green indicate samples that appear X-ray phase pure. See Table 4.1 for sample compositions and further detail.

resulting in samples containing secondary phases are indicated in purple coloring. Most compositions in the series result in a single phase spinel for AF4 and PT6 processing conditions (a), while the majority result in multiple or impurity phases for PT8 processing conditions (b). Dashed lines in the bottom plots indicate the specific participating ionic radii in each composition (again, nievely assuming a normal spinel configuration with strictly Co^{3+} and A^{2+} cations). All 12 compositions fall within the typical tolerance factor window for spinel oxides (∼0.85)[213], where the tolerance factor, τ, is defined

$$\tau = \frac{\sqrt{3}(R_{Co} + R_O)}{2(\langle R_A \rangle + R_O)}, \tag{4.1}$$

R_{Co} and R_O represent the ionic radiui of Co^{3+} and O^{2-}, and $\langle R_A \rangle$ represents the average radius of A^{2+}.

Table 4.1 lists all 5, 6, and 7 A-component compositions made in this work along with sample abbreviations used. All *as-formed* and *post-treatment* samples were screened with XRD analysis to assess phase identity, phase purity, degree of crystallinity, and (to the extent possible) cation site inversion, γ. Representative data are shown in SI Figure S4.1 for all samples. Rietveld refinement (discussed below) was used to confirm secondary phases and estimate phase impurity levels. In Table 4.1 and Figure 4.2 synthesis conditions resulting in single spinel phases are indicated with green coloring, while those resulting in impurity phases (either cobalt chloride hydrate (h), rock salt (r), tenorite CuO (c), or secondary spinel phase (s)) are indicated in purple coloring.

A few details are immediately apparent. First, many of the compositions in this work result in single phase spinel oxides in their *as-formed* state. To the best of our knowledge, these CCOs are reported here for the first time. Figure 4.2 reveals that the average ionic radii of the A-site cations (and the corresponding spinel tolerance factor) plays a key role in determining which compositions will form a single phase spinel in AF4 and PT6 samples. Samples with tolerance factors below 0.874 (assuming a normal spinel structure) result in a single spinel phase. Those with larger tolerance

factors result in impurity phases, primarily including rock salt AO or tenorite CuO phases.

Second, the spinel oxides in this work are metastable; when processed at 1000, the spinel phase segregates into multiple spinel phases (the secondary spinel phase is indicated by "s" in Table 4.1). This segregation is also corroborated by the STEM-EDS analysis presented below, indiciating segregation of Fe and Mn relative to other A-site atoms. In Group 1 (n=5 cation combinations) of Table 4.1, *5C5*, does not contain Mn and does not result in a secondary spinel phase for PT10 conditions. Conversely, compositions *2C4* (A= Fe and Zn) and *2C5* (A= Mn and Zn) (listed in SI Table S4.1, and representative data shown in SI Figure S4.2) exhibit a secondary spinel phase for PT10 conditions. This suggests that regardless of any other component present, Mn consistently prefers to segregate to a secondary spinel phase, while Fe's behavior depends on the other components involved. This observation is reasonable given that tetrahedrally coordinated Mn and Fe possess larger ionic radii (0.66 Å for Mn^{2+} and 0.63 Å for Fe^{2+}) in comparison to other components (as illustrated in the bottom panels of Figure 4.2).

Thirdly, Table 4.1 and Figure 4.2 reveal that the number of cations participating, represented by n, is just one of several considerations in phase stability and selection in the PT8 series. Which cations are present can play a dominant role. Take, for instance, Group 2 (Increased number of cations, with Mg included) and Group 3 (Increased number of cations, without Mg included) in Table 4.1: the incorporation of Mg in the A-site results in a smaller thermal stability window for the CCO spinel phases. When Mg is left out, additional cations result in a wider thermal stability window for a single CCO spinel phase. The presence of Mg over-rides the influence of increasing n in the compositions explored.

Further, in SI Table S4.1, compositions *2C1* (A= Mg and Zn), *2C3* (A= Ni and Zn), *4C1* (A= Mg, Mn, Fe, and Zn) and *4C2* (A= Mn, Fe, Ni and Zn) all result in rock salt impurities for PT10 conditions (representative data are shown in SI Figure S4.2). These samples all contain Mg or Ni. Mg shows high favorability for the rock

salt phase formation; for example, the study of *4C1* shows a tiny rock salt impurity peak in PT8 while *4C2* does not (see SI Figure S4.2). Based on these results, samples *5C7* and *5C8* in Group 4 (without Ni or Mg) in Table 4.1 were designed and synthesized without impurity phases under PT8 conditions. All of these results support the conclusion that the incorporation of Mg or Ni contributes to rock salt AO impurity formation.

The phase formation energies of possible binary impurities (known binary oxides of cations involved) are shown in Figure 4.3, arranged by cation valence state. The information provides some thermodynamic rationale for the specific impurity phases encountered in our study. As mentioned above, all compositions containing Ni or Mg lead to rock salt impurities with heat treatment. Tenorite-line (CuO) formation appears in sample *2C2* (A= Cu and Zn, AF4, PT6, PT8, and PT10), *5C2* (PT8 and PT10), *5C5* (AF4, PT6, PT8, and PT10), *5C7* (PT10) and *5C8* (PT10). The phase formation energies for 2+ cations shown in Figure 4.3 range between -601.6 kJ/mol for rock salt MgO[214] and -157.3 kJ/mol[214] for tenorite CuO. We note Ni, Mg, and Cu are notably absent in the group of mixed valent A_3O_4 spinels, which included the Co, Fe, Cr, and Mn cases (appearing at the far right of Figure 4.3). Such findings infer the importance of cation selection in determining the structural stability and impurity phase formation.

The impurity phases found here with higher *post-treatment* temperature are counter indicative of the entropy stabilization effect – increasing the *post-treatment* temperature is expected to enhance the entropic contribution ($-T\Delta S_{mix}$) to the overall Gibbs free energy and hence is expected to favor the structure of a single phase. Therefore, other factors contribute to the lowering of mixing (i.e., diminishing the effect of the configurational entropy) at high temperatures. Compositional heterogeneity is therefore an important factor to consider in the *post-treatment* procedure.

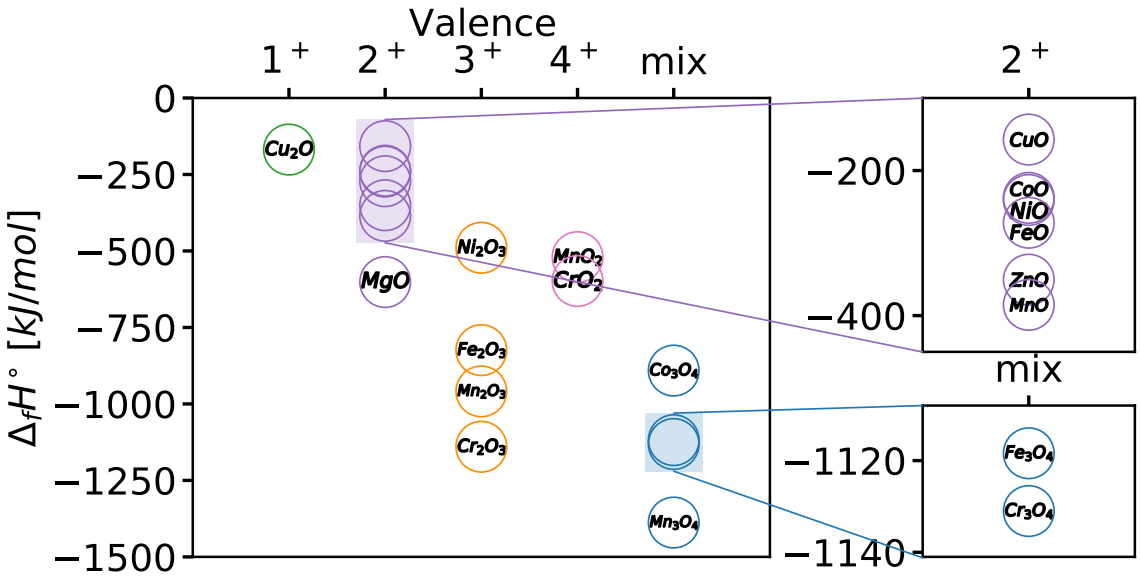


Figure 4.3: Phase formation energy, ΔH_f°, for possible binary oxide impurities resulting from the inclusion of single cations with different oxidation states.

4.3.2 Case study: $(Mg_{0.2}Mn_{0.2}Fe_{0.2}Cu_{0.2}Zn_{0.2})Co_2O_4$ (5C1)

Phase Formation

Composition *5C1* presents a single phase spinel structure for AF4 and PT6 conditions, but is observed to separate into a spinel with MgO impurity for PT8 conditions and exhibit a second (Mn and Fe rich) spinel phase for PT10 conditions. This solid-state phase transformation process was examined in greater detail using in situ HTXRD and TGA/DSC (Figure 4.4). A reconstructive phase transformation from spinel to rock salt begins around 714 °C and is nearly complete around 1100 °C. Upon slow cooling, the rock salt phase decomposes into two spinels phases and a remnant rock salt phase. The irreversible phase transformation confirms that the initial spinel *5C1* is metastable.

Throughout this thermal cycle the heat flow is endothermic. The phase transformation from spinel (4:3 O:A) to rock salt (1:1 O:A) is accompanied by a corresponding loss of oxygen. For *5C1* reduction to a stoichiometric rock salt formula corresponds with a 6.8% mass loss. In the measured weight loss, initial heating results in a 2.5% weight loss, likely due to adsorbed water and surface hydroxyls, and subsequent 5.3% weight loss. Faint diffraction intensity corresponding to a spinel is present with the rock salt Bragg peaks above 1100 °C. Together, this suggests some phase coexistence and perhaps oxygen nonstoichiometry.

For rock salt and for distinct spinel phases to form we propose the phase transformation must be diffusional, though over different characteristic lengths for the oxygen and anion substructures. The transformation from spinel to rock salt is well known, for instance in the Li-Mn-N-O system[210], where delithiation of the spinel results in rock salt formation. Transformation between the two structures effectively constitutes ordering of cation vacancies and interstitials. Meanwhile, a change in oxygen stoichiometry implies oxygen diffusion from the bulk to the powder surface. Thus, recovery of the spinel upon cooling is expected to have a kinetic limitation dependent upon temperature and ambient oxygen partial pressure. Together, this

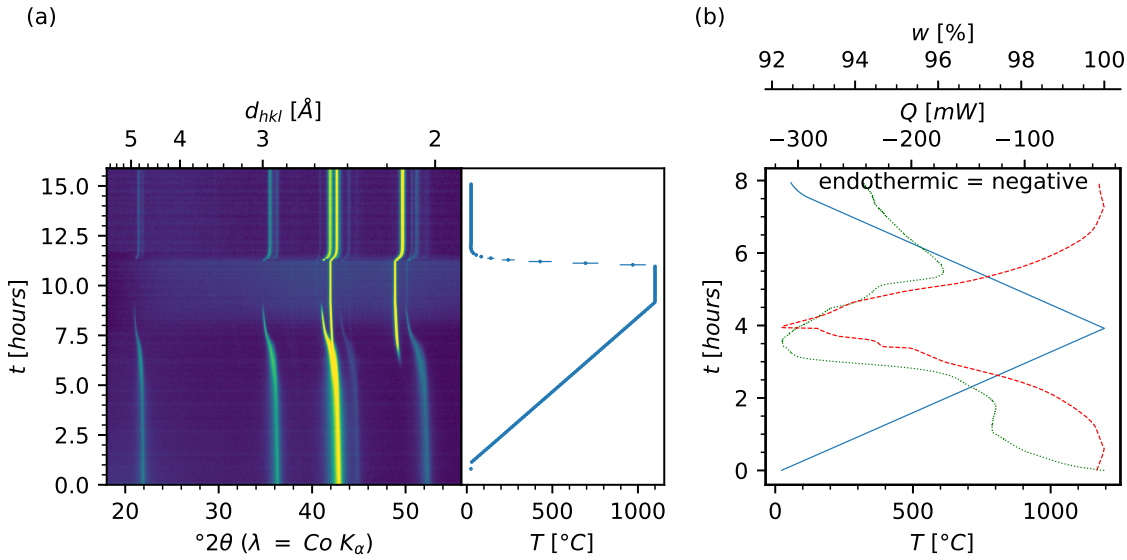


Figure 4.4: (a) Logarithmic powder diffraction intensities collected step-wise in 11 °C intervals to 1100 °C, over an isothermal dwell, and free-cooling to room temperature. (b) Thermal analysis signals collected over a heating and cooling cycle with 300 °C/h ramp rate: temperature (blue —), weight change (green ⋯), and heat flow (red - - -).

analysis implies that the *as-formed* spinel is metastable. Further evidence for incipient cation segregation in the metastable *as-formed* spinel is presented below.

Microscopy

SEM images corresponding to the *5C1* sample series (AF4, PT6, PT8, PT10) are depicted in SI Figure S4.4. Notably, the AF4 sample exhibits a wide particle size distribution (ranging from 10 to 100 nm). This finding is in agreement with the XRD results shown in SI Figure S4.1, where the AF4 sample exhibits a stronger peak asymmetry. Peak width and asymmetry decrease in PT6 and PT8 samples, indicating that higher *post-treatment* temperature results in larger particle sizes and a more homogeneous particle size distribution. The PT10 sample exhibits micron scale particle size. SEM/EDS characterization revealed that sample *5C1* AF4 is microscopically homogeneous in terms of cation composition (depicted in SI Figure S4.3).

The distribution of various elements among particles or domains was investigated at high resolution using STEM/EDS elemental mapping as depicted in Figure 4.5. Interestingly, the degree of heterogeneity is found to vary significantly in the *5C1* sample series on the nanoscale. In Figure 4.5 AF4, notable enrichment of Mg and Mn in specific grains is evident, along with a less severe enrichment of Fe. In PT6 and PT8 samples, the cation enrichments fade (samples feature more homogeneous cation distributions). At higher *post-treatment* temperatures, multiple phases are observed. In PT10, the migration of Mn, Fe, and Mg was observed to have occurred entirely out of some grains, while the enrichment of Co in select grains persisted.

Rietveld Analysis

Visual inspection of the XRD pattern in SI Figure S4.1 for *5C1* AF4 reveals broad and asymmetric diffraction peaks. The complex microstructure of the samples can be investigated in part by refinement of Bragg diffraction profiles. Conventional

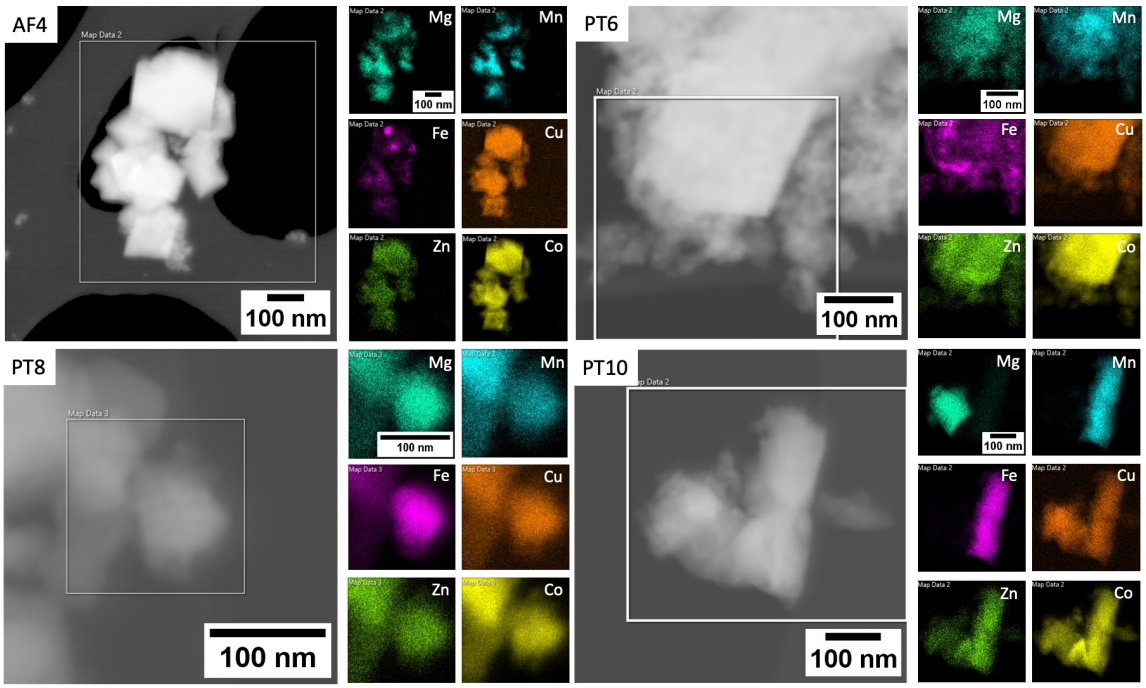


Figure 4.5: STEM/EDS elemental mapping of *5C1* AF4, PT6, PT8, and PT10 samples. Color maps indicate heterogeneous cation distributions of Mg, Mn and Fe for certain grains in the AF4 sample. In PT6 and PT8 samples, the cation enrichments fade (samples feature more homogeneous cation distributions). In the PT10 sample, Mn and Fe atoms are found in separate grains from Mg, and a modest enrichment of Co is observed in those grains with Mn and Fe. Cu and Zn remain distributed throughout all particles.

Rietveld refinement approaches were first tried and typical results are presented in Figure 4.6 (a) to (c). Refinement results for models incorporating crystallite size broadening (Figure 4.6 a), size and strain broadening (Figure 4.6 b), or two spinel phases (with unique phase fractions and lattice parameter, all other values constrained equal) (Figure 4.6 c) are shown for *5C1* AF4. Here, the random spinel structure was selected as the basis since it fits the phase better compared to the normal and inverse spinel structures. Models incorporating size and strain effects poorly fit the peak profile shapes. A two-phase model, on the other hand, provides a marked improvement in the quality of fit (R_{wp}=2.171%). This fit incorporates an additional phase fraction parameter and lattice parameter. Since we do not know the distribution of atoms residing within the potential multiple phases, the phase fraction provides limited information.

Spatially varying scalar variables, like occupancy, can result in asymmetric line broadening like that observed here. The resulting line broadening will have a profile proportional to the probability density function of the scalar variable, and anisotropy proportional to the resultant lattice strain [114]. In the case that the scalar variable is normally distributed and the resulting strain is isotropic, conventional microstrain broadening is recovered. Otherwise, a suitable probability density function must be derived or guessed. For example, earlier work by Leineweber[112, 113] employed an Edgeworth series to approximate non-Gaussian N distribution in $\epsilon - FeN_y$.

In this case, we do not know *a priori* what probability density function to assume, and we are not interested in the anisotropy of the strain response, but rather are interested in estimating the probability density function of the compositional fluctuation within coherently diffracting crystallite domains. Further, because we are insensitive to atom type, the distribution in question is further collapsed to fluctuation of atomic radius around its mean value. To this end, we constructed what we have termed a CL model embedding isotropic lattice strain by superimposing a hierarchically constrained set of phases of discrete volume.

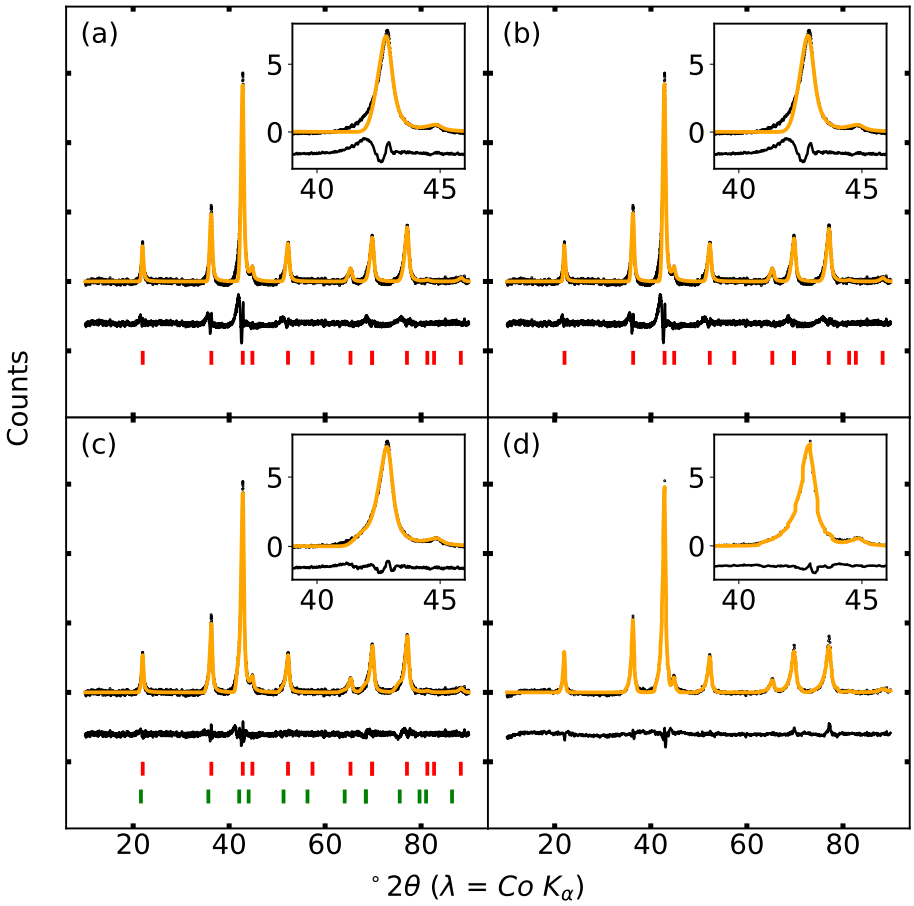


Figure 4.6: Rietveld refinements for *5C1* AF4 X-ray diffraction data with (a) crystalline grain size broadening (1 phase, no strain, $R_{wp} = 3.870\%$), (b) size and strain broadening (1 phase, refined strain, $R_{wp} = 3.869\%$), (c) two spinel phase model (phase fraction and cubic lattice parameter refined, no strain, $R_{wp} = 2.171\%$), and (d) CL phase model ($R_{wp} = 2.113\%$) applied. The XRD patterns were analyzed with the Rietveld method as embodied in the TOPAS-V7[36] program.

In this scheme, N identical crystal phase models are instantiated with fixed lattice volumes spanning the average observed value. Each model is given a refinable scale parameter (s_i), however each value is constrained by a weighted (w_i) penalty (p)

$$p = \Sigma_i w_i \sqrt{(s_{i+1} - s_i)^2}, \tag{4.2}$$

such that neighboring values cannot differ significantly, resulting in a locally linear or smoothly varying distribution. Because extraneous instrumental line broadening is controlled for, the resulting distribution of s_i should closely resemble the unknown distribution of the atomic radii. As shown in Figure 4.6 (d), the overall agreement with the experimental diffraction pattern was significantly improved ($R_{wp} = 2.113\%$). This parameterization of the CCO structure provides a rapid means by which to examine the heterogeneity of the A-site cation distribution through full profile refinement, as demonstrated in the following section.

4.3.3 Line profile analysis as a screening tool

Asymmetric peak shapes observed in data cannot be adequately explained by conventional microstrain models and crystallite size models, which assume symmetric intensity distributions. To address this misfit, there is a need for an asymmetric line broadening mechanism. The CL model with inhomogeneous cation distribution (and lattice volume) constructs the total intensity by a weighted sum of phases, and is proposed here as a powerful screening tool for analysis of microstrain-like line-broadening data, like nano-materials. By properly characterizing and modeling the peak profile of microstrain-like data, more reliable and relevent crystallographic information can be obtained.

By applying the CL phase to all $(n\mathrm{A}_{1/n})\mathrm{Co}_2\mathrm{O}_4$ ($n \geq 5$) AF4, PT6, and PT8 samples (Representative data are shown in SI Figure S4.1), the A-site (tetrahedral site) ionic radius distribution can be extracted from lattice parameters and atomic positions. The distribution of lattices is seen to decrease (from left to right) with

increasing *post-treatment* temperature, shown in Figure 4.7. This finding confirms the conclusion already suggested by the XRD, SEM, and TEM results, that the samples formed at low-T have broad asymmetric intensity distributions, inferring spatially heterogeneous cation distributions. Samples that experienced *post-treatment* feature increasingly sharp and symmetric diffraction peaks, inferring less heterogeneity of the cation distribution. At higher *post-treatment* temperatures, temperature activiated de-mixing leads to multiple distinct spinel phases. Together, this suggests the *as-formed* spinel is kinetically stabilized and possesses local chemical ordering.

Interestingly, an exampination of the degree of inversion (the fraction of A-site ions occupying the octahedral sites)[246], γ, extracted from CL refinements groups the samples into two categories: those incorporating Mg (represented by red squares in Figure 4.7) and those without Mg (represented by green squares in Figure 4.7). In Figure 4.8, the inversion parameter γ in *as-formed* samples is found to be relatively random. With increasing *post-treatment* temperature the compositions containing Mg (highlighted in red) trend towards an inverse structure, while those without Mg (highlighted in green) trend towards a normal spinel structure.

In Figure 4.7 we have ordered compositions from top to bottom in order of increasing predicted average octahedral ionic radius (assuming the detected inverse spinel structure model for compositions highlighted in red), and increasing tetrahedral ionic radius (assuming the detected normal spinel structure model for compositions highlighted in green). The lack of clear trends with respect to average predicted site radii implies that additional factors (cation valence, nanoscale segregated phases, oxygen defects, etc.) play roles in directing crystal-chemical trends in this series. In conclusion, line profile analysis, along with the CL model, is a valuable tool for screening material structure variations in compositional and processing condition series. Further investigations are necessary to better understand the impact of cation distribution on chemical short-range order in this series of spinel oxides.

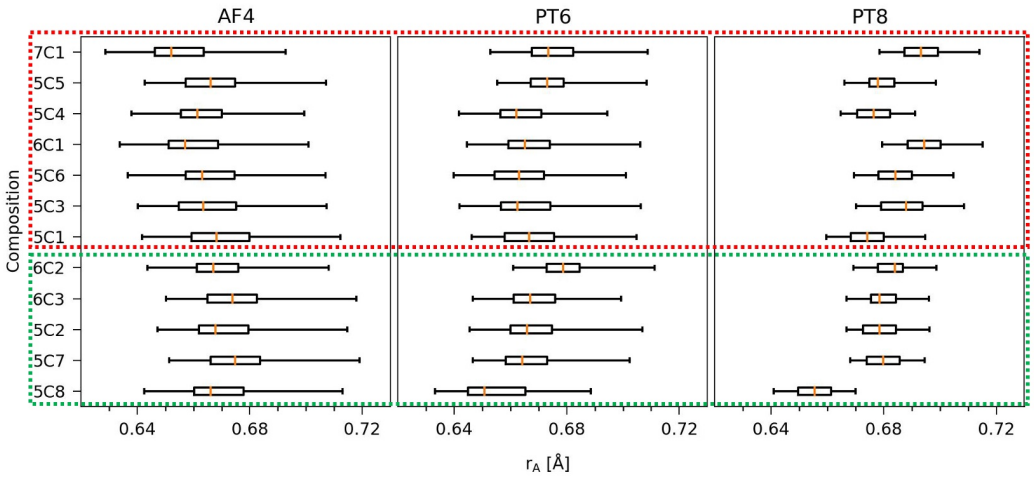


Figure 4.7: Tetrahedral site ionic radius (r_A) distribution extracted from CL Rietveld refinement results for $(n\mathrm{A}_{1/n})\mathrm{Co}_2\mathrm{O}_4$ ($n \geq 5$) samples. The heat treatment conditions are listed at the top of each column, while the composition identities of each series is shown on the left of each row. The compositions are ordered by increasing calculated average octahedral site radius (where an inverse spinel structure is assumed) and calculated average tetrahedral site radius (where a normal spinel structure is assumed) for the compositions in the red box and green box, respectively.

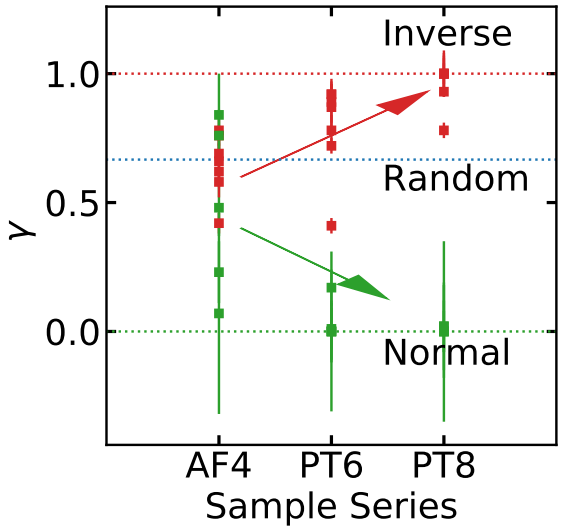


Figure 4.8: The degree of inversion, γ, for samples $(n\mathrm{A}_{1/n})\mathrm{Co}_2\mathrm{O}_4$ ($n \geq 5$), obtained from CL refinements, with error bars included. The heat treatment condition for each sample is listed on the x-axis. The samples are grouped into two categories: those with Mg in the compositions (represented by red squares) and those without Mg in the composition (represented by green squares). The red and green arrows indicate the structural trend observed with increasing *post-treatment* temperature.

4.4 Conclusion

This work has elucidated that the LTST method successfully results in single phase CCO spinels $(n\mathrm{A}_{1/n})\mathrm{Co}_2\mathrm{O}_4$ with high surface areas and heterogeneous microstructures that can be tuned with *post-treatment*. At least 12 distinct $\mathrm{ACo}_2\mathrm{O}_4$ samples were identified with four or more equimolar A cations in this work: a great number more are likely feasible through alternate or non-equimolar A cation combinations. The CCOs are all found to be metastable, partitioning into two distinct spinel phases upon *post-treatment* at 1000 °C (or lower). It was found that phase selection and stability are impacted by both which cation species are present and how many cation species are included. When Mg or Ni are present in the compositional series, the lower enthalpy of formation of MgO (in PT8 and PT10) and NiO (in PT10) dominates, resulting in CCO spinels with rock salt phase impurities. It was found that the onset of rock salt impurity phase with increasing calcination temperature can be suppressed or eliminated in samples without Mg by increasing the number n of participating cations in the series.

A detailed characterization of *5C1* via in situ HTXRD, SEM/EDS, STEM/EDS, and Rietveld refinement uncovers significant and varying cation segregation in AF4, PT6, PT8, and PT10 samples. *Post-treatment* is seen to effectively redistribute A-site cation short-range order, in an important confirmation of the ability to tune lattice heterogeneity in this family of medium entropy spinel oxides. We demonstrated that CL model refinements are adept at capturing the unusual diffraction peak profiles of CCOs in this series. We utilized the models to demonstrate that an intermediate processing temperature gives rise to more compositionally homogenous CCOs in our series. It is anticipated such models will find wide use in the structural description of HEOs, ESOs, and CCOs, providing much-needed descriptors of the intrinsic lattice strain, nano-segregated phases, and multi-structured natures apt to be present and key to material properties in these series. Overall, this work demonstrates there are many potentially interesting metastable nanophases that can be prepared via LTST

methods in this compositional series, and that there is great potential for tuning their morphologies and atomic structures.

Chapter 5

Excellent Bifunctional Oxygen Evolution and Reduction Electrocatalysts $(5A_{1/5})Co_2O_4$ and their Tunability

The synthesis and crystal-chemical trends in an extensive family of nano CCO $(nA_{1/n})Co_2O_4$ (A = combinations of Mg, Cr, Mn, Fe, Co, Ni, Cu, and Zn) spinels were presented in Chapter 4. It is widely recognized that several end-member compositions in this series serve as economically viable, earth-abundant, cost-effective, and efficient electrocatalysts, facilitating both the oxygen evolution reaction (OER) and oxygen reduction reaction (ORR). In the work herein, five-cation compositions in the family $(5A_{1/5})Co_2O_4$ (A = combinations of transition metals, Mg, Mn, Fe, Ni, Cu, and Zn) have been studied to determine their suitability as highly active and thermally stable bifunctional OER and ORR electrocatalysts. Among the different low-temperature soft-templating (LTST) samples, those subjected to 600 °C post-annealing heat treatment exhibited superior performance in alkaline media. One specific composition, $(Mn_{0.2}Fe_{0.2}Ni_{0.2}Cu_{0.2}Zn_{0.2})Co_2O_4$ exhibited an exceptional

overpotential (260 mV at 10 mA cm^{-2}) for OER, a favorable Tafel slope of 68 mV dec^{-1}, excellent onset potential (0.9 V) for ORR and lower than 6% H_2O_2 yields over a potential range of 0.2 to 0.8 V vs the reversible hydrogen electrode (RHE). Furthermore, this catalyst displayed stability over a 22-hour chronoamperometry measurement as confirmed by X-ray photoelectron spectroscopy (XPS) analysis. Considering the outstanding performance, the low cost and scalability of the synthesis method, and the demonstrated tunability through chemical substitutions and processing variables, the CCO ACo_2O_4 spinel oxides are highly promising candidates for future sustainable electrocatalytic applications.

Chapter 5– *Excellent Bifunctional Oxygen Evolution and Reduction Electrocatalysts ($5A_{1/5}$)Co_2O_4 and their Tunability*– is reprinted (adapted) with permission from *ACS Mater. Au* 2024, *in press*DOI: 10.1021/acsmaterialsau.3c00088 [247]. Copyright 2024 American Chemical Society. The authors of the work are Xin Wang, Harish Singh, Manashi Nath, Kurt Lagemann, and Katharine Page.

5.1 Introduction

Water splitting to produce hydrogen via the electrolysis pathway is considered a promising direction towards carbon-free energy production, especially considering the potential utilization of widely distributed renewable (wind, solar, geothermal) and nuclear energy sources.[284] A key research challenge lies in improving the energy efficiency for converting electricity to hydrogen over a wide range of operating conditions[45]. With this regard, designing and developing economically feasible, earth-abundant, inexpensive, efficient electrocatalysts for the oxygen evolution reaction (OER) is a critical research factor[138, 249, 304]. Even further, searching for electrocatalysts which can boost both the OER and the oxygen reduction reaction (ORR) simultaneously is crucial for deploying hydrogen production in a usable form, e.g., fuel cells[138], metal-air batteries[86].

Efficiently developing bifunctional electrocatalysts for OER and ORR presents two major challenges. Traditional electrocatalyst research primarily focuses on noble metal (Pt, Ir, Ru, etc.) incorporation, inappropriate for large-scale deployment due to low abundance and high cost[115]. In addition, the best catalysts for OER activity may not excel in ORR, and vice versa[86]. One promising avenue of research focuses on low cost transition-metal-based materials, among which cobalt-based spinel-type oxides are particularly promising as bifunctional electrocatalysts[302, 121].

Currently, a number of Co-based spinel-type oxides, including binary oxides such as Co_3O_4 as well as related ternary oxides with formula ACo_2O_4 (A = Mn, Ni, Cu, Fe, Zn, etc.), have shown promise as non-noble metal bifunctional catalysts. As summarized by Qin Zhao et al. in their review paper[302], several strategies are commonly employed to enhance OER and ORR properties in the family of spinels, including morphology optimization[136, 111, 89, 23, 201, 151, 41, 242, 14, 301], defect tuning[129, 40], composition engineering (active noble metal substitution[90, 31], and complex multi-metal synergistic effects[133, 212, 115, 283, 250]), structure/phase regulating[299] and utilization of conductive substrates[125, 111, 130, 285, 300, 270, 60, 9, 122, 128, 280, 24, 280, 4, 274, 43, 117, 76, 131, 239, 244, 3, 72, 26, 293, 283, 4, 250]. By implementing these emerging techniques, the performance of electrocatalysts for both OER and ORR can be significantly improved. A key figure of merit for assessing OER catalysts is a reduced overpotential value for overcoming the kinetic barrier (thermodynamic potential, 1.23 V) at current density 10 mA cm^{-2}[240]. For reference, the best reported OER noble-metal catalysts have overpotentials close to 200 mV[222]. Furthermore, the proximity of the onset potential to 1.0 V is a critical performance indicator for ORR. The best ORR catalysts, Pt-based materials, exhibit an ORR onset potential just below 1.0 V[216, 266, 30] and maintain a yield of H_2O_2 below 5% over a potential range of 0.2 to 0.7 V vs RHE[72].

Figure 5.1 presents extracted values of the promising ORR onset potential values (in V) and low OER overpotential values (in mV) from the spinel oxide literature

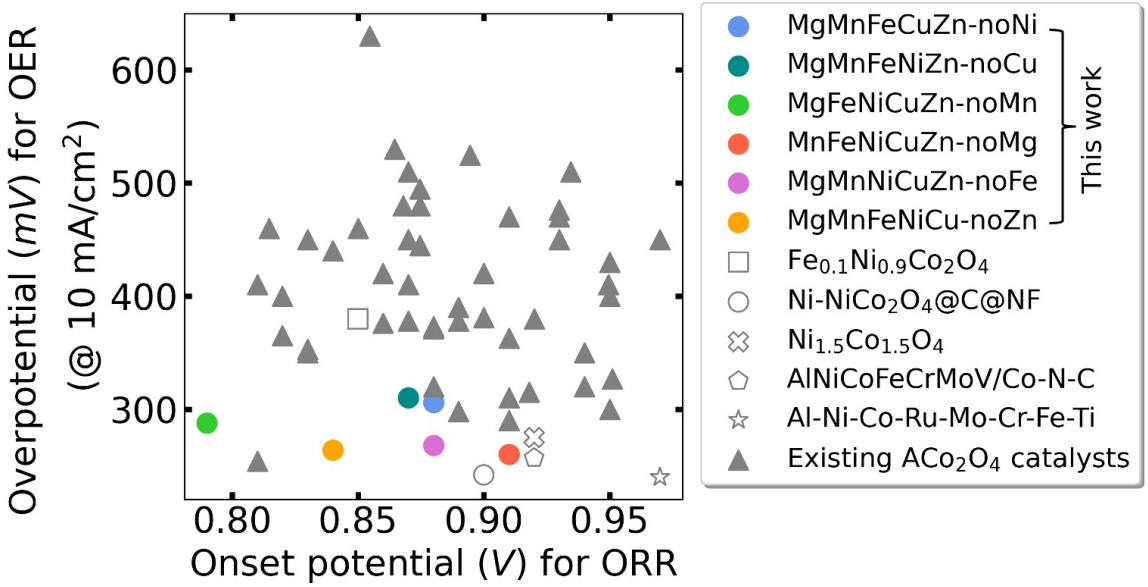


Figure 5.1: Overpotential (measured at 10 mA cm^{-2}) for OER versus onset potential for ORR for the best-performing $(5A_{1/5})Co_2O_4$ spinel CCOs in this work (solid colored circles) compared to existing ACo_2O_4 based electrocatalysts from references cited[302, 136, 111, 89, 23, 201, 151, 41, 242, 14, 301, 129, 40, 90, 31, 133, 212, 115, 283, 250, 299, 125, 111, 130, 285, 300, 270, 60, 9, 122, 128, 280, 24, 280, 4, 274, 43, 117, 76, 131, 239, 244, 3, 72, 26, 293, 283, 4, 250] (solid grey triangles). Several notable benchmarks are highlighted with hollow grey markers[133, 72, 301, 283, 90]. See text for further details.

mentioned above (solid grey triangles). Their corresponding substrate and drop-casted mass (mass loading, ML) for OER and ORR studies are summarized in Table S5.1. It should be noted here that a low overpotential for OER and higher onset potential for ORR is more desirable as explained above. Hence more efficient catalysts are expected to occupy the bottom region of this plot and towards the right. Among these catalysts, the complex nitrogen-doped 'nanonetwork' assembled from porous and defective $NiCo_2O_4$@C nanowires grown on nickel foam ('N-$NiCo_2O_4$@C@NF', represented by a hollow grey circle in Figure 5.1) stands out with its significantly low OER overpotential of 242 mV, and relatively high ORR onset potential (0.90 V vs RHE)[72]. '$Ni_{1.5}Co_{1.5}O_4$'[301] (represented by a hollow grey 'X' in Figure 5.1), an atomically-thin nickel-doped spinel cobalt oxide, exhibits bifunctional catalytic performances with the overpotential of 275 mV for OER and the onset potential of 0.92 V for ORR. A seven-component "high entropy oxide" (HEO), 'AlNiCoFeCrMoV' integrated with so-called 'Co-N-C' (grey hollow pentagon in Figure 5.1) achieves a highly bifunctional HEO/Co-N-C nanocomposite electrocatalyst, with an overpotential of 257 mV for OER and an onset potential of 0.92 V for ORR. These values are comparable to those of precious metal containing catalysts. One eight-component spinel HEO, 'Al-Ni-Co-Ru-Mo-Cr-Fe-Ti', represented by a hollow grey star in Figure 5.1 also stands out as a promising bifunctional catalyst (overpotential of 240 mV for OER and onset potential of 0.97 mV for ORR), but it notably includes the precious noble metal, Ru[90].

The strategy of compositional complexity in the cobalt spinel oxide system presents an alternative approach to complicated synthesis and processing routes and precious metal incorporation for bifunctional OER and ORR electrocatalysts. HEOs (commonly referred to as single-phase oxides where five or more metal cations occupy a specific crystallographic lattice site in a random manner with configurational entropy equal to or higher than 1.5R per mole of metals/cations, where R represents the universal gas constant.) and related compositionally complex oxide (CCO, encompassing medium-entropy and non-equimolar composition oxides)

phases offer a number of potential advantages attractive to improved designs for the activity, structural stability, and tunability of electrocatalysts. The sluggish diffusion kinetics associated with decreased cation mobilities reported in a number of CCOs to date[303, 228, 116] may lead to slower particle coarsening relative to simpler phases. The increased configurational entropy in CCO/HEO/entropy stabilized oxide (ESO) phases may offer intrinsic phase stability at high temperatures. Perhaps the most beneficial effect predicted to offer advantages for catalysis is the so-called 'cocktail effect', whereby the catalytic activity of mixed metal cations enriches the type and/or strength of orbital hybridization relative to individual (or less complex) active cation sites. This phenomenon is already well explored in complex oxides, for example, in the enhanced activity reported for $M_{0.1}Ni_{0.9}Co_2O_4$ (M=Mn, Fe, Zn, and Cu) spinels[133] ($Fe_{0.1}Ni_{0.9}Co_2O_4$ is represented by a hollow grey square in Figure 5.1), cerium-doped $CoMn_2O_4$ (Ce-CMO-X) spinels[31], $La_{1.5}Sr_{0.5}NiMn_{0.5}Ru_{0.5}O_6$ double perovskite[185], and others described in a number of reviews[86, 99, 121]. Nonetheless, few bifunctional HEO or CCO catalysts have been studied to date.

We recently reported on a low temperature soft templating (LTST) reaction route for a wide number of $(nA_{1/n})Co_2O_4$ spinel oxides[245]. Figure 5.2 (a) displays the spinel oxide structure with an inverse cation site model assumed (in the inverse spinel structure the red tetrahedral cation sites are completely occupied by Co atoms, while blue octahedral cation sites are occupied by 50% Co and 50% A atoms). The chemical compositions, spinel structure, and morphology features make the phases clear candidates for bifunctional electrocatalysts. In this work, we explore the OER and ORR electrocatalytic activity of a family of nano $(5A_{1/5})Co_2O_4$ spinel oxides where A contains 5 equimolar component combinations of the elements Mg, Mn, Fe, Ni, Cu and Zn. Compared to the existing literature on cobaltites as bifunctional OER and ORR electrocatalysts, the LTST prepared electrocatalysts in this work post-annealed at 600 °C (solid colored circles displayed in Figure 5.1) demonstrate significantly promising bifunctional OER and ORR performance. Furthermore,

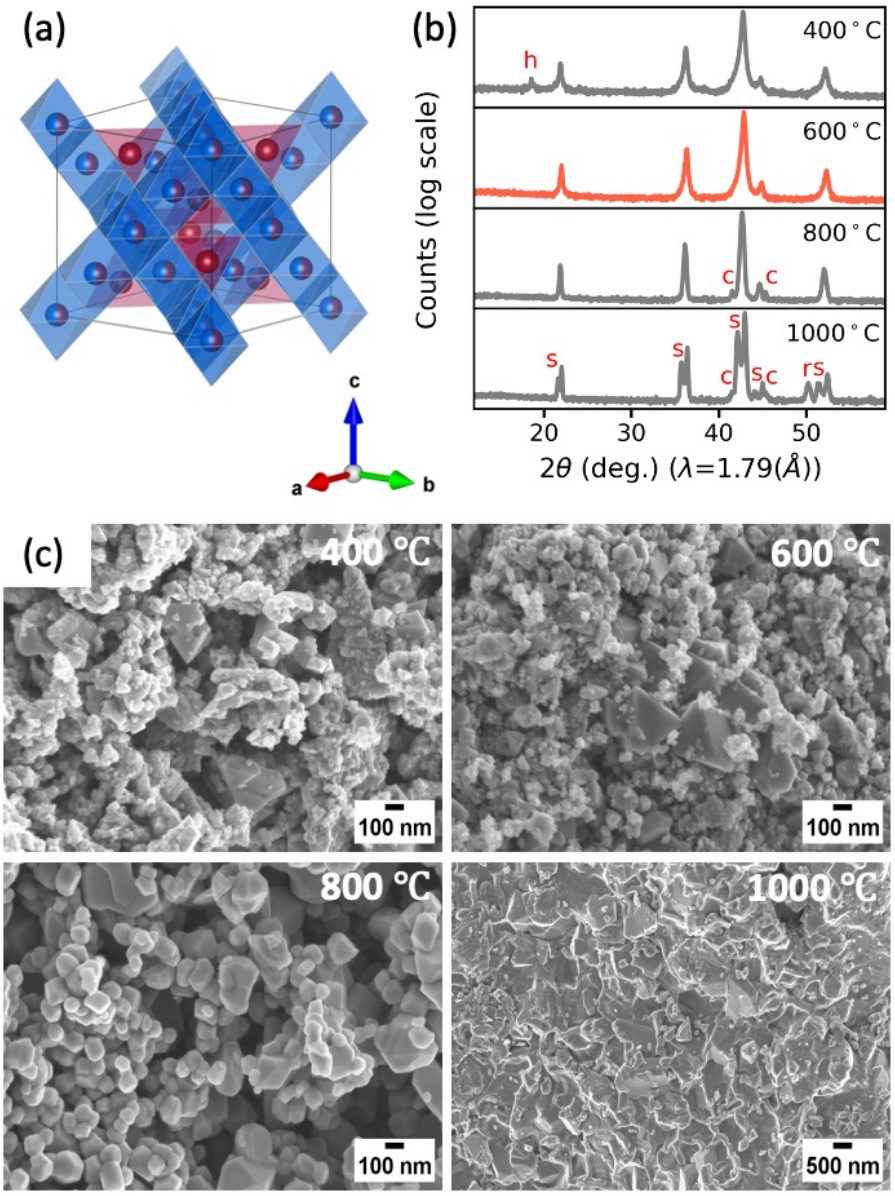


Figure 5.2: (a) The cubic spinel oxide unit cell model with an inverse structure assumed. The red tetrahedral cation sites are completely occupied by Co atoms, while blue octahedral cation sites are occupied by 50% Co and 50% A atoms. Oxygen atoms decorating the corners of the shaded polyhedra are omitted for clarity. (b) XRD patterns of the MnFeNiCuZn-noMg cobaltite series, including the as prepared sample (400 °C), and samples post-annealed at 600 °C, 800 °C and 1000 °C. Impurities are coded: $CoCl_2{\cdot}2H_2O$ ("h"); tenorite CuO ("c"); rock salt ("r"); and secondary spinel ("s"). (c) Corresponding SEM images for samples in (b).

catalytic trends for OER and ORR are demonstrated to be tunable through post-processing and specific cation selection, indicating a promising design strategy for optimizing new bifunctional catalysts.

5.2 Experimental

5.2.1 Material synthesis

The synthesis and phase stability of a large family of $(nA_{1/n})Co_2O_4$ (n=1 to 7) spinel nanostructures were recently reported using a low temperature soft-templating (LTST) reaction route[245]. The structuring agent, Pluronic P123 (3.2g), was dissolved in 20 mL Ethyl Alcohol. Next, 0.5 mL Hydrochloric acid (HCl) was added to the solution and stirred using a magnetic stir bar until the Pluronic P123 was completely dissolved. Then, the desired stoichiometric amounts (1 g $(nA_{1/n})Co_2O_4$ as the target) of inorganic nitrate/chloride hydrate precursor solutions in wt.% of metal were added into the solution. The entire mixed solution was stirred for 30 mins using a magnetic stirrer. Subsequently, the mixed solution was transferred to a petri dish and placed under a fume hood for 24 h to allow for evaporation, resulting in the formation of a wet gel. Once the evaporation was complete, the gel was then transferred to a furnace and subjected to calcination at 400°C for a duration of 5 h. Finally, post-annealing treatments were conducted at temperatures of 600°C, 800°C, or 1000°C for 5 h. For samples in the present work, n=5 refers to an equiatomic combination of five transition metal cations on the A-site. Sample compositions studied are listed in Table 5.1, along with an indication of phase purity trends. Representative X-ray diffraction (XRD) data and scanning electron microscopy (SEM) images are shown in Figure 5.2 (b,c). XRD patterns of all samples involved in this work can be viewed in our previous work[245].

We have incorporated different combinations of 5 equiatomic A elements (with Mg, Mn, Fe, Ni, Cu, and Zn as choices) in each nanocatalyst. The first five elements

Table 5.1: The target compositions with formula $(5A_{1/5})Co_2O_4$ involved in this work. Samples are obtained after calcination at 400 °C and following post-annealing heat treatment at 600 °C, 800 °C and 1000 °C. Conditions resulting in X-ray pure phases are labeled with check marks and conditions resulting in phase mixtures are labeled with impurity abbreviations. Impurities are coded: $CoCl_2{\cdot}2H_2O$ ("h"); tenorite CuO ("c"); rock salt ("r"); and secondary spinel ("s").

Name	400 °C	600 °C	800 °C	1000 °C
MgMnFeCuZn-noNi	✓	✓	r	r+s
MgMnFeNiZn-noCu	✓	✓	r	r+s
MgFeNiCuZn-noMn	c+r	c+r	c+r	c+r
MnFeNiCuZn-noMg	h	✓	c	c+r+s
MgMnNiCuZn-noFe	r	r	r	r+s
MgMnFeNiCu-noZn	✓	✓	r	r+s

listed in the sample names denote the 5 cations incorporated, while the term "no$X$" indicates the absence of a specific element X in that composition. All compositions were initially calcined at 400 °C for 5 hr and later heat treated at 600 °C, 800 °C, or 1000 °C for 5 hr as described in our previous work[245].

5.2.2 Structure and morphology characterization

X-ray diffraction (XRD)

X-ray diffraction (XRD) data were measured using a PANalytical Empyrean diffractometer equipped with a Co X-ray source. The XRD patterns were measured between 10 and 90° 2θ with a step size of 0.026°. The use of Co Kα radiation was found key in uncovering minor impurity phases (the X-ray fluorescence for these samples with Cu Kα sources masked the presence of minor impurity phases). Rietveld refinements were carried out with the TOPAS-V7 program[36] utilizing a "continuous lattice" model[245] to capture nanoscale inhomogeneity. The cation site inversion parameter (the fraction of A-site ions occupying the octahedral sites, γ[250, 245]) and crystalline size (CS) were also refined.

Scanning electron microscopy/energy dispersive X-ray specstropy (SEM/EDS)

Specimens for scanning electron microscopy (SEM) and energy dispersive specstropy (EDS) were prepared by gently dispersing the finely-ground powders onto a standard carbon tape, ensuring optimal sample distribution. The morphologies of the specimens were then characterized using the Zeiss Auriga high resolution SEM. Elemental analysis was carried out with the Zeiss EVO SEM.

X-ray photoelectron spectroscopy (XPS)

X-ray photoelectron spectroscopy (XPS) was conducted with an Al X-ray source on a KRATOS AXIS 165 spectrometer to investigate the surface chemical composition and the valence states of the elements involved before and after the OER stability

studies. The acquisition of all XPS data was carried out without any sputtering to accurately examine the surface chemistry.

5.2.3 Electrochemical characterization

Electrode preparation

To prepare the homogeneous catalyst ink for analyzing the OER and ORR activity of catalysts, 4 mg of catalyst was dispersed in 300 μL of ethanol and mixed with Nafion (0.8 μL, 5 wt.%). For OER measurements, the ink required an additional step of 1 hour ultrasonication to ensure its homogeneity. Subsequently, 100 μL of the homogenized ink was dropped onto carbon cloth with a geometric area of 0.283 cm^2. For ORR measurements, the glassy carbon electrode (GC) was polished using 1 and 0.05 μm alumina powder, and then sonicated first in isopropanol and then in distilled water. Next, 20 μL of the catalyst ink was drop casted onto the glassy carbon working electrode with a geometric area of 0.196 cm^2. Finally, the electrode was dried under ambient conditions.

Water splitting and oxygen reduction reaction measurements

An IviumStat potentiostat was used for investigating the bifunctional OER and ORR electrocatalytic performance of CCO $(5A_{1/5})Co_2O_4$ electrodes. The setup of electrochemical measurements is a three-electrode cell system. The graphite rod is the counter electrode, and the Ag|AgCl (KCl-saturated) is the reference electrode. The 5 mm diameter rotating ring disk electrode (RRDE) is the working electrode for ORR (in O_2-saturated 1 M KOH at different rotational rates between 400 and 2000 rpm (10 mV s^{-1})) while catalyst loaded carbon cloth is the working electrode for OER (in N_2-saturated 1 M KOH).

Tafel plot

Tafel slopes of the 600 °C series were calculated by polarization curve fitting to examine the OER performance. The Tafel equation is given below:

$$\epsilon = \alpha + \frac{2.3RT}{\alpha nF} \log j \tag{5.1}$$

where α is the charge transfer coefficient, n is the number of electrons involved in the reaction, F is the Faraday constant and other symbols have their usual meanings. The Tafel equation illustrates the dependency of the overpotential ϵ on the current density j. The Tafel slope is given by $2.3RT/\alpha nF$.

Electrochemically active surface area (ECSA)

The electrochemically active surface area (ECSA) was obtained according to the equation:

$$ECSA = \frac{C_{DL}}{C_S} \tag{5.2}$$

where C_{DL} is the double payer capacitance and C_S is the specific capacitance (0.04 mF cm^{-2}, taken from similar catalysts[28]). An average of the absolute values of cathodic and anodic slopes is calculated to obtain the value of C_{DL}. Roughness factor (RF) is another important factor which relates to the surface roughness. It can be defined as $ECSA/0.283$, where 0.283 cm^2 is the geometric electrode area used for OER.

5.3 Results and Discussion

5.3.1 Bifunctional OER and ORR electrocatalysts

A screening of OER performance across the MgMnFeCuZn-noNi, MgMnFeNiZn-noCu, MgFeNiCuZn-noMn, MnFeNiCuZn-noMg, MgMnNiCuZn-noFe, and MgMnFeNiCu-noZn series revealed that the samples treated at different processing temperatures (400 °C, 600 °C, 800 °C and 1000 °C) exhibit varying overpotential for OER.

Representative OER overpotential results for the samples involved are presented in SI Figure S5.1 (a). The series of 600 °C processed samples present superior catalytic activity compared to the 400 °C, 800 °C and 1000 °C sample series. The trend in overpotential values observed is 600 °C < 1000 °C < 800 °C < 400 °C for nearly all compositions (except MgMnFeNiZn-noCu, for which the overpotential of the 400 °C sample ≋ that of the 800 °C sample). In our pursuit of developing a high-performance bifunctional catalyst, we have conducted ORR with the best OER set (the 600 °C series) in this study. To assess their electrokinetic activity, we employed a RRDE setup.

A selection of electrocatalytic data for the sample series is presented in Figure 5.3, with key values summarized in Table 5.2. The OER electrocatalytic activity of the 600 °C series were evaluated using linear sweep voltammetry (LSV) measurements, as illustrated in Figure 5.3 (a). The extracted overpotential values at 10 mA cm^{-2} are those presented as colored symbols in Figure 5.3, demonstrating they are among the lowest recorded OER overpotential values for cobaltite-based electrocatalysts in literature. For samples studied here, the MnFeNiCuZn-noMg-600 °C sample exhibits the highest OER catalytic activity, with an overpotential of approximately 260 mV. This falls within the "ideal" range (200 to 300 mV at 10 mA cm^{-2}) defined by Muhammad Tahir et al. in their review paper[222]. Additionally, the MnFeNiCuZn-noMg-600 °C exhibits a high current density (exceeding 150 mA cm^{-2}), indicating favorable conductivity. The corresponding Tafel slopes extracted from OER electrocatalytic activity are displayed in Figure 5.3 (b). The Tafel slope values indicate that MnFeNiCuZn-noMg-600 °C has the lowest Tafel slope of 68 mV/dec, outperforming N-NiCo2O4@C@NF (86 mV dec^{-1})[72] and approaching the performance of Al-Ni-Co-Ru-Mo-Cr-Fe-Ti (51.3 mV dec^{-1})[90]. The reaction kinetics are enhanced when the Tafel slope is smaller, leading to a higher current density and subsequent increased oxygen generation. The low Tafel slope of MnFeNiCuZn-noMg-600 °C suggests that it is comparable to other existing highly efficient catalysts. The ECSA values are presented in Figure 5.3 (c) and are listed in Table 5.2 for the

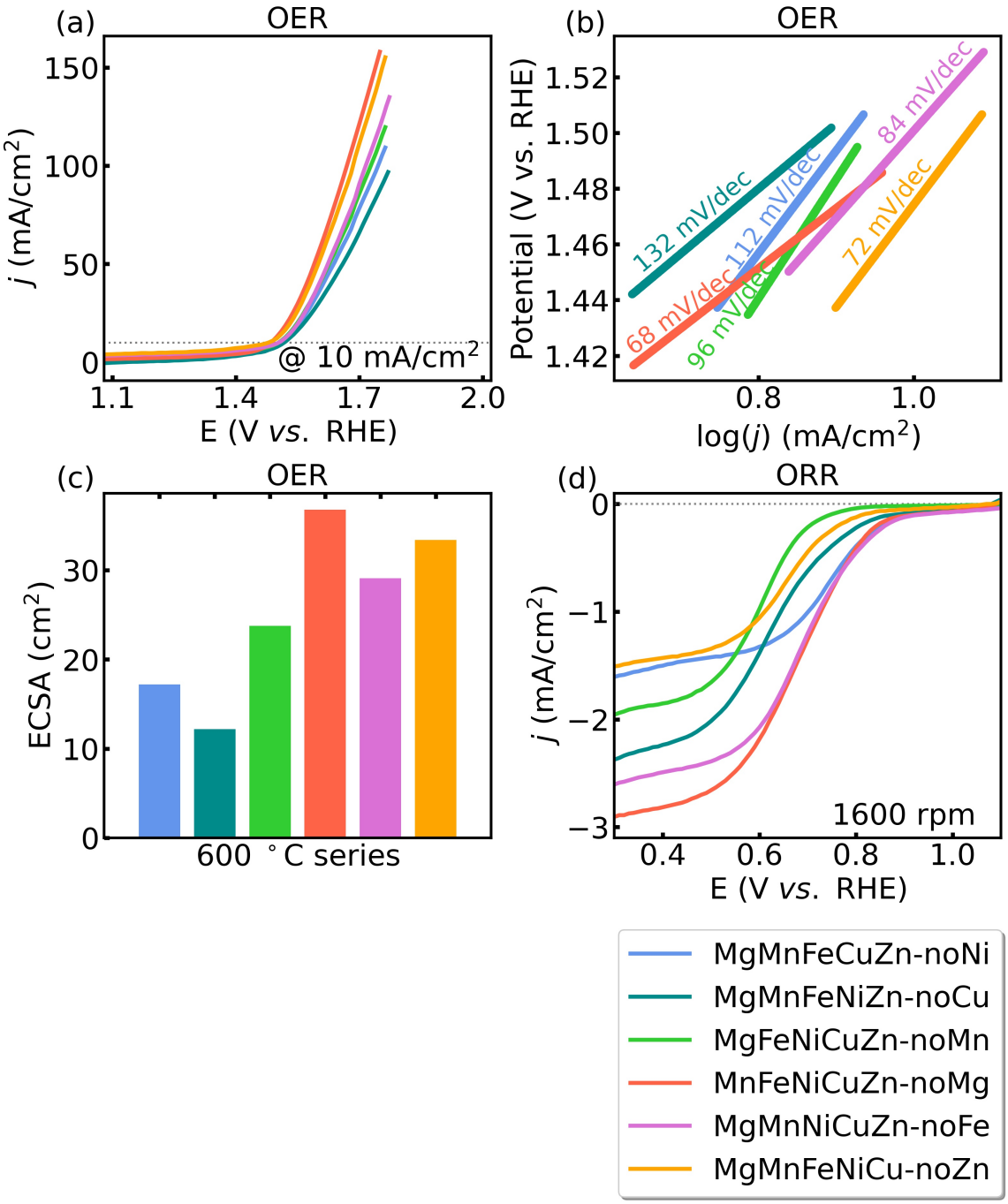


Figure 5.3: (a) OER LSV polarization curves, (b) OER Tafel plots, (c) OER ECSA, and (d) ORR LSV polarization curves at a rotating speed of 1600 rpm for the 600 °C sample series.

Table 5.2: The OER (overpotential η mV @ 10 mA cm^{-2}, Tafel slope (mV dec^{-1}), and ECSA (cm^2)) and ORR (onset potential E_0 (V), number of electrons n @ 0.3 V, and % H_2O_2) catalytic activities of the electrocatalysts involved in this work compared to the values from selected benchmark catalysts.

Sample	OER η	OER Tafel	OER ECSA	ORR E_0	ORR n	ORR % H_2O_2
Al-Ni-Co-Ru-Mo-Cr-Fe-Ti[90]	240	51.3	/	0.97	/	/
N-$NiCo_2O_4$@C@NF[72]	242	86	65	0.90	3.8	6.7
AlNiCoFeCrMoV/Co-N-C[283]	257	/	/	0.92	/	/
MnFeNiCuZn-noMg$^{\text{This work}}$	260	68	36.8	0.91	3.96	4.8
MgMnFeNiCu-noZn$^{\text{This work}}$	264	72	33.4	0.84	3.21	8.2
MgMnNiCuZn-noFe$^{\text{This work}}$	268	84	29.1	0.88	3.85	6.4
$Ni_{1.5}Co_{1.5}O_4$[301]	275	54	/	0.92	/	/
MgFeNiCuZn-noMn$^{\text{This work}}$	288	96	23.78	0.79	3.10	8.6
MgMnFeCuZn-noNi$^{\text{This work}}$	306	112	17.2	0.88	3.90	5.1
MgMnFeNiZn-noCu$^{\text{This work}}$	310	132	12.2	0.87	3.34	7.4
$Fe_{0.1}Ni_{0.9}Co_2O_4$[133]	380	/	/	0.85	/	/

600 °C series. The ECSA plays a pivotal role in the field of electrocatalysis, particularly in reactions like the OER which is of paramount importance for various energy conversion and storage technologies, including water electrolysis[208, 209]. The ECSA values range between 12.2 cm^2 and 36.8 cm^2 for the 600 °C sample series, representing moderate values compared, for example, to the reported 65 cm^2 of N-$NiCo_2O_4$@C@NF[72]. The favorable electrocatalytic properties of the series despite their modest ECSAs suggest these compositionally complex samples may have high intrinsic performance relative to previously reported cobaltite-based bifunctional catalysts. Amongst the multimetal oxide series studied here, it is notable that the MnFeNiCuZn-noMg-600°C stands out with the highest ECSA value in the context of the OER, indicative of a significantly larger active surface area available for electrochemical reactions. This implies the presence of a higher density of catalytic sites, rendering the material exceptionally efficient in facilitating the OER process[161]. The composition of the MnFeNiCuZn-noMg likely provides a synergistic combination of metal oxides that create a unique surface structure and electronic environment, leading to the observed higher ECSA value. The C_{DL} values of the different catalyst compositions were also compared (shown in SI Table S5.2), which shows a similar trend as the ECSA. Another crucial parameter to consider is the RF, which characterizes the surface roughness of the catalyst composite and can have an impact on the observed catalytic characteristics. An increase in ECSA leads to a higher surface RF, serving as an additional determinant affecting catalytic activity. This is typically beneficial because a rough catalytic surface exposes more catalytic sites to the electrolyte. The RF value determined for the MnFeNiCuZn-noMg-600 °C electrode (130.03) surpasses that of other synthesized compositions, aligning with the enhanced OER catalytic activity observed in the MnFeNiCuZn-noMg-600°C sample. These choices were made to optimize the electrochemical conditions for each reaction, ensuring a reliable and controlled experimental setup.

The polarization curves for ORR recorded at the rotation rate of 1600 rpm are shown in Figure 5.3 (d). Additional polarization curves at 400, 800, 1200, and

2000 rpm can be found in SI Figure S5.2. Among the various multimetal oxide catalysts studied, the MnFeNiCuZn-noMg-600°C electrode emerged as the standout performer. Its diffusion current densities were found to be remarkably high, akin to those achieved with the industry-standard 20% Pt/C catalyst[209]. Notably, the onset potentials observed for MnFeNiCuZn-noMg-600 °C were 0.91 V vs. RHE, indicating its excellent catalytic activity for ORR. Moreover, this electrode exhibited a diffusion-limiting current density of 2.94 mA cm^{-2}, surpassing the performance of all other electrocatalysts investigated in this study. The various diffusion-limiting currents observed in different catalysts can be attributed to their unique electronic structures and corresponding redox properties. Catalysts with higher intrinsic activity often display more prominent limiting diffusion currents. Additionally, the chemical composition of a catalyst, especially when alloyed with other elements, significantly influences the diffusion current density during the ORR. Variations in crystallographic facets, defects, or the presence of specific active sites can lead to differences in ORR kinetics, thereby influencing the limiting diffusion current.

The electron transfer and hydrogen peroxide yields (% H_2O_2) of the ORR were also investigated (results for sample MnFeNiCuZn-noMg-600 °C are shown in SI Figure S5.3). The % H_2O_2 generated is lower than 6% over a potential range of 0.2 to 0.8 V vs RHE (it is 4.8% at 0.3 V). This is lower than that reported for the highly performing N-$NiCo_2O_4$@C@NF[72], which remains lower than 8% over the potential range of 0.2 to 0.7 V vs RHE (and is 6.7% at 0.3 V). Furthermore, the number of electrons transferred at 0.3 V vs RHE ranged between 3.1 to 3.96 for the 600 °C series electrocatalysts in this work, suggesting a predominant four-electron pathway for ORR. The parallel trends observed in the fitted lines in the Koutecky-Levich plots (K-L, shown in SI Figure S5.4) imply that the ORR follows similar electron transfer pathways at various potentials. This suggests that the underlying mechanisms governing the ORR remain consistent across different conditions and potentials. Extracted values for OER overpotential, Tafel slope, and ECSA, as well as ORR onset potential, number of electrons transferred (n), and % H_2O_2 production

at 0.3 V vs RHE, are summarized in Table 5.2 for the 600 °C sample series and selected benchmark electrocatalysts, arranged in increasing order of OER overpotential.

In essence, MnFeNiCuZn-noMg-600°C has demonstrated exceptional potential as a high-performance bifunctional catalyst, particularly in the context of the ORR and OER in alkaline conditions. Its impressive electrocatalytic properties, characterized by high current densities and favorable onset potentials, make it a promising candidate for integrated electrolyzer and fuel cell systems.

5.3.2 Stability of MnFeNiCuZn-noMg-600 °C

The long-term stability of electrocatalysis processes in alkaline medium for Co-based spinel catalysts will be important for determining their overall suitability for applications[121]. The long-term stability of MnFeNiCuZn-noMg-600 °C, the best performing bifunctional OER and ORR catalyst in our series, was assessed using chronoamperometry where a three-electrode setup was employed with a catalyst-coated carbon cloth as the working electrode, graphite rod as counter and Ag|AgCl as the reference electrode, where a constant potential was applied and the resulting current density was measured over time (the results of the 22 hr test are shown in Figure 5.4 (a)). The increase in current density observed with time in the Chronoamperometry plot can be attributed to surface reconstruction effects. For instance, an evolving surface morphology may expose new catalytic sites or enhance the electrochemically active surface area. This, in turn, facilitates more efficient OER kinetics and contributes to the observed rise in current density over time. The electrode exhibited excellent stability, with no degradation of current density. Furthermore, Figure 5.4 (b) illustrates the lack of change in the LSV curves of OER before and after the 22-hr chronoamperometry test, indicating promising stability of MnFeNiCuZn-noMg-600 °C in alkaline media.

Additionally, XPS measurements were conducted on MnFeNiCuZn-noMg-600 °C before and after OER to analyze changes in surface element configurations and

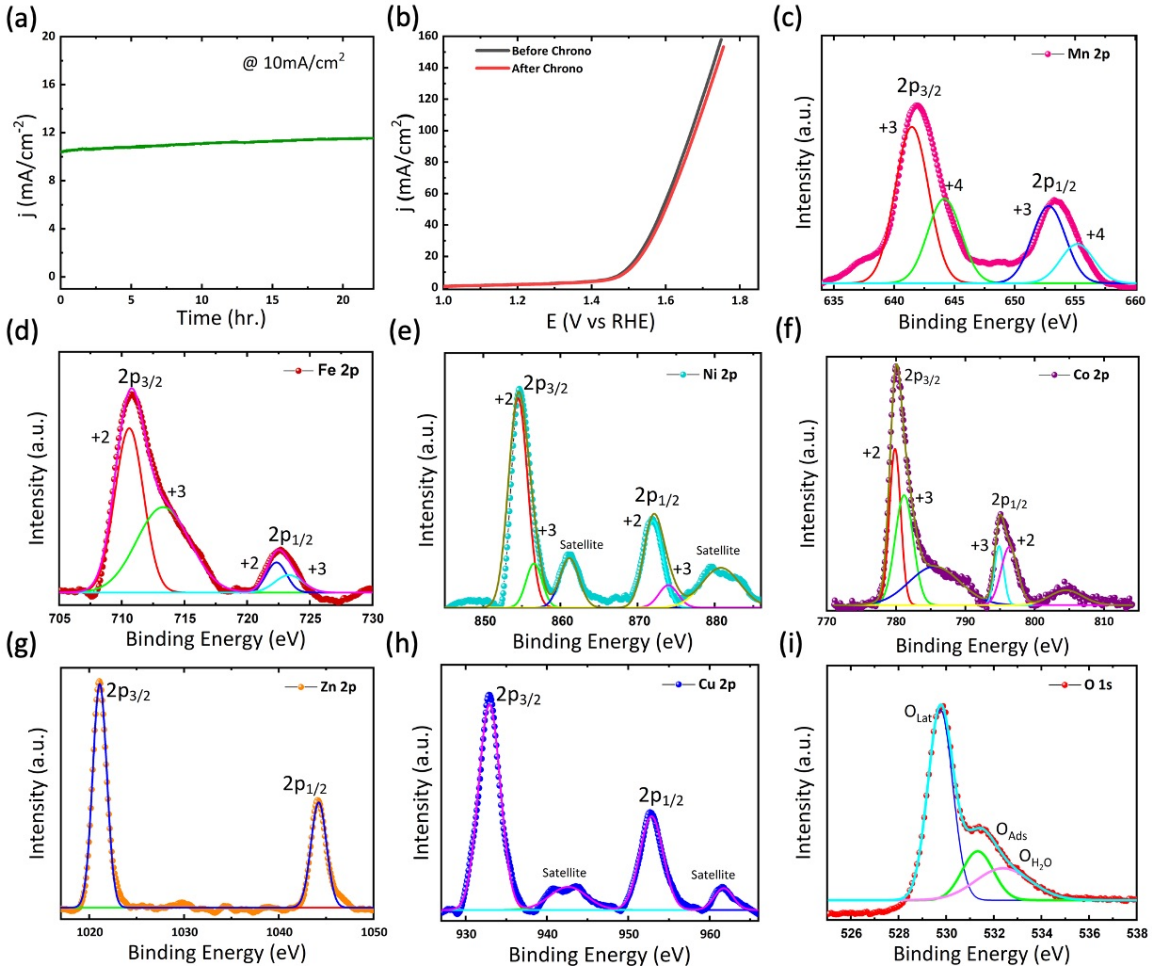


Figure 5.4: (a) Chronoamperometry plot of the catalyst MnFeNiCuZn-noMg-600 °C, shown to maintain the current density 10 mA cm^{-2} over 22 hr for OER. (b) The LSV polarization curves of sample MnFeNiCuZn-noMg-600 °C before and after chronoamperometry. The before OER XPS spectra of (c) Mn 2p, (d) Fe 2p, (e) Ni 2p, (f) Co 2p, (g) Zn 2p, (h) Cu 2p, and (i) O 1s are for the MnFeNiCuZn-noMg-600 °C electrode. The comparison of before and after OER XPS spectra can be found in SI Figure S5.5.

electronic states. The XPS data collected before OER are presented in Figure 5.4 (c,d,e,f,g,h,i) for elements Mn, Fe, Ni, Co, Zn, Cu and O, respectively. The peaks in the XPS spectra can be attributed to (c) Mn $2p_{3/2}$ and Mn $2p_{1/2}$, (d) Fe $2p_{3/2}$ and Fe $2p_{1/2}$, (e) Ni $2p_{3/2}$ and Ni $2p_{1/2}$, (f) Co $2p_{3/2}$ and Co $2p_{1/2}$, (g) Zn $2p_{3/2}$ and Zn $2p_{1/2}$, (h) Cu $2p_{3/2}$ and Cu $2p_{1/2}$, and (i) O 1s. In Figure 5.4 (c), the high-resolution XPS spectra of the Mn 2p peak are depicted. The Mn 2p peak exhibits a doublet, attributed to spin-orbit splitting, with two distinct states, 3/2 and 1/2. These states display varying binding energies at 641.8 and 653.2 eV. In the Fe 2p spectrum (depicted in Figure 5.4 (d)), the peaks observed at 710.2 eV and 723.9 eV are indicative of bivalent iron (Fe^{2+}), while the peaks at 712.8 and 724.1 eV are assigned to trivalent iron (Fe^{3+}). The Ni 2p XPS spectrum shown in Figure 5.4 (e) reveals key information about the chemical and oxidation state of Ni within the material. The specific binding energies of the Ni $2p_{3/2}$ and Ni $2p_{1/2}$ core level peaks were identified at 854.2 eV and 871.7 eV, respectively. The Ni $2p_{3/2}$ and Ni $2p_{1/2}$ peaks represent transitions of electrons from the 2p energy level to the 3/2 and 1/2 spin-orbit states, providing insights into the electronic configuration of Ni in the sample. Notably, accompanying these main peaks were satellite peaks observed at 861.4 eV and 880.1 eV, associated with the Ni $2p_{3/2}$ and Ni $2p_{1/2}$ core levels, respectively. The presence of satellite peaks is significant because it suggests that the material comprises additional electronic transitions and interactions. The detection of satellite peaks at 861.4 eV and 880.1 eV in this context shows that Ni is involved in a +2 oxidation state within the main lattice. In Figure 5.4 (f), the XPS spectrum analysis has revealed that the primary metal peaks in the Co $2p_{3/2}$ and Co $2p_{1/2}$ regions exhibit binding energies at 780.2 eV and 796.1 eV, respectively. Additionally, within both the Co $2p_{3/2}$ and Co $2p_{1/2}$ regions, there are satellite peaks observed on the side with higher binding energy relative to the main peak of each region. This observation supports the confirmation that the oxidation state of Co is predominantly +2. The higher binding energy of the satellite peaks relative to the main peaks within the Co 2p regions aligns with the characteristics expected for Co in the +2 state.[132] These two

satellite peaks also indicate the presence of additional electronic states associated with the cobalt atoms. The satellite peak can arise from charge redistribution or electronic transitions within the cobalt atoms. Charge redistribution implies a rearrangement of electrons within the cobalt atoms, potentially influenced by factors such as the local environment, the presence of neighboring atoms, or specific surface conditions. This redistribution of charge can lead to the creation of additional electronic states, contributing to the appearance of the satellite peak. In Figure 5.4 (g), the XPS spectrum for Zn 2p illustrates the binding energies of Zn $2p_{3/2}$ at approximately 1021.6 eV and Zn $2p_{1/2}$ centered around 1044.1 eV. It indicates a single +2 valence. XPS spectra collected after OER are shown in SI Figure S5.5. There are no significant shifts observed in the binding energies of the Mn, Fe, Ni, Co, and Zn elements after OER activity. Negligible binding energy shifts observed for most of the sample metal ions indicate a maintenance of stable oxidation states during OER without undergoing substantial chemical transformations or degradation. It should be noted that in OER electrocatalysis, it is expected that oxyhydroxide species will form at the local catalytic site through the catalyst activation step. The lack of observable shifts however indicates that there is no bulk conversion to oxyhydroxide species or significant alterations in the chemical states of these elements during extended OER activity. Elements like Mn, Fe, Ni, Co, and Zn may exhibit different inherent redox potentials, making them less susceptible to changes in oxidation states during electrochemical processes. There are two marked changes in the XPS spectra before and after OER (beyond differences in intensities, attributed to the measurements being completed in different areas of the sample): (1) In Figure 5.4 (h), the core-level and shake-up satellite lines of Cu 2p are presented. The Cu 2p3/2 and 2p1/2 core levels are situated at approximately 933.2 and 952.9 eV, respectively. However, in the XPS spectra after OER, SI Figure S5.5 (f), Cu^{1+} peaks appear around 932.1 eV after OER in addition to the Cu^{2+} peaks initially present (shown in SI Figure S5.5(f)). More careful XPS analysis has revealed that Cu is present in +1 and +2 oxidation states even in the sample that before OER measurement. Hence the presence of Cu^{1+}

in the sample is primarily due to mixed oxidation state in the pristine sample and does not change significantly after OER. Furthermore, to substantiate the dominance of Cu^{2+} oxidation, our analysis considered the presence of a satellite peak around 943.2 eV. The identification of this satellite peak is particularly significant, as it serves as a spectral indicator affirming the prevalence of Cu^{2+} oxidation states.[191, 307] (2) The O 1s peak at 529 eV in Figure 5.4 (i) indicates the presence of O^{2-} within a metal oxide lattice (O_{Lat}), while the peak at 531 eV suggests the presence of adsorbed oxygen-containing species (O_{Ads}). This peak's intensity is commonly utilized to measure the concentration of oxygen vacancies within the surface oxide lattice. The small peak observed at 533 eV is associated with water adsorption (O_{H_2O})[248]. This latter peak disappears after OER activity, indicating a loss of adsorbed water. The lack of changes in the case of Mn, Fe, Ni, Co and Zn indicates a stable surface chemistry of this catalyst. The CCO catalyst may possess a robust surface structure that preserves the oxidation states of the constituent elements, even in the presence of the highly oxidative OER conditions. This stability could arise from the synergistic interactions among the different metal species, forming a protective layer that prevents excessive oxidation or reduction.

5.3.3 Tunability through cation selection and post-annealing

With the implementation of the straightforward LTST synthesis method, there exists substantial potential for enhancing the catalytic properties of bifunctional OER and ORR ACo_2O_4 electrocatalysts through cation selection and reaction parameter optimization. Trends in crystallinity, phase purity, and morphology were shown for various sample thermal treatments for the MnFeNiCuZn-noMg composition in Figure 5.2. Panel (b) displays the XRD patterns of the series, including the 400 °C, 600 °C, 800 °C and 1000 °C samples. Rietveld refinements were completed to identify phases present, crystallite size (CS) and cation site inversion parameter (γ). In the case of the MnFeNiCuZn-noMg series, the 400 °C sample contains a processing product impurity

$CoCl_2 \cdot 2H_2O$ (labeled as "h"), while the 800 °C sample contains a small amount of CuO ("c"). The 1000 °C sample exhibits CuO, rock salt ("r") and secondary spinel ("s") impurities. Only the 600 °C sample is composed purely of a single spinel phase. A summary of phase purity results achieved for all samples is given in Table 5.1.

SEM results for the MnFeNiCuZn-noMg composition series are displayed in Figure 5.2 (c). The 400 °C sample exhibits a wide particle size distribution (with both large octahedral shaped particles and smaller spheroidal agglomerates). EDS analysis presented in SI Figure S5.6 reveals the sample exhibits homogeneous distributions of all analyzed elements at the resolution probed. Higher post-treatment temperatures (600 °C and 800 °C) lead to larger particle sizes and a more homogeneous particle size distribution, consistent with the results from Rietveld refinements.[245] The 1000 °C treated sample displays particle sizes in the micrometer-scale (bulk) range. High resolution SEM was conducted on the heat treatment series of two other compositions: MgMnFeCuZn-noNi and MgFeNiCuZn-noMn, as illustrated in SI Figure S5.7. Similar observations are made regarding the morphology and particle size distribution trends. Overall, these findings provide valuable insights into the modification of sample purity and morphology achieved through different post-treatment temperatures.

As previously mentioned (also shown in SI Figure S5.1 (a)), the MnFeNiCuZn-noMg-400 °C exhibits the poorest OER performance as compared to 600 °C, 800 °C, and 1000 °C post-annealed samples. Remarkably, even though the 1000 °C series exhibits micrometer scale particle sizes, they demonstrate excellent OER performance (comparable to the 600 °C sample series). On the other hand, the 800 °C series exhibits a more uniform particle size distribution but falls short of the performance observed in the 1000 °C series. These trends suggest that particle size is not the predominant factor in determining OER performance and that post-annealing is an effective tuning parameter for CCO nanocatalysts in this series. Further investigation is required to determine whether the higher 600 °C performance trend can be attributed to phase purity, a tuning towards cation short range order at the atomic

or nanoscale, a morphological improvement facilitated by the unique cation diffusion processes in compositionally complex systems, or some other effects.

The XRD patterns and SEM images of the 600 °C sample series are compared in Figure 5.5 (a,b), respectively. The XRD patterns reveal that MgFeNiCuZn-noMn-600 °C and MgMnNiCuZn-noFe-600 °C samples have small impurities, while the remaining four samples appear single phase. The SEM images of all compositions reveal qualitatively similar particle size distributions and morphologies. These observations together with the noted variation in OER and ORR performance across the compositional series suggest the varying combination of multimetal cations, referred to as "cation selection" in this study, plays an important role. Interestingly, the sample MnFeNiCuZn-noMg, MgMnNiCuZn-noFe, MgMnFeNiCu-noZn have better bifunctional OER and ORR catalytic activity, relative to MgMnFeCuZn-noNi, MgMnFeNiZn-noCu, and MgFeNiCuZn-noMn. This suggests that Mn, Cu, and Ni play a significant role in both OER and ORR. This departs from the catalytic activity trends observed for OER in the end member compositions in alkaline solution, which reflects the order: $ZnCo_2O_4 > NiCo_2O_4 > FeCo_2O_4 > Co_3O_4 > MnCo_2O_4$[75]. Thus, the work herein provides another example of the multi-metal enhancement effects observed in compositionally complex electrocatalysts. By comparing CCOs with each distinct combination of 5 out of 6 selected cations occupying the A-site (ACo_2O_4), the relative influence of each metal cation on the bifunctional OER and ORR performance can be efficiently screened. This approach allowed us to collect valuable performance information through a small subset of possible compositions. These findings indicate a promising pathway for designing new materials in the vast design space available for CCOs. In our future work, we will investigate the potential of improving the bifunctional OER and ORR activities of the CCO ACo_2O_4 family by exploring various combinations of only Mn, Cu, and Ni incorporation.

Beyond cation selection, our work demonstrates electrocatalytic properties in the CCO ACo_2O_4 family can be influenced through processing variations in the LTST

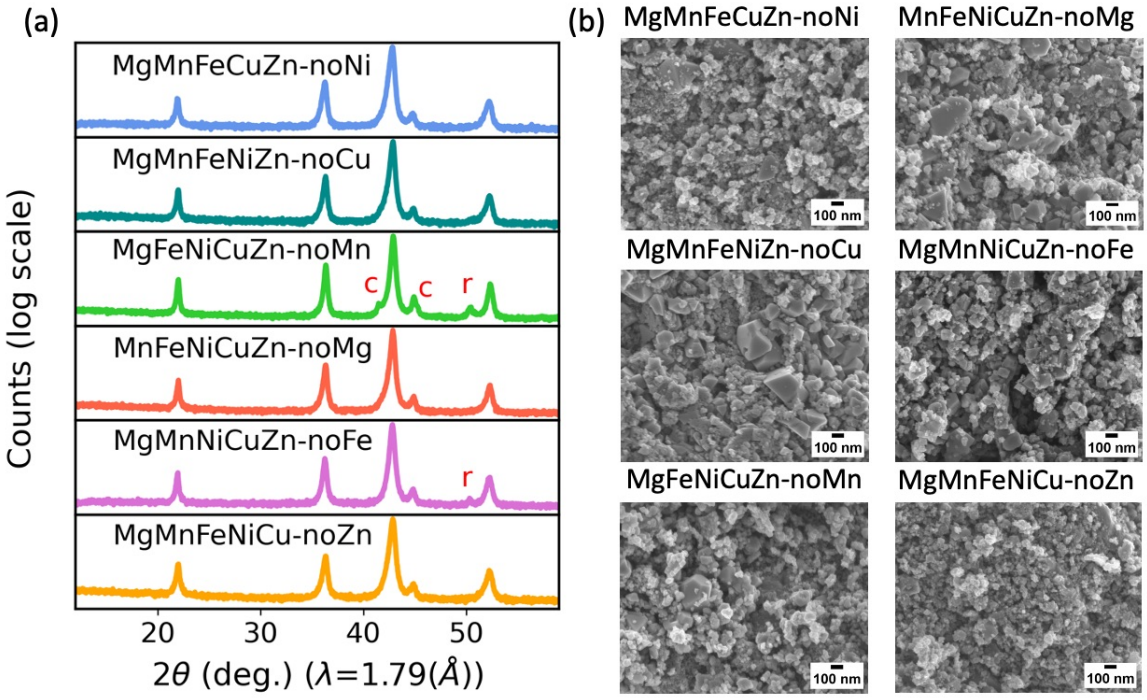


Figure 5.5: XRD patterns of (a) 600 °C series, MgMnFeCuZn-noNi, MgMnFeNiZn-noCu, MgFeNiCuZn-noMn, MnFeNiCuZn-noMg, MgMnNiCuZn-noFe, and MgMnFeNiCu-noZn samples. Impurities are coded: tenorite CuO ("c") and rock salt ("r"). SEM images in (b) reveal the morphology of the samples in (a).

synthesis method. A series of spider plots corresponding to increasing post-annealing temperature is given in Figure 5.6, created to illustrate the complex correlations between the measured OER overpotential (η, mV), crystalline domain size determined from Rietveld analysis (CS, nm), and cation site inversion determined from Rietveld analysis (γ) for the compositions studied (the analysis involved in determining the latter two parameters are described in detail in our previous work[245]). As annealing temperature increases from 400 °C to 800 °C (the series of spider plots from left to right), η initially decreases and then increases (this correlation is provided as a separate plot in SI Figure S5.1 (a)). As may be expected, the average crystallinity of all samples increases with increasing annealing temperature, but they do so at varying rates. Interestingly, the cation site inversion parameter, γ, is also revealed to vary significantly with heat treatment.

For all compositions treated at 400 °C, γ is near 2/3 (representing a near random spinel structure where A-site cations and Co^{3+} are present in 1/3 and 2/3 ratios on both the tetrahedral and octahedral sites, respectively). For most compositions, γ approaches 1 at higher temperatures (representing an inverse spinel structure with all A-site cations occupying the octahedral site and half of the Co^{3+} occupying the tetrahedral site) as temperature increases. The highest performing OER catalyst, MnFeNiCuZn-noMg, is an exception– it exhibits a decrease in γ with higher annealing temperatures and approaches 0 at 800 °C (representing a normal spinel structure with A-site cations only occupying the tetrahedral site and Co^{3+} only occupying the octahedral site). These correlations are shown individually in SI Figure S5.1 (c) for further clarity. To be clear, only the simplest normal, inverse, and random site models were considered due to the relative insensitivity of X-ray diffraction to shared transition metal site occupancies (with all the A atom occupancies constrained to be equivalent on each spinel cation site and each cation site constrained to have a total occupancy of 1)[245]. Nonetheless, the trends from the Rietveld refinement indicate significant changes in cation site ordering that vary across the series. The details of the Rietveld refinement with "continuous lattice" model for the 600 °C sample series

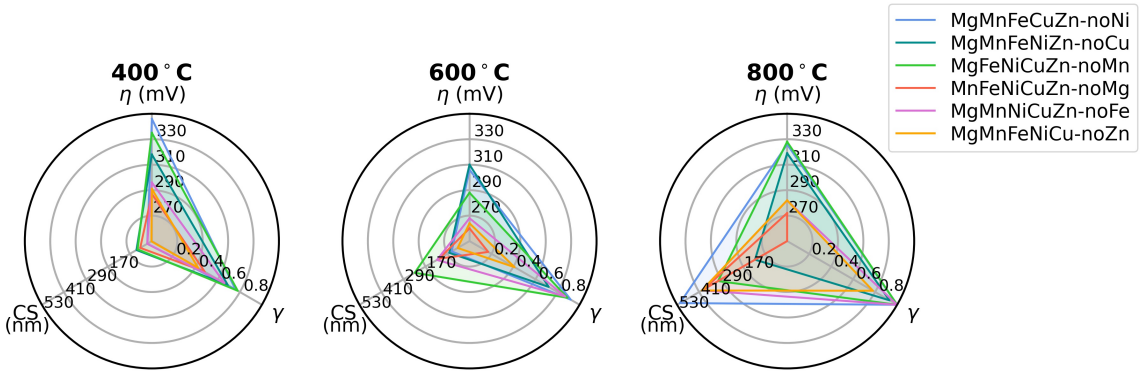


Figure 5.6: Overpotential (η, measured at 10 mA cm^{-2}) of OER, crystalline size (CS, nm) and cation site inversion (γ) for all 6 compositions $(5A_{1/5})Co_2O_4$, MgMnFeCuZn-noNi (blue), MgMnFeNiZn-noCu (teal), MgFeNiCuZn-noMn (green), MnFeNiCuZn-noMg (orange), MgMnNiCuZn-noFe (pink), and MgMnFeNiCu-noZn (yellow). Left to right, correlations are depicted for as prepared samples (400 °C), and samples post-annealed at 600 °C and 800 °C.

were included in SI Table S5.3, which provides information about R_{wp}, median of the lattice parameter (a_m, Å), crystallite size (CS), cation site inversion parameter (γ), atomic position of oxygen (u). The isotropic atomic displacement parameters (U_{iso}, Å^2) for the tetrahedral site, octahedral site, and oxygen were fixed as 0.005, 0.005, and 0.010 Å^2, respectively, for all compositions. At the same time, the surface oxidation states obtained from XPS measurements indicate a partial inverse spinel structure, creating a complex and intriguing scenario. Extended X-ray absorption fine structure, X-ray absorption near edge structure, nuclear magnetic resonance, Mössbauer spectroscopy, neutron diffraction, or other complementary measurements would be necessary to study the cation site occupancy trends in fine detail. Finally, the comparison between η and CS and η and γ for the series do not illicit clear trends (the relationships are shown individually in SI Figure S5.1 (b,d), respectively). Rather, it can be inferred that morphology, chemistry, and thermal history are interconnected tuning factors in the electrocatalytic performance of CCO ACo_2O_4 samples studied here.

Overall, the enhanced OER efficiency and effective ORR activity observed for MnFeNiCuZn-noMg-600 °C can be attributed to a synergistic interplay of several key elements. MnFeNiCuZn-noMg (along with other compositions reported in this study) benefits from a diverse array of transition metal cations, each of which can act as a potential catalytic site with varying degrees of electrochemical tunability. This amalgamation of metal ions creates a unique and advantageous chemical environment for catalysis, wherein each metal may contribute its own catalytic properties, as well as influence the local electron density around the neighboring cations. The specific chemical environments and OER activities are shown to be impacted by thermal annealing, revealing an additional tuning parameter in optimizing efficient CCO catalysts. Finally, the MnFeNiCuZn-noMg-600 °C catalyst possesses a substantial electrochemically active surface area. A larger electrochemical surface area equates to more active sites available for electrocatalysis leading to higher current density. Hence, the outstanding OER activity of MnFeNiCuZn-noMg-600 °C is most likely the

outcome of a harmonious interplay between its diverse composition, expansive surface area, unique (amalgamated) electronic structure, and the electrochemical tunability of the catalytic site. This intricate combination renders this catalyst exceptionally effective for OER and indicates a promising direction for simultaneously improving ORR.

5.4 Conclusion

Nano CCO $(5A_{1/5})Co_2O_4$ phases made by LTST methods show great promise as tunable bifunctional electrocatalysts for water splitting technologies. The sample MnFeNiCuZn-noMg-600 °C shows an exceptional overpotential for OER at 260 mV at 10 mA cm^{-2} and excellent onset potential, 0.91 V, for ORR. It was demonstrated that thermal heat treatment of nanostructured phases can be used to drive cation diffusion and 'tune' the structures towards high activity. The results presented suggest that further tuning of morphology, cation short-range ordering/nanostructuring, and composition will lead to further enhancement in this family of cobaltites. Furthermore, based on the compositional screening herein, it is anticipated that exchanging non-catalytically active cations such as Mg for larger proportions of catalytically active cations such as Mn, Cu and Ni, will result in further performance enhancements. Overall, this work displays the great potential of LTST to produce nano CCOs for bifunctional catalytic design. The reaction route provides a straightforward way to screen potential CCO compositions for catalytic activity, explore the potential synergistic effects of incorporating many metal cations, and understand the impact of thermal annealing and associated cation short range order. These directions will be explored in future work.

Chapter 6

Impact of Thermal Annealing on Magnetic Properties in Nano Compositionally Complex Spinel Cobaltite - $(Mg_{0.2}Mn_{0.2}Fe_{0.2}Cu_{0.2}Zn_{0.2})Co_2O_4$

The promising bifunctional electrocatalytic properties in our family of nano CCO cobaltites with formula $(nA_{1/n})Co_2O_4$ were presented in Chapter 5. With a high proportion of Co and other magnetically active cations, the magnetic properties of the nano CCO spinel family are of additional interest. The work in this chapter explores the sensitivity of the magnetic properties in the composition $(Mg_{0.2}Mn_{0.2}Fe_{0.2}Cu_{0.2}Zn_{0.2})Co_2O_4$ to local chemical segregation and phase evolution introduced through variation in post-processing heat treatment temperature. A combination of X-ray diffraction, scanning transmission electron microscopy with energy dispersive X-ray spectroscopy (STEM-EDS), first-order reversal curve (FORC) magnetometry, and neutron diffraction/total scattering analyses was employed to

understand both average and local structure-property evolution. The post-annealing process triggers local and long-range cation diffusion, resulting in changes in the distribution of atoms residing on the tetrahedral and octahedral sites of the spinel structure as well as nanoscale heterogeneity, inducing magnetic phase separation and soft to hard phase transformations, phenomena not readily observable through M vs T (magnetization vs. temperature) and M vs H (magnetization vs. magnetizing field) measurements alone. Even minor magnetic cation migration on an atomic scale can be detected through FORC measurements, a sensitivity beyond the detection capabilities of neutron total scattering analysis. This work additionally highlights the necessity of a combination of advanced characterization techniques for understanding the broader crystal-chemical class of compositionally complex oxides.

The work in Chapter 6– *Impact of Thermal Annealing on Magnetic Properties in Nano Compositionally Complex Spinel Cobaltite - $(Mg_{0.2}Mn_{0.2}Fe_{0.2}Cu_{0.2}Zn_{0.2})Co_2O_4$*– is currently under development as a manuscript to be submitted in 2024. The authors of the work are Xin Wang, Cameron S. Jorgensen, Corisa Kons, Yuanpeng Zhang, Jue Liu, Peter C. Metz, Eleonora Calì, Dustin A. Gilbert, and Katharine Page.

6.1 Introduction

Limited research has been conducted on the utilization of nanostructured high entropy oxides (HEOs) or compositionally complex oxides (CCOs) as a platform for developing complex functional oxides. It is widely acknowledged in the scientific community that complex oxides can exhibit a notable degree of chemical short-range order (CSRO), distinct nanoscale phase segregation, and local lattice distortion. Moreover, specific local atomic ordering patterns and their coherent length scales are often tied to distinct physical properties[174, 290, 291, 279]. For example, Ni/Mn sublattice order/disorder affects the surface and near-surface properties to control electrochemical performance of $LiNi_{0.44}Mn_{1.56}O_4$ lithium-ion batteries (LiBs)[5], local compositional disorder generates tunable magnetic properties in single

crystal $La(Cr_{0.2}Mn_{0.2}Fe_{0.2}Co_{0.2}Ni_{0.2})O_3$ films[148], and the ratio of Co^{3+}/Co^{2+} and M^{3+}/M^{2+} on the octahedral site determines the oxygen evolution reaction (OER) activity of MCo_2O_4 (M = Mn, Fe, Co, Ni, and Zn) spinels[75]. Other complex oxides are imbued with unique properties via nano-scale phase segregation, including relaxor ferroelectrics[188, 98], birefringent garnets[272], and spinel and rock salt exchange spring magnets[7] and electrochemical cycling platforms[271]. Others feature coherent architectures with fine compositional gradients that enable distinct physicochemical properties[206, 264]. Clearly, design paradigms for control of chemical and phase segregation and coupling at the atomic and nano scales are of broad interest. Following this reasoning, the extraordinary complexity found in HEOs and CCOs are hypothesized to present rich opportunities for harnessing complex diffusion dynamics in tailored synthesis approaches to stabilize novel local atomic configurations and defects, enabling rational design of highly performant materials[105, 245, 124].

From the perspective of magnetic behavior, particularly in oxides, properties will depend on the elements present, their valence states, and their specific coordination environments within the structure. Among the 3d transition metals, cobalt is essentially important in advanced magnetic materials, exhibiting high saturation magnetization (M_S) and high Curie temperature (T_C)[153]. The end member cobaltites ACo_2O_4 (A=Mg, Mn, Fe, Ni, Cu, Zn, Co) are earth-abundant ferrimagnets that crystallize in the spinel structure[190, 143, 147, 16, 155, 8, 159]. In the normal spinel structure (Figure 6.1 (a)), large divalent cations occupy the tetrahedral A-site exclusively, while Co occupies the octahedral B-site. Figure 6.1 (b) displays the corresponding ferrimagnetic structure with calculated magnetic moments on tetrahedral and octahedral cation sites aligned in opposite directions along the c-axis. Commonly, there is some cation mixing between the A- and B- sites; the fraction of A-site cations occupying the B-site, called the inversion parameter (γ), ranges from 0 for normal spinel to 1 for inverse spinel, and the degree of inversion influences the ferrimagnetism[198]. Additionally, the magnetic properties of spinels, including

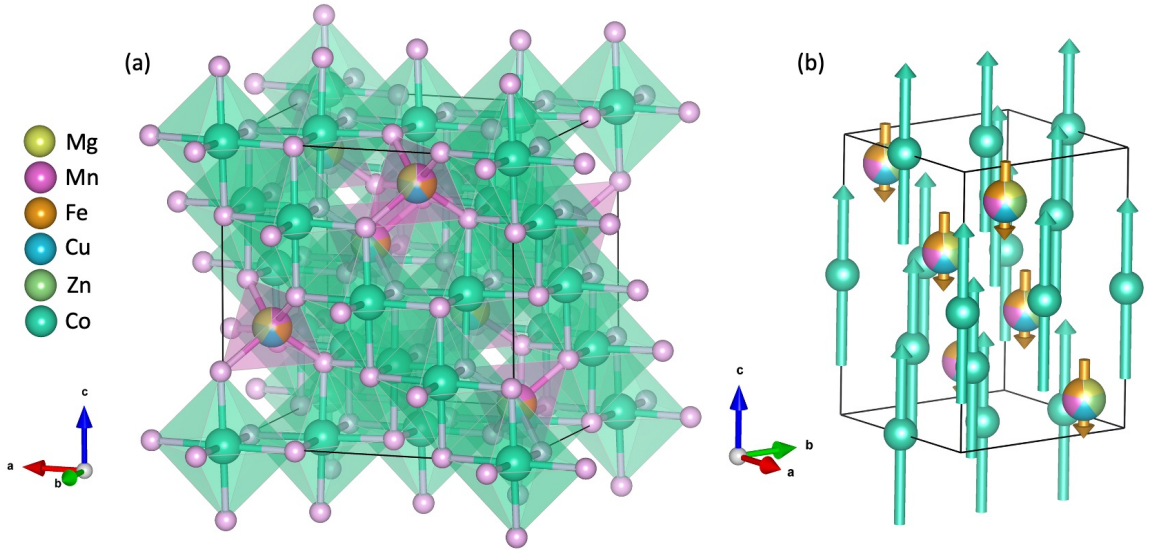


Figure 6.1: (a) Normal spinel unit cell comprises pink tetrahedra (A-sites) and green octahedra (Co-sites), with atoms labeled in their respective colors. The A-site cations, including Mg, Mn, Fe, Cu, and Zn occupy the tetrahedral site, while Co occupies only the octahedral site. (b) The corresponding room-temperature zero-field magnetic spinel structure depicts calculated magnetic moments pointing down on the tetrahedral site and pointing up on the octahedral site.

the blocking temperature, saturation magnetization, remnant magnetization, and coercivity, are known to be influenced by factors such as nanocrystalline shape[211] and compositional tuning[157, 273]. Compositionally complex cobaltites expand upon this design space considerably, as the local and long-range nuclear and spin structures will depend on a large number of metal-oxygen-metal couples due to the many cation types, varying coordination geometries, valence and spin states HEOs and CCOs possess[198].

In the high-entropy paradigm, configurational entropy (S_{config}) may stabilize otherwise unfavorable structures; yet, in the spinel system, the configurational entropy is found to be consistently smaller than 1.5 R, where R is the universal gas constant, even when the number of distinct cations on the A site reaches 8[246]. Note that the S_{config} threshold for classification as HEO is 1.5 R. Our previous study[245] of CCO cobaltites synthesized by a low-temperature soft-templating (LTST) method revealed that the phase selectivity and temperature stability are primarily influenced by the chemical composition rather than the number of participating cations and that these cobaltites are metastable rather than entropy stabilized. Additionally, our investigation[247] of their electrocatalytic properties highlighted that the bifunctional oxygen evolution reaction (OER) and oxygen reduction reaction (ORR) is significantly influenced by cation combination and post-annealing temperatures. Thus, it becomes apparent that the synthesis conditions play an essential role in determining the metastable state of the sample and in the resulting material behavior.[246] Consequently, this family of compounds provides a versatile phase space where competing thermodynamic factors and sluggish cation diffusion can be exploited to tailor cation site inversion, the heterogeneity of the cation distribution over different length scales, and the resulting material properties.

To accelerate the development of HEO and CCO complex functional oxides, it is crucial to understand to what extent their local environments (geometry, distortion, coordination) can be controlled and linked to functional properties. In this chapter, we investigate the sensitivity of magnetic properties to the thermal history

of nanostructured compositionally complex oxide $(Mg_{0.2}Mn_{0.2}Fe_{0.2}Cu_{0.2}Zn_{0.2})Co_2O_4$ spinel phases. High-resolution scanning transmission electron microscopy (STEM), first-order reversal curve (FORC) measurements from bulk magnetometry, and average and local atomic structure analysis from neutron total scattering experiments are combined to reveal trends in structure-property relationships. By controlling post-annealing temperatures (600°C, 800°C, and 1000°C) and hence the degree of cation diffusion in the system, the chemical short-range order, cation site preference, phase segregation, and the morphology of nanostructures can be tuned. The resulting specific local ordering patterns lead to distinct magnetic behaviors, highlighting the potential of nanostructured HEO and CCO materials as highly tunable platforms for magnetic applications.

6.2 Methods

6.2.1 Materials synthesis

CCOs with the composition $(Mg_{0.2}Mn_{0.2}Fe_{0.2}Cu_{0.2}Zn_{0.2})Co_2O_4$ were synthesized using a low-temperature soft templating (LTST) reaction method, the details of which were previously published[245]. The gel obtained from the evaporation of room temperature solution was initially calcined at 400°C, leading to the formation of the as-formed sample in this work. Subsequently, post-annealing treatments were conducted on pellets made from the as-formed sample, separately, at temperatures of 600°C, 800°C, and 1000°C.

6.2.2 Characterization

X-ray diffraction (XRD)

XRD measurements were conducted on all four samples using Co Kα radiation with a PANalytical Empyrean diffractometer. The XRD patterns were collected from 10

to 90° 2θ with a step size of 0.026°. The specimen was prepared by placing a small amount of finely ground powder onto a sample holder, after which a glass slide was used to spread it evenly to ensure a flat surface.

Electron microscopy

The sample morphology at the nanoscale was examined by scanning transmission electron microscopy (STEM) using a JEOL JEM-2100F microscope. The incident beam was operated at 200 kV. To determine the chemical composition and elemental distribution, energy dispersive X-ray spectroscopy (EDS) (80 mm X-Max detector, Oxford Instruments) was employed. To prepare the STEM-EDS specimen, the powder samples were sonicated in high-purity propan-2-ol and then drop-cast on copper grids coated with a holey carbon film (3.05 mm diam. 300 mesh, TAAB Laboratories Equipment Ltd).

6.2.3 Magnetic measurements

The magnetometry measurements on all samples were carried out using a vibrating sample magnetometer (VSM) as part of a Quantum Design PPMS DynaCool system. The field cooled (FC) and zero field cooling (ZFC) methods were employed to investigate temperature-dependent magnetometry (M vs T). To begin, the powder sample was cooled to 2 K without any applied magnetic field. Next, a 10 mT field was applied, and the magnetic moment was recorded as the temperature was increased from 2 K to 400 K, performing the ZFC measurement. After completing the ZFC measurement, the applied field was maintained at 10 mT, and the magnetization was measured as the temperature was decreased from 400 K to 2 K to obtain the FC curve.

The magnetic phase fractions[61], quantified interactions[63], and reversal mechanisms[46] were investigated using the first-order reversal curve (FORC) technique[179, 180, 187, 63]. The protocol of FORC measurements starts with first applying a large

positive field to saturate the sample, then the field is gradually reduced to a specific reversal field (H_R), and then the magnetization is measured as the applied field (H) is increased from H_R to saturation. This process is repeated to obtain a family of FORCs at H_R between the negative and positive saturation. The FORC distribution, $\rho\ (H,\ H_R)$ is defined as applying a mixed second-order derivative to the dataset:

$$\rho(H, H_R) = \frac{-1}{2M_S} \frac{\partial^2 M(H, H_R)}{\partial H \partial H_R} \tag{6.1}$$

where M_S is the magnetization saturation. In effect, the derivative $\partial M/\partial H$ of each FORC branch is compared to its adjacent neighbors, capturing any new or moving magnetic switching events. Measurements conducted with increasing magnetic field, e.g. the H axis, are probing magnetic up-switching events from a negative to a positive orientation, while H_R probes down-switching events. FORC measurements were conducted to examine all four samples processed at various temperatures, focusing on the small bump observed at low temperatures in M vs T plots for each sample. The specific temperatures 5 K and 100 K were applied to all four samples. The resulting FORC diagram represents a contour plot of $\rho\ (H,\ H_R)$. Associating H with up-switching events and H_R with down-switching, the data is transformed into a new coordinate system representing the local coercivity and bias: $H_C = (H - H_R)/2$ and $H_B = (H + H_R)/2$.

Finally, magnetic hysteresis (M_H) loop measurements at 5 K and 100 K were extracted from the family of FORCs for all the samples. All measurements were normalized to the sample mass.

6.2.4 Neutron total scattering measurements

Time of flight (TOF) neutron powder diffraction (NPD) data and neutron total scattering data were collected on the Nanoscale Ordered Materials Diffractometer (NOMAD) at the Spallation Neutron Source (SNS) at Oak Ridge National Laboratory (ORNL)[164]. For each sample, approximately 0.3 g of dried powder was dried at 200

°C for two days and loaded into a 3 mm diameter quartz capillary. Data collection for all four samples was performed at 300 K in a temperature-controlled Ar cryostream. Data reduction, including normalization, background subtraction, and absorption correction, was carried out using the MantidTotalScattering (MTS) framework. Pair distribution function (PDF) data was Fourier transformed from total scattering data using a Q_{max} = of 32 Å^{-1}.

6.2.5 Rietveld and PDF refinement

Rietveld refinements were carried out with the TOPAS-V7 program[36]. For the main spinel phase structure (S.G. $Fd\bar{3}m$) the background, scale factors, lattice parameters (a), A-, B-, and O-site isotropic atomic displacement parameters (B_{iso}), and oxygen atom positions (u) were refined. Only lattice parameters and scale factors were refined for the impurities present in samples that were post-annealed at 800°C and 1000°C. It was found necessary to employ a 2-spinel phase model to fit the 1000°C data. A lattice parameter and phase fraction were refined for the secondary spinel phase. The atomic displacement parameters were constrained as equal to those in the main spinel phase. To address the intricate nature of the cation site mixing in this nano CCO, the A- and B- sites of spinel phases were treated as pseudo-atoms; only the average scattering length on each site was refined. Finally, isotropic crystallite size and microstrain broadening were applied to describe the nanomaterial peak broadening in the phases[109, 295].

The magnetic scattering was fitted with a ferrimagnetic structure (S.G. $I4_1/am'd'$) with spins on tetrahedral and octahedral cation sites aligned in opposite directions along the c-axis (See Figure 6.1 (b)). The magnetic lattice parameters are related to the main spinel lattice as $a_{mag} = b_{mag} = \sqrt{2}a_{main}/2$ and $a_{main} = c_{mag}$, respectively. Likewise, the scale factor of the magnetic phase was constrained in proportion to the relative unit cell volume (V_{mag}/V_{main}=1/2). The magnetic structure model was also constructed with pseudo-atoms, where the average magnetic moments on both the

tetrahedral and octahedral sites were refined. More details of the model can be found in our previously published paper on CCO spinel ferrites [246].

Structure refinements against PDF data were also performed using TOPAS-V7[36], utilizing both a single-phase spinel model (1-phase) and the two-spinel phase (2-phase) model described above for all sample data. The 2-phase model was found to more accurately capture the low r peak shapes across the data series, with significantly improved goodness of fit R_W values and smaller atomic displacement parameters (B, Å^2) compared to the single spinel phase (1-phase) model. The refinements conducted with 10 Å and 30 Å PDF data ranges using both the 1-phase and 2-phase models are illustrated in supplemental information (SI) Figure S6.1 and Figure S6.2, respectively. The corresponding extracted phase percentages (p, %), lattice parameters (a, Å), average scattering lengths ($\langle b \rangle$, fm), and the atomic displacement parameters of tetrahedral cation, octahedral cation, and oxygen atom sites (B_{eq}, Å^2) are compared in Figure S6.3 and Figure S6.4, respectively. The minor influence of magnetic scattering was ignored in PDF modeling, based on the small intensity of magnetic scattering observed via Rietveld refinement. However, it was found necessary to include the impurity phase, MgO, to achieve satisfactory PDF fits for the sample post-annealed at 1000°C. Instrument resolution effects were modeled using parameters determined through the refinement of a nickel powder data set.

6.3 Results and Discussion

6.3.1 Phase purity and nanoscale heterogeneity

The post-annealing process induced changes in the phase purity as well as particle size and morphology of samples, as revealed by X-ray powder diffraction (Figure 6.2(a)) and bright-field TEM analysis (Figure 6.2(b-e)). The XRD patterns for the samples calcined at 400°C and post-annealed at 600°C confirm the expected cubic spinel

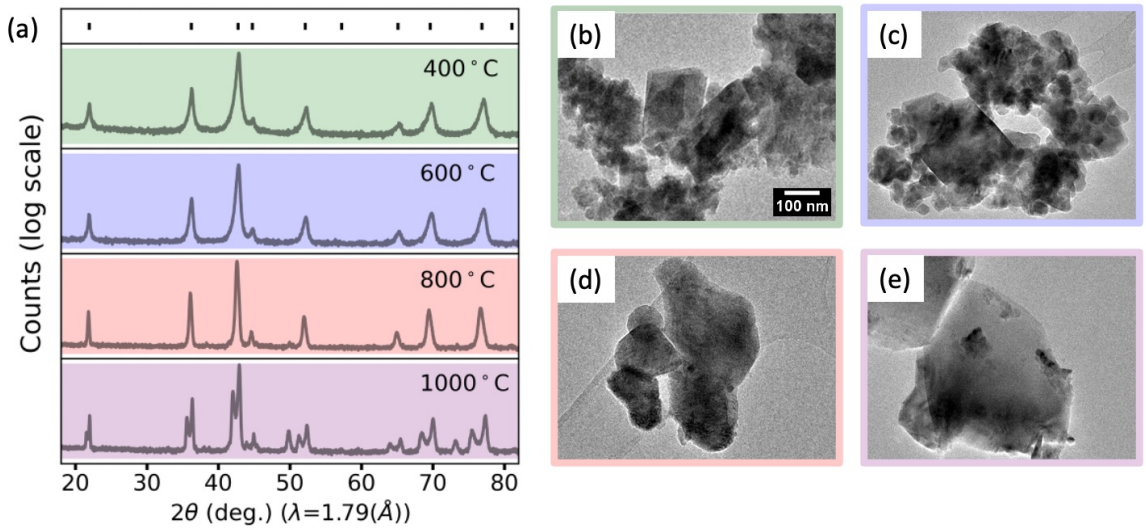


Figure 6.2: (a) XRD pattern comparison of samples indicating a single spinel phase for 400°C and 600°C samples and impurity/secondary phases for 800°C and 1000°C samples. The small black solid (h k l) ticks placed in the bar on top of the XRD patterns indicate Bragg peak locations of the main spinel phase. (b-e) TEM image comparison of samples (b) calcined at 400°C, and post-annealed at (c) 600°C, (d) 800°C, and (e) 1000°C. The samples calcined at 400°C and post-annealed at 600°C display broad particle size distributions. In contrast, the sample post-annealed at 800°C exhibits particle sizes of 100 nm or more. The sample post-annealed at 1000°C consists of micron-scale sized particles. Note the same scale bar applies to all four TEM images in (b-e).

$Fd\bar{3}m$ structure. However, increasing post-annealing temperature led to the formation of additional phases; the XRD pattern of the sample post-annealed at 800°C reveals the presence of tenorite (CuO) and rocksalt (MgO), and the XRD pattern of the sample post-annealed at 1000°C exhibits CuO and MgO, as well as a secondary spinel phase. Rietveld refinements for samples post-annealed at 800°C and 1000°C are shown in the SI Figure S6.5. Further insight can be gained by considering changes in the diffraction peak shapes of the samples. Broad and asymmetric peaks were observed within the samples calcined at 400°C and post-annealed at 600°C, suggesting the possible existence of multiple different nanostructured regions rather than a true solid solution[245]. The trend towards sharper, more symmetric peaks in the post-annealed samples indicates equilibration towards greater chemical homogeneity as well as increased crystallite size.

These microstructure characteristics are further supported by the STEM images shown in Figure 6.2 (b-e), where the samples calcined at 400°C and post-annealed at 600°C exhibit a broader particle size distribution compared to the other two post-annealed samples. Further, the distribution of elements among representative particles or domains in the samples was examined via STEM-EDS elemental mapping (Figure 6.3). It can be seen, by comparing the maps for samples (a) calcined at 400°C, (b) post-annealed at 600°C, (c) post-annealed at 800°C and (d) post-annealed at 1000°C, that post-annealing induces a redistribution of cations among particles and grains. In the as-formed 400°C condition, Mg, Mn, and Fe are enriched in specific domains, with a similar but less pronounced inhomogeneous distribution for Zn (Figure 6.3(a)). In samples post-annealed at 600°C (Figure 6.3(b)) and 800°C (Figure 6.3(c)) the cation distributions appear slightly more homogeneous, though certain grains maintain enrichment of select elements. In the sample post-annealed at 800°C (Figure 6.3(c)) MgO precipitation was identified, in agreement with XRD analysis. It should be noted that the phase fraction of the CuO impurity captured with XRD analysis is less than 2% via Rietveld refinement, making it challenging to observe via the STEM-EDS technique. Lastly, for the sample post-annealed at

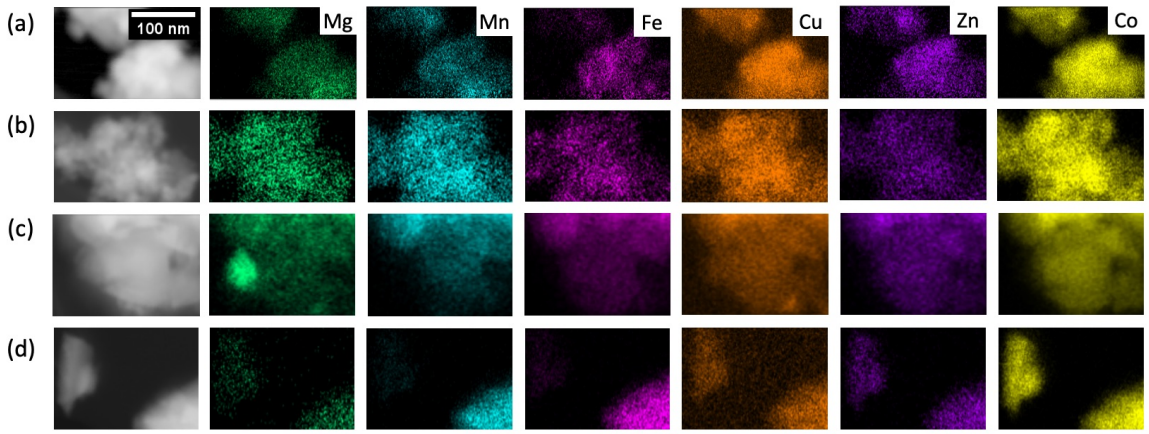


Figure 6.3: STEM-EDS map of $(Mg_{0.2}Mn_{0.2}Fe_{0.2}Cu_{0.2}Zn_{0.2})Co_2O_4$ spinel (a) as prepared at 400°C, and after post-annealing heat treatment at (b) 600°C, (c) 800°C, and (d) 1000°C. Note the first column of images on the left are STEM high-angle annular dark-field (HAADF) images. The scale bar in the top left corner applies to all images.

1000°C (Figure 6.3(d)), both the precipitation of MgO and a deficiency of Mn and Fe in a sizable fraction of particles are apparent.

In summary, intermediate post-annealing temperatures are seen to induce cation diffusion and reduce the heterogeneity of the initial cation distributions. At higher post-annealing temperatures, rocksalt and tenorite impurities precipitate. Above 800°C, separate spinel phases emerge; one with only Mg, Cu, Zn, and Co, and another necessarily enriched in Fe and Mn. These observations reveal a complex phase evolution occurring over multiple length-scales in the CCO spinel and align with the XRD analysis indicating the 1000°C sample is composed of two distinct spinel phases.

6.3.2 Magnetic phase segregation

The results of temperature-dependent magnetometry and magnetic hysteresis measurements for all four samples are shown in Figure 6.4 and Figure 6.5, respectively. For all the samples, increasing the measurement temperature decreases the sample magnetic moment and weakens the ferrimagnetism, as is normally expected.

The Curie temperatures, T_Cs, for the samples post-annealed at 1000°C and 800°C are $\approx$ 200 K and $\approx$ 300 K, respectively, while the T_Cs of the samples calcined at 400°C and post-annealed at 600°C are higher than 400 K, beyond the limits of our instrument. In the FC measurements, shown in Figure 6.4, the sample post-annealed at 800°C exhibits two minor peaks below 100 K, while the sample post-annealed at 600°C exhibits similar but much weaker features (see inset for detail).

The magnetic hysteresis measurements for all the samples measured at 100 K show a typical hysteresis loop with a coercivity of between 0.5 kOe for the sample calcined at 400°C and 2.2 kOe for the sample treated at 1000°C. Measurement performed at 5 K starts to show a stepped transition, with the reversal of a magnetically soft phase occurring near $H = 0$, followed by a long tail that extends beyond 1 T, corresponding to a magnetically hard phase.

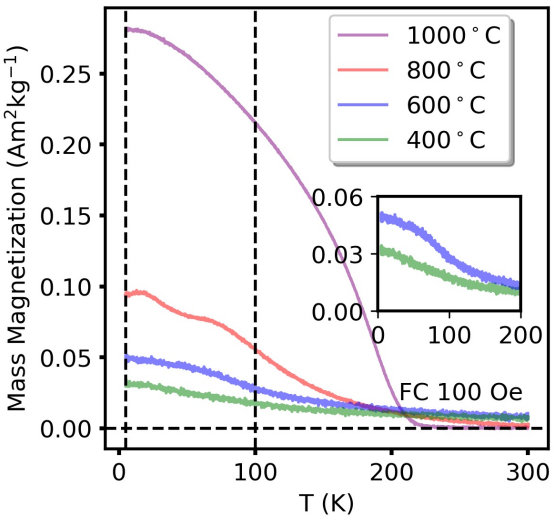


Figure 6.4: The field-cooled (FC) comparison for all four samples over a temperature range of 2 K to 400 K with an applied field of 100 Oe. The accompanying inset reveals a slight bump in the sample post-annealed at 600°C, while no such feature is observed in the sample calcined at 400°C. The heat-treatment temperatures are indicated in the legend. The temperatures (5 K and 100 K) used in all FORC measurements are denoted by black dashed vertical lines.

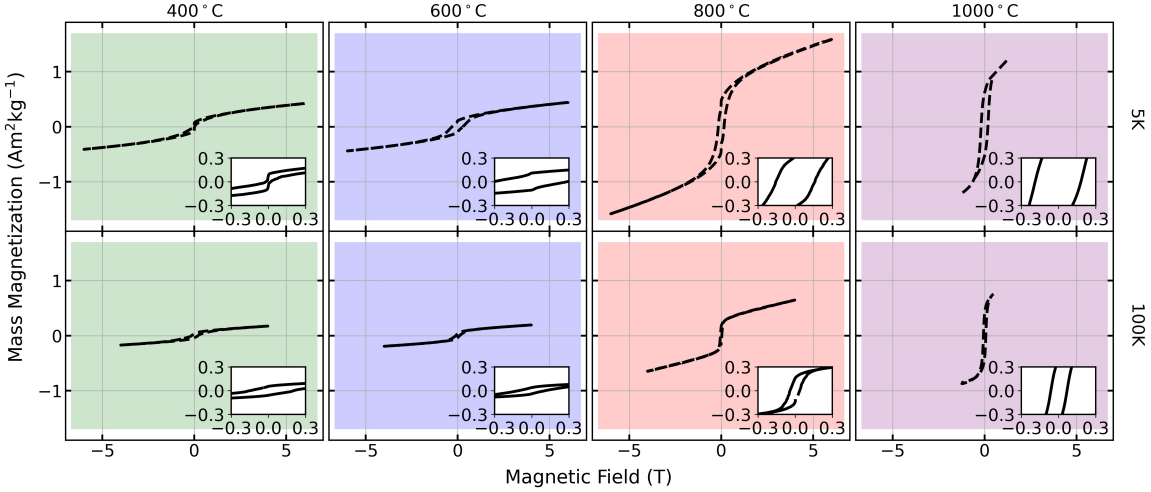


Figure 6.5: Magnetometry data for all four samples measured at 5 K (top panels), and 100 K (bottom panels). The heat-treatment temperatures are indicated at the top of each column. Insets display the distinct widths and shapes of hysteresis loops near zero field at smaller scale .

More details about the magnetic structure and reversals can be ascertained from the FORC distributions for all of the samples, measured at 5 K and 100 K, which are shown in Figure 6.6. The FORC distributions for the sample calcined at 400°C measured at 5 K and 100 K (Figure 6.6(a) and (b)) are dominated by the same general feature located at $H_C = H_B \approx 0$, corresponding to the soft magnetic phase and showing no coupling to any hard phase. The FORC distribution measured at 100 K (Figure 6.6(d)) on the sample post-annealed at 600°C shows a similar structure. By contrast, the FORC distributions measured at 5 K (Figure 6.6(c)) reveal two distinct features: Feature 1 is predominantly oriented along the H_C axis and Feature 2 is aligned along the H_B axis, corresponding to the hard and soft phases, respectively. Feature 1 indicates the emergence of a hard phase typically observed in bulk magnets, and in particular in geomagnetism[187]. In contrast, Feature 2 indicates a magnetically soft – likely reversible behavior. Broadening of the Feature 2, as well as their mutual proximity in the FORC distribution, suggests that these features are coexistent, and coupled. The soft phase in particular is centered at $H_B = 0$ and is reasonably symmetric along the H_B axis, indicating that it is dominating the reversal behavior, 'dragging' the hard phase with it during reversal.

Moving to the sample treated at 800°C, at 100 K, the Feature 1 dominates the FORC distribution, centered at $H_C \approx 500$ Oe, although some of the Feature 2 persists. The 5 K data also shows a further enhancement of Feature 1 and the features are still coupled. Compared to the sample treated at 600°C Feature 2 now is notably asymmetric, with a feature extending towards -H_B, indicating that Feature 1 is biasing its reversal. This indicates an increase in the magnetic volume of the hard phase and its effective anisotropy. This trend is enhanced in the final sample, which was post-annealed at 1000°C. In both the 5 K and 100 K measurements Feature 1 dominates the FORC distribution, and the feature representing the soft phase is asymmetric (at 100 K) and fully biased (at 5 K). This indicates that nearly all of the soft phase is coupled to and dominated by an adjacent hard phase. The trends indicate that all of the samples have a mixture of magnetic hard and soft phases,

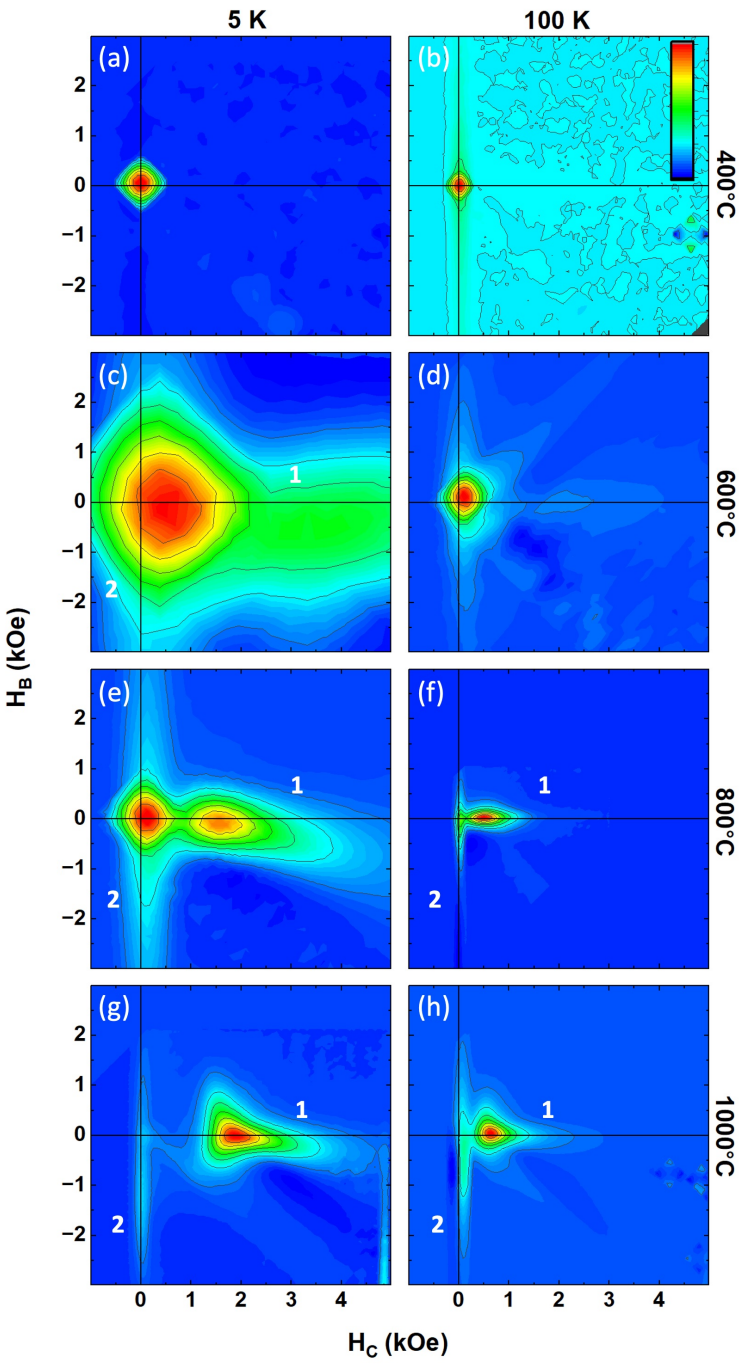


Figure 6.6: The comparison of FORC measurements at 5 K and 100 K for the sample calcined at (a, b) 400°C and the samples post-annealed at (c, d) 600°C, (e, f) 800°C, and (g, h) 1000°C. An intensity scale is displayed at the top right of (b). The feature labels "1" and "2" appearing in FORC plots for samples post-annealed at 600°C, 800°C, and 1000°C represent the primary feature orienting along the H_C axis, and the weak secondary feature along the H_B axis, respectively.

with the hard phase being vanishingly weak in the samples calcined at 400°C, and increasing to dominate in the samples annealed at 1000°C. The FORCs indicate that these phases are coexistent, with strong magnetic coupling, allowing the soft phase to cause a premature reversal of the hard, and later the hard to anchor and bias the reversal of the soft phase. Finally, it is notable that the hard feature in particular is a well-established signature of localized reversal – as contrasted with e.g. reversal by domain propagation. This structure indicates that the material is rich in soft nucleation sites which initialize localized structures, and pinning sites, which restrict long-range domain propagation. Combining the FORC measurements with the temperature dependent magnetization, it is likely that the soft phase is transforming into the hard phase, which has a lower T_C, eventually achieving a configuration that is magnetically hard at low temperatures, but non-magnetic at room temperature. Finally, the integral of each FORC feature corresponds to the magnetic moment associated with each feature; comparing the relative weights can be used to determine a magnetic phase fraction[61]. Treating the sample calcined at 400°C as predominantly soft phase, and the 1000°C as hard phase, the saturation moments can be calculated, and the phase fractions for the 600°C and 800°C samples determined. These phase fractions, shown in SI Figure S6.6, quantify the progression of the hard phase in the context of the soft phase; it is shown to be similar in all samples. In this specific case, with a large number of cations that can take up positions in two different crystallographic sites and deplete or concentrate in populations within specific particles/grains, it is challenging to determine whether there is a non-magnetic phase and the saturation magnetization of each phase present. This prevents direct determination of the exact structural cation migration from FORC analysis. Regardless, these results complement nanoscale STEM-EDS analysis which indicates thermally activated cation diffusion leads to different heterogeneous distributions (and magnetic properties) in post-annealed samples. These results are distinctly different from the average structure inferred by XRD which indicate distinct spinel phases only in the sample that is post-annealed at 1000°C. That is, FORC analysis appears

sensitive to incipient demixing of the as-synthesized material at shorter length scales than probed by Bragg diffraction.

6.3.3 Average and local structure

The average and short-range order of these materials was further examined using neutron total scattering. Figure 6.7 illustrates the comparison of neutron diffraction and PDF data obtained at 300 K. Panel (a) compares the Bragg scattering data collected from the 31° 2θ detector bank (bank 2), including the prominent magnetic diffraction peak, (101), (d=4.75 Å), while panel (b) compares data from the higher resolution 154° 2θ detector bank (bank 5), where the presence of two spinel phases is indicated by clear peak splitting in the 1000°C sample data. The PDFs collected at 300 K for all four samples exhibit striking similarity over the first 10 Å (Figure 6.7(c)); a similar comparison over 1.7 to 50 Å shows that the degree of similarity diminishes as the range expands (SI Figure S6.7).

Figure 6.7(d and e) provides an example of the Bragg and PDF data fits, for the sample calcined at 400°C, we extended the refinement methods to all samples. A summary of the Rietveld and PDF refinements results is provided in SI Table S6.1. The key extracted parameters are summarized in Figure 6.8.

The Rietveld refinement analysis revealed that the phase percentage of the main spinel remained near 100% across treatment conditions except in the sample post-annealed at 1000°C (Figure 6.8 (a)) which results in a secondary spinel phase. The lattice parameter of the main spinel trends larger throughout the various heat treatments until the emergence of the secondary spinel at 1000°C (Figure 6.8 (b)). This secondary spinel has a larger lattice parameter than the main spinel. The average scattering length ($\langle b \rangle$) refined for the tetrahedral and octahedral sites of the main spinel revealed a trend towards a normal spinel structure with increasing post-annealing temperature until phase separation occurs (Figure 6.8 (c)). The calculated $\langle b \rangle$ for normal and random spinel configurations for both tetrahedral and octahedral

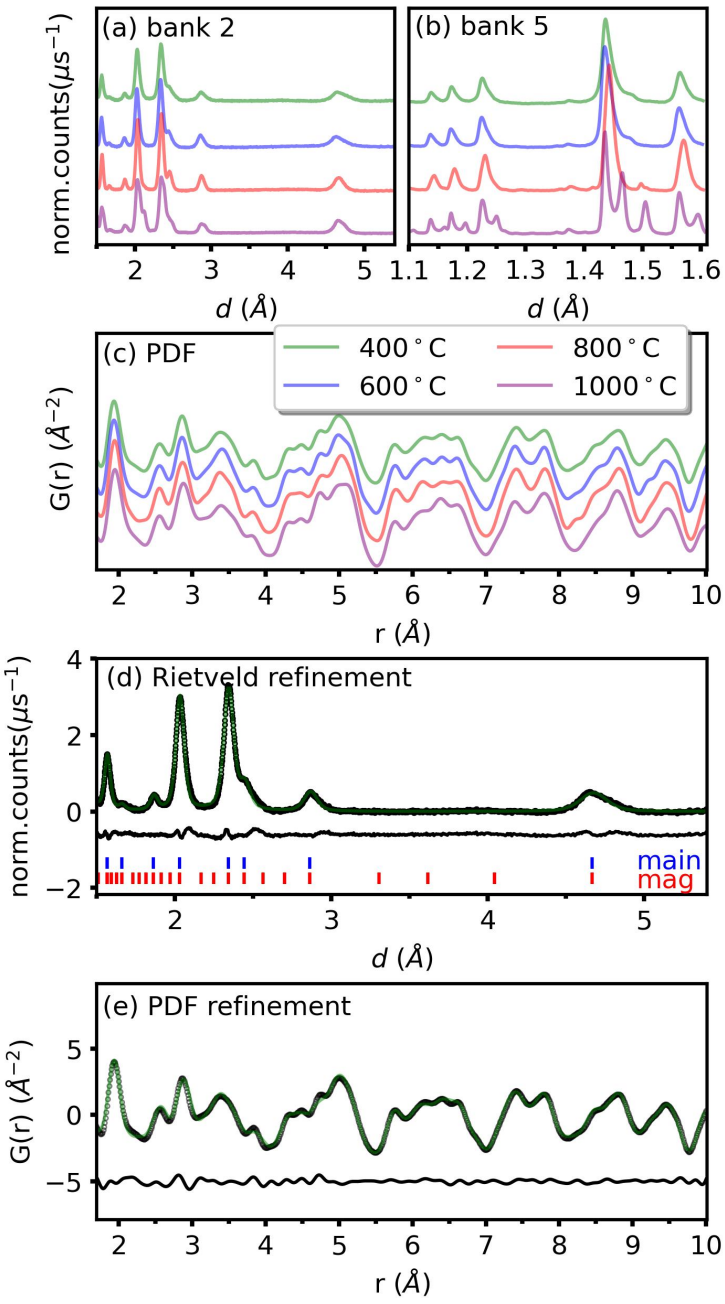


Figure 6.7: The comparison of neutron diffraction data from the 31° 2θ detector bank (bank 2) (a) and 154° 2θ detector bank (bank 5) (b) for the samples that were calcined at 400°C, and post-annealed at 600°C, 800°C, and 1000°C. (c) Corresponding PDF data of the sample series. The heat-treatment temperatures are specified by the legend in (c). The fit results for (d) Rietveld refinement of Bragg data (R_{wp}= 4.94%) and (e) total scattering data (R_{wp}= 11.97%) for the nanocrystalline CCO sample calcined at 400°C. The phase markers of the main spinel phase (main) and magnetic phase (mag) are displayed below the difference curve in (d).

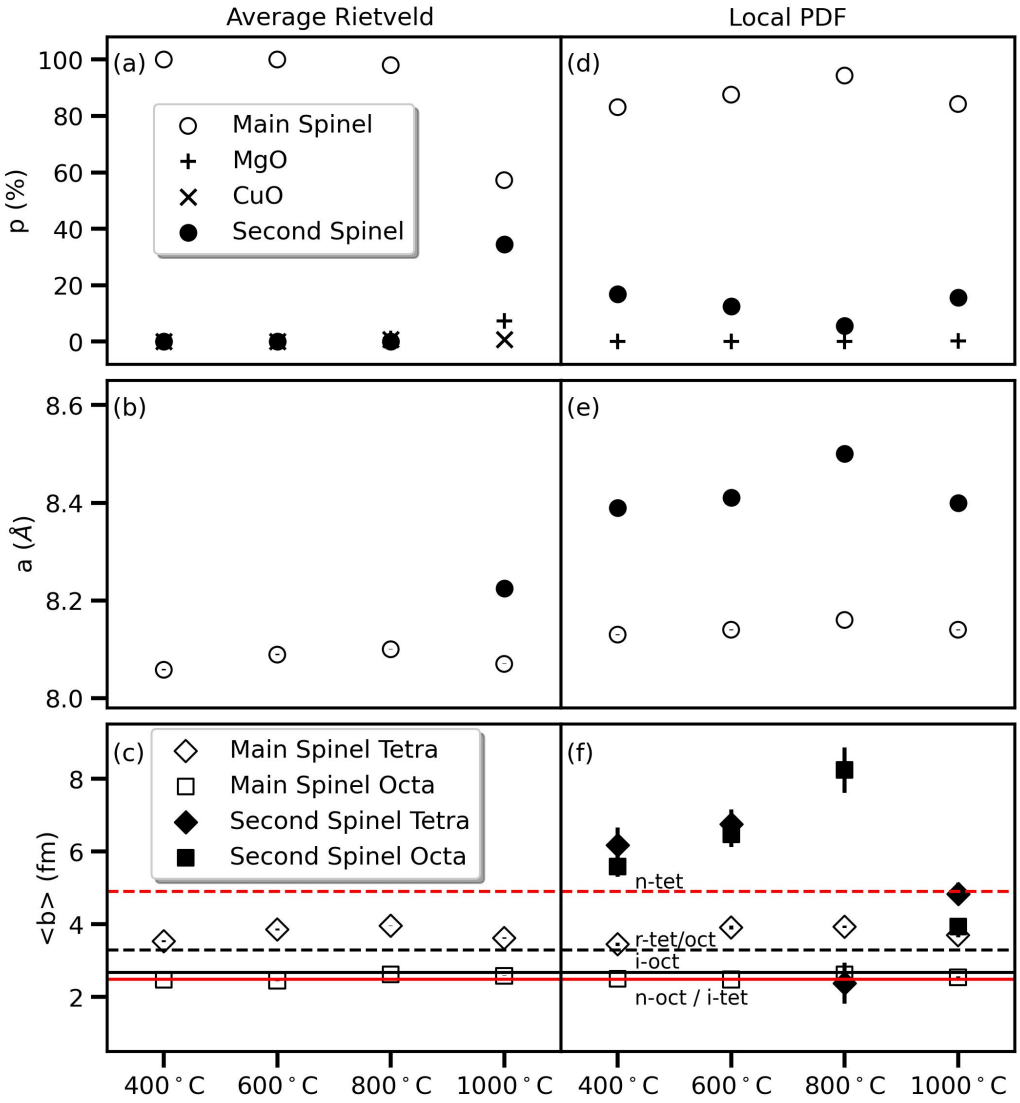


Figure 6.8: Results of modeling neutron diffraction data (a, b, c) and PDF data (d, e, f) for the samples calcined at 400°C, and samples post-annealed at 600°C, 800°C, and 1000°C. (a, d) compares model phase percentages (p, %), (b, e) compares lattice parameters (a, Å), and (c, f) compares average scattering lengths of tetrahedral and octahedral sites obtained from refinement ($\langle b \rangle$, fm). Note that the red dashed line and red solid line indicate the calculated average scattering length on the tetrahedral site (n-tet) and octahedral site (n-oct) of a normal spinel structure, respectively. The red solid line and black solid line indicate the calculated average scattering length on the tetrahedral site (i-tet) and octahedral site (i-oct) with an inverse spinel configuration, respectively. The black dashed line represents the calculated average scattering lengths on both tetrahedral and octahedral sites in a random spinel configuration.

sites for a sample of this composition are indicated with red dashed (normal-tetra), red solid (normal-octa), and black dashed (random) lines in Figure 6.8 (c and f). The refined values fall within this range for all samples. Finally, we note that because site occupancies are underdetermined in this Rietveld analysis, the presence or absence of cation vacancies cannot be disproved.

Analysis of the PDF data over 1-10 Å yields further insight into the presence of distinct short range order (SRO) motifs in the samples. Structure refinement from PDF indicates the presence of the secondary spinel at all sample treatment conditions (Figure 6.8 (d)). This indicates that all samples feature local atomic configurations that resemble the long-range ordered 2-phase state present in the 1000°C sample: however, the amounts and length-scales of the chemically/structurally distinct regions (the extents of SRO) change with post-annealing temperature. The sample post-annealed at 800°C revealed the smallest secondary component fraction in the local structure analysis. The lattice parameters of both the main and secondary spinels model phases used for PDF fits expand with an increase in post-annealing temperature (Figure 6.8 (e)) until the secondary spinel phase segregation is observed at long-range in the sample post-annealed at 1000°C. The refined site-average scattering lengths complement the inference of bulk diffusion and corresponding changes in CSRO obtained from STEM-EDS (Figure 6.3). In the secondary spinel phase model, $\langle b \rangle$ in the octahedral and tetrahedral sites are initially similar and larger than the values $\langle b \rangle$ in the main spinel, but diverge sharply in the post-annealed 800°C state. They return to a similar state in the sample post-annealed at 1000°C (Figure 6.8 (f)). This is consistent with STEM-EDS and FORC, which showed the emergence of a region enriched in Mn and Fe (b_{Mn}= -3.73 fm, b_{Fe} = 9.45 fm) and a large portion of magnetic hard phase in the sample post-treated at 800°C. However, in the sample that is post-annealed at 1000°C, nearly all of the soft phase is coupled to and dominated by an adjacent hard phase. In summary, PDF analysis indicates a continual rearrangement of cation site distribution leading, at post-annealing temperatures above 800°C, to long-range de-mixing and phase segregation.

Local rearrangement of the cation site distribution influences the strength of ferrimagnetism in distinct phases, and phase segregation into coherent or incoherent domains affects bulk magnetism. Illustrative idealized examples of cation distribution in Figure 6.9(a-d) showcase two effects that occur: the site inversion (γ) effect, and the phase segregation effect. The corresponding and distinct calculated magnetic moments (μB) for the models are given in Figure 6.9 (e).

Models (a, b) describe a single-phase normal and random spinel, respectively. Models representing phase segregation are shown in (c, d), generated based on the STEM-EDS map of the sample post-annealed at 1000°C (Figure 6.3 (d)). A normal structure was assumed for $(Mg_{1/3}Cu_{1/3}Zn_{1/3})Co_2O_4$ (c) since Mg and Zn are known to prefer the tetrahedral site and Cu demonstrates a partial preference, while an inverse structure was assumed for $(Co)(Mn_{0.5}Fe_{0.5}Co)O_4$ (d) due to the established preference of Mn^{2+} and Fe^{2+} for the octahedral site.[68]

The average magnetic moment in the random spinel is slightly smaller than for the ordered normal spinel, however phase segregation of a spinel enriched in Mn and Fe results in a large net-enhancement of the average magnetic moment. A region with CSRO similar to this model would present as a hard magnetic phase, as indicated in FORC measurements. In this picture, regions depleted in Fe and Mn (and necessarily enriched in Mg, Cu, and Zn) represent a more soft (frustrated) magnetic phase, where spins are essentially diluted. In that way, the FORC provides valuable insights into the site inversion and local phase segregation effects occurring across the annealing series, supporting the observation of two spinel phases in PDF local structure refinement in all samples and a precipitated second spinel phase at 1000°C via Rietveld refinement.

6.4 Conclusion

In summary, we have followed the magnetic properties, chemical segregation, and phase evolution of a nanostructured metastable compositionally complex spinel oxide

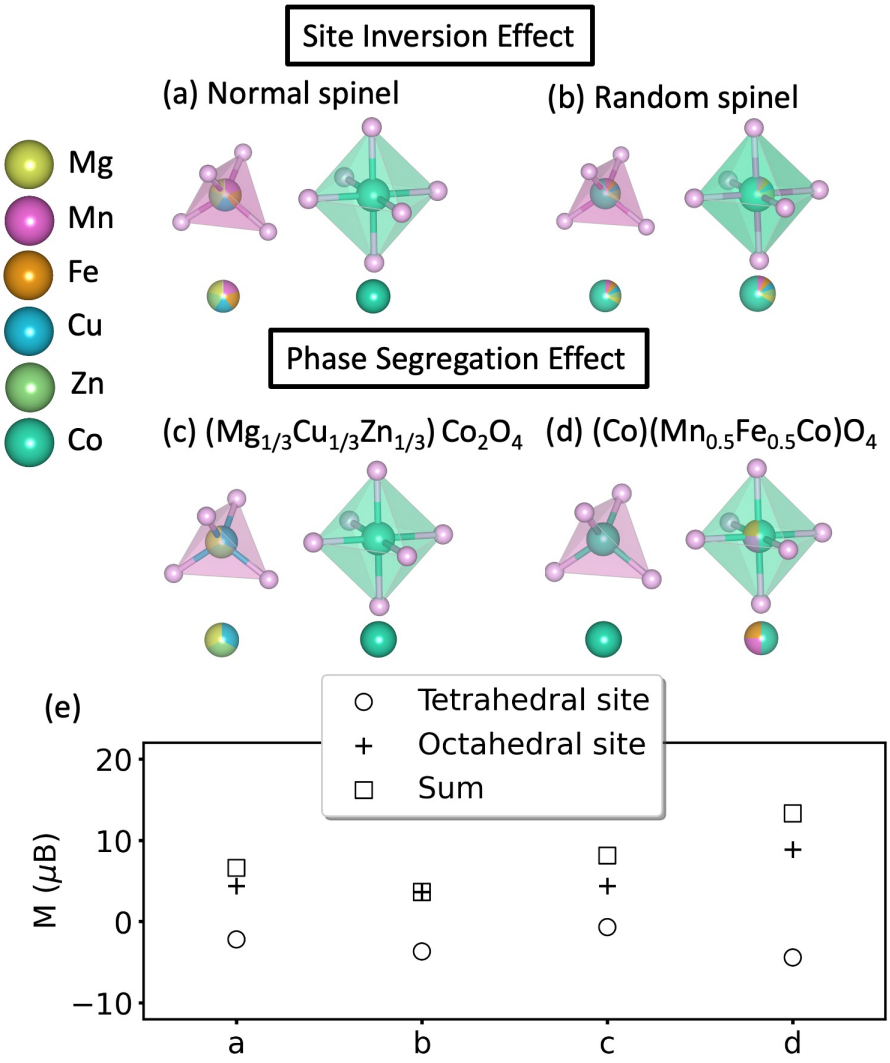


Figure 6.9: Idealized illustrations of cation populations possible within a CCO spinel cobaltite, representing two observed effects: site inversion, represented by a possible (a) normal spinel, and (b) random spinel; and phase segregation, represented with (c) $(Mg_{1/3}Cu_{1/3}Zn_{1/3})Co_2O_4$, and (d) $(Co)(Mn_{0.5}Fe_{0.5}Co)O_4$. (e) Calculated magnetic moments (M) for the models described in (a, b, c, d) on tetrahedral, and octahedral sites as well as the total sum of the magnetic moment.

with chemical composition $(Mg_{0.2}Mn_{0.2}Fe_{0.2}Cu_{0.2}Zn_{0.2})Co_2O_4$, annealed at increasing post-processing temperatures.

To understand the structure-property evolution in this series, the structural features at different length scales must be considered. A combination of FORC, STEM-EDS, and neutron total scattering analyses reveals a two-step process in the structure-property evolution. As synthesized by the LTST route at 400°C, the CCO is a weak room temperature ferrimagnetic, with an approximately random configuration of cations across its tetrahedral and octahedral sites. STEM-EDS reveals enrichment of Mg, Mn, and Fe in certain grains, while FORC analysis supports a random distribution of cations. The first step, activated by post-processing at 600°C, involves local migration of cations from a more random configuration to a more chemically specific arrangement among the tetrahedral and octahedral site occupancies. FORC analysis reveals the presence of soft and hard magnetic phases which are not distinctly evident via STEM-EDS but are consistent with the local structure picture of multiple spinel structures via neutron total scattering. In the second step in samples annealed to 800 °C and above, PDF and FORC analysis indicate the system begins de-mixing into discrete segregated phases. STEM-EDS and neutron diffraction uncover long-range phase segregation of the sample post-annealed at 1000°C. These findings emphasize the sensitivity of FORC analysis in identifying magnetic signatures as unique fingerprints.

The observation of rich complexity and structure-property tunability in a single CCO composition subjected to different post-processing temperatures highlights the great propensity and flexibility of CCOs as platforms in the design of complex functional oxides. In the magnetism space, one could imagine in the future designing bulk hard-soft exchange spring magnets, or exchange bias magnets through the careful selection of involved cations, the degree of local cation mixing, and the propensity of nano-segregated chemical short-range order in complex nanostructured phases.

Finally, this work reveals challenges in quantitatively capturing the crystal-chemical trends in a CCO oxide featuring multiple cation sites, cation site inversion,

and differing degrees of nanoscale chemical short-range order/phase segregation. The combined use of STEM-EDS, neutron diffraction/PDF, and FORC analyses only partially revealed the details of the detected multiple chemically segregated regions in the series. These findings underscore the need for combined characterization and analysis techniques when approaching complexity in CCOs. Further development of advanced characterization techniques for the broader crystal-chemical class of CCOs is warranted.

Chapter 7

Conclusions

The work in this dissertation has demonstrated the structure-property trends of complex functional ceramics (CFCs) can be effectively directed by incorporating varying levels of chemical short range order (CSRO) among their cation/anion arrangements, invoking significant atomic disorder and lattice distortion.

In Chapter 2, CSRO is investigated in the family of perovskite tantalum oxynitrides $ATaO_2N$ (A=Ba, Sr, and Ca) with a combination of neutron total scattering, density functional theory (DFT), and *ab initio* molecular dynamics (AIMD) simulations. Specifically, dielectric properties are examined as a function of A cation size, Ta displacements, octahedral tilting, and local anion ordering across the series. In $BaTaO_2N$, the presence of local N *cis* ordering and the associated Ta off-centering synergistically contribute to stabilizing the local point charge dipole correlations within the TaO_4N_2 octahedra, resulting in its notably high dielectric constant. In contrast, in $SrTaO_2N$ and $CaTaO_2N$, octahedral tilting plays a dominant role in stabilizing the overall system energy, consequently leading to a decrease in the dielectric constants.

In Chapter 3, a family of AFe_2O_4 (where A includes five cations of Mg, Fe, Co, Ni, Cu, Mn, and Zn) was investigated as a case study for understanding the impact of CSRO on the magnetic properties in compositionally complex oxide (CCO) spinels.

Contrary to the conventional expectation of a random cation configuration among high entropy oxide (HEO)s, two of the samples present an average inverse spinel structure, leading to noticeable disparities in apparent bulk magnetization, local magnetic ordering/interactions, and spin collinearity across the series. A competition between crystal field stabilization energy and high configurational entropy lead to specific CSRO motifs, driven by variations in the thermal processing history of the series.

Chapters 4 through 6 of this thesis investigated the phase stability, control of CSRO, and catalytic and magnetic structure-property trends in a novel family of metastable nano compositionally complex ACo_2O_4 spinel oxides (where A includes different combinations of Mn, Fe, Cu, Zn, Mg, and Ni). In Chapter 4, an eco-friendly low-temperature soft-templating (LTST) route was explored to examine the influence of increased compositional complexity and processing parameters on resulting phases. The findings indicate thermal processing variations facilitate different degrees of local and long-range cation diffusion, impacting the extent of cation site inversion, nanoscale heterogeneity, and phase segregation, as well as particle size and particle morphology trends. Additionally, the phase selectivity and the temperature stability window for the CCO spinel series were found to depend strongly upon A-site composition and only modestly on the number of elements (n) present on the A-site. Overall, a high degree of tunability was uncovered through the choice of participating cations and reaction post-annealing conditions.

In Chapter 5, iterations of ACo_2O_4 featuring five A cation combinations of Mn, Fe, Cu, Zn, Mg, and Ni, were studied as bifunctional electrocatalysts for both the oxygen evolution reaction (OER) and oxygen reduction reaction (ORR). Specifically, the sample $(Mn_{0.2}Fe_{0.2}Ni_{0.2}Cu_{0.2}Zn_{0.2})Co_2O_4$, subjected to a post-annealing temperature at 600°C, exhibits an exceptional low overpotential (260 mV at 10 mA cm-2) for OER and excellent onset potential (0.9 V) for ORR compared to current spinel oxide bifunctional electrocatalysts. Post-annealing temperature was seen to influence morphology, particle size, and OER performance across the compositions studied.

Furthermore, the OER activity could be finely tuned by variation in the specific combination of cations present on the A-site. This discovery within materials excluding noble metals and avoiding extreme morphology heralds a new chapter in the exploration of superior multifunctional catalysts with multi-metal configurations.

In Chapter 6, the investigation delved into the sensitivity of the magnetic properties within the CCO composition $(Mg_{0.2}Mn_{0.2}Fe_{0.2}Cu_{0.2}Zn_{0.2})Co_2O_4$, exploring the impact of local chemical segregation and phase evolution introduced by varying post-processing temperatures. A comprehensive methodology encompassing X-ray diffraction, scanning transmission electron microscopy with energy dispersive X-ray spectroscopy (STEM-EDS), first-order reversal curve (FORC) magnetometry, and neutron diffraction/total scattering analyses was employed to understand both average and local structure-property evolution. Careful adjustment of the post-annealing temperature as a synthesis parameter offers fertile ground for controlling the magnetic properties of CCO compounds. This control over local and long-range cation diffusion leads to alterations in the distribution of atoms within the tetrahedral and octahedral sites of the spinel structure, along with inducing nanoscale heterogeneity and magnetic phase separation. Such tailored adjustments offer a promising pathway for further advancements in this field.

The limitations revealed in seeking to precisely determine tetrahedral and octahedral site occupancies of the elements in CCOs with the characterization methods utilized in this dissertation, including X-ray diffraction, neutron diffraction, and neutron total scattering, point to current capability gaps. These findings highlight the importance of future efforts to incorporate additional experimental probes and theoretical approaches. Techniques like hard and soft X-ray absorption near edge spectroscopy (XANES), soft X-ray magnetic circular dichroism (XMCD), and ^{57}Fe Mössbauer spectroscopy (with and without external magnetic field) are recommended as effective tools for investigating local structures. Pursuing materials modeling at multiple length scales, including experimental 'small-box' pair distribution function

(PDF) fits, experimental 'large-box' (RMCProfile) analysis, and theoretical 'large-box' (*ab initio* molecular dynamics, AIMD) analysis have potential to provide valuable insights into cation valence and their corresponding occupancies on tetrahedral and octahedral sites in these spinel CCOs or other complex structure systems in the future.

Multiple material properties are demonstrated to be highly sensitive to the local atomic arrangements and nanoscale heterogeneity induced by thermal processing variations in this work. The research presented in this dissertation underscores the difficulties associated with achieving a true solid solution through optimal (statistically random) cation site mixing. While a homogeneous cation distribution may appear to be present at the microscale or nanoscale in specific phases or particles, it does not guarantee true homogeneity across all material length scales. This emphasizes the critical need for detailed descriptions of reaction conditions and thorough experimental characterization of the crystal-chemical structure from the local to the long-range scale to accurately discern and understand property behaviors. Coupled and advanced structure probes such as X-ray and neutron total scattering and high resolution scanning transmission electron microscopy with energy dispersive X-ray spectroscopy are necessary. Combined theoretical and experimental approaches add great benefits. Material properties are often sensitive and can indicate structural complexity, even when it is not apparent by bulk structure probes. In cases where magnetic cations are under consideration, the FORC method is recommended as a valuable tool for detecting variations in local and long-range order of magnetically active cations.

The research efforts undertaken in this dissertation foster the development of design principles and strategies for fine-tuning the functional properties of CFCs and foreshadow the utilization of CCOs as innovative nanostructured materials, tunable through fine-processing control of diffusion, phase segregation, and particle morphology.

Bibliography

[1] Acedera, R. A. E., Gupta, G., Mamlouk, M., and Balela, M. D. L. (2020). Solution combustion synthesis of porous Co_3O_4 nanoparticles as oxygen evolution reaction (OER) electrocatalysts in alkaline medium. *Journal of Alloys and Compounds*, 836:154919. 5

[2] Aguiar, R., Logvinovich, D., Weidenkaff, A., Rachel, A., Reller, A., and Ebbinghaus, S. G. (2008). The vast colour spectrum of ternary metal oxynitride pigments. *Dyes and Pigments*, 76(1):70–75. 18

[3] Ahmed, M. S., Choi, B., and Kim, Y.-B. (2018). Development of highly active bifunctional electrocatalyst using Co_3O_4 on carbon nanotubes for oxygen reduction and oxygen evolution. *Scientific reports*, 8(1):2543. xxxi, 108, 109, 239

[4] Aijaz, A., Masa, J., Rösler, C., Xia, W., Weide, P., Botz, A. J., Fischer, R. A., Schuhmann, W., and Muhler, M. (2016). $Co@Co_3O_4$ encapsulated in carbon nanotube-grafted nitrogen-doped carbon polyhedra as an advanced bifunctional oxygen electrode. *Angewandte Chemie International Edition*, 55(12):4087–4091. xxxi, 108, 109, 238

[5] Aktekin, B., Massel, F., Ahmadi, M., Valvo, M., Hahlin, M., Zipprich, W., Marzano, F., Duda, L., Younesi, R., Edstrom, K., et al. (2020). How Mn/Ni ordering controls electrochemical performance in high-voltage spinel $LiNi_{0.44}Mn_{1.56}O_4$ with fixed oxygen content. *ACS Applied Energy Materials*, 3(6):6001–6013. 136

[6] Albedwawi, S. H., AlJaberi, A., Haidemenopoulos, G. N., and Polychronopoulou, K. (2021). High entropy oxides-exploring a paradigm of promising catalysts: A review. *Materials & Design*, 202:109534. 4, 49

[7] Algarou, N. A., Slimani, Y., Almessiere, M. A., Baykal, A., Guner, S., Manikandan, A., and Ercan, I. (2020). Enhancement on the exchange coupling behavior of $SrCo_{0.02}Zr_{0.02}Fe_{11.96}O_{19}/MFe_2O_4$ (M=Co, Ni, Cu, Mn, and Zn) as hard/soft magnetic nanocomposites. *Journal of Magnetism and Magnetic Materials*, 499:166308. 137

[8] Ali, S., Ullah, H., AlObaid, A. A., and Al-Muhimeed, T. I. (2021). Crystal field splitting, half metallic ferromagnetism, structural, mechanical and magneto-electronic properties of spinels type structure compounds MgX_2O_4 (X= Fe and Co) for spintronic applications. *The European Physical Journal Plus*, 136(7):1–15. 137

[9] An, T., Ge, X., Hor, T. A., Goh, F. T., Geng, D., Du, G., Zhan, Y., Liu, Z., and Zong, Y. (2015). Co_3O_4 nanoparticles grown on N-doped Vulcan carbon as a scalable bifunctional electrocatalyst for rechargeable zinc-air batteries. *RSC Advances*, 5(92):75773–75780. xxxi, 108, 109, 238

[10] Anu, R. and Vinod, K. (2021). Study of magnetic and optical transitions in MFe_2O_4 (M= Co, Zn, Fe, Mn) with spinel structure. *Nanosystems: physics, chemistry, mathematics*, 12(4):481–491. 52

[11] Aroyo, M. I., Perez-Mato, J. M., Capillas, C., Kroumova, E., Ivantchev, S., Madariaga, G., Kirov, A., and Wondratschek, H. (2006). Bilbao crystallographic server: I. Databases and crystallographic computing programs. *Zeitschrift für Kristallographie-Crystalline Materials*, 221(1):15–27. 26

[12] Attfield, J. P. (2013). Principles and applications of anion order in solid oxynitrides. *Crystal growth & design*, 13(10):4623–4629. 23, 38

[13] Balaz, S., Porter, S. H., Woodward, P. M., and Brillson, L. J. (2013). Electronic structure of tantalum oxynitride perovskite photocatalysts. *Chemistry of Materials*, 25(16):3337–3343. 23

[14] Béjar, J., Álvarez-Contreras, L., Ledesma-García, J., Arjona, N., and Arriaga, L. (2019). Electrocatalytic evaluation of Co_3O_4 and $NiCo_2O_4$ rosettes-like hierarchical spinel as bifunctional materials for oxygen evolution (OER) and reduction (ORR) reactions in alkaline media. *Journal of Electroanalytical Chemistry*, 847:113190. xxxi, 108, 109, 239

[15] Bersuker, I. B. (2001). Modern aspects of the Jahn - Teller effect theory and applications to molecular problems. *Chemical reviews*, 101(4):1067–1114. 19

[16] Bitla, Y., Chin, Y.-Y., Lin, J.-C., Van, C. N., Liu, R., Zhu, Y., Liu, H.-J., Zhan, Q., Lin, H.-J., Chen, C.-T., et al. (2015). Origin of metallic behavior in $NiCo_2O_4$ ferrimagnet. *Scientific reports*, 5(1):1–8. 5, 83, 137

[17] Blöchl, P. E. (1994). Projector augmented-wave method. *Physical review B*, 50(24):17953. 14

[18] Blößer, A., Kurz, H., Timm, J., Wittkamp, F., Simon, C., Hayama, S., Weber, B., Apfel, U.-P., and Marschall, R. (2020). Tailoring the size, inversion parameter, and absorption of phase-pure magnetic $MgFe_2O_4$ nanoparticles for photocatalytic degradations. *ACS Applied Nano Materials*, 3(11):11587–11599. 52

[19] Borges, F., Melo, D., Câmara, M., Martinelli, A., Soares, J., De Araujo, J., and Cabral, F. (2006). Magnetic behavior of nanocrystalline $MnCo_2O_4$ spinels. *Journal of magnetism and magnetic materials*, 302(2):273–277. 5, 83

[20] Bouferrache, K., Charifi, Z., Baaziz, H., Alsaad, A. M., and Telfah, A. (2020). Electronic structure, magnetic and optic properties of spinel compound $NiFe_2O_4$. *Semiconductor Science and Technology*, 35(9):095013. 52

[21] Burdett, J. K. et al. (1995). *Chemical bonding in solids*. Oxford University Press. 19

[22] Camp, P. J., Fuertes, A., and Attfield, J. P. (2012). Subextensive entropies and open order in perovskite oxynitrides. *Journal of the American Chemical Society*, 134(15):6762–6766. 23, 38

[23] Cao, X., Jin, C., Lu, F., Yang, Z., Shen, M., and Yang, R. (2014). Electrochemical properties of $MnCo_2O_4$ spinel bifunctional catalyst for oxygen reduction and evolution reaction. *Journal of The Electrochemical Society*, 161(5):H296. xxxi, 108, 109, 238

[24] Cao, X., Yan, W., Jin, C., Tian, J., Ke, K., and Yang, R. (2015). Surface modification of $MnCo_2O_4$ with conducting polypyrrole as a highly active bifunctional electrocatalyst for oxygen reduction and oxygen evolution reaction. *Electrochimica Acta*, 180:788–794. xxxi, 108, 109, 238

[25] Cervera-Gabalda, L., Zielińska-Jurek, A., and Gómez-Polo, C. (2022). Tuning the photocatalytic performance through magnetization in Co−Zn ferrite nanoparticles. *Journal of Magnetism and Magnetic Materials*, 560:169617. 54

[26] Chakrabarty, S., Mukherjee, A., Su, W.-N., and Basu, S. (2019). Improved bi-functional ORR and OER catalytic activity of reduced graphene oxide supported $ZnCo_2O_4$ microsphere. *International Journal of Hydrogen Energy*, 44(3):1565–1578. xxxi, 108, 109, 239

[27] Chen, H., Qiu, N., Wu, B., Yang, Z., Sun, S., and Wang, Y. (2020a). A new spinel high-entropy oxide $(Mg_{0.2}Ti_{0.2}Zn_{0.2}Cu_{0.2}Fe_{0.2})_3O_4$ with fast reaction kinetics and excellent stability as an anode material for lithium ion batteries. *RSC Advances*, 10(16):9736–9744. 52

[28] Chen, J., Li, H., Pei, Z., Huang, Q., Yuan, Z., Wang, C., Liao, X., Henkelman, G., Chen, Y., and Wei, L. (2020b). Catalytic activity atlas of ternary Co−Fe−V

metal oxides for the oxygen evolution reaction. *Journal of Materials Chemistry A*, 8(31):15951–15961. 117

[29] Chen, T.-Y., Wang, S.-Y., Kuo, C.-H., Huang, S.-C., Lin, M.-H., Li, C.-H., Chen, H.-Y. T., Wang, C.-C., Liao, Y.-F., Lin, C.-C., et al. (2020c). In operando synchrotron X-ray studies of a novel spinel $(Ni_{0.2}Co_{0.2}Mn_{0.2}Fe_{0.2}Ti_{0.2})_3O_4$ high-entropy oxide for energy storage applications. *Journal of Materials Chemistry A*, 8(41):21756–21770. 52

[30] Chen, W., Huang, J., Wei, J., Zhou, D., Cai, J., He, Z.-D., and Chen, Y.-X. (2018). Origins of high onset overpotential of oxygen reduction reaction at Pt-based electrocatalysts: A mini review. *Electrochemistry Communications*, 96:71–76. 108

[31] Chen, X., Han, F., Chen, X., Zhang, C., and Gou, W. (2022). Cerium-doped $CoMn_2O_4$ spinels as highly efficient bifunctional electrocatalysts for ORR/OER reactions. *Catalysts*, 12(10):1122. xxxi, 108, 109, 111, 240

[32] Cheviré, F., Tessier, F., and Marchand, R. (2006). Optical properties of the perovskite solid solution $LaTiO_2N{-}ATiO_3$ (A= Sr, Ba). *European Journal of Inorganic Chemistry*. 18

[33] Cieslak, J., Reissner, M., Berent, K., Dabrowa, J., Stygar, M., Mozdzierz, M., and Zajusz, M. (2021). Magnetic properties and ionic distribution in high entropy spinels studied by Mössbauer and ab initio methods. *Acta Materialia*, 206:116600. 52

[34] Clark, L., Oró-Solé, J., Knight, K. S., Fuertes, A., and Attfield, J. P. (2013). Thermally robust anion-chain order in oxynitride perovskites. *Chemistry of Materials*, 25(24):5004–5011. 23

[35] Clarke, S. J., Hardstone, K. A., Michie, C. W., and Rosseinsky, M. J. (2002). High-temperature synthesis and structures of perovskite and n=1 ruddlesden-popper tantalum oxynitrides. *Chemistry of materials*, 14(6):2664–2669. 31, 32

[36] Coelho, A. A. (2018). TOPAS and TOPAS-academic: an optimization program integrating computer algebra and crystallographic objects written in C^{++}. *Journal of Applied Crystallography*, 51(1):210–218. xxx, 25, 59, 99, 115, 143, 144

[37] Dai, S., Li, M., Wang, X., Zhu, H., Zhao, Y., and Wu, Z. (2021). Fabrication and magnetic property of novel $(Co,Zn,Fe,Mn,Ni)_3O_4$ high-entropy spinel oxide. *Journal of Magnetism and Magnetic Materials*, 536:168123. 52

[38] Danyang, L., Liping, S., Qiang, L., Tian, X., Lihua, H., and Hui, Z. (2022). High-entropy oxide $(Fe_{0.2}Zn_{0.2}Co_{0.2}Ni_{0.2}Cu_{0.2})Fe_2O_4$: an efficient and stable spinel-type electrocatalyst for H_2O_2 production in alkaline media. *Journal of Alloys and Compounds*, 913:165148. 52, 53

[39] Davies, J. E., Hellwig, O., Fullerton, E. E., Denbeaux, G., Kortright, J. B., and Liu, K. (2004). Magnetization reversal of Co/Pt multilayers: Microscopic origin of high-field magnetic irreversibility. *Physical Review B*, 70(22):224434. 69

[40] Deeloed, W., Priamushko, T., Cízek, J., Suramitr, S., and Kleitz, F. (2022). Defect-engineered hydroxylated mesoporous spinel oxides as bifunctional electrocatalysts for oxygen reduction and evolution reactions. *ACS Applied Materials & Interfaces*, 14(20):23307–23321. xxxi, 108, 109, 239

[41] Devaguptapu, S. V., Hwang, S., Karakalos, S., Zhao, S., Gupta, S., Su, D., Xu, H., and Wu, G. (2017). Morphology control of carbon-free spinel $NiCo_2O_4$ catalysts for enhanced bifunctional oxygen reduction and evolution in alkaline media. *ACS Applied Materials & Interfaces*, 9(51):44567–44578. xxxi, 108, 109, 239

[42] Dinnebier, R., , and Billinge, S. (2008). Powder diffraction: theory and practice. 25

[43] Dou, S., Li, X., Tao, L., Huo, J., and Wang, S. (2016). Cobalt nanoparticle-embedded carbon nanotube/porous carbon hybrid derived from MOF-encapsulated

Co_3O_4 for oxygen electrocatalysis. *Chemical Communications*, 52(62):9727–9730. xxxi, 108, 109, 238

[44] Dove, M. T. and Dove, M. T. (2003). *Structure and dynamics: an atomic view of materials*, volume 1. Oxford University Press. 11

[45] Dresp, S. and Strasser, P. (2021). Electro-catalysts for oxygen electrodes in seawater electrolyzers (OER) and reversible electrolyzers (OER/ORR). In *Metal Oxide-Based Nanostructured Electrocatalysts for Fuel Cells, Electrolyzers, and Metal-Air Batteries*, pages 83–103. Elsevier. 107

[46] Dumas, R. K., Li, C.-P., Roshchin, I. V., Schuller, I. K., and Liu, K. (2007). Magnetic fingerprints of sub-100 nm Fe dots. *Physical Review B*, 75(13):134405. 141

[47] Dąbrowa, J., Stygar, M., Mikuła, A., Knapik, A., Mroczka, K., Tejchman, W., Danielewski, M., and Martin, M. (2018). Synthesis and microstructure of the $(Co,Cr,Fe,Mn,Ni)_3O_4$ high entropy oxide characterized by spinel structure. *Materials Letters*, 216:32–36. 4, 52

[48] Egami, T. and Billinge, S. J. (2003). *Underneath the Bragg peaks: structural analysis of complex materials*. Elsevier. 26

[49] El Maazouzi, A., Masrour, R., and Jabar, A. (2020). Thickness-dependent magnetic properties of inverse spinel Fe_3O_4. *Phase Transitions*, 93(7):733–740. 52

[50] Farrow, C. L., Juhas, P., Liu, J. W., Bryndin, D., Božin, E. S., Bloch, J., Proffen, T., and Billinge, S. J. L. (2007). PDFfit2 and PDFgui: computer programs for studying nanostructure in crystals. *Journal of Physics: Condensed Matter*, 19(33):335219. 26, 59

[51] Flegel, S., Möckel, M., and Bennett, J. (2017). Covariance size and the breakdown of gaussianity in GEO uncertainty predictions. In *Proceedings of the 7th European Space Debris Conference*. 61

[52] Flegel, S. K. and Bennett, J. C. (2020). State Uncertainty Normality Detection. *J. Astronaut. Sci.*, 67:1044–1062. 61

[53] Fracchia, M., Manzoli, M., Anselmi-Tamburini, U., and Ghigna, P. (2020). A new eight-cation inverse high entropy spinel with large configurational entropy in both tetrahedral and octahedral sites: Synthesis and cation distribution by X-ray absorption spectroscopy. *Scripta Materialia*, 188:26–31. 52

[54] Frandsen, B. A. and Billinge, S. J. L. (2015). Magnetic structure determination from the magnetic pair distribution function (mPDF): ground state of MnO. *Acta Crystallographica Section A: Foundations and Advances*, 71(3):325–334. 73

[55] Frandsen, B. A., Yang, X., and Billinge, S. J. L. (2014). Magnetic pair distribution function analysis of local magnetic correlations. *Acta Crystallographica Section A: Foundations and Advances*, 70(1):3–11. 73

[56] Franklin, R. E. (1950). The interpretation of diffuse X-ray diagrams of carbon. *Acta crystallographica*, 3(2):107–121. 7

[57] Fu, M., Ma, X., Zhao, K., Li, X., and Su, D. (2021). High-entropy materials for energy-related applications. *Iscience*, 24:102177. 4, 49

[58] Fuertes, A. (2020). Nitride tuning of transition metal perovskites. *APL Materials*, 8(2):020903. 23, 38

[59] Gao, J., Wang, Y., Liu, Y., Hu, X., Ke, X., Zhong, L., He, Y., and Ren, X. (2017). Enhancing dielectric permittivity for energy-storage devices through tricritical phenomenon. *Scientific reports*, 7(1):1–10. 22

[60] Ge, X., Liu, Y., Goh, F. T., Hor, T. A., Zong, Y., Xiao, P., Zhang, Z., Lim, S. H., Li, B., Wang, X., et al. (2014). Dual-phase spinel $MnCo_2O_4$ and spinel $MnCo_2O_4$/nanocarbon hybrids for electrocatalytic oxygen reduction and evolution. *ACS Applied Materials & Interfaces*, 6(15):12684–12691. xxxi, 108, 109, 238, 239

[61] Gilbert, D. A., Liao, J.-W., Wang, L.-W., Lau, J. W., Klemmer, T. J., Thiele, J.-U., Lai, C.-H., and Liu, K. (2014a). Probing the A1 to L1 transformation in FeCuPt using the first order reversal curve method. *APL Materials*, 2(8). 141, 152

[62] Gilbert, D. A., Murray, P. D., De Rojas, J., Dumas, R. K., Davies, J. E., and Liu, K. (2021). Reconstructing phase-resolved hysteresis loops from first-order reversal curves. *Scientific Reports*, 11(1):4018. 58

[63] Gilbert, D. A., Zimanyi, G. T., Dumas, R. K., Winklhofer, M., Gomez, A., Eibagi, N., Vicent, J., and Liu, K. (2014b). Quantitative decoding of interactions in tunable nanomagnet arrays using first order reversal curves. *Scientific Reports*, 4(1):4204. 57, 69, 141

[64] Glazer, A. (1972). The classification of tilted octahedra in perovskites. *Acta Crystallographica Section B: Structural Crystallography and Crystal Chemistry*, 28(11):3384–3392. 19

[65] Goldschmidt, V. M. (1926). Die gesetze der krystallochemie. *Naturwissenschaften*, 14(21):477–485. 19

[66] Gonçalves, J. M., Rocha, D. P., Silva, M. N., Martins, P. R., Nossol, E., Angnes, L., Rout, C. S., and Munoz, R. A. (2021). Feasible strategies to promote the sensing performances of spinel MCo_2O_4 (M= Ni, Fe, Mn, Cu and Zn) based electrochemical sensors: a review. *Journal of Materials Chemistry C*, 9(25):7852–7887. 5, 83

[67] Gorter, E. W. (1950). Magnetization in ferrites: saturation magnetization of ferrites with spinel structure. *Nature*, 165(4203):798–800. 52, 54

[68] Grimes, R. W., Anderson, A. B., and Heuer, A. H. (1989). Predictions of cation distributions in AB_2O_4 spinels from normalized ion energies. *Journal of the American Chemical Society*, 111(1):1–7. 157

[69] Grzesik, Z., Smoła, G., Miszczak, M., Stygar, M., Dąbrowa, J., Zajusz, M., Świerczek, K., and Danielewski, M. (2020). Defect structure and transport properties of $(Co,Cr,Fe,Mn,Ni)_3O_4$ spinel-structured high entropy oxide. *Journal of the European Ceramic Society*, 40(3):835–839. 52

[70] Günther, E., Hagenmayer, R., and Jansen, M. (2000). Strukturuntersuchungen an den oxidnitriden $SrTaO_2N$, $CaTaO_2N$ und $LaTaON_2$ mittels neutronen-und röntgenbeugung. *Zeitschrift für anorganische und allgemeine Chemie*, 626(7):1519–1525. 32

[71] Gurman, S. (1982). EXAFS studies in materials science. *Journal of Materials Science*, 17(6):1541–1570. xv, 12

[72] Ha, Y., Shi, L., Yan, X., Chen, Z., Li, Y., Xu, W., and Wu, R. (2019). Multifunctional electrocatalysis on a porous N-doped $NiCo_2O_4$@ C nanonetwork. *ACS Applied Materials & Interfaces*, 11(49):45546–45553. xxxi, 108, 109, 110, 118, 120, 121, 122

[73] Halasyamani, P. S. and Poeppelmeier, K. R. (1998). Noncentrosymmetric oxides. *Chemistry of Materials*, 10(10):2753–2769. 19

[74] Harada, J. K., Charles, N., Poeppelmeier, K. R., and Rondinelli, J. M. (2019). Heteroanionic materials by design: progress toward targeted properties. *Advanced Materials*, 31(19):1805295. 21

[75] Harada, M., Kotegawa, F., and Kuwa, M. (2022). Structural changes of spinel MCo_2O_4 (M= Mn, Fe, Co, Ni, and Zn) electrocatalysts during the oxygen evolution reaction investigated by in situ X-ray absorption spectroscopy. *ACS Applied Energy Materials*, 5(1):278–294. 129, 137

[76] He, X., Yin, F., Yuan, S., Liu, N., and Huang, X. (2016). Hybrid spinel oxides/n-doped reduced graphene oxide as highly-active bifunctional electrocatalysts for oxygen reduction/evolution reactions. *ChemElectroChem*, 3(7):1107–1115. xxxi, 108, 109, 238

[77] Henze, N. and Zirkler, B. (1990). A class of invariant consistent tests for multivariate normality. *Communications in statistics-Theory and Methods*, 19(10):3595–3617. 61

[78] Higashi, M., Abe, R., Takata, T., and Domen, K. (2009). Photocatalytic overall water splitting under visible light using $ATaO_2N$ (A= Ca, Sr, Ba) and WO_3 in a IO_3^-/I^- shuttle redox mediated system. *Chemistry of Materials*, 21(8):1543–1549. 18

[79] Hinuma, Y., Moriwake, H., Zhang, Y.-R., Motohashi, T., Kikkawa, S., and Tanaka, I. (2012). First-principles study on relaxor-type ferroelectric behavior without chemical inhomogeneity in $BaTaO_2N$ and $SrTaO_2N$. *Chemistry of Materials*, 24(22):4343–4349. xxiv, xxxvii, 23, 27, 28, 41, 217

[80] Hirakawa, T., Shimokawa, Y., Tokuzumi, W., Sato, T., Tsushida, M., Yoshida, H., Hinokuma, S., Ohyama, J., and Machida, M. (2019). Multicomponent spinel oxide solid solutions: a possible alternative to platinum group metal three-way catalysts. *ACS Catalysis*, 9(12):11763–11773. 52

[81] Hitoki, G., Takata, T., Kondo, J. N., Hara, M., Kobayashi, H., and Domen, K. (2002). An oxynitride, TaON, as an efficient water oxidation photocatalyst under visible light irradiation ($\lambda \leq$ 500 nm). *Chemical Communications*, pages 1698–1699. 18

[82] Hocine, K., Cheref, O., Bettine, K., Rached, D., Benalia, S., Rabah, M., Benkhettou, N., and Rached, H. (2020). The structural, electronic, optical and

thermo-electric properties of oxynitride perovskite $CaTaO_2N$. In *Spin*, volume 10, page 2050007. 23

[83] Hosono, A., Sun, S.-K., Masubuchi, Y., and Kikkawa, S. (2016). Additive sintering and post-ammonolysis of dielectric $BaTaO_2N$ oxynitride perovskite. *Journal of the European Ceramic Society*, 36(14):3341–3345. 18, 21

[84] Howard, C. J. and Stokes, H. T. (1998). Group-theoretical analysis of octahedral tilting in perovskites. *Acta Crystallographica Section B: Structural Science*, 54(6):782–789. 19

[85] Howard, C. J. and Stokes, H. T. (2002). Group-theoretical analysis of octahedral tilting in perovskites. *Acta Crystallographica Section B*, 58(3-2):565–565. 19

[86] Huang, Z.-F., Wang, J., Peng, Y., Jung, C.-Y., Fisher, A., and Wang, X. (2017). Design of efficient bifunctional oxygen reduction/evolution electrocatalyst: recent advances and perspectives. *Advanced Energy Materials*, 7(23):1700544. 107, 108, 111

[87] Jansen, M. and Letschert, H.-P. (2000). Inorganic yellow-red pigments without toxic metals. *Nature*, 404(6781):980–982. 18

[88] Jiang, S., Hu, T., Gild, J., Zhou, N., Nie, J., Qin, M., Harrington, T., Vecchio, K., and Luo, J. (2018). A new class of high-entropy perovskite oxides. *Scripta Materialia*, 142:116–120. 4, 49

[89] Jin, C., Lu, F., Cao, X., Yang, Z., and Yang, R. (2013). Facile synthesis and excellent electrochemical properties of $NiCo_2O_4$ spinel nanowire arrays as a bifunctional catalyst for the oxygen reduction and evolution reaction. *Journal of Materials Chemistry A*, 1(39):12170–12177. xxxi, 108, 109, 238

[90] Jin, Z., Lyu, J., Hu, K., Chen, Z., Xie, G., Liu, X., Lin, X., and Qiu, H.-J. (2022). Eight-component nanoporous high-entropy oxides with low Ru contents as

high-performance bifunctional catalysts in Zn-air batteries. *Small*, 18(12):2107207. xxxi, 108, 109, 110, 118, 120

[91] Johnston, H., Black, A. P., Kayser, P., Oró-Solé, J., Keen, D. A., Fuertes, A., and Attfield, J. P. (2018). Dimensional crossover of correlated anion disorder in oxynitride perovskites. *Chemical Communications*, 54(41):5245–5247. 23, 38

[92] Jorge, A. B., Oró-Solé, J., Bea, A. M., Mufti, N., Palstra, T. T., Rodgers, J. A., Attfield, J. P., and Fuertes, A. (2008). Large coupled magnetoresponses in $EuNbO_2N$. *Journal of the American Chemical Society*, 130(38):12572–12573. 18

[93] Jothi, P. R., Liyanage, W., Jiang, B., Paladugu, S., Olds, D., Gilbert, D. A., and Page, K. (2022). Persistent structure and frustrated magnetism in high entropy rare-earth zirconates. *Small*, 18(5):2101323. 5, 83

[94] Kasahara, A., Nukumizu, K., Hitoki, G., Takata, T., Kondo, J. N., Hara, M., Kobayashi, H., and Domen, K. (2002). Photoreactions on $LaTiO_2N$ under visible light irradiation. *The Journal of Physical Chemistry A*, 106(29):6750–6753. 18

[95] Kawano, S., Achiwa, N., Yamamoto, N., and Higashi, S.-n. (1976). Metal-ion distribution and magnetic structure of Fe-substituted cobaltite spinel: $FeCo_2O_4$. *Materials Research Bulletin*, 11(8):911–916. 5, 83

[96] Kaxiras, E. (2003). *Atomic and electronic structure of solids*. 11

[97] Keen, D. A. (2001). A comparison of various commonly used correlation functions for describing total scattering. *Journal of Applied Crystallography*, 34(2):172–177. 7, 60

[98] Khannanov, B. K., Zalessky, V., Golovenchits, E., Sanina, V., Smirnova, T., Shcheglov, M., Bokov, V., and Lushnikov, S. (2020). Separation of phases and charge states in relaxor ferroelectric $PbCo_{1/3}Nb_{2/3}O_3$. *Journal of Experimental and Theoretical Physics*, 130:439–445. 137

[99] Kim, J. S., Kim, B., Kim, H., and Kang, K. (2018). Recent progress on multimetal oxide catalysts for the oxygen evolution reaction. *Advanced Energy Materials*, 8(11):1702774. 111

[100] Kim, Y.-I. (2014). Effects of KCl flux on the morphology, anion composition, and chromaticity of perovskite oxynitrides, $CaTaO_2N$, $SrTaO_2N$, and $LaTaON_2$. *Ceramics International*, 40(4):5275–5281. 18

[101] Kim, Y.-I. and Lee, E. (2011). Constant-wavelength neutron diffraction study of cubic perovskites $BaTaO_2N$ and $BaNbO_2N$. *Journal of the Ceramic Society of Japan*, 119(1389):371–374. 33

[102] Kim, Y.-I., Si, W., Woodward, P. M., Sutter, E., Park, S., and Vogt, T. (2007). Epitaxial thin-film deposition and dielectric properties of the perovskite oxynitride $BaTaO_2N$. *Chemistry of materials*, 19(3):618–623. 18, 21

[103] Kim, Y.-I., Woodward, P. M., Baba-Kishi, K. Z., and Tai, C. W. (2004). Characterization of the structural, optical, and dielectric properties of oxynitride perovskites AMO_2N (A= Ba, Sr, Ca; M= Ta, Nb). *Chemistry of materials*, 16(7):1267–1276. 3, 18, 19, 21, 24, 25, 32

[104] Ko, S.-T., Lee, T., Qi, J., Zhang, D., Peng, W.-T., Wang, X., Tsai, W.-C., Sun, S., Wang, Z., Bowman, W. J., et al. (2023). Compositionally complex perovskite oxides: Discovering a new class of solid electrolytes with interface-enabled conductivity improvements. *Matter*, 6(7):2395–2418. 82

[105] Kotsonis, G. N., Almishal, S. S., Marques dos Santos Vieira, F., Crespi, V. H., Dabo, I., Rost, C. M., and Maria, J.-P. (2023). High-entropy oxides: Harnessing crystalline disorder for emergent functionality. *Journal of the American Ceramic Society*, 106(10):5587–5611. 137

[106] Kresse, G. and Furthmüller, J. (1996). Efficient iterative schemes for ab initio total-energy calculations using a plane-wave basis set. *Physical review B*, 54(16):11169. 28

[107] Kresse, G. and Joubert, D. (1999). From ultrasoft pseudopotentials to the projector augmented-wave method. *Physical review b*, 59(3):1758. 28

[108] Kubo, A., Giorgi, G., and Yamashita, K. (2017). Anion ordering in $CaTaO_2N$: structural impact on the photocatalytic activity. insights from first-principles. *Chemistry of Materials*, 29(2):539–545. 23

[109] Larson, A. and Dreele, R. V. (2000). General structure analysis system (GSAS). *Los Alamos National Laboratory Report LAUR*, pages 86–748. 143

[110] Lavorato, G. C., Das, R., Xing, Y., Robles, J., Litterst, F. J., Baggio-Saitovitch, E., Phan, M.-H., and Srikanth, H. (2020). Origin and shell-driven optimization of the heating power in core/shell bimagnetic nanoparticles. *ACS Applied Nano Materials*, 3(2):1755–1765. 54

[111] Lee, D. U., Kim, B. J., and Chen, Z. (2013). One-pot synthesis of a mesoporous $NiCo_2O_4$ nanoplatelet and graphene hybrid and its oxygen reduction and evolution activities as an efficient bi-functional electrocatalyst. *Journal of Materials Chemistry A*, 1(15):4754–4762. xxxi, 108, 109, 238

[112] Leineweber, A. (2009). Description of anisotropically microstrain-broadened line profiles by Edgeworth series. *Zeitschrift fur Kristallographie*, 224(9):432–445. 98

[113] Leineweber, A. (2010). Composition-induced microstrain broadening: From pattern decomposition to whole powder pattern modelling procedures. *Materials Science Forum*, 651(4):131–153. 98

[114] Leineweber, A. and Mittemeijer, E. J. (2006). Anisotropic microstrain broadening due to compositional inhomogeneities and its parametrisation. *Zeitschrift fur Kristallographie, Supplement*, 1(23):117–122. 98

[115] Li, A., Kong, S., Guo, C., Ooka, H., Adachi, K., Hashizume, D., Jiang, Q., Han, H., Xiao, J., and Nakamura, R. (2022a). Enhancing the stability of cobalt spinel oxide towards sustainable oxygen evolution in acid. *Nature Catalysis*, 5(2):109–118. xxxi, 108, 109

[116] Li, C., Meng, B., Fan, S., Ping, X., Fang, C., Lin, W., Chen, Y., and Zhang, H. (2022b). Rare-earth-tantalate high-entropy ceramics with sluggish grain growth and low thermal conductivity. *Ceramics International*, 48(8):11124–11133. 111

[117] Li, G., Wang, X., Fu, J., Li, J., Park, M. G., Zhang, Y., Lui, G., and Chen, Z. (2016). Pomegranate-inspired design of highly active and durable bifunctional electrocatalysts for rechargeable metal-air batteries. *Angewandte Chemie International Edition*, 55(16):4977–4982. xxxi, 108, 109, 238

[118] Li, H., Zhou, Y., Liang, Z., Ning, H., Fu, X., Xu, Z., Qiu, T., Xu, W., Yao, R., and Peng, J. (2021). High-entropy oxides: Advanced research on electrical properties. *Coatings*, 11(6):628. 4, 49

[119] Li, L., Zhao, J., and Gui, Z. (2004). The thermal sensitivity and dielectric properties of $SrTiO_3$-based ceramics. *Ceramics international*, 30(7):1073–1078. 2

[120] Li, R., Huang, Y., Zhu, D., Ho, W., Lee, S., and Cao, J. (2020). A review of Co_3O_4-based catalysts for formaldehyde oxidation at low temperature: Effect parameters and reaction mechanism. *Aerosol Science and Engineering*, 4(3):147–168. 5, 83

[121] Li, S., Hao, X., Abudula, A., and Guan, G. (2019). Nanostructured Co-based bifunctional electrocatalysts for energy conversion and storage: current status and perspectives. *Journal of Materials Chemistry A*, 7(32):18674–18707. 108, 111, 123

[122] Li, X., Fang, Y., Lin, X., Tian, M., An, X., Fu, Y., Li, R., Jin, J., and Ma, J. (2015). Mof derived Co_3O_4 nanoparticles embedded in N-doped mesoporous carbon layer/MWCNT hybrids: extraordinary bi-functional electrocatalysts for OER and ORR. *Journal of Materials Chemistry A*, 3(33):17392–17402. xxxi, 108, 109, 238

[123] Liang, B., Ai, Y., Wang, Y., Liu, C., Ouyang, S., and Liu, M. (2020). Spinel-type $(FeCoCrMnZn)_3O_4$ high-entropy oxide: facile preparation and supercapacitor performance. *Materials*, 13(24):5798. 52

[124] Liang, J., Liu, J., Wang, H., Li, Z., Cao, G., Zeng, Z., liu, S., Guo, Y., Zeng, M., and Fu, L. (2024). Synthesis of ultrathin high-entropy oxides with phase controllability. *Journal of the American Chemical Society*. 137

[125] Liang, Y., Li, Y., Wang, H., Zhou, J., Wang, J., Regier, T., and Dai, H. (2011). Co_3O_4 nanocrystals on graphene as a synergistic catalyst for oxygen reduction reaction. *Nature materials*, 10(10):780–786. xxxi, 83, 108, 109, 238

[126] Lin, C.-C., Chang, C.-W., Kaun, C.-C., and Su, Y.-H. (2021). Stepwise evolution of photocatalytic spinel-structured $(Co,Cr,Fe,Mn,Ni)_3O_4$ high entropy oxides from first-principles calculations to machine learning. *Crystals*, 11(9):1035. 52

[127] Liu, J., Shao, G., Liu, D., Chen, K., Wang, K., Ma, B., Ren, K., and Wang, Y. (2020). Design and synthesis of chemically complex ceramics from the perspective of entropy. *Materials Today Advances*, 8:100114. 4, 49

[128] Liu, S., Li, L., Ahn, H. S., and Manthiram, A. (2015). Delineating the roles of Co_3O_4 and N-doped carbon nanoweb (CNW) in bifunctional Co_3O_4/CNW catalysts for oxygen reduction and oxygen evolution reactions. *Journal of Materials Chemistry A*, 3(21):11615–11623. xxxi, 108, 109, 238

[129] Liu, W., Bao, J., Xu, L., Guan, M., Wang, Z., Qiu, J., Huang, Y., Xia, J., Lei, Y., and Li, H. (2019). $NiCo_2O_4$ ultrathin nanosheets with oxygen vacancies as

bifunctional electrocatalysts for Zn-air battery. *Applied Surface Science*, 478:552–559. xxxi, 108, 109, 239

[130] Liu, Y., Higgins, D. C., Wu, J., Fowler, M., and Chen, Z. (2013). Cubic spinel cobalt oxide/multi-walled carbon nanotube composites as an efficient bifunctional electrocatalyst for oxygen reaction. *Electrochemistry communications*, 34:125–129. xxxi, 108, 109, 238

[131] Liu, Z.-Q., Cheng, H., Li, N., Ma, T. Y., and Su, Y.-Z. (2016). $ZnCo_2O_4$ quantum dots anchored on nitrogen-doped carbon nanotubes as reversible oxygen reduction/evolution electrocatalysts. *Advanced Materials*, 28(19):3777–3784. xxxi, 108, 109, 239

[132] Lu, Y., Deng, Y., Lu, S., Liu, Y., Lang, J., Cao, X., and Gu, H. (2019). MOF-derived cobalt–nickel phosphide nanoboxes as electrocatalysts for the hydrogen evolution reaction. *Nanoscale*, 11(44):21259–21265. 125

[133] Lu, Y.-T., Chien, Y.-J., Liu, C.-F., You, T.-H., and Hu, C.-C. (2017). Active site-engineered bifunctional electrocatalysts of ternary spinel oxides, $M_{0.1}Ni_{0.9}Co_2O_4$ (M: Mn, Fe, Cu, Zn) for the air electrode of rechargeable zinc-air batteries. *Journal of Materials Chemistry A*, 5(39):21016–21026. xxxi, 108, 109, 111, 120

[134] Luo, T., Shan, X., Zhao, J., Feng, H., Zhang, Q., Yu, H., and Liu, J. (2019). Improvement of quality factor of $SrTiO_3$ dielectric ceramics with high dielectric constant using sm2o3. *Journal of the American Ceramic Society*, 102(7):3849–3853. 2

[135] Ma, J., Zhao, B., Xiang, H., Dai, F.-Z., Liu, Y., Zhang, R., and Zhou, Y. (2022). High-entropy spinel ferrites MFe_2O_4 (M= Mg, Mn, Fe, Co, Ni, Cu, Zn) with tunable electromagnetic properties and strong microwave absorption. *Journal of Advanced Ceramics*, 11(5):754–768. 52, 53

[136] Ma, S., Sun, L., Cong, L., Gao, X., Yao, C., Guo, X., Tai, L., Mei, P., Zeng, Y., Xie, H., et al. (2013). Multiporous $MnCo_2O_4$ microspheres as an efficient bifunctional catalyst for nonaqueous $Li-O_2$ batteries. *The Journal of Physical Chemistry C*, 117(49):25890–25897. xxxi, 108, 109, 238

[137] Mahmood, A., Azam, S., Irfan, M., Kamran, M. A., Alharbi, T., Majid, A., Iqbal, M. W., Muhammad, S., Al-Sehemi, A. G., Khan, S. A., et al. (2020). Cation effect on electronic, optical and thermoelectric properties of perovskite oxynitrides: Density functional theory. *Materials Science in Semiconductor Processing*, 107:104800. 18

[138] Maiyalagan, T., Jarvis, K. A., Therese, S., Ferreira, P. J., and Manthiram, A. (2014). Spinel-type lithium cobalt oxide as a bifunctional electrocatalyst for the oxygen evolution and oxygen reduction reactions. *Nature communications*, 5(1):1–8. 107

[139] Mao, A., Quan, F., Xiang, H.-Z., Zhang, Z.-G., Kuramoto, K., and Xia, A.-L. (2019). Facile synthesis and ferrimagnetic property of spinel $(CoCrFeMnNi)_3O_4$ high-entropy oxide nanocrystalline powder. *Journal of Molecular Structure*, 1194:11–18. 4, 52

[140] Mao, A., Xiang, H.-Z., Zhang, Z.-G., Kuramoto, K., Zhang, H., and Jia, Y. (2020a). A new class of spinel high-entropy oxides with controllable magnetic properties. *Journal of Magnetism and Magnetic Materials*, 497:165884. 52

[141] Mao, A., Xie, H.-X., Xiang, H.-Z., Zhang, Z.-G., Zhang, H., and Ran, S. (2020b). A novel six-component spinel-structure high-entropy oxide with ferrimagnetic property. *Journal of Magnetism and Magnetic Materials*, 503:166594. 52

[142] Marchand, R., Pors, F., Laurent, Y., Regreny, O., Lostec, J., and Haussonne, J. (1986). Perovskites oxynitrurees utilisees en tant que materiaux dielectriques. *Le Journal de Physique Colloques*, 47(C1):C1–901. 18

[143] Mariappan, C., Kumar, R., and Prakash, G. V. (2015). Functional properties of $ZnCo_2O_4$ nano-particles obtained by thermal decomposition of a solution of binary metal nitrates. *RSC Advances*, 5(34):26843–26849. 137

[144] Marik, S., Singh, D., Gonano, B., Veillon, F., Pelloquin, D., and Breard, Y. (2020a). Enhanced magnetic frustration in a new high entropy diamond lattice spinel oxide. *Scripta Materialia*, 186:366–369. 52

[145] Marik, S., Singh, D., Gonano, B., Veillon, F., Pelloquin, D., and Bréard, Y. (2020b). Long range magnetic ordering and magneto-(di) electric effect in a new class of high entropy spinel oxide. *Scripta Materialia*, 183:107–110. 52

[146] Martin, R. M. (2020). *Electronic structure: basic theory and practical methods*. Cambridge University Press. 11

[147] Masoudpanah, S. (2022). Microwave absorption properties of $ZnCo_2O_4$ and $MnCo_2O_4$ powders synthesized by oxalate-assisted hydrothermal method. *Journal of Materials Research and Technology*, 20:3750–3759. 137

[148] Mazza, A. R., Skoropata, E., Sharma, Y., Lapano, J., Heitmann, T. W., Musico, B. L., Keppens, V., Gai, Z., Freeland, J. W., Charlton, T. R., et al. (2022). Designing magnetism in high entropy oxides. *Advanced Science*, 9(10):2200391. 137

[149] McCormack, S. J. and Navrotsky, A. (2021). Thermodynamics of high entropy oxides. *Acta Materialia*, 202:1–21. 4, 49, 82

[150] McDonnell, M. T., Olds, D. P., Page, K. L., Neufeind, J. C., Tucker, M. G., Bilheux, J. C., Zhou, W., and Peterson, P. F. (2017). ADDIE: Advanced diffraction

environment–a software environment for analyzing neutron diffraction data. *Acta Crystallogr., Sect. A: Found. Adv.*, 73:a377. 58

[151] Menezes, P. W., Indra, A., Sahraie, N. R., Bergmann, A., Strasser, P., and Driess, M. (2015). Cobalt–manganese-based spinels as multifunctional materials that unify catalytic water oxidation and oxygen reduction reactions. *ChemSusChem*, 8(1):164–171. xxxi, 108, 109, 238

[152] Mohammadabadi, F. H., Masoudpanah, S. M., Alamolhoda, S., and Koohdar, H. R. (2021). Electromagnetic microwave absorption properties of high entropy spinel ferrite $((MnNiCuZn)_{1-x}Co_xFe_2O_4)$/graphene nanocomposites. *Journal of Materials Research and Technology*, 14:1099–1111. 52, 53

[153] Mohapatra, J., Xing, M., Elkins, J., and Liu, J. P. (2020). Hard and semi-hard magnetic materials based on cobalt and cobalt alloys. *Journal of Alloys and Compounds*, 824:153874. 5, 83, 137

[154] Moriga, T., Ikeuchi, K., Mashima, R., Aoki, D., and Murai, K.-I. (2007). Influence of cation nonstoichiometry on the optical properties of the perovskite-type oxynitride $LaTiO_2N$. *Journal of the Ceramic Society of Japan*, 115(1346):637–639. 18

[155] Mouhib, Y., Belaiche, M., Briche, S., Ferdi, C. A., and Iffer, E. (2018). Elaboration, characterization and first principle studies of $MnCo_2O_4$ nanomaterials prepared from non-standard raw materials. *Materials Research Express*, 6(3):035508. 137

[156] Mousavi, S. (2014). The effect of sintering time on the electrical properties of $CaTiO_3$ ceramics. *Digest J Nanomater Biostruct*, 9(3):1059–1063. 2

[157] Musicó, B., Wright, Q., Ward, T. Z., Grutter, A., Arenholz, E., Gilbert, D., Mandrus, D., and Keppens, V. (2019). Tunable magnetic ordering through cation

selection in entropic spinel oxides. *Physical Review Materials*, 3(10):104416. xvi, 4, 52, 53, 54, 55, 56, 57, 65, 67, 139

[158] Musicó, B. L., Gilbert, D., Ward, T. Z., Page, K., George, E., Yan, J., Mandrus, D., and Keppens, V. (2020). The emergent field of high entropy oxides: Design, prospects, challenges, and opportunities for tailoring material properties. *APL Materials*, 8(4):040912. 4, 49

[159] Nakhowong, R. and Chueachot, R. (2017). Synthesis and magnetic properties of copper cobaltite ($CuCo_2O_4$) fibers by electrospinning. *Journal of Alloys and Compounds*, 715:390–396. 5, 83, 137

[160] Nan, C.-W., Bichurin, M., Dong, S., Viehland, D., and Srinivasan, G. (2008). Multiferroic magnetoelectric composites: Historical perspective, status, and future directions. *Journal of applied physics*, 103(3):031101. 52

[161] Nath, M., De Silva, U., Singh, H., Perkins, M., Liyanage, W. P., Umapathi, S., Chakravarty, S., and Masud, J. (2021). Cobalt telluride: a highly efficient trifunctional electrocatalyst for water splitting and oxygen reduction. *ACS Applied Energy Materials*, 4(8):8158–8174. 121

[162] Navrotsky, A. and Kleppa, O. J. (1967). The thermodynamics of cation distributions in simple spinels. *Journal of Inorganic and nuclear Chemistry*, 29(11):2701–2714. 52

[163] Navrotsky, A. and Kleppa, O. J. (1968). Thermodynamics of formation of simple spinels. *Journal of Inorganic and Nuclear Chemistry*, 30(2):479–498. 52

[164] Neuefeind, J., Feygenson, M., Carruth, J., Hoffmann, R., and Chipley, K. K. (2012). The nanoscale ordered materials diffractometer NOMAD at the spallation neutron source SNS. *Nuclear Instruments and Methods in Physics Research Section B: Beam Interactions with Materials and Atoms*, 287:68–75. 58, 142

[165] Nguyen, T. X., Patra, J., Chang, J.-K., and Ting, J.-M. (2020). High entropy spinel oxide nanoparticles for superior lithiation–delithiation performance. *Journal of Materials Chemistry A*, 8(36):18963–18973. 52

[166] Nosé, S. (1984). A unified formulation of the constant temperature molecular dynamics methods. *The Journal of chemical physics*, 81(1):511–519. 28

[167] Oehler, F. and Ebbinghaus, S. G. (2016). Photocatalytic properties of CoO_x-loaded nano-crystalline perovskite oxynitrides ABO_2N (A= Ca, Sr, Ba, La; B= Nb, Ta). *Solid State Sciences*, 54:43–48. 18

[168] Olds, D., Saunders, C. N., Peters, M., Proffen, T., Neuefeind, J., and Page, K. (2018). Precise implications for real-space pair distribution function modeling of effects intrinsic to modern time-of-flight neutron diffractometers. *Acta Crystallographica Section A: Foundations and Advances*, 74(4):293–307. 7

[169] Orisakwe, E., Marchal, R., Fontaine, B., Gautier, R., and Halet, J.-F. (2016). Structural and electronic structures of alkaline-earth transition metal oxynitride perovskites. *Journal of the Ceramic Society of Japan*, 124(10):1056–1062. 23, 38

[170] Oró-Solé, J., Clark, L., Bonin, W., Attfield, J. P., and Fuertes, A. (2013). Anion-ordered chains in a d_1 perovskite oxynitride: $NdVO_2N$. *Chemical Communications*, 49(24):2430–2432. 19, 23, 38

[171] Oses, C., Toher, C., and Curtarolo, S. (2020). High-entropy ceramics. *Nature Reviews Materials*, 5(4):295–309. 4, 49

[172] Page, K., Stoltzfus, M. W., Kim, Y.-I., Proffen, T., Woodward, P. M., Cheetham, A. K., and Seshadri, R. (2007). Local atomic ordering in $BaTaO_2N$ studied by neutron pair distribution function analysis and density functional theory. *Chemistry of materials*, 19(16):4037–4042. 3, 19, 22, 28, 33, 38, 42, 45

[173] Parida, T., Karati, A., Guruvidyathri, K., Murty, B. S., and Markandeyulu, G. (2020). Novel rare-earth and transition metal-based entropy stabilized oxides with spinel structure. *Scripta Materialia*, 178:513–517. 52, 53

[174] Pelc, D., Spieker, R. J., Anderson, Z., Krogstad, M., Biniskos, N., Bielinski, N., Yu, B., Sasagawa, T., Chauviere, L., Dosanjh, P., et al. (2022). Unconventional short-range structural fluctuations in cuprate superconductors. *Scientific reports*, 12(1):20483. 136

[175] Perdew, J. P., Burke, K., and Ernzerhof, M. (1996). Generalized gradient approximation made simple. *Physical review letters*, 77(18):3865. 28

[176] Perdew, J. P., Ruzsinszky, A., Csonka, G. I., Vydrov, O. A., Scuseria, G. E., Constantin, L. A., Zhou, X., and Burke, K. (2008). Restoring the density-gradient expansion for exchange in solids and surfaces. *Physical review letters*, 100(13):136406. 28

[177] Peterson, P., Gutmann, M., Proffen, T., and Billinge, S. (2000). PDFgetN: a user-friendly program to extract the total scattering structure factor and the pair distribution function from neutron powder diffraction data. *Journal of Applied Crystallography*, 33(4):1192–1192. 25

[178] Phakatkar, A. H., Saray, M. T., Rasul, M. G., Sorokina, L. V., Ritter, T. G., Shokuhfar, T., and Shahbazian-Yassar, R. (2021). Ultrafast synthesis of high entropy oxide nanoparticles by flame spray pyrolysis. *Langmuir*, 37(30):9059–9068. 52

[179] Pike, C. R., Roberts, A. P., and Verosub, K. L. (1999). Characterizing interactions in fine magnetic particle systems using first order reversal curves. *Journal of Applied Physics*, 85(9):6660–6667. 57, 141

[180] Pike, C. R., Ross, C. A., Scalettar, R. T., and Zimanyi, G. (2005). First-order reversal curve diagram analysis of a perpendicular nickel nanopillar array. *Physical Review B*, 71(13):134407. 69, 141

[181] Proffen, T., Egami, T., Billinge, S., Cheetham, A., Louca, D., and Parise, J. (2002). Building a high resolution total scattering powder diffractometer–upgrade of NPD at MLNSC. *Applied Physics A*, 74(1):s163–s165. 24

[182] Qin, M., Vega, H., Zhang, D., Adapa, S., Wright, A. J., Chen, R., and Luo, J. (2022). 21-component compositionally complex ceramics: Discovery of ultrahigh-entropy weberite and fergusonite phases and a pyrochlore-weberite transition. *Journal of Advanced Ceramics*, 11(4):641–655. 82

[183] Radoń, A., Hawełek, Ł., Łukowiec, D., Kubacki, J., and Włodarczyk, P. (2019). Dielectric and electromagnetic interference shielding properties of high entropy (Zn,Fe,Ni,Mg,Cd)Fe_2O_4 ferrite. *Scientific Reports*, 9(1):20078. 52, 53

[184] Ravel, B., Kim, Y., Woodward, P., and Fang, C. (2006). Role of local disorder in the dielectric response of $BaTaO_2N$. *Physical Review B*, 73(18):184121. 19, 46

[185] Retuerto, M., Calle-Vallejo, F., Pascual, L., Lumbeeck, G., Fernandez-Diaz, M. T., Croft, M., Gopalakrishnan, J., Pena, M. A., Hadermann, J., Greenblatt, M., et al. (2019). $La_{1.5}Sr_{0.5}NiMn_{0.5}Ru_{0.5}O_6$ double perovskite with enhanced ORR/OER bifunctional catalytic activity. *ACS Applied Materials & Interfaces*, 11(24):21454–21464. 111

[186] Rietveld, H. M. (1969). A profile refinement method for nuclear and magnetic structures. *Journal of applied Crystallography*, 2(2):65–71. 7

[187] Roberts, A. P., Pike, C. R., and Verosub, K. L. (2000). First-order reversal curve diagrams: A new tool for characterizing the magnetic properties of natural samples. *Journal of Geophysical Research: Solid Earth*, 105(B12):28461–28475. 57, 141, 150

[188] Roncal-Herrero, T., Harrington, J., Zeb, A., Milne, S. J., and Brown, A. P. (2018). Nanoscale compositional segregation and suppression of polar coupling in a relaxor ferroelectric. *Acta Materialia*, 158:422–429. 137

[189] Rost, C. M., Sachet, E., Borman, T., Moballegh, A., Dickey, E. C., Hou, D., Jones, J. L., Curtarolo, S., and Maria, J.-P. (2015). Entropy-stabilized oxides. *Nature communications*, 6(1):1–8. 2, 3, 49

[190] Roth, W. (1964). The magnetic structure of Co_3O_4. *Journal of Physics and Chemistry of Solids*, 25(1):1–10. 137

[191] Sajeev, A., Paul, A. M., Nivetha, R., Gothandapani, K., Gopal, T. S., Jacob, G., Muthuramamoorty, M., Pandiaraj, S., Alodhayb, A., Kim, S. Y., et al. (2022). Development of cu3n electrocatalyst for hydrogen evolution reaction in alkaline medium. *Scientific Reports*, 12(1):2004. 127

[192] Sakayori, K.-i., Matsui, Y., Abe, H., Nakamura, E., Kenmoku, M., Hara, T., Ishikawa, D., Kokubu, A., Hirota, K.-i., and Ikeda, T. I. T. (1995). Curie temperature of $BaTiO_3$. *Japanese journal of applied physics*, 34(9S):5443. 2

[193] Salian, A. and Mandal, S. (2021). Entropy stabilized multicomponent oxides with diverse functionality–a review. *Critical Reviews in Solid State and Materials Sciences*, 47:142. 4, 49

[194] Sanchez-Lievanos, K. R., Stair, J. L., and Knowles, K. E. (2021). Cation distribution in spinel ferrite nanocrystals: Characterization, impact on their physical properties, and opportunities for synthetic control. *Inorganic Chemistry*, 60(7):4291–4305. PMID: 33734686. 54

[195] Sarkar, A., Breitung, B., and Hahn, H. (2020). High entropy oxides: the role of entropy, enthalpy and synergy. *Scripta Materialia*, 187:43–48. 4, 49, 82

[196] Sarkar, A., Djenadic, R., Usharani, N. J., Sanghvi, K. P., Chakravadhanula, V. S., Gandhi, A. S., Hahn, H., and Bhattacharya, S. S. (2017). Nanocrystalline

multicomponent entropy stabilised transition metal oxides. *Journal of the European Ceramic Society*, 37(2):747–754. 83

[197] Sarkar, A., Eggert, B., Witte, R., Lill, J., Velasco, L., Wang, Q., Sonar, J., Ollefs, K., Bhattacharya, S. S., Brand, R. A., et al. (2021a). Comprehensive investigation of crystallographic, spin-electronic and magnetic structure of $(Co_{0.2}Cr_{0.2}Fe_{0.2}Mn_{0.2}Ni_{0.2})_3O_4$: Unraveling the suppression of configuration entropy in high entropy oxides. *Acta Materialia*, 226:117581. 52, 54, 63

[198] Sarkar, A., Kruk, R., and Hahn, H. (2021b). Magnetic properties of high entropy oxides. *Dalton Transactions*, 50(6):1973–1982. 50, 137, 139

[199] Sarkar, A., Wang, Q., Schiele, A., Chellali, M. R., Bhattacharya, S. S., Wang, D., Brezesinski, T., Hahn, H., Velasco, L., and Breitung, B. (2019). High-entropy oxides: fundamental aspects and electrochemical properties. *Advanced Materials*, 31(26):1806236. 4, 49, 82

[200] Selima, S. S., Khairy, M., and Mousa, M. A. (2019). Comparative studies on the impact of synthesis methods on structural, optical, magnetic and catalytic properties of $CuFe_2O_4$. *Ceramics International*, 45(5):6535–6540. 52

[201] Serov, A., Andersen, N. I., Roy, A. J., Matanovic, I., Artyushkova, K., and Atanassov, P. (2015). $CuCo_2O_4$ ORR/OER bi-functional catalyst: influence of synthetic approach on performance. *Journal of The Electrochemical Society*, 162(4):F449. xxxi, 108, 109, 239

[202] Shannon, R. D. (1993). Dielectric polarizabilities of ions in oxides and fluorides. *Journal of Applied physics*, 73(1):348–366. 18

[203] Sharifianjazi, F., Moradi, M., Parvin, N., Nemati, A., Rad, A. J., Sheysi, N., Abouchenari, A., Mohammadi, A., Karbasi, S., Ahmadi, Z., et al. (2020). Magnetic $CoFe_2O_4$ nanoparticles doped with metal ions: a review. *Ceramics International*, 46(11):18391–18412. 52

[204] Shaw, S. K., Gangwar, A., Sharma, A., Alla, S. K., Kavita, S., Vasundhara, M., Meena, S. S., Maiti, P., and Prasad, N. K. (2021). Structural and magnetic properties of nanocrystalline equi-atomic spinel high-entropy oxide $(AlCoFeMnNi)_3O_4$ synthesised by microwave assisted co-precipitation technique. *Journal of Alloys and Compounds*, 878:160269. 52

[205] Shetgaonkar, S. S., Salkar, A. V., and Morajkar, P. P. (2021). Advances in electrochemical and catalytic performance of nanostructured $FeCo_2O_4$ and its composites. *Chemistry–An Asian Journal*, 16(19):2871–2895. 5, 83

[206] Shi, Y., Jiang, P., Wang, S., Chen, W., Wei, B., Lu, X., Qian, G., Kan, W. H., Chen, H., Yin, W., et al. (2022). Slight compositional variation-induced structural disorder-to-order transition enables fast Na^+ storage in layered transition metal oxides. *Nature Communications*, 13(1):7888. 137

[207] Sholl, D. S. and Steckel, J. A. (2022). *Density functional theory: a practical introduction*. John Wiley & Sons. 11

[208] Singh, H., Liyanage, W. P., and Nath, M. (2022a). Carbon nanotube encapsulated metal selenide nanostructures for efficient electrocatalytic oxygen evolution reaction. *Chemical Communications*, 58(60):8360–8363. 121

[209] Singh, H., Marley-Hines, M., Chakravarty, S., and Nath, M. (2022b). Multi-walled carbon nanotube supported manganese selenide as a highly active bifunctional OER and ORR electrocatalyst. *Journal of Materials Chemistry A*, 10(12):6772–6784. 121, 122

[210] Song, J., Shin, D. W., Lu, Y., Amos, C. D., Manthiram, A., and Goodenough, J. B. (2012). Role of oxygen vacancies on the performance of $L[Ni_{0.5-x}Mn_{1.5+x}]O_4$ (x= 0, 0.05, and 0.08) spinel cathodes for lithium-ion batteries. *Chemistry of Materials*, 24(15):3101–3109. 94

[211] Song, Q. and Zhang, Z. J. (2004). Shape control and associated magnetic properties of spinel cobalt ferrite nanocrystals. *Journal of the American Chemical Society*, 126(19):6164–6168. 139

[212] Song, W., Ren, Z., Chen, S.-Y., Meng, Y., Biswas, S., Nandi, P., Elsen, H. A., Gao, P.-X., and Suib, S. L. (2016). Ni-and Mn-promoted mesoporous Co_3O_4: a stable bifunctional catalyst with surface-structure-dependent activity for oxygen reduction reaction and oxygen evolution reaction. *ACS Applied Materials & Interfaces*, 8(32):20802–20813. xxxi, 108, 109, 239

[213] Song, Z. and Liu, Q. (2020). Tolerance factor and phase stability of the normal spinel structure. *Crystal Growth & Design*, 20(3):2014–2018. 90

[214] Speight, J. G. (2017). *Lange's handbook of chemistry*. McGraw-Hill Education. 92

[215] Spurling, R. J., Lass, E. A., Wang, X., and Page, K. (2022). Entropy-driven phase transitions in complex ceramic oxides. *Physical Review Materials*, 6(9):090301. 82

[216] Stamenkovic, V. R., Fowler, B., Mun, B. S., Wang, G., Ross, P. N., Lucas, C. A., and Markovic, N. M. (2007). Improved oxygen reduction activity on Pt_3Ni (111) via increased surface site availability. *science*, 315(5811):493–497. 108

[217] Stygar, M., Dąbrowa, J., Moździerz, M., Zajusz, M., Skubida, W., Mroczka, K., Berent, K., Świerczek, K., and Danielewski, M. (2020). Formation and properties of high entropy oxides in Co−Cr−Fe−Mg−Mn−Ni−O system: Novel $(Cr,Fe,Mg,Mn,Ni)_3O_4$ and $(Co,Cr,Fe,Mg,Mn)_3O_4$ high entropy spinels. *Journal of the European Ceramic Society*, 40(4):1644–1650. 52

[218] Su, Y., Liu, H., Li, C., Liu, J., Song, Y., and Wang, F. (2019). Hydrothermal-assisted defect engineering in spinel Co_3O_4 nanostructures as bifunctional catalysts for oxygen electrode. *Journal of Alloys and Compounds*, 799:160–168. 5

[219] Sugimoto, M. (1999). The past, present, and future of ferrites. *Journal of the American Ceramic Society*, 82(2):269–280. 52

[220] Sun, S.-K., Zhang, Y.-R., Masubuchi, Y., Motohashi, T., and Kikkawa, S. (2014). Additive sintering, postannealing, and dielectric properties of $SrTaO_2N$. *Journal of the American Ceramic Society*, 97(4):1023–1027. 21

[221] Sun, Y. and Dai, S. (2021). High-entropy materials for catalysis: A new frontier. *Science Advances*, 7(20):eabg1600. 4, 49

[222] Tahir, M., Pan, L., Idrees, F., Zhang, X., Wang, L., Zou, J.-J., and Wang, Z. L. (2017). Electrocatalytic oxygen evolution reaction for energy conversion and storage: a comprehensive review. *Nano Energy*, 37:136–157. 108, 118

[223] Takeuchi, T., Betourne, E., Tabuchi, M., Kageyama, H., Kobayashi, Y., Coats, A., Morrison, F., Sinclair, D., and West, A. (1999). Dielectric properties of spark-plasma-sintered $BaTiO_3$. *Journal of materials science*, 34(5):917–924. 2

[224] Teng, Z., Zhu, L., Tan, Y., Zeng, S., Xia, Y., Wang, Y., and Zhang, H. (2020). Synthesis and structures of high-entropy pyrochlore oxides. *Journal of the European Ceramic Society*, 40(4):1639–1643. 4, 49

[225] Trujillo-Ortiz, A., Hernandez-Walls, R., Barba-Rojo, K., and Cupul-Magana, L. (2007). Hzmvntest: Henze-zirkler's multivariate normality test. *A MATLAB file*, pages 81–83. 61

[226] Tucker, M. G., Keen, D. A., Dove, M. T., Goodwin, A. L., and Hui, Q. (2007). RMCProfile: reverse monte carlo for polycrystalline materials. *Journal of Physics: Condensed Matter*, 19(33):335218. 26, 60

[227] Usharani, N. J., Sanghavi, H., and Bhattacharya, S. S. (2021). Factors influencing phase formation and band gap studies of a novel multicomponent high entropy $(Co,Cu,Mg,Ni,Zn)_2TiO_4$ orthotitanate spinel. *Journal of Alloys and Compounds*, 888:161390. 52

[228] Vayer, F., Decorse, C., Berardan, D., and Dragoe, N. (2021). New entropy-stabilized oxide with pyrochlore structure: $Dy_2(Ti_{0.2}Zr_{0.2}Hf_{0.2}Ge_{0.2}Sn_{0.2})_2O_7$. *Journal of Alloys and Compounds*, 883:160773. 111

[229] Vega, H., Qin, M., and Luo, J. (2023). Thermodynamics of dual-phase compositionally complex ceramics: A case study of ultrahigh-entropy fluorite-bixbyite refractory oxides. *Journal of the European Ceramic Society*, 43(5):2104–2114. 82

[230] Venturini, J., Tonelli, A. M., Wermuth, T. B., Zampiva, R. Y. S., Arcaro, S., Viegas, A. D. C., and Bergmann, C. P. (2019). Excess of cations in the sol-gel synthesis of cobalt ferrite ($CoFe_2O_4$): A pathway to switching the inversion degree of spinels. *Journal of Magnetism and Magnetic Materials*, 482:1–8. 52

[231] Verwey, E. J. W. and Heilmann, E. L. (1947). Physical properties and cation arrangement of oxides with spinel structures I. Cation arrangement in spinels. *The Journal of Chemical Physics*, 15(4):174–180. 52

[232] Vinnik, D. A., Trofimov, E. A., and Zhivulin, V. E. (2020a). The conditions and results of ferrite based on multicomponent crystal formation in high entropic oxide systems. In *Solid State Phenomena*, volume 299, pages 246–251. Trans Tech Publ. 52

[233] Vinnik, D. A., Trofimov, E. A., Zhivulin, V. E., Gudkova, S. A., Zaitseva, O. V., Zherebtsov, D. A., Starikov, A. Y., Sherstyuk, D. P., Amirov, A. A., Kalgin, A. V., et al. (2020b). High entropy oxide phases with perovskite structure. *Nanomaterials*, 10(2):268. 4, 49

[234] Wang, B., Wang, C., Yu, X., Cao, Y., Gao, L., Wu, C., Yao, Y., Lin, Z., and Zou, Z. (2022a). General synthesis of high-entropy alloy and ceramic nanoparticles in nanoseconds. *Nature Synthesis*, 1(2):138–146. 5, 83

[235] Wang, C.-H., Kennedy, B. J., Menezes de Oliveira, A. L., Polt, J., and Knight, K. S. (2017a). The impact of anion ordering on octahedra distortion and phase transitions in $SrTaO_2N$ and $BaTaO_2N$. *Acta Crystallographica Section B: Structural Science, Crystal Engineering and Materials*, 73(3):389–398. 23

[236] Wang, D., Jiang, S., Duan, C., Mao, J., Dong, Y., Dong, K., Wang, Z., Luo, S., Liu, Y., and Qi, X. (2020a). Spinel-structured high entropy oxide $(FeCoNiCrMn)_3O_4$ as anode towards superior lithium storage performance. *Journal of Alloys and Compounds*, 844:156158. 52

[237] Wang, D., Liu, Z., Du, S., Zhang, Y., Li, H., Xiao, Z., Chen, W., Chen, R., Wang, Y., Zou, Y., and Wang, S. (2019). Low-temperature synthesis of small-sized high-entropy oxides for water oxidation. *Journal of Materials Chemistry A*, 7(42):24211–24216. 52, 83

[238] Wang, G., Qin, J., Feng, Y., Feng, B., Yang, S., Wang, Z., Zhao, Y., and Wei, J. (2020b). Sol–gel synthesis of spherical mesoporous high-entropy oxides. *ACS Applied Materials & Interfaces*, 12(40):45155–45164. 52, 83

[239] Wang, J., Wu, Z., Han, L., Lin, R., Xin, H. L., and Wang, D. (2016). Hollow-structured carbon-supported nickel cobaltite nanoparticles as an efficient bifunctional electrocatalyst for the oxygen reduction and evolution reactions. *ChemCatChem*, 8(4):736–742. xxxi, 108, 109, 238

[240] Wang, S., Lu, A., and Zhong, C.-J. (2021a). Hydrogen production from water electrolysis: role of catalysts. *Nano Convergence*, 8:1–23. 108

[241] Wang, S.-F., Wang, Y.-R., Wu, Y.-C., and Liu, Y.-J. (2009). Densification, microstructural evolution, and dielectric properties of hexagonal $Ba(Ti_{1-x}Mn_x)O_3$ ceramics sintered with fluxes. *Journal of alloys and compounds*, 480(2):499–504. 2

[242] Wang, W., Kuai, L., Cao, W., Huttula, M., Ollikkala, S., Ahopelto, T., Honkanen, A.-P., Huotari, S., Yu, M., and Geng, B. (2017b). Mass-production of

mesoporous $MnCo_2O_4$ spinels with manganese (IV)-and cobalt (II)-rich surfaces for superior bifunctional oxygen electrocatalysis. *Angewandte Chemie*, 129(47):15173–15177. xxxi, 108, 109, 239

[243] Wang, X., Jiang, B., Zhang, Y., Kim, Y.-I., and Page, K. (2021b). Influence of cation size on the local atomic structure and electronic properties of Ta perovskite oxynitrides. *Inorganic Chemistry*, 60(18):14190–14201. 15, 18

[244] Wang, X., Li, Y., Jin, T., Meng, J., Jiao, L., Zhu, M., and Chen, J. (2017c). Electrospun thin-walled $CuCo_2O_4$@C nanotubes as bifunctional oxygen electrocatalysts for rechargeable Zn–air batteries. *Nano letters*, 17(12):7989–7994. xxxi, 108, 109, 239

[245] Wang, X., Metz, P., Calì, E., Jothi, P. R., Lass, E. A., and Page, K. (2023). Phase selectivity and stability in compositionally complex nano $(nA_{1/n})Co_2O_4$. *Chemistry of Materials*, 35(17):7283–7291. xx, 15, 81, 111, 113, 115, 128, 131, 137, 139, 140, 146, 240

[246] Wang, X., Musicó, B. L., Kons, C., Metz, P. C., Keppens, V., Gilbert, D. A., Zhang, Y., and Page, K. (2022b). Local cation order and ferrimagnetism in compositionally complex spinel ferrites. *APL Materials*, 10(12):121102. 15, 49, 84, 101, 139, 144

[247] Wang, X., Singh, H., Nath, M., Lagemann, K., and Page, K. (2024). Excellent bifunctional oxygen evolution and reduction electrocatalysts $(5\,A_{1/5})Co_2O_4$ and their tunability. *ACS Materials Au*. 16, 107, 139

[248] Wang, X., Zuo, Y., Horta, S., He, R., Yang, L., Ostovari Moghaddam, A., Ibáñez, M., Qi, X., and Cabot, A. (2022c). Cofenimnznb as a high-entropy metal boride to boost the oxygen evolution reaction. *ACS Applied Materials & Interfaces*, 14(42):48212–48219. 127

[249] Wang, Y., Zheng, X., and Wang, D. (2022d). Design concept for electrocatalysts. *Nano Research*, pages 1–23. 107

[250] Wang, Z., Huang, J., Wang, L., Liu, Y., Liu, W., Zhao, S., and Liu, Z.-Q. (2022e). Cation-tuning induced d-band center modulation on Co-based spinel oxide for oxygen reduction/evolution reaction. *Angewandte Chemie International Edition*, 61(16):e202114696. xxxi, 108, 109, 115, 239

[251] Welberry, T. R. and Weber, T. (2016). One hundred years of diffuse scattering. *Crystallography Reviews*, 22(1):2–78. 6

[252] Windiks, R. and Delley, B. (2003). Massive thermostatting in isothermal density functional molecular dynamics simulations. *The Journal of chemical physics*, 119(5):2481–2487. 28

[253] Withers, R., Liu, Y., Woodward, P., and Kim, Y.-I. (2008). Structurally frustrated polar nanoregions in $BaTaO_2N$ and the relationship between its high dielectric permittivity and that of $BaTiO_3$. *Applied Physics Letters*, 92(10):102907. 22

[254] Witte, R., Sarkar, A., Kruk, R., Eggert, B., Brand, R. A., Wende, H., and Hahn, H. (2019). High-entropy oxides: An emerging prospect for magnetic rare-earth transition metal perovskites. *Physical Review Materials*, 3(3):034406. 4, 49

[255] Witte, R., Sarkar, A., Velasco, L., Kruk, R., Brand, R. A., Eggert, B., Ollefs, K., Weschke, E., Wende, H., and Hahn, H. (2020). Magnetic properties of rare-earth and transition metal based perovskite type high entropy oxides. *Journal of Applied Physics*, 127(18):185109. 4, 49

[256] Wolff, H. and Dronskowski, R. (2008). First-principles and molecular-dynamics study of structure and bonding in perovskite-type oxynitrides ABO_2N (A= Ca, Sr, Ba; chemformulaunknown-optionb= Ta, Nb). *Journal of computational chemistry*, 29(13):2260–2267. xvii, 23, 217

[257] Woodward, P. M. (1997a). Octahedral tilting in perovskites. I. geometrical considerations. *Acta Crystallographica Section B: Structural Science*, 53(1):32–43. 19

[258] Woodward, P. M. (1997b). Octahedral tilting in perovskites. II. structure stabilizing forces. *Acta Crystallographica Section B: Structural Science*, 53(1):44–66. 19

[259] Wright, A. J. and Luo, J. (2020). A step forward from high-entropy ceramics to compositionally complex ceramics: a new perspective. *Journal of Materials Science*, 55(23):9812–9827. 2, 82

[260] Wright, A. J., Wang, Q., Hu, C., Yeh, Y.-T., Chen, R., and Luo, J. (2021). Single-phase duodenary high-entropy fluorite/pyrochlore oxides with an order-disorder transition. *Acta Materialia*, 211:116858. 82

[261] Wright, A. J., Wang, Q., Huang, C., Nieto, A., Chen, R., and Luo, J. (2020a). From high-entropy ceramics to compositionally-complex ceramics: A case study of fluorite oxides. *Journal of the European Ceramic Society*, 40(5):2120–2129. 82

[262] Wright, A. J., Wang, Q., Ko, S.-T., Chung, K. M., Chen, R., and Luo, J. (2020b). Size disorder as a descriptor for predicting reduced thermal conductivity in medium-and high-entropy pyrochlore oxides. *Scripta Materialia*, 181:76–81. 82

[263] Wright, A. J., Wang, Q., Yeh, Y.-T., Zhang, D., Everett, M., Neuefeind, J., Chen, R., and Luo, J. (2022). Short-range order and origin of the low thermal conductivity in compositionally complex rare-earth niobates and tantalates. *Acta Materialia*, page 118056. 82

[264] Wu, P.-C., Huang, R., Hsieh, Y.-H., Wang, B., Yen, M., Ho, S.-Z., Kumamoto, A., Zhong, C., Song, H., Chen, Y.-C., et al. (2019). Electrical polarization induced by atomically engineered compositional gradient in complex oxide solid solution. *NPG Asia Materials*, 11(1):17. 137

[265] Wu, R., Sun, J., Xu, C., and Chen, H. (2021). $MgCo_2O_4$-based electrode materials for electrochemical energy storage and conversion: a comprehensive review. *Sustainable Energy & Fuels*. 5, 83

[266] Xia, W., Mahmood, A., Liang, Z., Zou, R., and Guo, S. (2016). Earth-abundant nanomaterials for oxygen reduction. *Angewandte Chemie International Edition*, 55(8):2650–2676. 108

[267] Xiang, H., Xing, Y., Dai, F.-z., Wang, H., Su, L., Miao, L., Zhang, G., Wang, Y., Qi, X., Yao, L., et al. (2021a). High-entropy ceramics: Present status, challenges, and a look forward. *Journal of Advanced Ceramics*, 10:385. 4, 49

[268] Xiang, H.-Z., Xie, H.-X., Chen, Y.-X., Zhang, H., Mao, A., and Zheng, C.-H. (2021b). Porous spinel-type $(Al_{0.2}CoCrFeMnNi)_{0.58}O_{4-\delta}$ high-entropy oxide as a novel high-performance anode material for lithium-ion batteries. *Journal of Materials Science*, 56(13):8127–8142. 52

[269] Xiang, H.-Z., Xie, H.-X., Mao, A., Jia, Y.-G., and Si, T.-Z. (2020). Facile preparation of single phase high-entropy oxide nanocrystalline powders by solution combustion synthesis. *International Journal of Materials Research*, 111(3):246–249. 52

[270] Xu, C., Lu, M., Zhan, Y., and Lee, J. Y. (2014). A bifunctional oxygen electrocatalyst from monodisperse $MnCo_2O_4$ nanoparticles on nitrogen enriched carbon nanofibers. *RSC Advances*, 4(48):25089–25092. xxxi, 108, 109, 238

[271] Xu, C., Reeves, P. J., Jacquet, Q., and Grey, C. P. (2021). Phase behavior during electrochemical cycling of Ni-rich cathode materials for Li-ion batteries. *Advanced Energy Materials*, 11(7):2003404. 137

[272] Xu, H., Jin, S., Lee, S., and Brown, P. E. (2023). Cation ordering, twinning, and pseudo-symmetry in silicate garnet: The study of a birefringent garnet with orthorhombic structure. *American Mineralogist*, 108(3):572–583. 137

[273] Xu, L., Zhen, C., Shui, Z., Xu, D., Liu, L., Ma, L., Zhao, D., and Hou, D. (2022). Jahn–Taller distortion on exchange interactions between cations in $Mn_xCu_{1-x}Co_2O_4$ system. *Journal of Physics D: Applied Physics*, 55(43):435003. 139

[274] Xu, N., Liu, Y., Zhang, X., Li, X., Li, A., Qiao, J., and Zhang, J. (2016). Self-assembly formation of bi-functional Co_3O_4/MnO_2-CNTs hybrid catalysts for achieving both high energy/power density and cyclic ability of rechargeable zinc-air battery. *Scientific Reports*, 6(1):1–10. xxxi, 108, 109, 238

[275] Xu, X. and Jiang, H. (2019). First-principles investigation on anion order, electronic structure and dielectric properties of $BaTaO_2N$. *Journal of Materials Chemistry A*, 7(24):14583–14591. 21

[276] Xu, X. and Jiang, H. (2020). Anion order in perovskite oxynitrides AMO_2N (A= Ba, Sr, Ca; M= Ta, Nb): a first-principles based investigation. *RSC Advances*, 10(41):24410–24418. 19, 21, 23

[277] Yagi, S., Ichikawa, Y., Yamada, I., Doi, T., Ichitsubo, T., and Matsubara, E. (2013). Synthesis of binary magnesium–transition metal oxides via inverse coprecipitation. *Japanese journal of applied physics*, 52(2R):025501. 83

[278] Yamasita, D., Takata, T., Hara, M., Kondo, J. N., and Domen, K. (2004). Recent progress of visible-light-driven heterogeneous photocatalysts for overall water splitting. *Solid state ionics*, 172(1-4):591–595. 18

[279] Yan, M.-Y., Shu, L.-H., Xing, Y., Chen, L.-D., Zhang, X.-Y., and Zhang, S.-T. (2022). Tailoring magnetic and dielectric properties of $Yb_2Ti_2O_7$ pyrochlore through structural distortion. *Applied Physics Letters*, 121(26). 136

[280] Yan, W., Yang, Z., Bian, W., and Yang, R. (2015). $FeCo_2O_4$/hollow graphene spheres hybrid with enhanced electrocatalytic activities for oxygen reduction and oxygen evolution reaction. *Carbon*, 92:74–83. xxxi, 108, 109, 238, 239

[281] Yang, M., Oró-Solé, J., Rodgers, J. A., Jorge, A. B., Fuertes, A., and Attfield, J. P. (2011). Anion order in perovskite oxynitrides. *Nature chemistry*, 3(1):47–52. 3, 19, 22, 23, 25, 32, 38

[282] Yeh, J.-W., Chen, S.-K., Lin, S.-J., Gan, J.-Y., Chin, T.-S., Shun, T.-T., Tsau, C.-H., and Chang, S.-Y. (2004). Nanostructured high-entropy alloys with multiple principal elements: novel alloy design concepts and outcomes. *Advanced engineering materials*, 6(5):299–303. 2

[283] Yu, T., Xu, H., Jin, Z., Zhang, Y., and Qiu, H.-J. (2023). Noble metal-free high-entropy oxide/Co−NC bifunctional electrocatalyst enables highly reversible and durable Zn-air batteries. *Applied Surface Science*, 610:155624. xxxi, 108, 109, 120, 239

[284] Zhang, B., Zhang, S.-X., Yao, R., Wu, Y.-H., and Qiu, J.-S. (2021). Progress and prospects of hydrogen production: Opportunities and challenges. *Journal of Electronic Science and Technology*, 19(2):100080. 107

[285] Zhang, C., Antonietti, M., and Fellinger, T.-P. (2014). Blood ties: Co_3O_4 decorated blood derived carbon as a superior bifunctional electrocatalyst. *Advanced Functional Materials*, 24(48):7655–7665. xxxi, 108, 109, 238

[286] Zhang, D., Chen, Y., Feng, T., Yu, D., An, K., Chen, R., and Luo, J. (2022a). Discovery of a reversible redox-induced order-disorder transition in a 10-component compositionally complex ceramic. *Scripta Materialia*, 215:114699. 82

[287] Zhang, D., Chen, Y., Vega, H., Feng, T., Yu, D., Everett, M., Neuefeind, J., An, K., Chen, R., and Luo, J. (2023a). Long-and short-range orders in 10-component compositionally complex ceramics. *Advanced Powder Materials*, 2(2):100098. 82

[288] Zhang, D., De Santiago, H. A., Xu, B., Liu, C., Trindell, J. A., Li, W., Park, J., Rodriguez, M. A., Coker, E. N., Sugar, J. D., McDaniel, A. H., Lany, S., Ma, L., Wang, Y., Collins, G., Tian, H., Li, W., Qi, Y., Liu, X., and Luo, J.

(2023b). Compositionally complex perovskite oxides for solar thermochemical water splitting. *Chemistry of Materials*, 35(5):1901–1915. 82

[289] Zhang, D., Park, J., Xu, B., Liu, C., Li, W., Liu, X., Qi, Y., and Luo, J. (2023c). Unusual aliovalent doping effects on oxygen non-stoichiometry in medium-entropy compositionally complex perovskite oxides. *Dalton Transactions*, 52:1082–1088. 82

[290] Zhang, J., Ji, W.-J., Xu, J., Geng, X.-Y., Zhou, J., Gu, Z.-B., Yao, S.-H., and Zhang, S.-T. (2017). Giant positive magnetoresistance in half-metallic double-perovskite Sr_2CrWO_6 thin films. *Science advances*, 3(11):e1701473. 136

[291] Zhang, Q., Zhang, Y., Matsuda, M., Garlea, V. O., Yan, J., McGuire, M. A., Tennant, D. A., and Okamoto, S. (2022b). Hidden local symmetry breaking in a kagome-lattice magnetic weyl semimetal. *Journal of the American Chemical Society*, 144(31):14339–14350. 136

[292] Zhang, R.-Z. and Reece, M. J. (2019). Review of high entropy ceramics: design, synthesis, structure and properties. *Journal of Materials Chemistry A*, 7(39):22148–22162. 4, 49, 83

[293] Zhang, Y., Chen, Z., Tian, J., Sun, M., Yuan, D., and Zhang, L. (2022c). Nitrogen doped $CuCo_2O_4$ nanoparticles anchored on beaded-like carbon nanofibers as an efficient bifunctional oxygen catalyst toward zinc-air battery. *Journal of Colloid and Interface Science*, 608:1105–1115. xxxi, 108, 109, 239

[294] Zhang, Y., Eremenko, M., Krayzman, V., Tucker, M. G., and Levin, I. (2020a). New capabilities for enhancement of RMCProfile: instrumental profiles with arbitrary peak shapes for structural refinements using the reverse monte carlo method. *Journal of Applied Crystallography*, 53(6). 7, 26, 61

[295] Zhang, Y., Liu, J., and Tucker, M. G. (2023d). Lorentz factor for time-of-flight neutron bragg and total scattering. *Acta Crystallographica Section A: Foundations and Advances*, 79(1). 143

[296] Zhang, Y., Lu, T., Ye, Y., Dai, W., Zhu, Y., and Pan, Y. (2020b). Stabilizing oxygen vacancy in entropy-engineered $CoFe_2O_4$-type catalysts for Co-prosperity of efficiency and stability in an oxygen evolution reaction. *ACS Applied Materials & Interfaces*, 12(29):32548–32555. 52, 53

[297] Zhang, Y.-R., Motohashi, T., Masubuchi, Y., and Kikkawa, S. (2011). Local anionic ordering and anisotropic displacement in dielectric perovskite $SrTaO_2N$. *Journal of the Ceramic Society of Japan*, 119(1391):581–586. 19, 22, 25, 31, 32

[298] Zhang, Y.-R., Motohashi, T., Masubuchi, Y., and Kikkawa, S. (2012). Sintering and dielectric properties of perovskite $SrTaO_2N$ ceramics. *Journal of the European Ceramic Society*, 32(6):1269–1274. 18, 25

[299] Zhang, Z., Li, J., Qian, J., Li, Z., Jia, L., Gao, D., and Xue, D. (2022d). Significant change of metal cations in geometric sites by magnetic-field annealing $FeCo_2O_4$ for enhanced oxygen catalytic activity. *Small*, 18(7):2104248. xxxi, 108, 109, 239

[300] Zhao, A., Masa, J., Xia, W., Maljusch, A., Willinger, M.-G., Clavel, G., Xie, K., Schlogl, R., Schuhmann, W., and Muhler, M. (2014). Spinel Mn−Co oxide in n-doped carbon nanotubes as a bifunctional electrocatalyst synthesized by oxidative cutting. *Journal of the American Chemical Society*, 136(21):7551–7554. xxxi, 108, 109, 238

[301] Zhao, J., He, Y., Wang, J., Zhang, J., Qiu, L., Chen, Y., Zhong, C., Han, X., Deng, Y., and Hu, W. (2022). Regulating metal active sites of atomically-thin nickel-doped spinel cobalt oxide toward enhanced oxygen electrocatalysis. *Chemical Engineering Journal*, 435:134261. xxxi, 108, 109, 110, 120

[302] Zhao, Q., Yan, Z., Chen, C., and Chen, J. (2017). Spinels: controlled preparation, oxygen reduction/evolution reaction application, and beyond. *Chemical Reviews*, 117(15):10121–10211. xxxi, 108, 109

[303] Zhao, Z., Xiang, H., Dai, F.-Z., Peng, Z., and Zhou, Y. (2019). $(La_{0.2}Ce_{0.2}Nd_{0.2}Sm_{0.2}Eu_{0.2})_2Zr_2O_7$: A novel high-entropy ceramic with low thermal conductivity and sluggish grain growth rate. *Journal of Materials Science & Technology*, 35(11):2647–2651. 111

[304] Zheng, X., Yang, J., Xu, Z., Wang, Q., Wu, J., Zhang, E., Dou, S., Sun, W., Wang, D., and Li, Y. (2022). Ru−Co pair sites catalyst boosts the energetics for the oxygen evolution reaction. *Angewandte Chemie International Edition*, 61(32):e202205946. 107

[305] Zhou, H. Y., Liu, X. Q., Zhu, X. L., and Chen, X. M. (2018). $CaTiO_3$ linear dielectric ceramics with greatly enhanced dielectric strength and energy storage density. *Journal of the American ceramic society*, 101(5):1999–2008. 2

[306] Zhu, H., Xie, H., Zhao, Y., Dai, S., Li, M., and Wang, X. (2021). Structure and magnetic properties of a class of spinel high-entropy oxides. *Journal of Magnetism and Magnetic Materials*, 535:168063. 52

[307] Zhuang, J., Lu, B., Gu, F., Zhong, Z., and Su, F. (2018). Ordered mesoporous Cu−Ca−Zr: A superior catalyst for direct synthesis of methyl formate from syngas. *Carbon Resources Conversion*, 1(2):174–182. 127

[308] Ziani, A., Le Paven, C., Le Gendre, L., Marlec, F., Benzerga, R., Tessier, F., Chevire, F., Hedhili, M. N., Garcia-Esparza, A. T., Melissen, S., Sautet, P., Le Bahers, T., and Takanabe, K. (2017). Photophysical properties of $SrTaO_2N$ thin films and influence of anion ordering: A joint theoretical and experimental investigation. *Chemistry of Materials*, 29(9):3989–3998. 21

Appendix

A Supplemental Information for Chapter 2

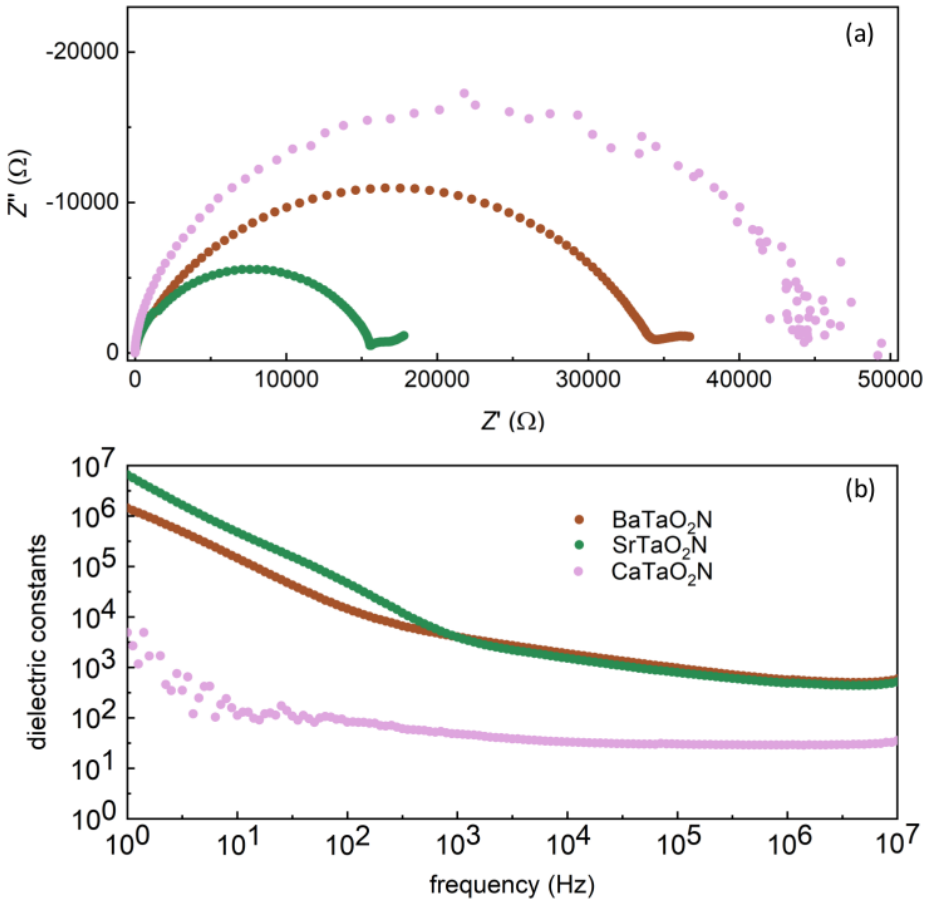


Figure S2.1: AC impedance data of polycrystalline $ATaO_2N$ (A = Ba, Sr, Ca) measured at 295 K, in the frequency range of 1 Hz-10 MHz. (a) Nyquist plots (Z in ohm for A = Ba and Sr, and kohm for A = Ca) and (b) frequency-dependence of dielectric constants. Taking into account the sample geometry, bulk electrical conductivities are evaluated as 1.6×10^{-4} S/cm, 1.3×10^{-4} S/cm, and 3.1×10^{-8} S/cm for A = Ba, Sr, and Ca, respectively. Note that the impedance (Z', Z") of $CaTaO_2N$ is plotted on a different scale.

Table S2.1: Lattice parameters, occupancies and isotropic atomic displacement parameters and R_{wp} values resulting from Rietveld refinement of neutron powder diffraction (NPD) data for $SrTaO_2N$ and $CaTaO_2N$ with disordered, occupancy (occ.) refined, fixed *trans* and fixed 50/50-75/25 models.

Param.	Disordered	Occ. Refined	Fixed *trans*	50/50-75/25
$SrTaO_2N$ in $I4/mcm$				
a=b (Å)	5.70522(9)	5.70530(9)	5.70583(9)	5.70519(9)
c (Å)	8.0836(2)	8.0836(2)	8.0840(2)	8.0836(2)
O/N 4a site occ.	0.6667/0.3333	0.32(1)/0.68(1)	0/1	0.5/0.5
O/N 8h site occ.	0.6667/0.3333	0.84(1)/0.16(1)	1/0	0.75/0.25
Sr 4b site U_{iso} (Å^2)	0.0116(2)	0.0111(2)	0.0109(2)	0.0114(2)
Ta 4c site U_{iso} (Å^2)	0.0077(2)	0.0081(2)	0.0086(1)	0.0081(2)
O/N 4a site U_{iso}(Å^2)	0.0172(9)	0.0223(8)	0.0344(7)	0.0171(7)
O/N 8h site U_{iso}(Å^2)	0.0189(5)	0.0148(5)	0.0073(3)	0.0185(4)
R_{wp} (%)	3.26	3.23	3.35	3.24
$CaTaO_2N$ in $Pnma$				
a (Å)	5.6229(2)	5.6231(2)	5.6222(2)	5.6230(2)
b (Å)	7.9000(3)	7.9001(3)	7.9008(3)	7.9003(3)
c (Å)	5.5539(2)	5.5539(2)	5.5543(2)	5.5541(2)
O/N 4c site occ.	0.6667/0.3333	0.71(1)/0.29(1)	0/1	0.5/0.5
O/N 8d site occ.	0.6667/0.3333	0.65(1)/0.35(1)	1/0	0.75/0.25
Ca 4c site U_{iso} (Å^2)	0.0199(5)	0.0199(5)	0.0191(6)	0.0202(5)
Ta 4b site U_{iso} (Å^2)	0.0067(2)	0.0068(2)	0.0075(3)	0.0065(2)
O/N 4c site U_{iso}(Å^2)	0.0168(5)	0.0147(8)	0.0412(7)	0.0249(6)
O/N 8d site U_{iso}(Å^2)	0.0141(3)	0.0152(5)	0.0003(3)	0.0100(3)
R_{wp} (%)	3.18	3.18	3.68	3.22

Table S2.2: Anisotropic atomic displacement parameters and R_{wp} values resulting from Rietveld refinement of neutron powder diffraction (NPD) data for $SrTaO_2N$ and $CaTaO_2N$ with disordered anisotropic and fixed 50/50-75/25 anisotropic models.

atom	Wyck.	U_{11}	U_{22}	U_{33}	U_{12}	U_{13}	U_{23}
$SrTaO_2N$ in $I4/mcm$ with disordered anisotropic model, R_{wp}=3.17%							
Sr	4*b*	0.0091(9)	0.0091(9)	0.0173(19)			
Ta	4*c*	0.0077(2)	0.0077(2)	0.0077(2)			
O1/N1	4*a*	0.0276(15)	0.0276(15)	0.0237(20)			
O2/N2	8*h*	0.0112(7)	0.0112(7)	0.0247(14)	0.0070(8)		
$SrTaO_2N$ in $I4/mcm$ with fixed 50/50-75/25 anisotropic model, R_{wp}=3.16%							
Sr	4*b*	0.0088(8)	0.0088(8)	0.0173(18)			
Ta	4*c*	0.0081(2)	0.0081(2)	0.0081(2)			
O1/N1	4*a*	0.0241(11)	0.0241(11)	0.0201(19)			
O2/N2	8*h*	0.0128(6)	0.0128(6)	0.0241(14)	0.0086(8)		
$CaTaO_2N$ in $Pnma$ with disordered anisotropic model, R_{wp}=3.17%							
Ca	4*c*	0.0279(20)	0.0087(19)	0.0261(18)		0.0040(17)	
Ta	4*b*	0.0067(3)	0.0067(3)	0.0067(3)			
O1/N1	4*c*	0.0208(14)	0.0108(14)	0.0200(13)		0.0000(11)	
O2/N2	8*d*	0.0135(7)	0.0130(8)	0.0173(8)	0.0017(7)	0.0015(8)	0.0018(8)
$CaTaO_2N$ in $Pnma$ with fixed 50/50-75/25 anisotropic model, R_{wp}=3.21%							
Ca	4*c*	0.0289(21)	0.0089(20)	0.0267(18)		0.0027(18)	
Ta	4*b*	0.0067(3)	0.0067(3)	0.0067(3)			
O1/N1	4*c*	0.0316(15)	0.0189(15)	0.0273(14)		0.0000(12)	
O2/N2	8*d*	0.0089(7)	0.0090(7)	0.0132(7)	0.0023(7)	0.0009(8)	0.0022(8)

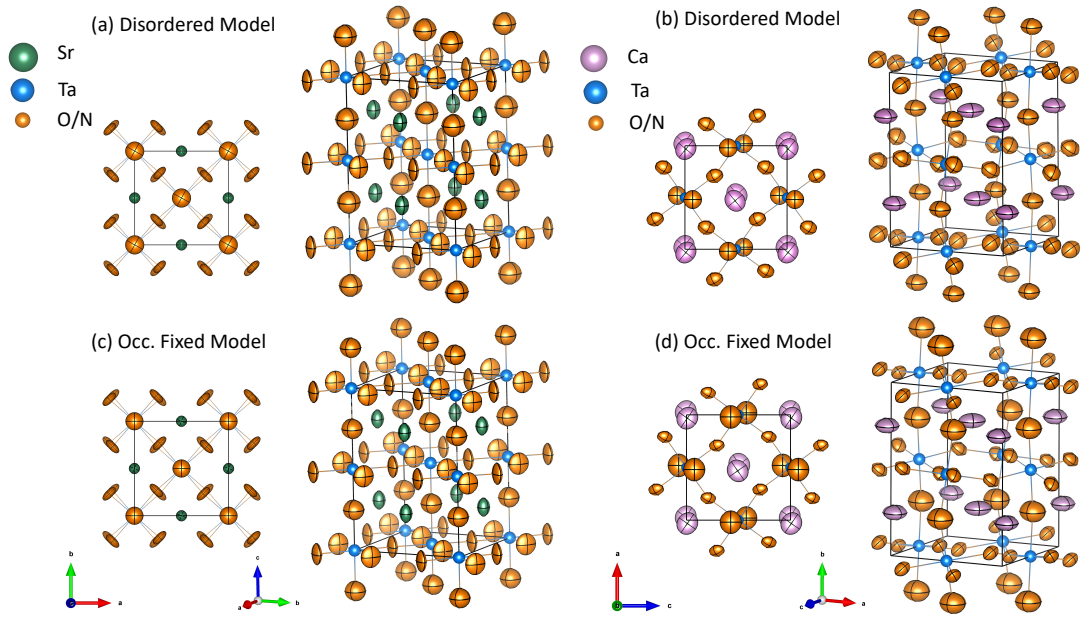


Figure S2.2: (a, b) Disordered anisotropic structure model and (c, d) fixed 50/50-75/25 anistropic structure model shown with 99% probability thermal ellipsoids for $SrTaO_2N$ and $CaTaO_2N$, respectively.

Table S2.3: Total number (No.) of refined parameters, increased number (No.) of refined parameters comparing with the refinements which used average structures and R_{wp} values in the range from 1.5 to 6 Å PDF refinements for $SrTaO_2N$ and $CaTaO_2N$ with average structures and sub-lattice structures.

$SrTaO_2N$	$I4/mcm$	$I\bar{4}2m$	$I422$	$I4m$	$I\bar{4}$	$Ibam$	$Ima2$
Total No.	9	10	10	11	12	10	16
Increased No.	0	1	1	2	3	1	7
R_{wp} (%)	11.03	23.15	10.18	32.58	27.07	10.00	9.17
$CaTaO_2N$	$Pnma$	$P2_1c$	$P2_1m$	$Pmn2_1$	$P2_12_12_1$	$Pmc2_1$	$Pna2_1$
Total No.	16	21	23	26	24	26	24
Increased No.	0	5	7	10	8	10	8
R_{wp} (%)	15.70	9.90	13.53	7.78	9.00	10.18	8.57

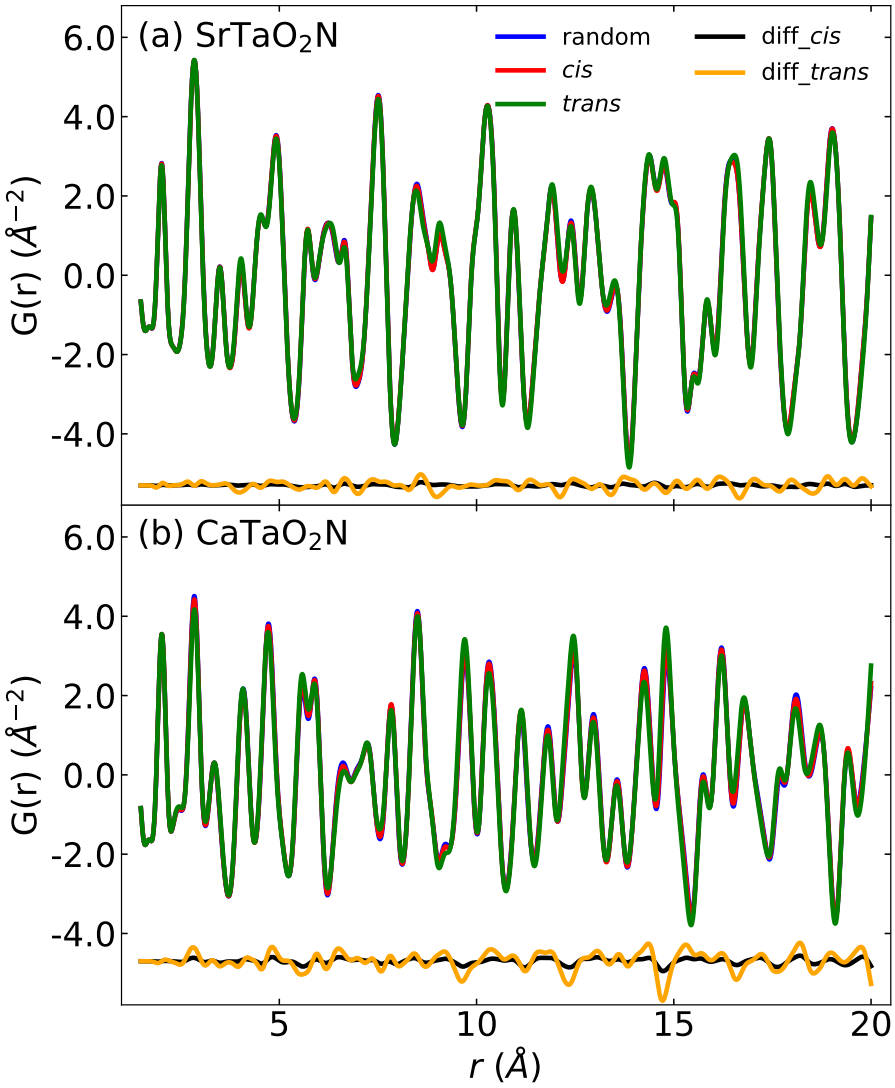


Figure S2.3: (a) $SrTaO_2N$ and (b) $CaTaO_2N$ PDF sensitivity test of random/*cis*/*trans* models. Random models are given as blue, *cis* models are given as red and *trans* models are green. The black and orange difference curves describe the difference between random structure and *cis*/*trans*.

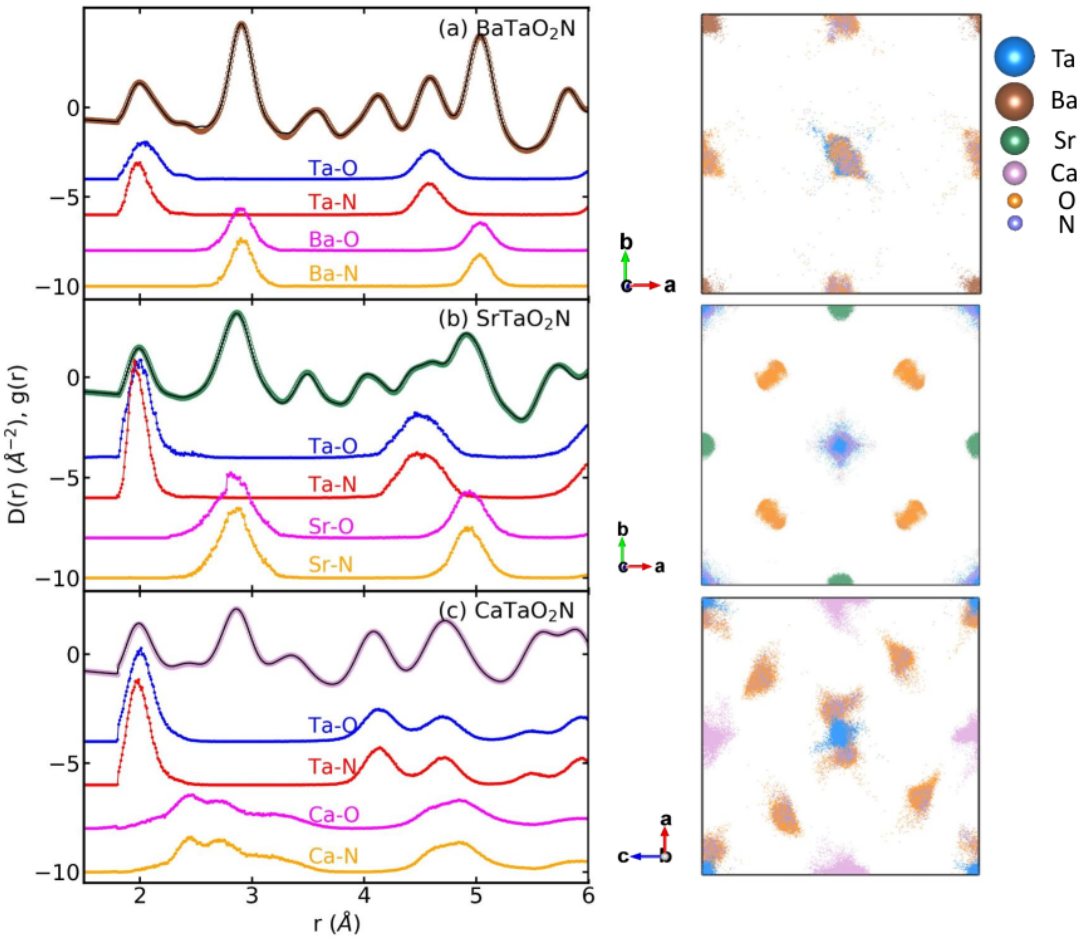


Figure S2.4: (a-c) Calculated PDFs and partial PDFs resulting from the first series of RMC fits to data. Data are shown as brown, green, and mauve circles for $BaTaO_2N$, $SrTaO_2N$, and $CaTaO_2N$, respectively. Fits are shown as black lines through the data, while blue, red, magenta, and orange solid lines are the partial PDFs of Ta-O, Ta-N, A-O and A-N. Resulting point clouds of corresponding model structures are shown at the right of each panel.

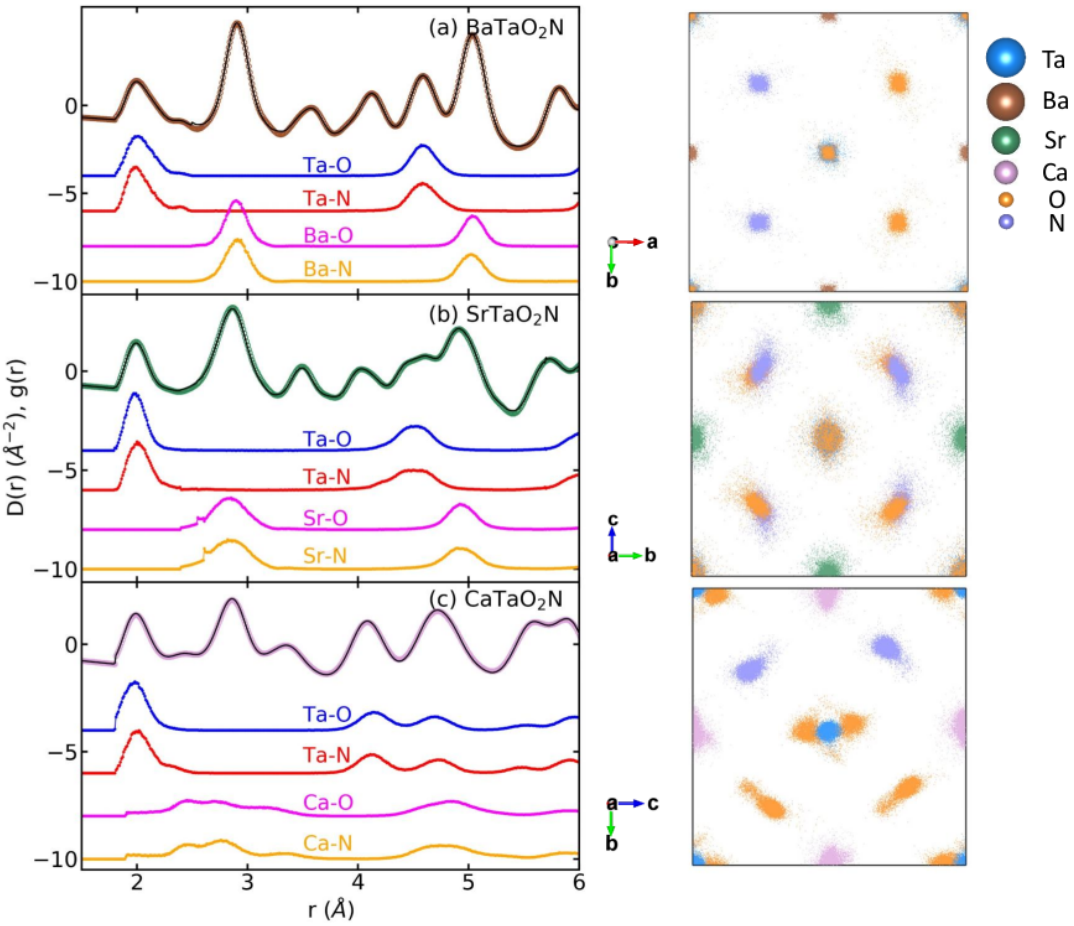


Figure S2.5: (a-c) Calculated PDFs and partial PDFs resulting from the second series (with *cis* N ordering) of RMC fits to data. Data are shown as brown, green, and mauve circles for $BaTaO_2N$, $SrTaO_2N$, and $CaTaO_2N$, respectively. Fits are shown as black lines through the data, while blue, red, magenta, and orange solid lines are the partial PDFs of Ta-O, Ta-N, A-O and A-N. Resulting point clouds of corresponding model structures are shown at the right of each panel.

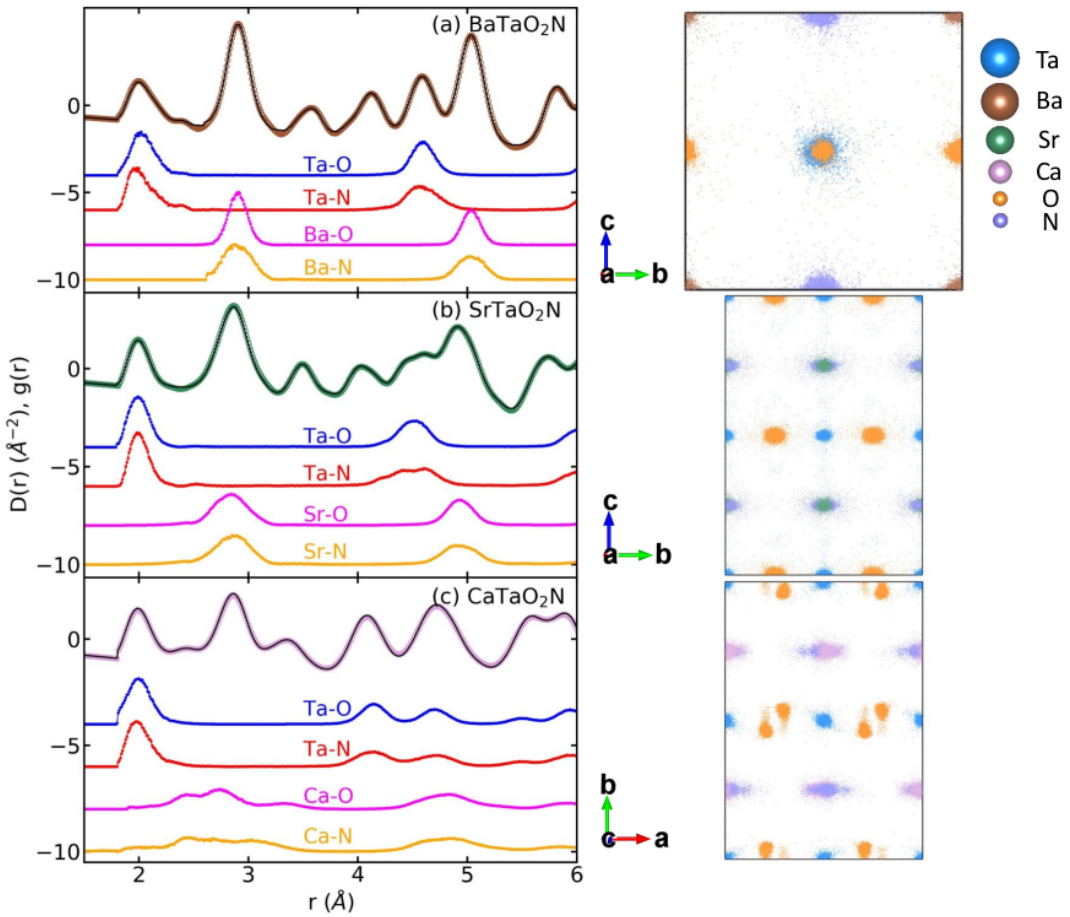


Figure S2.6: (a-c) Calculated PDFs and partial PDFs resulting from the second series (with *trans* N ordering) of RMC fits to data. Data are shown as brown, green, and mauve circles for $BaTaO_2N$, $SrTaO_2N$, and $CaTaO_2N$, respectively. Fits are shown as black lines through the data, while blue, red, magenta, and orange solid lines are the partial PDFs of Ta-O, Ta-N, A-O and A-N. Resulting point clouds of corresponding model structures are shown at the right of each panel.

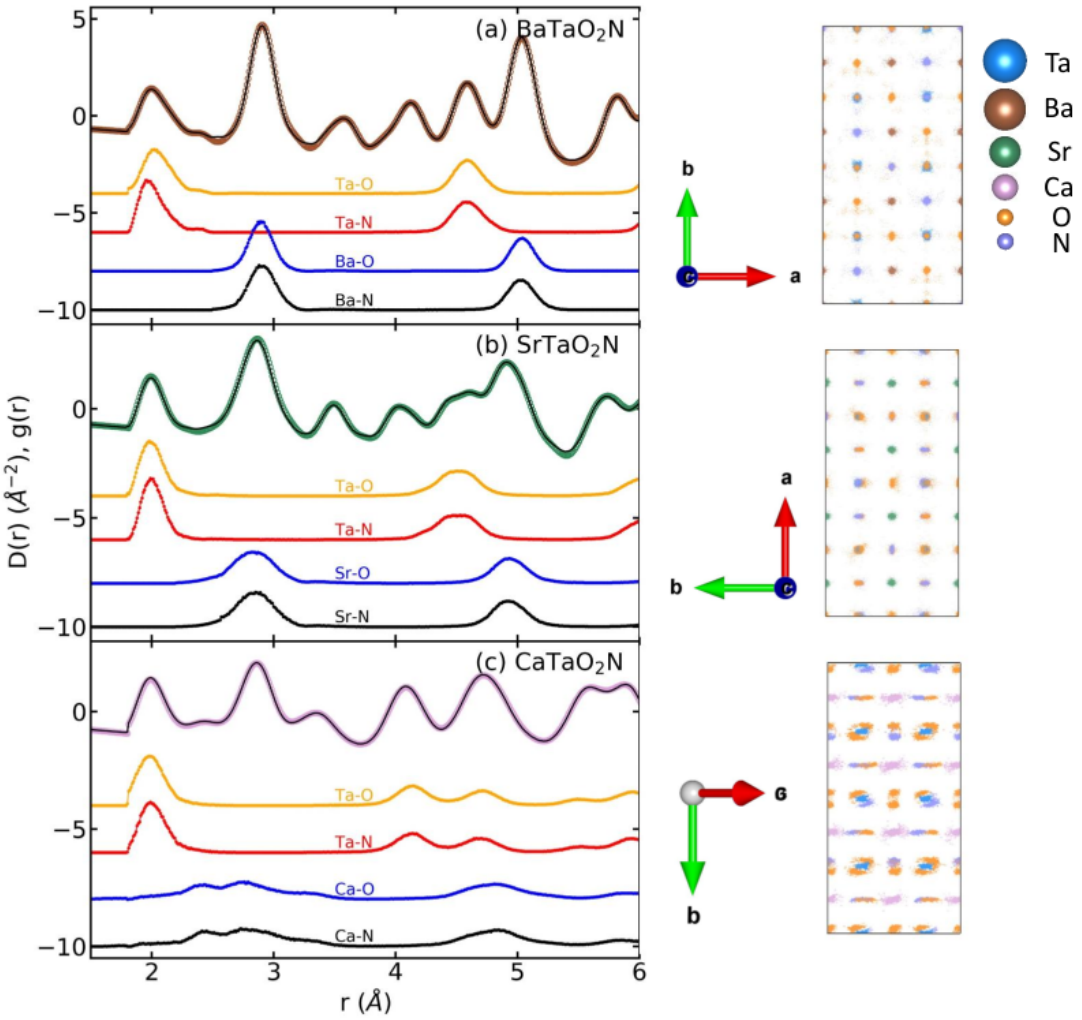


Figure S2.7: (a-c) Calculated PDFs and partial PDFs resulting from the third series (with *cis* N supercell ordering) of RMC fits to data. Data are shown as brown, green, and mauve circles for $BaTaO_2N$, $SrTaO_2N$, and $CaTaO_2N$, respectively. Fits are shown as black lines through the data, while blue, red, magenta, and orange solid lines are the partial PDFs of Ta-O, Ta-N, A-O and A-N. Resulting point clouds of corresponding model structures are shown at the right of each panel.

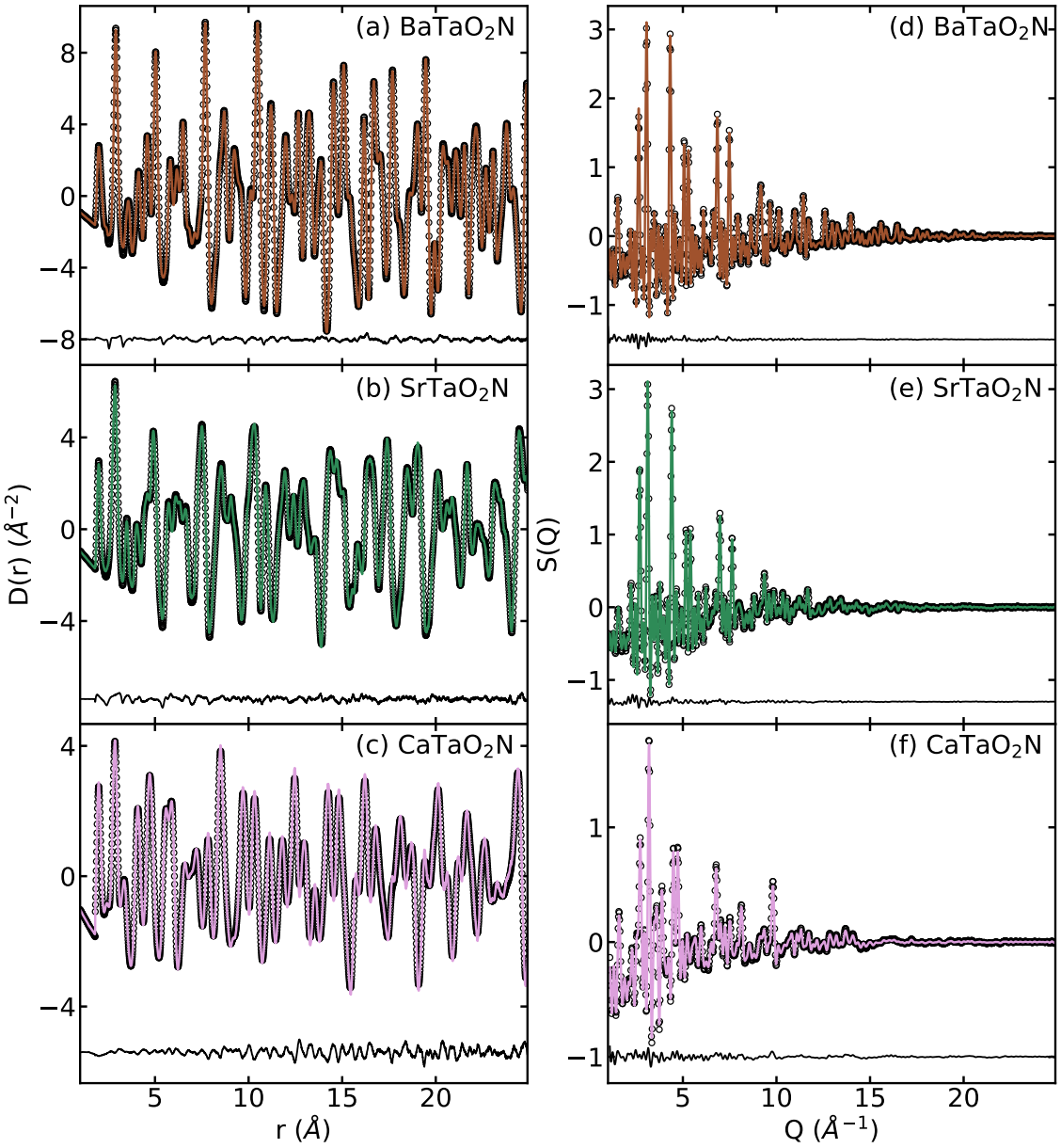


Figure S2.8: (a-c) Calculated PDFs and (d-f) S(Q) resulting from (third series) of RMC refinement. Data are shown as black circles, with resulting fits shown as solid lines through the data (brown lines for $BaTaO_2N$, green lines for $SrTaO_2N$, and mauve lines for $CaTaO_2N$). Black solid lines show the difference between data and fits.

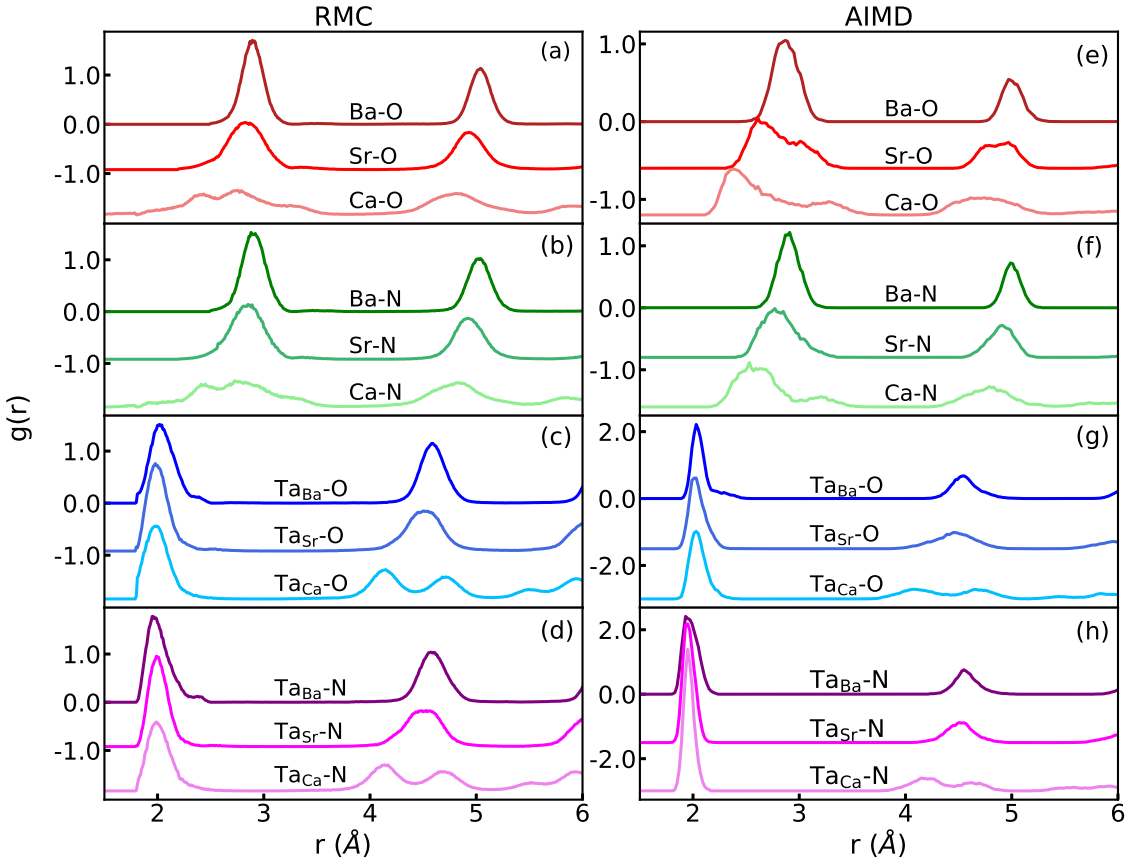


Figure S2.9: The corresponding partial pair distribution functions (pPDF) (a) A-O, (b) A-N, (c) Ta$_A$-O and (d) Ta$_A$-N, from RMCProfile(RMC), and radial distribution functions (RDF) (e) A-O, (f) A-N, (g) Ta$_A$-O and (h) Ta$_A$-N, from ab initio molecular dynamics (AIMD) simulations of ATaO$_2$N (A=Ba, Sr, Ca). The supercells used in RMC and AIMD have anion ordering of *cis*-TaO$_4$N$_2$ octahedra with '90-deg' configuration at axial N as proposed by Hinuma[79].

Table S2.4: Experimental[256] and Calculated (GGA+U) band gaps of most stable *cis* and *trans* configurations of BaTaO$_2$N, SrTaO$_2$N and CaTaO$_2$N.

	cis		*trans*		
	Band gap	Space	Band gap	Space	Band gap
	(eV)	group	(eV)	group	(eV)
BaTaO$_2$N	1.8	*Pbmm*	0.87	Pnma	0.9
SrTaO$_2$N	2.1	*Ima*2	1.35	Pnma	1.16
CaTaO$_2$N	2.4	*Pmn*2$_1$	1.96	Pnma	1.39

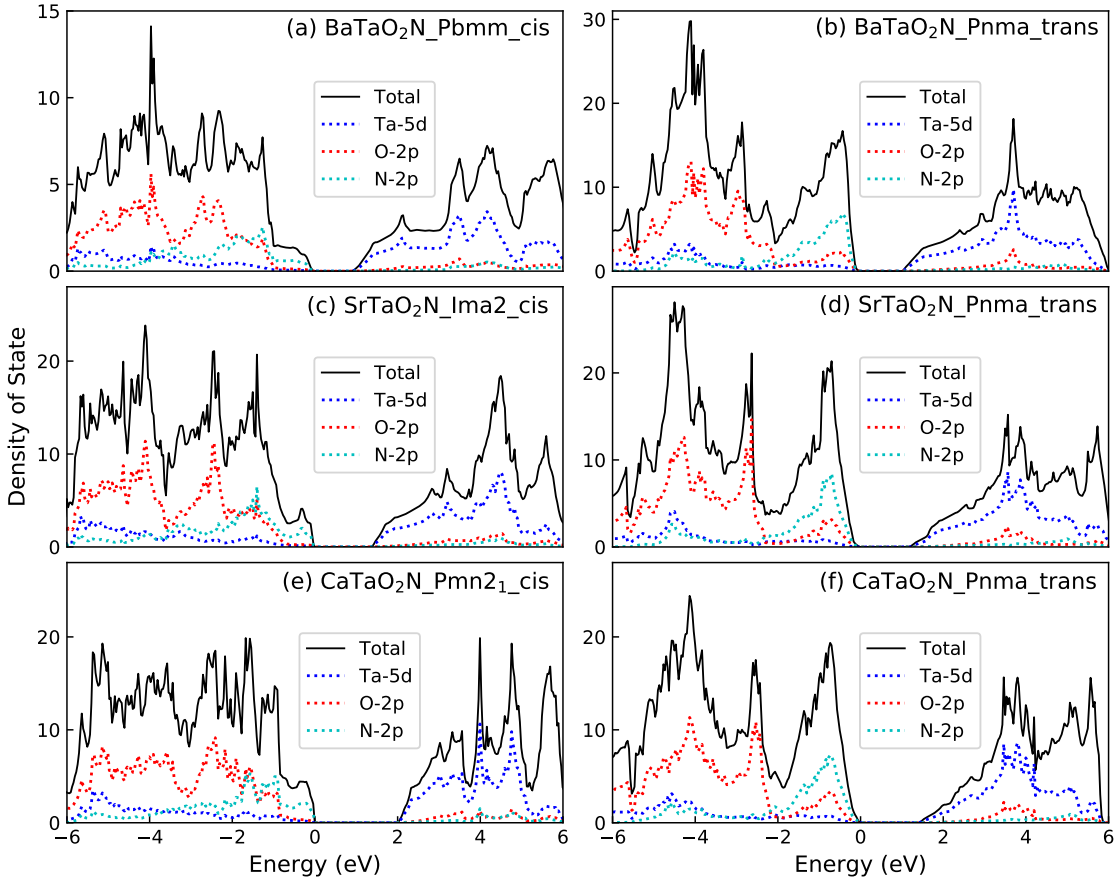


Figure S2.10: Total and partial density of electronic state of most stable *cis* and *trans* configurations of (a, b) $BaTaO_2N$, (c, d) $SrTaO_2N$ and (e, f) $CaTaO_2N$.

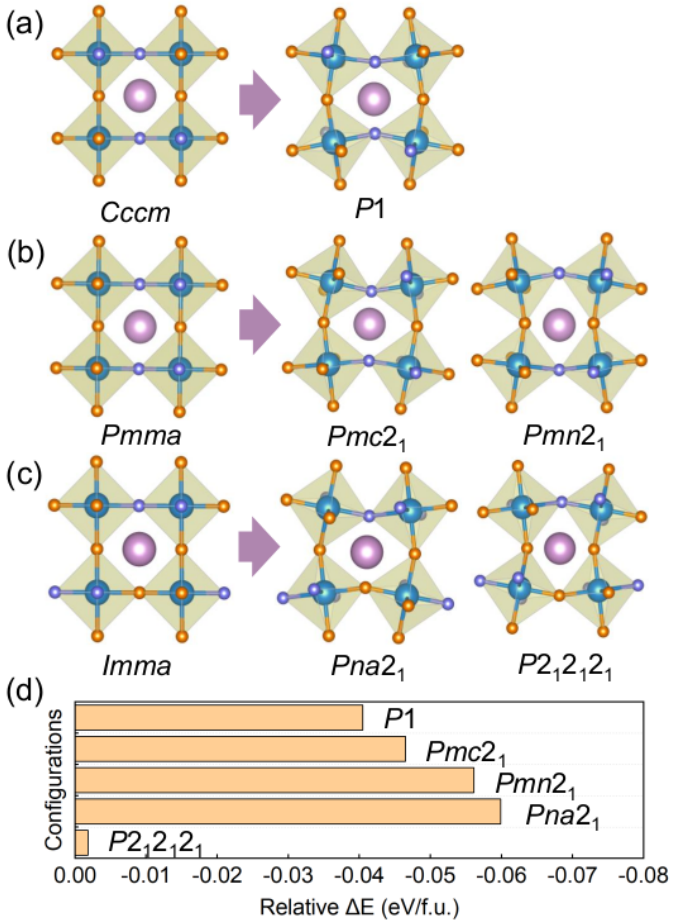


Figure S2.11: (a-c) Distinct *cis* N configurations accessible through anion ordering or tilting modification of a parent *Pnma* $CaTaO_2N$ structure. Each row contains configurations with a distinct motif of *cis* N order. The structures at the far left in each row involve no octahedral tilting (*Cccm*, *Pmma* and *Imma*), while the additional structures in each row include octahedral tilting ($P1$, $Pmc2_1$, $Pmn2_1$, $Pna2_1$, $P2_12_12_1$). (d) Relative energies for relaxed *cis* configurations of $CaTaO_2N$ shown in (a-c). The relative energies are shown in relation to the calculated energy of the $P2_12_12_1$ structure, which has the highest value.

Table S2.5: Neutron powder crystallographic data and refinement details for $SrTaO_2N$ and $CaTaO_2N$ with average models (fixed 50/50-75/25 model for $SrTaO_2N$ and disordered model for $CaTaO_2N$).

Param.	$SrTaO_2N$	$CaTaO_2N$
Source	Neutron time of flight (TOF)	Neutron time of flight (TOF)
Chemical formula	$SrTaO_2N$	$CaTaO_2N$
Formula weight (u)	314.575	267.033
Temperature (K)	290	290
Crystal system	Tetragonal	Orthorhombic
Space group (No.)	$I4/mcm$ (140)	$Pnma$ (62)
a (Å)	5.70519(9)	5.6229(2)
b (Å)	5.70519(9)	7.9000(3)
c (Å)	8.0836(2)	5.5539(2)
$\alpha = \beta = \gamma$ (Å)	90	90
V (Å^3)	263.114(10)	246.712(15)
Z	4	4
d-space range (Å)	0.5-3	0.5-3
χ^2	0.000160	0.000084
R_p (%)	2.28	2.16
R_{wp} (%)	3.24	3.18
Definition of R factors	$R_p = \frac{\sum \lvert y_t^o - y_t^c \rvert}{\sum y_t^o}$ $R_{wp} = \sqrt{\frac{\sum_t \omega_t (y_t^o - K y_t^c)^2}{\sum_t \omega_t (y_t^o)^2}}$	$R_p = \frac{\sum \lvert y_t^o - y_t^c \rvert}{\sum y_t^o}$ $R_{wp} = \sqrt{\frac{\sum_t \omega_t (y_t^o - K y_t^c)^2}{\sum_t \omega_t (y_t^o)^2}}$

B Supplemental Information for Chapter 3

KDE analysis was conducted for the projection of the magnetic moment distributions in the XY plane, as presented in Figure S3.9 for inverse spinel configurations and Figure S3.10 for random spinel configurations for all four samples. By comparison, the KDE map can be categorized into two groups – F1 and F3 verses F4 and F5. The major difference between these two groups is the degree of dispersion for magnetic moment distributions is larger in F1 and F3, as compared to that in F4 and F5.

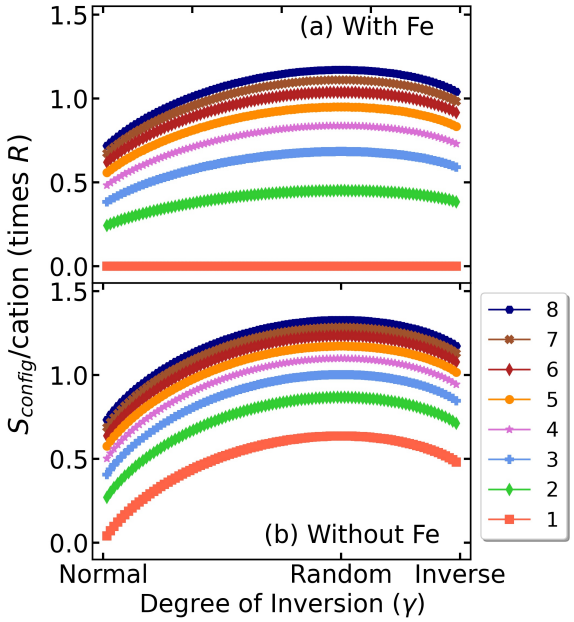


Figure S3.1: The calculated S_{config} of AFe_2O_4 HESOs with the degree of inversion (γ) changing from 0 to 1 and the assumption that there are N (from 1 to 8) cations ((a) with Fe included as one of the occupying 8 A site cations and (b) without Fe included as one of the occupying A site cations) (the γ values 0, 2/3, and 1 are labeled with the corresponding structure model (normal spinel, random solution, and inverse spinel, respectively.) It is shown that the samples in this study are better described as compositionally complex oxides (CCOs).

Table S3.1: Parameters for all the fitting model results of the normal, inverse and random solution F$d\bar{3}m$ spinel models applied for F1 Rietveld refinements. The table includes the refined magnetic moment (M), lattice parameter (a), oxygen position (u), isotropic atomic displacement parameters (U_{iso}) for the 8b, 16c, and 32e sites, and the resulting refinement goodness-of-fit, R_{wp}.

Sample	F1		
Best Model	Normal	Inverse	Random
M(μ_B/Å)	6.232	0.406	1.200
a (Å)	8.3801(2)	8.3796(1)	8.3795(1)
u (frac.)	0.2445(1)	0.2440(0)	0.2441(0)
$U_{iso,8b}$ (Å^2)	0.0010(1)	0.0057(1)	0.0028(1)
$U_{iso,16c}$ (Å^2)	0.0105(2)	0.0040(1)	0.0060(1)
$U_{iso,32e}$ (Å^2)	0.0095(2)	0.0079(1)	0.0075(1)
R_{wp}	8.54	5.19	5.49

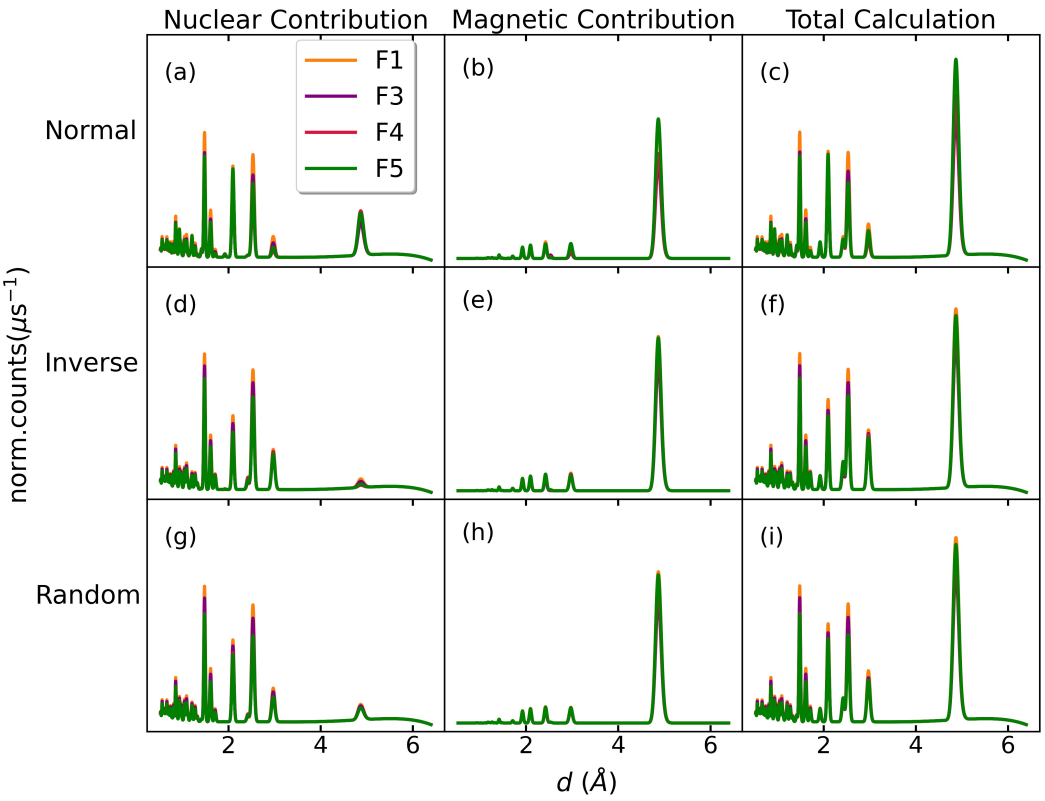


Figure S3.2: Comparison of calculated neutron diffraction patterns with nuclear contributions (1^{st} column), magnetic contributions (2^{nd} column) and total calculations (3^{rd} column) delineated with normal spinel (a,b,c), inverse spinel (d, e, f), random solution (g, h, i) structure models for samples F1, F3, F4, and F5.

Table S3.2: Parameters for all the fitting model results of the normal, inverse and random solution F$d\bar{3}m$ spinel models applied for F3 Rietveld refinements. The table includes the refined magnetic moment (M), lattice parameter (a), oxygen position (u), isotropic atomic displacement parameters (U_{iso}) for the 8b, 16c, and 32e sites, and the resulting refinement goodness-of-fit, R_{wp}.

Sample	F3		
Best Model	Normal	Inverse	Random
M(μ_B/Å)	11.299	0.215	1.876
a (Å)	8.3799(2)	8.3793(1)	8.3794(1)
u (frac.)	0.2447(1)	0.2438(0)	0.2440(0)
$U_{iso,8b}$ (Å^2)	0.0010(2)	0.0066(1)	0.0030(1)
$U_{iso,16c}$ (Å^2)	0.0136(3)	0.0035(1)	0.0060(1)
$U_{iso,32e}$ (Å^2)	0.0112(2)	0.0088(1)	0.0087(1)
R_{wp}	9.97	5.28	5.64

Table S3.3: Parameters for all the fitting model results of the normal, inverse and random solution F$d\bar{3}m$ spinel models applied for F4 Rietveld refinements. The table includes the refined magnetic moment (M), lattice parameter (a), oxygen position (u), isotropic atomic displacement parameters (U_{iso}) for the 8b, 16c, and 32e sites, and the resulting refinement goodness-of-fit, R_{wp}.

Sample	F4		
Best Model	Normal	Inverse	Random
M(μ_B/Å)	9.227	0.558	1.162
a (Å)	8.3894(3)	8.3899(1)	8.3894(1)
u (frac.)	0.2445(1)	0.2433(1)	0.2433(0)
$U_{iso,8b}$ (Å^2)	0.0010(3)	0.0154(2)	0.0054(1)
$U_{iso,16c}$ (Å^2)	0.0216(4)	0.0028(1)	0.0047(1)
$U_{iso,32e}$ (Å^2)	0.0137(3)	0.0116(2)	0.0085(1)
R_{wp}	11.35	6.64	5.14

Table S3.4: Parameters for all the fitting model results of the normal, inverse and random solution F$d\bar{3}m$ spinel models applied for F5 Rietveld refinements. The table includes the refined magnetic moment (M), lattice parameter (a), oxygen position (u), isotropic atomic displacement parameters (U_{iso}) for the 8b, 16c, and 32e sites, and the resulting refinement goodness-of-fit, R_{wp}.

Sample	F5		
Best Model	Normal	Inverse	Random
M(μ_B/Å)	3.918	0.668	0.532
a (Å)	8.3837(2)	8.3842(1)	8.3839(1)
u (frac.)	0.2444(1)	0.2434(1)	0.2436(0)
$U_{iso,8b}$ (Å^2)	0.0010(2)	0.0145(2)	0.0069(1)
$U_{iso,16c}$ (Å^2)	0.0175(3)	0.0038(1)	0.0069(1)
$U_{iso,32e}$ (Å^2)	0.0124(2)	0.0114(2)	0.0084(1)
R_{wp}	9.11	6.19	4.54

Table S3.5: Overall average atomic displacement parameters (ADPs) for tetrahedral and octahedral sites for F1 and F3, extracted from RMC configurations when a +2 valence state is assumed for all A cations in the AFe_2O_4 compositional series, and a +3 valence state is assumed for the remaining two Fe cations. "Tetra" designates the tetrahedral site, "Octa" the octahedral site, "Oxy" the oxygen site, "I" an inverse model and "R" a random model. ADPs are given in Å.

	U_{11}	U_{22}	U_{33}	U_{12}	U_{13}	U_{23}
F1-I-Tetra	0.00500	0.01070	0.00940	-0.00110	-0.00230	0.00030
F1-R-Tetra	0.00434	0.00738	0.00606	-0.00090	-0.00103	-0.00084
F3-I-Tetra	0.00639	0.01678	0.01606	-0.00378	-0.00453	0.00249
F3-R-Tetra	0.00429	0.00741	0.00586	-0.00095	-0.00093	-0.00084
F1-I-Octa	0.00616	0.01139	0.00843	-0.00219	0.00001	-0.00220
F1-R-Octa	0.00694	0.01151	0.00931	-0.00131	-0.00085	-0.00129
F3-I-Octa	0.00624	0.01422	0.00875	-0.00305	0.00083	-0.00366
F3-R-Octa	0.00733	0.01168	0.00999	-0.00123	-0.00113	-0.00188
F1-I-Oxy	0.00681	0.00908	0.00733	-0.00105	0.00035	-0.00042
F1-R-Oxy	0.00681	0.00874	0.00748	-0.00039	-0.00033	0.00043
F3-I-Oxy	0.00787	0.01139	0.00789	-0.00287	0.00118	-0.00135
F3-R-Oxy	0.00723	0.01006	0.00813	-0.00043	-0.00028	0.00060

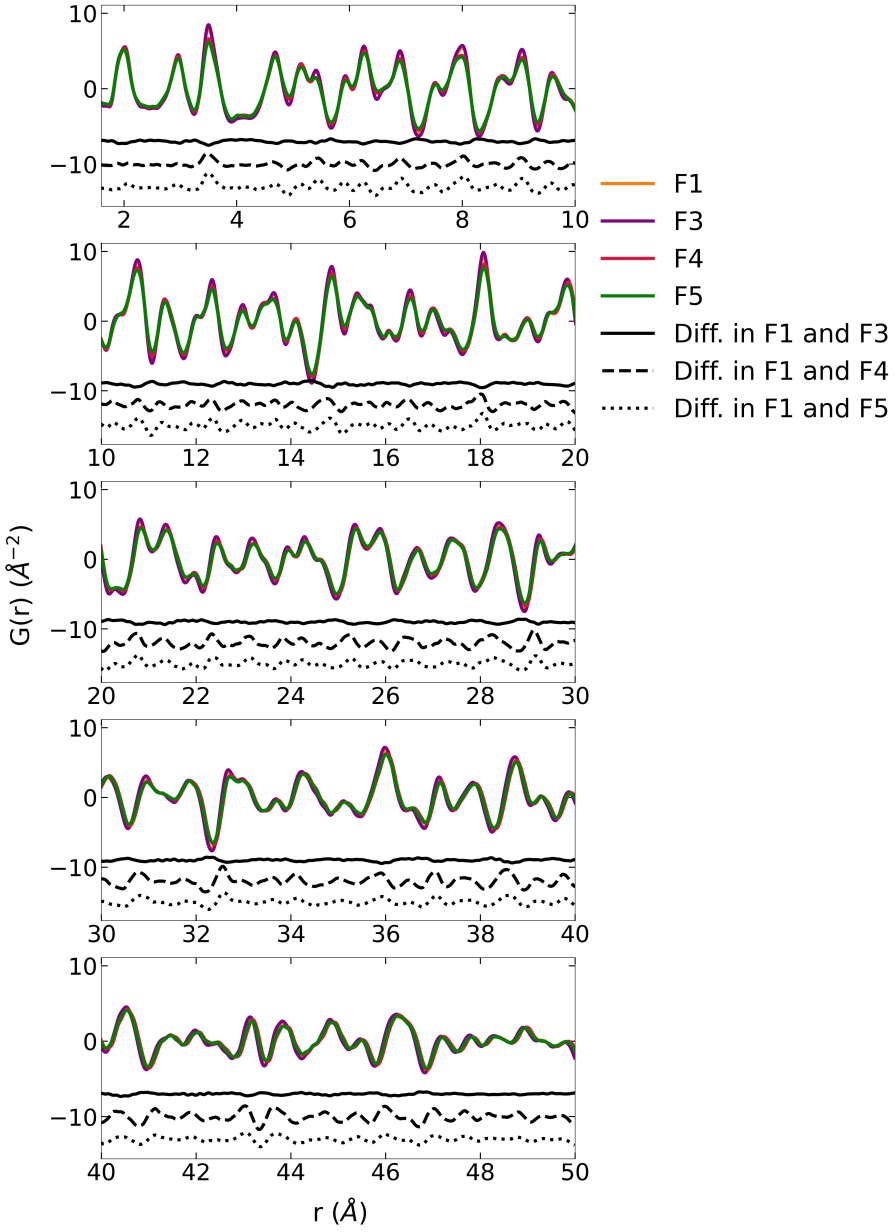


Figure S3.3: The PDF data comparison of F1 (orange line), F3 (purple line), F4 (red line), and F5 (green line) shown for every 10 Å between 1.7 Å and 50 Å). The differences between F1 and F3 (black solid line), F1 and F4 (black dashed line), and F1 and F5 (black dotted line) are shown below the PDF data.

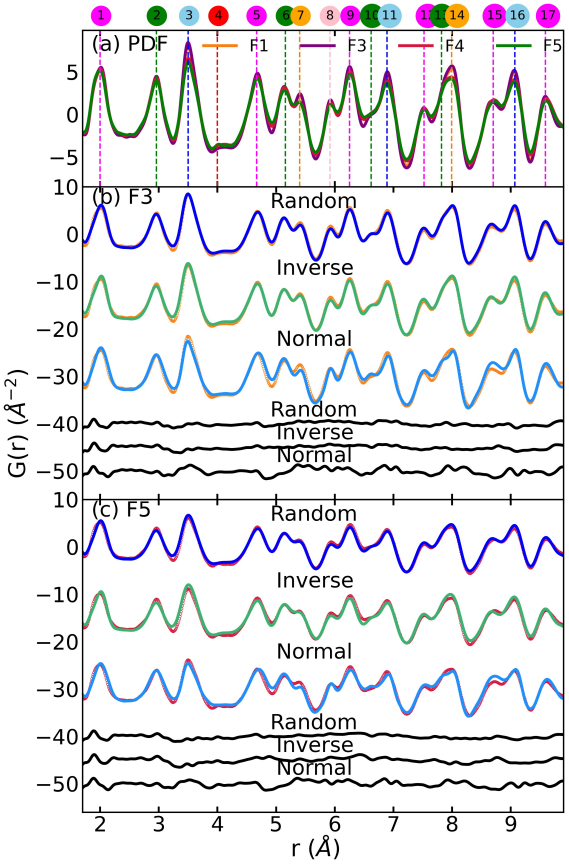


Figure S3.4: The PDF data comparison of F1 (orange line), F3 (purple line), F4 (red line), F5 (green line). The 6 peaks (1, 5, 9, 12, 15, 17) highlighted with magenta dashed lines correspond to A-O pairs. The 4 peaks (2, 6, 10, 13) indicated with green dashed lines arise from A_{oct}-A_{oct} and O-O pair correlations. The 3 peaks (3, 11, 16) contributed by A_{oct}-A_{tet},A_{tet}-A_{tet} and A-O are identified in sky blue dashed lines. The peak (4) around 4 Å highlighted in a red dashed line corresponds to an O-O correlation. The combination of A_{oct}-A_{tet} and A_{tet}-O pair correlations contribute the 2 peaks (7, 14) indicated by orange dashed lines. The peak (8) highlighted by a pink dashed line arises from A_{oct}-A_{oct},A_{tet}-A_{tet} and A-O pair correlations). A comparison of the PDF refinements for (b) F3 sample data and (c) F5 sample data using different structure models (random, inverse, and normal spinel ferrite models). PDF data for F3 and F5 samples are shown in orange and red dots, respectively. The blue, lemon green and sky blue solid curves present fits to the data completed with the random spinel structure, inverse spinel structure and normal spinel structure model, respectively. The fit difference curves displayed below the data and fits are represented as black solid curves. These results are similar to results for F1 and F4 samples presented in the main body of this work.

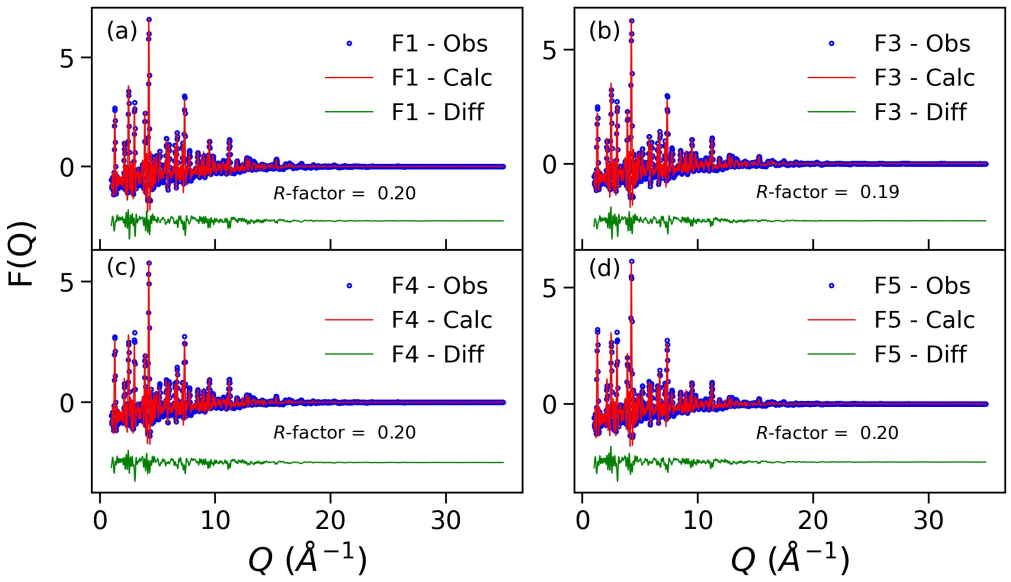


Figure S3.5: RMC fitting of $F(Q)$ data for (a) F1, (b) F3, (c) F4 and (d) F5 with inverse model assuming that a +2 valence state for all A cations in the AFe_2O_4 compositional series, and a +3 valence state for the remaining two Fe cations.

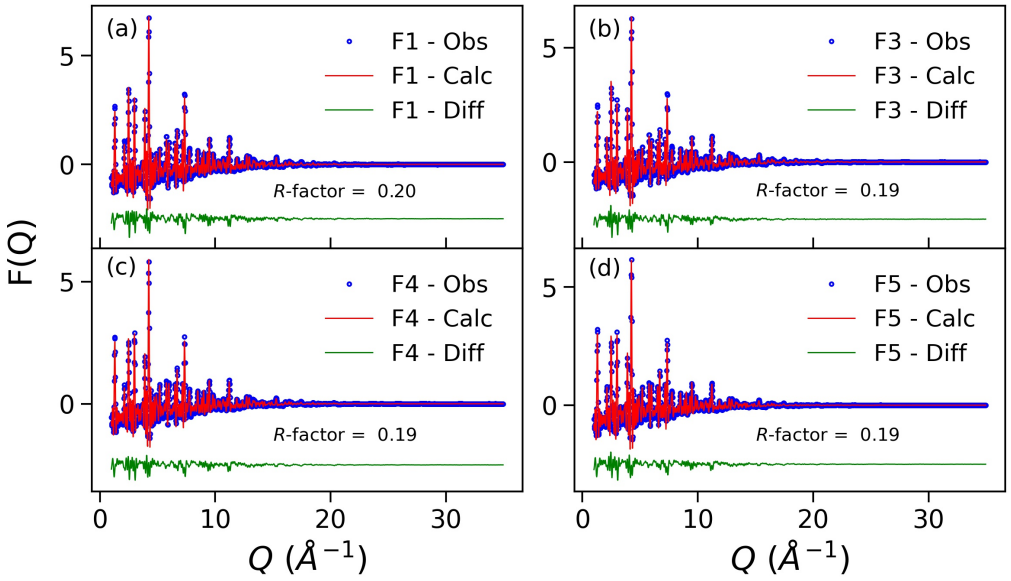


Figure S3.6: RMC fitting of $F(Q)$ data for (a) F1, (b) F3, (c) F4 and (d) F5 with random model assuming that a +2 valence state for all A cations in the AFe_2O_4 compositional series, and a +3 valence state for the remaining two Fe cations.

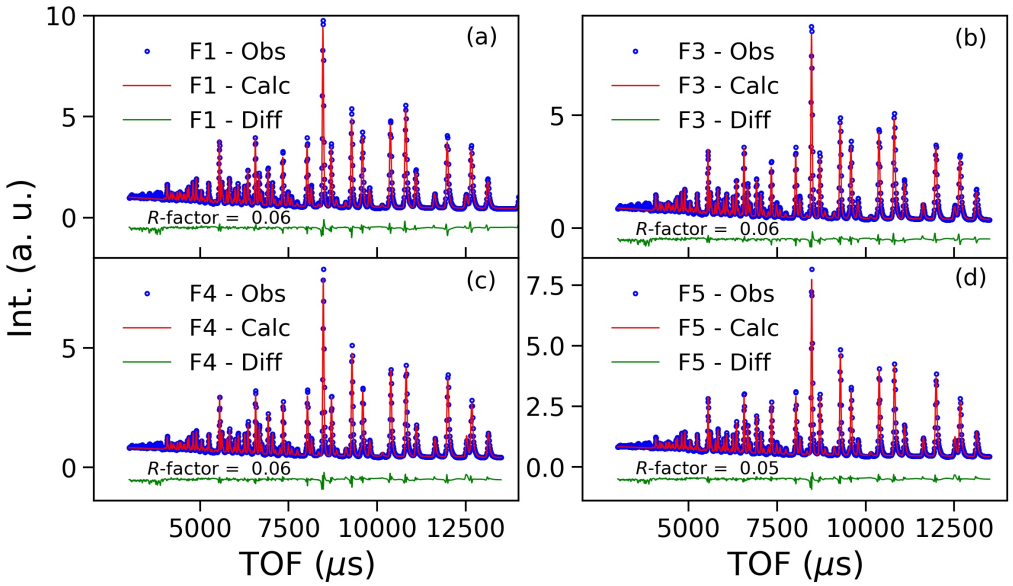


Figure S3.7: RMC fitting of Bragg data for (a) F1, (b) F3, (c) F4 and (d) F5 with inverse model assuming that a +2 valence state for all A cations in the AFe_2O_4 compositional series, and a +3 valence state for the remaining two Fe cations.

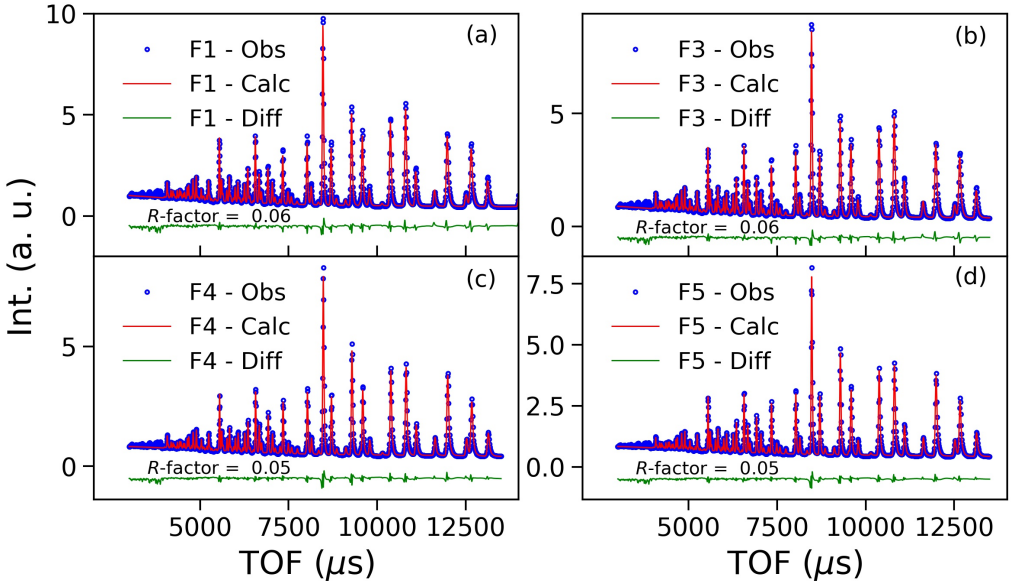


Figure S3.8: RMC fitting of Bragg data for (a) F1, (b) F3, (c) F4 and (d) F5 with random model assuming that a +2 valence state for all A cations in the AFe_2O_4 compositional series, and a +3 valence state for the remaining two Fe cations.

Table S3.6: Overall average atomic displacement parameters (ADPs) for tetrahedral and octahedral sites for F4 and F5, extracted from RMC configurations when a +2 valence state is assumed for all A cations in the AFe_2O_4 compositional series, and a +3 valence state is assumed for the remaining two Fe cations. "Tetra" designates the tetrahedral site, "Octa" the octahedral site, "Oxy" the oxygen site, "I" an inverse model and "R" a random model. ADPs are given in Å.

	U_{11}	U_{22}	U_{33}	U_{12}	U_{13}	U_{23}
F4-I-Tetra	0.02029	0.01293	0.01306	0.00144	-0.00053	0.00269
F4-R-Tetra	0.00828	0.00809	0.00633	-0.00006	-0.00108	-0.00060
F5-I-Tetra	0.02064	0.01310	0.01325	0.00136	-0.00064	0.00311
F5-R-Tetra	0.00915	0.00835	0.00709	-0.00013	-0.00104	-0.00019
F4-I-Octa	0.00619	0.00788	0.00738	-0.00006	-0.00041	-0.00132
F4-R-Octa	0.00753	0.01092	0.00958	0.00071	-0.00088	0.00212
F5-I-Octa	0.00715	0.00873	0.00807	0.00009	-0.00064	-0.00112
F5-R-Octa	0.00823	0.01133	0.00965	0.00108	-0.00103	-0.00186
F4-I-Oxy	0.01153	0.00923	0.00846	0.00047	0.00124	0.00039
F4-R-Oxy	0.01027	0.00899	0.00878	0.00044	0.00049	0.00019
F5-I-Oxy	0.01211	0.00982	0.00850	0.00053	0.00091	0.00068
F5-R-Oxy	0.01097	0.00948	0.00852	0.00059	0.00027	0.00065

Table S3.7: The average magnetic moments (in μ_B) on tetrahedral and octahedral sites from RMC simulations assuming a +2 valence state for all A cations in the AFe_2O_4 compositional series, and a +3 valence state for the remaining two Fe cations. The net magnetic moment is calculated in the following way, $Net\ moment = (abs(2 \times MM_{Octa}) - abs(MM_{Tetra}))/3$. "Tetra" is for tetrahedral site, "Octa" for octahedral site, "MM" for magnetic moment, "I" for inverse model, "R" for random model and "abs" for absolute value.

	Tetra	Octa	Net		Tetra	Octa	Net
F1-I	-3.77	+3.44	1.04	F4-I	-3.85	3.99	1.38
F1-R	-4.35	+3.10	0.62	F4-R	-4.41	3.34	0.76
F3-I	-3.71	+3.40	1.03	F5-I	-3.96	3.89	1.27
F3-R	-4.67	+2.95	0.41	F5-R	-4.16	3.49	0.94

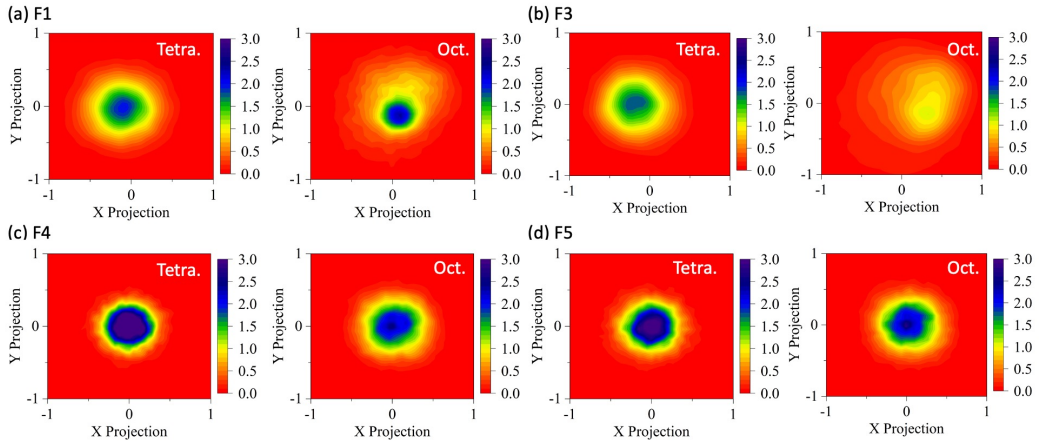


Figure S3.9: KDE for magnetic moments distribution in XY plane for all samples – (a) F1, (b) F3, (c) F4 and (d) F5 with inverse model assuming that a +2 valence state for all A cations in the AFe_2O_4 compositional series, and a +3 valence state for the remaining two Fe cations. "Tetra." denotes tetrahedral site, "Octa." denotes octahedral site.

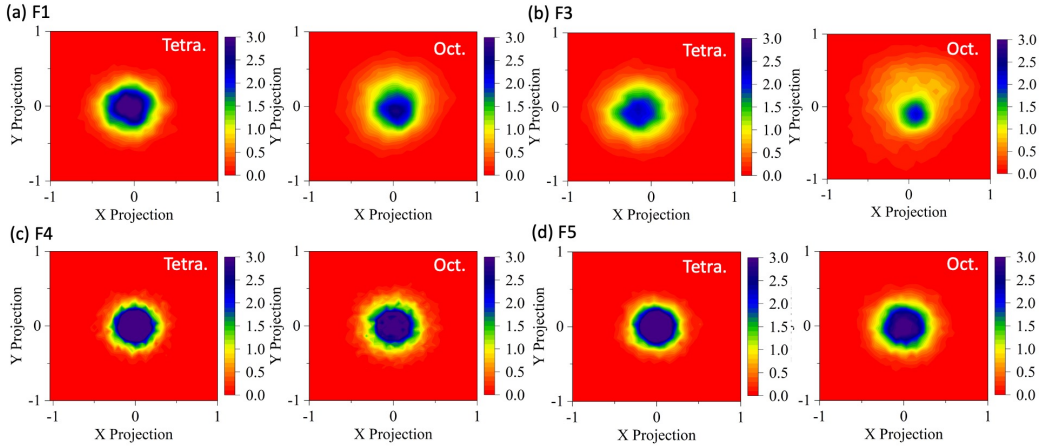


Figure S3.10: KDE for magnetic moments distribution in XY plane for all samples – (a) F1, (b) F3, (c) F4 and (d) F5 with random model assuming that a +2 valence state for all A cations in the AFe_2O_4 compositional series, and a +3 valence state for the remaining two Fe cations. "Tetra." denotes tetrahedral site, "Octa." denotes octahedral site.

C Supplemental Information for Chapter 4

Table S4.1: Compositions $(n\mathrm{A}_{1/n})\mathrm{Co}_2\mathrm{O}_4$ with n from 1 to 4 explored within this work. Samples are observed after calcination (as-formed 400 °C, AF4) and following post-annealing heat treatment (post-treatment 600 °C, PT6, etc.). Check marks indicate the presence of a specific element in that composition. Conditions resulting in X-ray pure phases are colored green and conditions resulting in phase mixtures are colored purple. Impurities are coded: ZnO ("z"); CuO ("c"); Co ("Co"); rock salt ("r"); secondary spinel ("s"); and $\mathrm{CoCl_2{\cdot}2H_2O}$ ("h").

Name	n	Mg	Cr	Mn	Fe	Co	Ni	Cu	Zn	AF4	PT6	PT8	PT10
1C1	1								✓	z+r	z	z	z
2C1	2	✓							✓	r	r	r	r
2C2	2							✓	✓	z+c	c	c	c
2C3	2						✓		✓	r	r	r	r
2C4	2				✓				✓	s	s	s	s
2C5	2			✓					✓	co+h	s		s
4C1	4	✓		✓	✓				✓	h		r	r+s
4C2	4			✓	✓		✓		✓	h			r+s

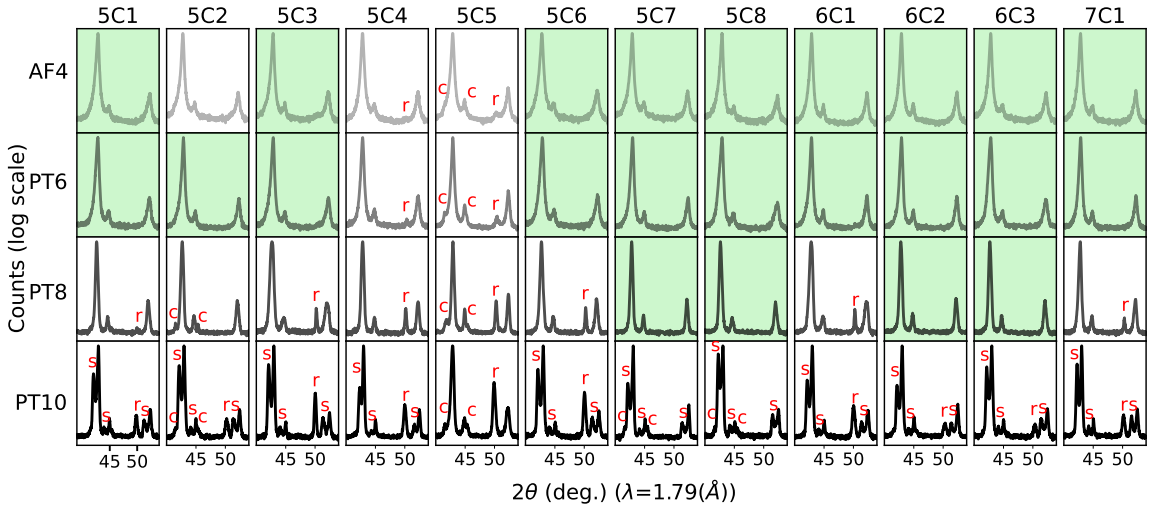


Figure S4.1: XRD patterns measured with a Co X-ray source and shown at logarithmic scale for spinel samples, 5C1, 5C2, 5C3, 5C4, 5C5, 5C6, 5C7, 5C8, 6C1, 6C2, 6C3, and 7C1 after different heat treatments (AF4, PT6, PT8, and PT10). Panels containing X-ray pure phases are colored green. Detected impurity phases are coded: CuO ("c"); rock salt ("r"); secondary spinel ("s"); and $CoCl_2{\cdot}2H_2O$ ("h").

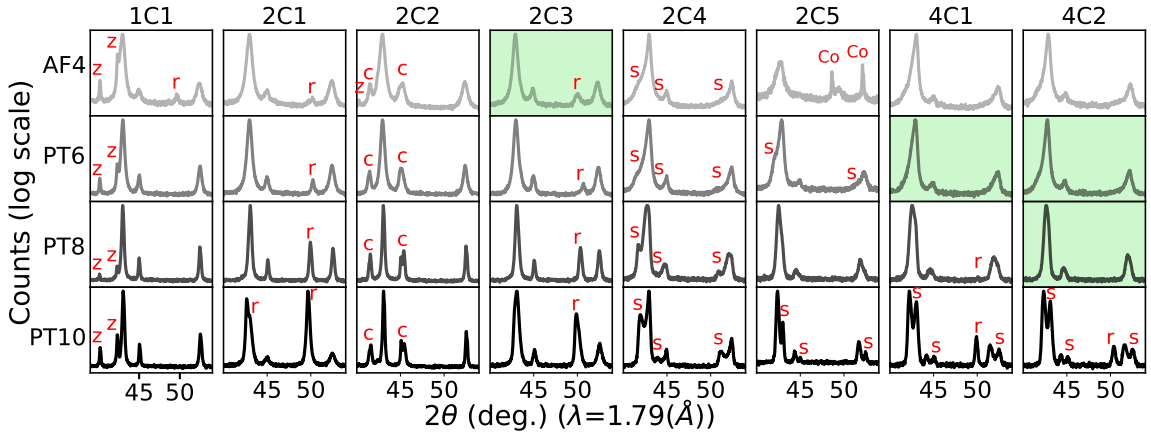


Figure S4.2: XRD patterns measured with a Co X-ray source and shown at logarithmic scale for spinel samples, 1C1, 2C1, 2C2, 2C3, 2C4, 2C5, 4C1 and 4C2 after different heat treatments (AF4, PT6, PT8, and PT10). Panels containing X-ray pure phases are colored green. Detected impurity phases are coded: ZnO ("z"); CuO ("c"); rock salt ("r"); secondary spinel ("s"); and Co ("Co").

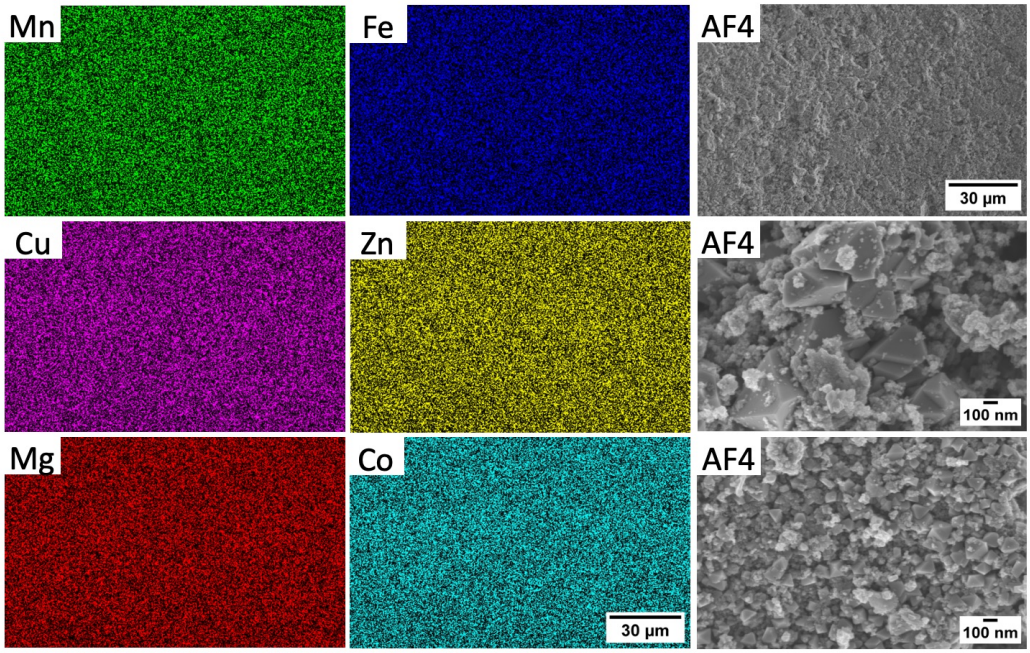


Figure S4.3: First Two Columns: SEM/EDS maps of each cation in sample 5C1 AF4, corresponding to the SEM image in the top right panel. Sample 5C1 AF4 is compositionally homogeneous on the microscale. Last Column: SEM images of sample 5C1 AF4 shown at two different magnifications and in several regions. The sample's morphology is heterogeneous at the nanoscale.

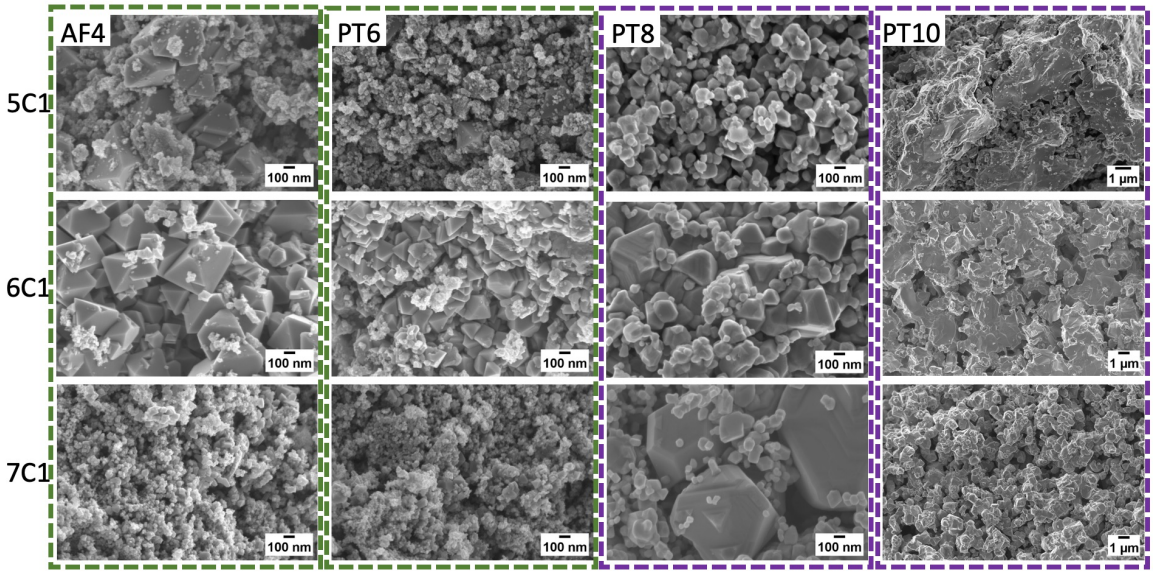


Figure S4.4: SEM images of samples 5C1 , 6C1, and 7C1 prepared AF4, PT6, PT8, PT10. Conditions resulting in X-ray pure phases are highlighted by green rectangles and conditions resulting in phase mixtures are highlighted by purple rectangles.

D Supplemental Information for Chapter 5

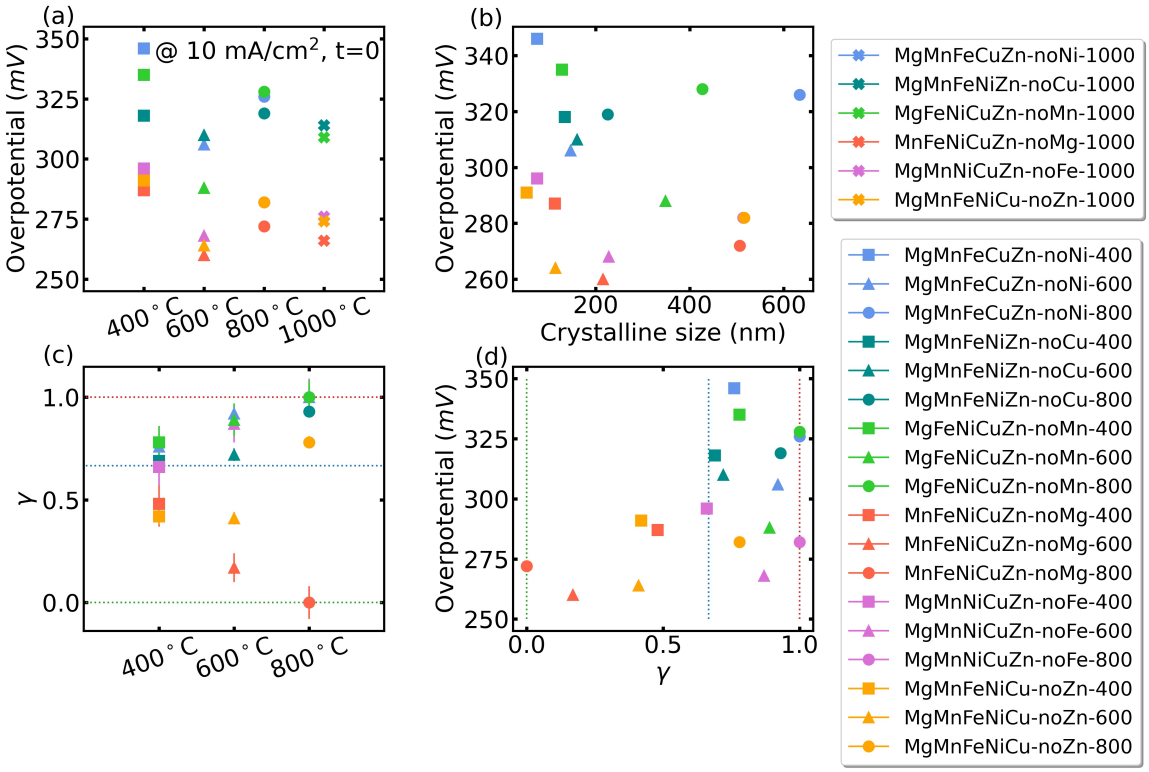


Figure S5.1: Correlations between (a) OER overpotential (mV) at 10 mA cm^{-2} and heat treatment temperature; (b) OER overpotential (mV) at 10 mA cm^{-2} and crystalline size (nm), (c) cation site inversion (γ) and heat treatment temperature, and (d) OER overpotential (mV) at 10 mA cm^{-2} and cation site inversion for MgMnFeCuZn-noNi (light blue symbols), MgMnFeNiZn-noCu (teal symbols), MgFeNiCuZn-noMn (green symbols), MnFeNiCuZn-noMg (orange symbols), MgMnNiCuZn-noFe (pink symbols), and MgMnFeNiCu-noZn series (yellow symbols). In the plots, solid squares denote 400°C annealed samples, solid triangles indicate 600°C annealed samples, solid circles represent 800°C annealed samples, and 'x's denote 1000°C annealed samples.

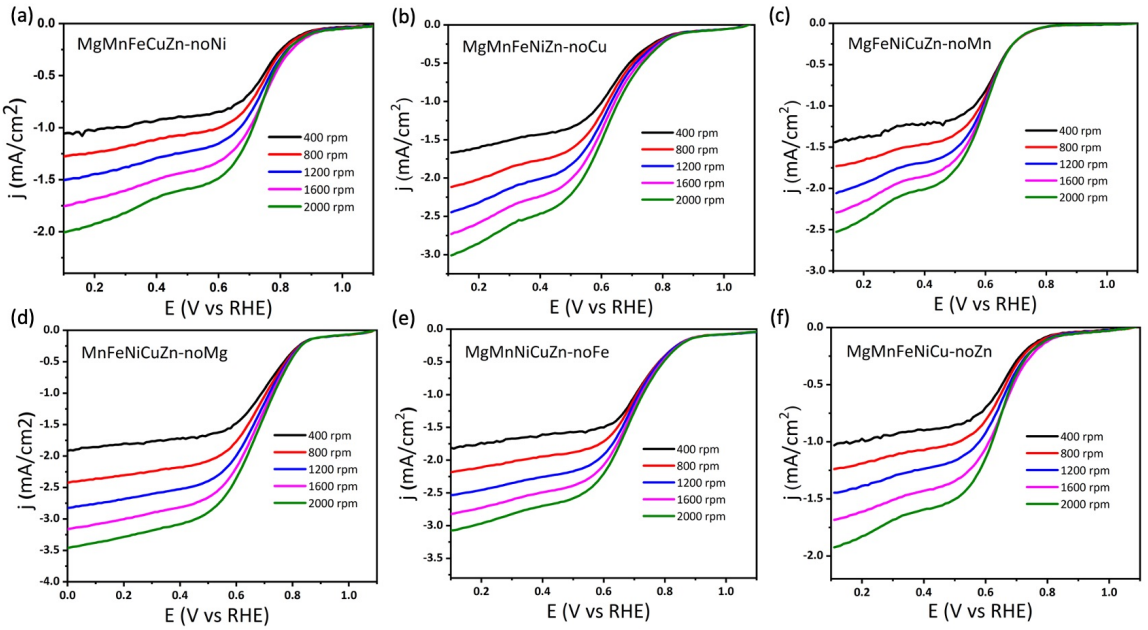


Figure S5.2: Linear sweep voltammograms of the MgMnFeCuZn-noNi, MgMnFeNiZn-noCu, MgFeNiCuZn-noMn, MnFeNiCuZn-noMg, MgMnNiCuZn-noFe, and MgMnFeNiCu-noZn 600 °C series of samples collected using the RDE set-up at rotating speeds of 400 rpm (black line), 800 rpm (red line), 1200 rpm (blue line), 1600 rpm (pink line), and 2000 rpm (green line).

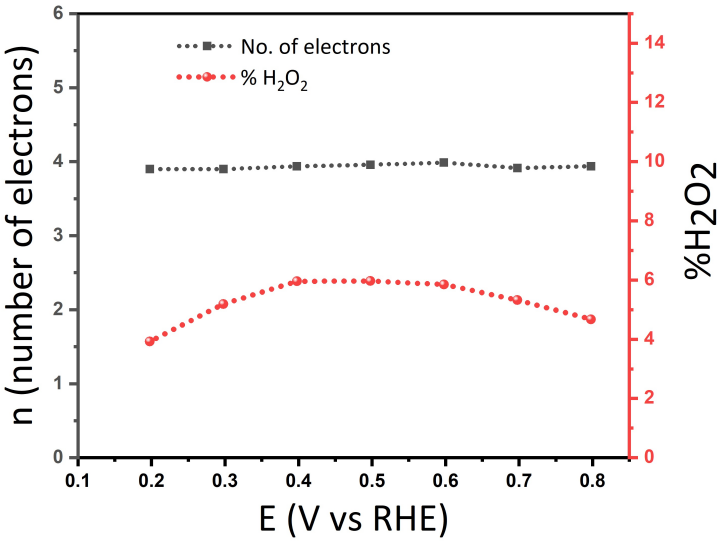


Figure S5.3: Plot of the H_2O_2 yields (red circle symbols) and electron-transfer numbers (black square symbols) for the MnFeNiCuZn-noMg-600 °C sample.

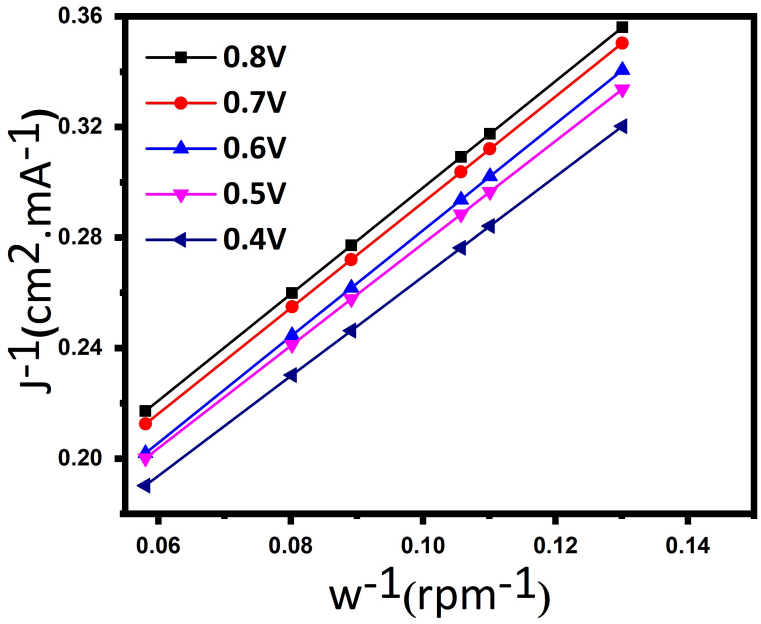


Figure S5.4: The Koutechy-Levich (K-L) plots at different electrode potentials for the MnFeNiCuZn-noMg-600 °C sample.

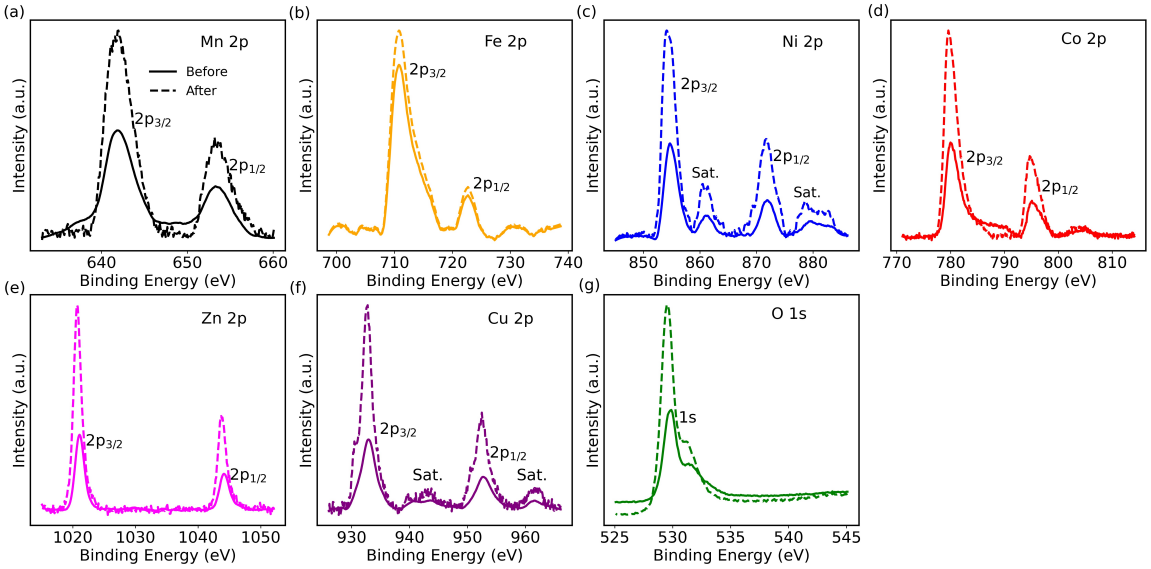


Figure S5.5: The before and after OER XPS spectra for (a) Mn 2p, (b) Fe 2p, (c) Ni 2p, (d) Co 2p, (e) Zn 2p, (f) Cu 2p, and (g) O 1s for the MnFeNiCuZn-noMg-600 °C sample electrode.

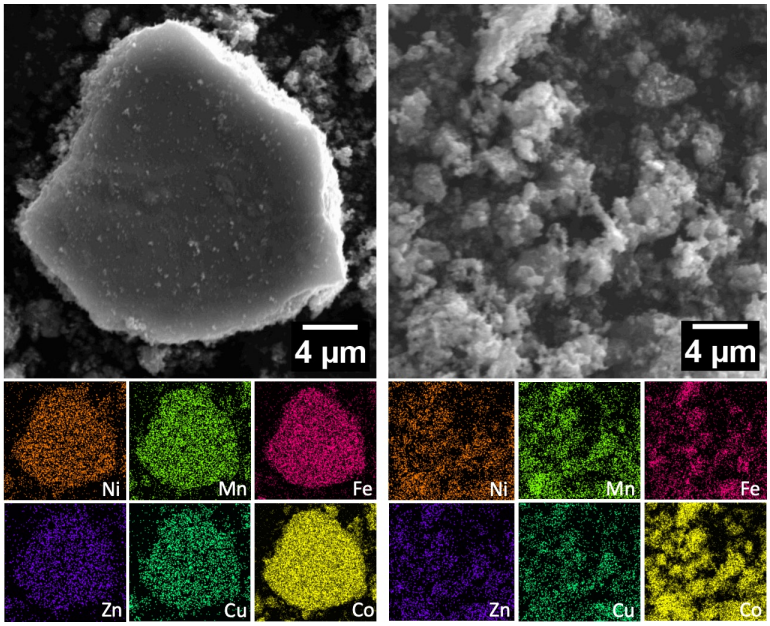


Figure S5.6: SEM/EDS maps of a micron sized particle (left) and collections of nanoparticles (right) for the sample MnFeNiCuZn-noMg-400 °C. Each cation type appears to be present and homogeneously distributed across the distinct particle morphologies.

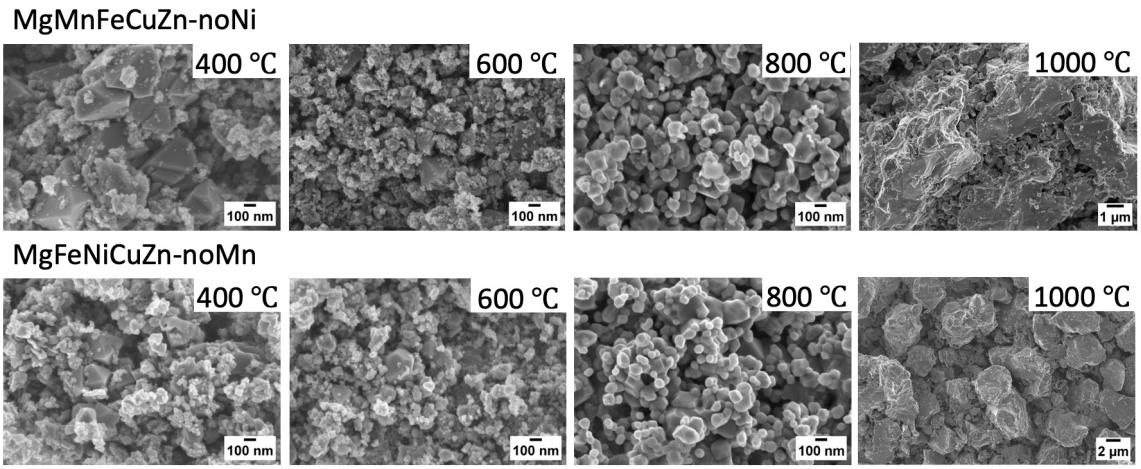


Figure S5.7: High resolution SEM images of samples MgMnFeCuZn-noNi (top row) and MgFeNiCuZn-noMn (bottom row) subjected to different heat treatment temperatures (increasing from left to right). Note the difference in scale bar (lower magnification) for the 1000°C sample images at the far right.

Table S5.1: The information of substrate and drop-casted mass (mass loading, ML) of OER and ORR catalytic measurements for the reference cited in Figure 1. The substrates are coded: carbon cloth ("CC"); glassy carbon ("GC"); nickel foam ("NF");pyrolytic graphite carbon ("PGC"); carbon fiber paper ("CFP").

Sample	OER	OER	ORR	ORR
	Substrate	ML ($mg\ cm^{-2}$)	Substrate	ML ($mg\ cm^{-2}$)
Co_3O_4/N-rmGO[125]	GC	0.2	GC	0.1
cCo_3O_4/MWCNT[130]	GC	0.41	GC	0.41
Co_3O_4@BDHC2[285]	GC	0.28	GC	0.28
Co_3O_4/N-doped VC[9]	GC	0.25	GC	0.25
Co_3O_4@C-MWCNTs[122]	GC	0.325	GC	0.325
Co_3O_4/CN[128]	GC	0.128	GC	0.128
Co@Co_3O_4/NC[4]	GC	0.21	GC	0.21
Co_3O_4/CNT-PC[43]	NF	1	GC	0.15
Co_3O_4/NPGC[117]	GC	0.2	GC	0.2
Co_3O_4/MnO_2-CNTs[274]	GC	0.1	GC	0.1
Co_3O_4-$MnCo_2O_4$/N-rGO[76]	GC	0.12	GC	0.12
$FeCo_2O_4$[280]	GC	1.006	GC	1.006
$MnCo_2O_4$[151]	GC	0.051	GC	/
$MnCo_2O_4$[24]	GC	0.4	GC	0.4
$MnCo_2O_4$,NCNT-500[300]	GC	0.21	GC	0.21
$MnCo_2O_4$-NCF[270]	GC	0.1	GC	0.1
$MnCo_2O_4$/N-rGO[60]	GC	0.1	GC	0.1
$MnCo_2O_4$-700[23]	GC	0.4	GC	0.4
$MnCo_2O_4$[136]	GC	/	GC	/
$NiCo_2O_4$[89]	GC	/	GC	/
$NiCo_2O_4$[111]	GC	0.4	GC	0.4
$NiCo_2O_4$[239]	GC	/	GC	/

Table S5.1 Continued

$ZnCo_2O_4$/N-CNT[131]	GC	0.2	GC	0.2
$MnCo_2O_4$/N-CNT[60]	GC	0.1	GC	0.1
$NiCo_2O_4$[41]	GC	/	GC	/
$ZnCo_2O_4$[26]	GC	0.15	GC	0.15
$ZnCo_2O_4$[26]	GC	0.15	GC	0.15
$CoCo_2O_4$[40]	GC	0.12	GC	0.25
$CoCo_2O_4$-$NaBH_4$[40]	GC	0.12	GC	0.25
$NiCo_2O_4$[40]	GC	0.12	GC	0.25
$NiCo_2O_4$-$NaBH_4$[40]	GC	0.12	GC	0.25
$ZnCo_2O_4$[40]	GC	0.12	GC	0.25
$ZnCo_2O_4$-$NaBH_4$[40]	GC	0.12	GC	0.25
$NiCo_2O_4$-air[129]	GC	0.28	GC	0.28
AlNiCoFeCrMoV[283]	GC	/	GC	/
$CuCo_2O_4$-SSM[201]	GC	0.2	GC	0.2
$NiCo_2O_4$[14]	GC	0.0485	GC	0.0485
$MnCo_2O_4$[242]	GC	/	GC	/
$FeCo_2O_4$[299]	GC	/	GC	/
N-$CuCo_2O_4$@CNFs[293]	GC	/	GC	/
$CuCo_2O_4$@C tube[244]	GC	0.28	GC	0.1
$MnCo_2O_4$/NCNTs[250]	GC	0.2	GC	0.2
$CoCo_2O_4$/NCNTs[250]	GC	0.2	GC	0.2
$NiCo_2O_4$/NCNTs[250]	GC	0.2	GC	0.2
$CuCo_2O_4$/NCNTs[250]	GC	0.2	GC	0.2
$ZnCo_2O_4$/NCNTs[250]	GC	0.2	GC	0.2
Co_3O_4/CNTs[3]	GC	0.153	GC	0.153
$FeCo_2O_4$/HrGOs[280]	GC	1.006	GC	1.006
5% Ni-Co_3O_4[212]	PGC	0.408	PGC	0.408

				Table S5.1 Continued
Ce-$CoMn_2O_4$-18%[31]	CFP	0.56	GC	0.051

Table S5.2: The C_{DL} comparison for the 600 °C sample series.

Sample	C_{DL}
MnFeNiCuZn-noMg	1.472
MgMnFeNiCu-noZn	1.336
MgMnNiCuZn-noFe	1.164
MgFeNiCuZn-noMn	0.951
MgMnFeCuZn-noNi	0.688
MgMnFeNiZn-noCu	0.488

Table S5.3: The R_{wp}, median of the lattice parameter (a_m, Å), crystallite size (CS), cation site inversion parameter (γ), and atomic positions of oxygen ($x = y = z = u$) of the Rietveld refinement with "continuous lattice" model[245] for the 600 °C sample series. The isotropic atomic displacement parameters of the tetrahedral site ($U_{iso,t}$, Å^2), octahedral site ($U_{iso,o}$, Å^2) and oxygen ($U_{iso,O}$, Å^2) were fixed as 0.005, 0.005, and 0.010 Å^2, respectively, for all compositions.

Name	R_{wp}	a_m (Å)	CS	γ	u
MgMnFeCuZn-noNi	2.11	8.1374	146.72(24.58)	0.92(0.04)	0.2397(0.0004)
MgMnFeNiZn-noCu	1.96	8.1307	158.04(23.35)	0.72(0.03)	0.2398(0.0003)
MgFeNiCuZn-noMn	3.67	8.1143	380.77(86.58)	0.90(0.08)	0.2388(0.0004)
MnFeNiCuZn-noMg	2.03	8.1283	215.57(34.55)	0.17(0.07)	0.2396(0.0003)
MgMnNiCuZn-noFe	2.48	8.1270	227.75(56.48)	0.87(0.09)	0.2398(0.0004)
MgMnFeNiCu-noZn	1.97	8.1294	114.09(14.10)	0.40(0.03)	0.2400(0.0003)

E Supplemental Information for Chapter 6

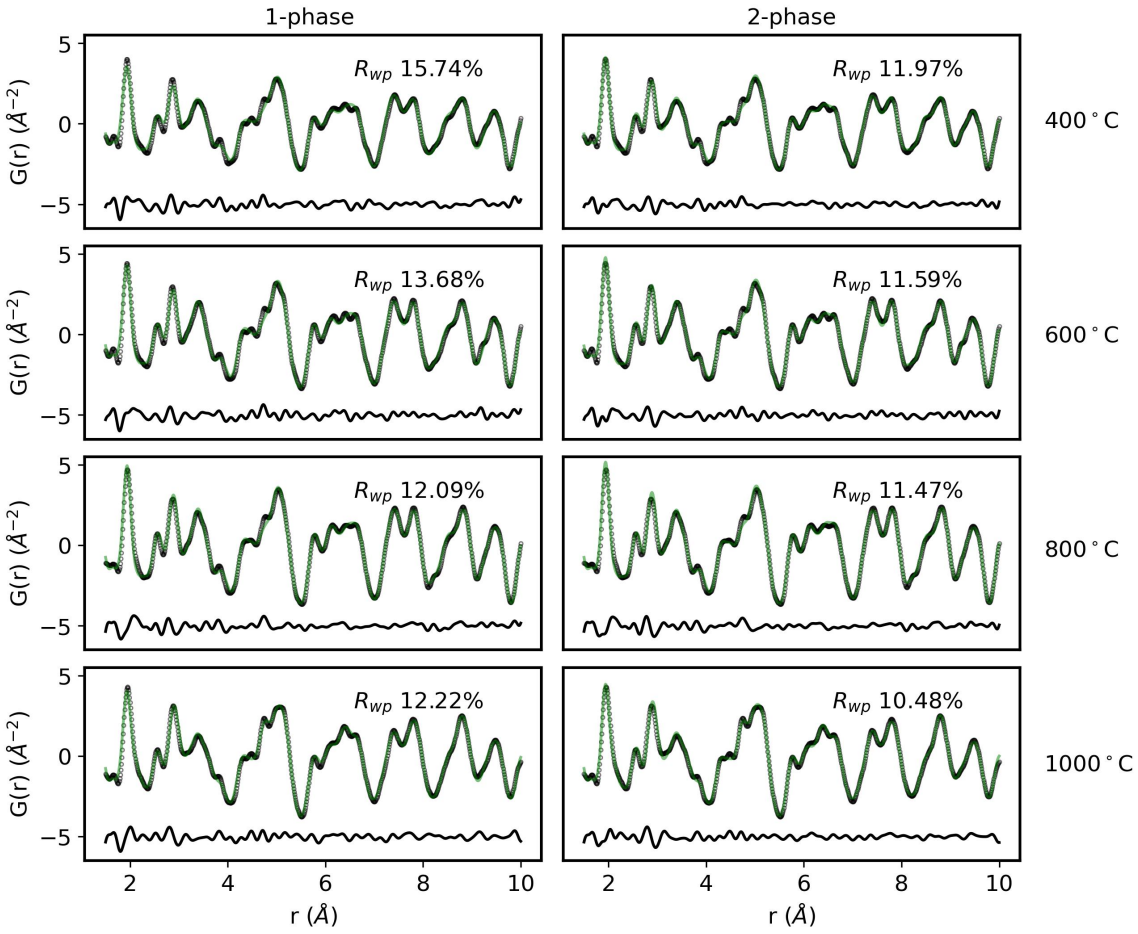


Figure S6.1: Comparison of refinement results for the 10 Å PDF data range for samples that were calcined at 400°C, post-annealed at 600°C, 800°C, and 1000°C, with a single spinel model (1-phase) on the left and a two component spinel model (2-phase) on the right. Goodness of fit factors are displayed in each panel.

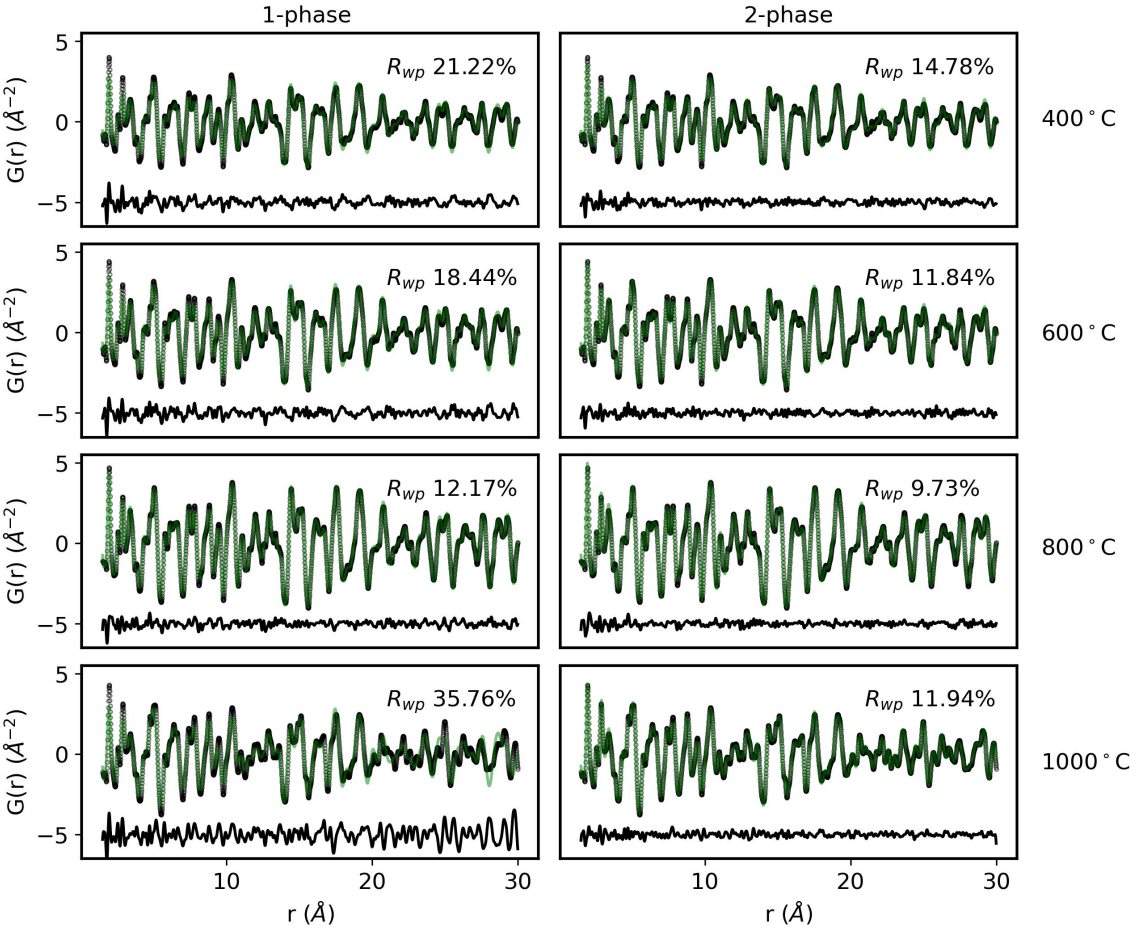


Figure S6.2: Comparison of refinement results for the 30 Å PDF data range for samples that were calcined at 400°C, post-annealed at 600°C, 800°C, and 1000°C, with a single spinel model (1-phase) on the left and a two component spinel model (2-phase) on the right. Goodness of fit factors are displayed in each panel.

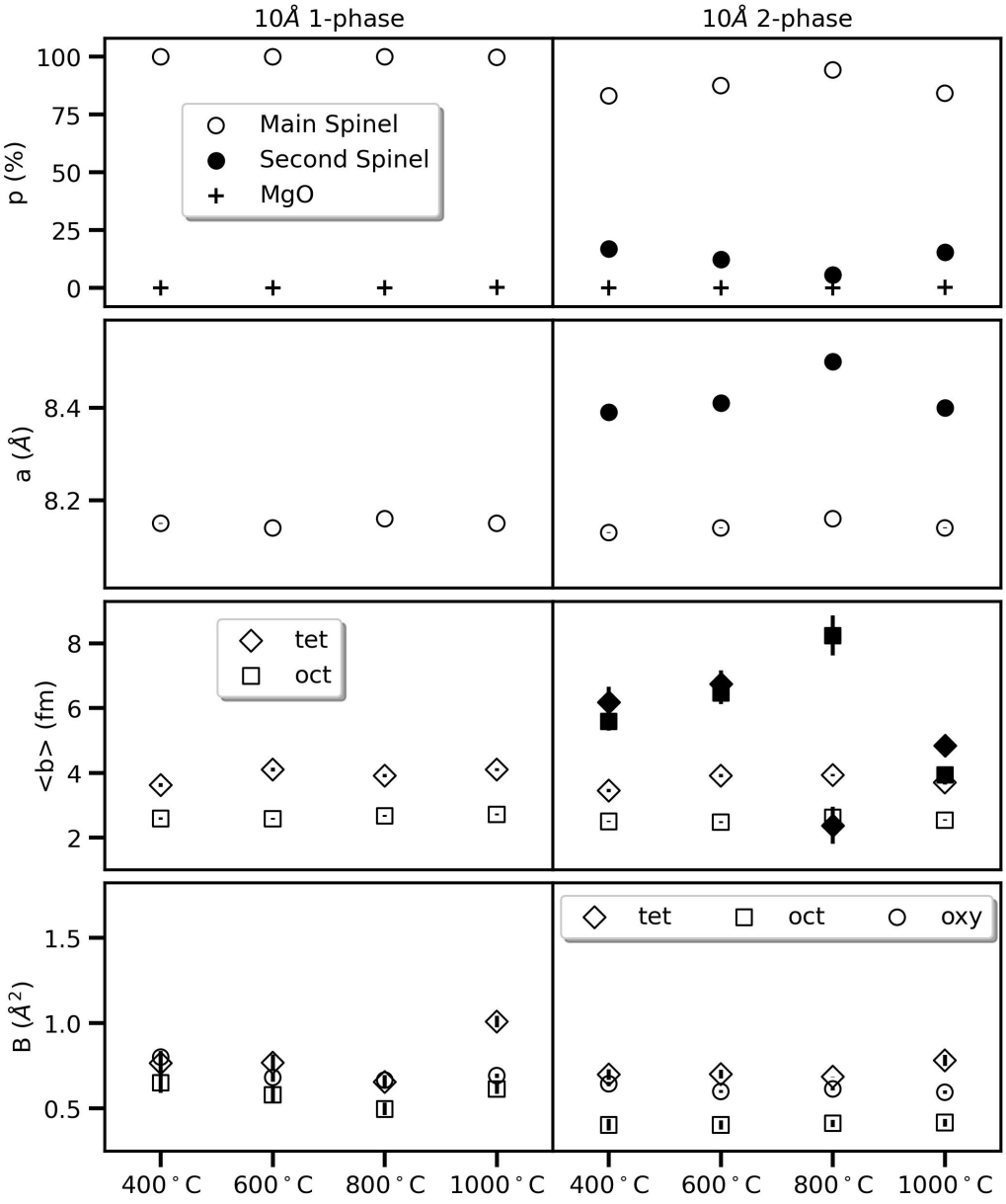


Figure S6.3: For the samples that were calcined at 400°C, post-annealed at 600°C, 800°C, and 1000°C– comparison of phase percentage (p, %), lattice parameter (a, Å), average scattering length ($\langle b \rangle$, fm), and the atomic displacement parameters (B, Å^2) of tetrahedral cation, octahedral cation, and oxygen sites extracted from refinement with 10 Å PDF data range with one-spinel phase (1-phase) model (left column) and two-spinel phase (2-phase) model (right column), respectively.

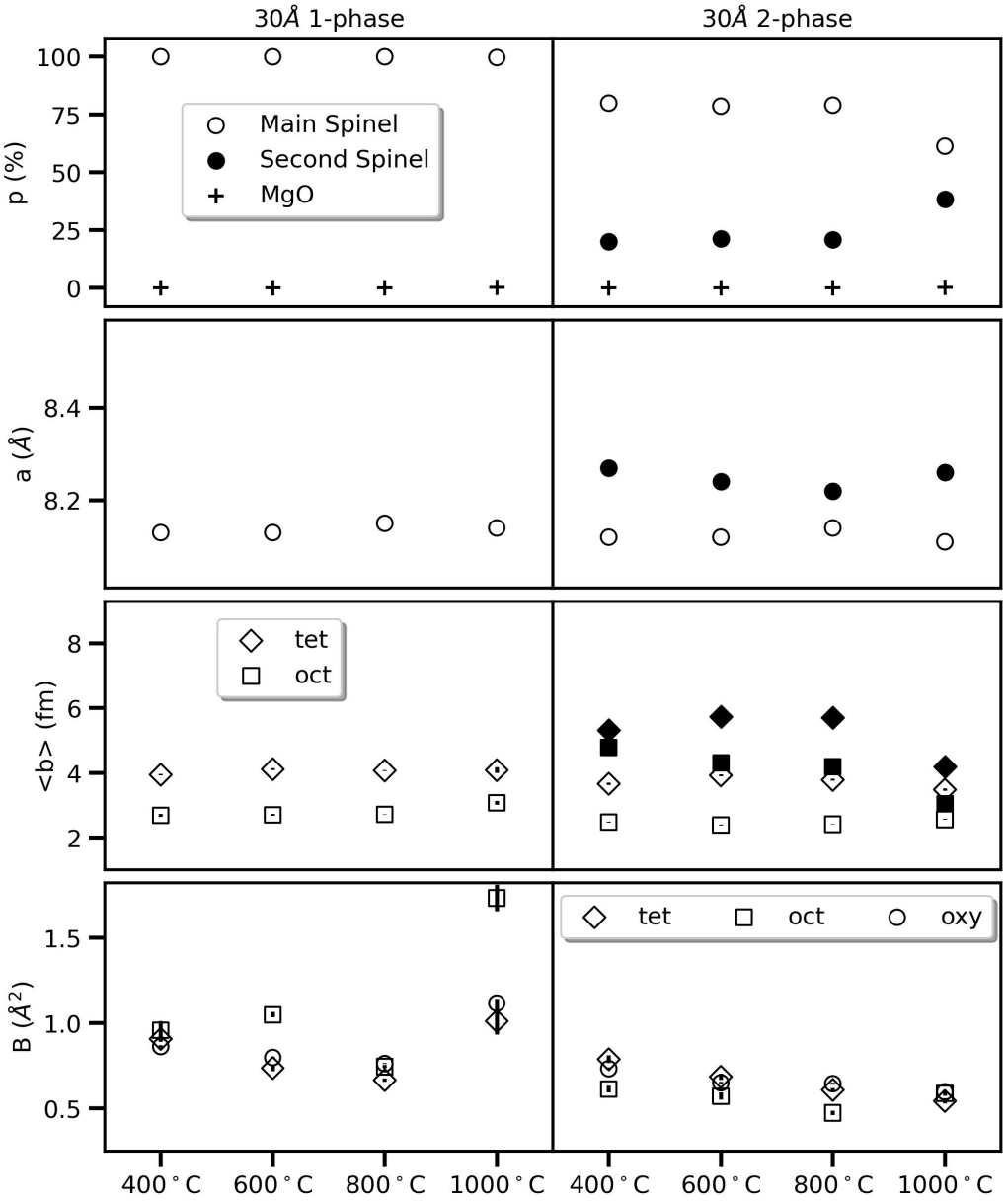


Figure S6.4: For the samples that were calcined at 400°C, and post-annealed at 600°C, 800°C, and 1000°C– the comparison of phase percentage (p, %), lattice parameter (a, Å), average scattering length ($\langle b \rangle$, fm), and the atomic displacement parameters (B, Å^2) of tetrahedral cation, octahedral cation, and oxygen sites extracted from refinement with 30 Å PDF data range with one-spinel phase (1-phase) model (left column) and two-spinel phase (2-phase) model (right column), respectively.

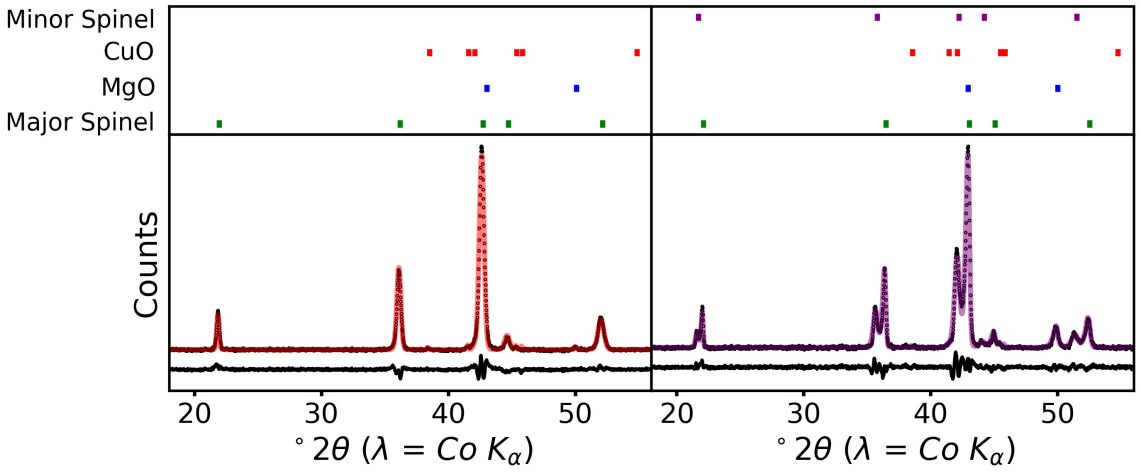


Figure S6.5: Rietveld refinement fits to data for the sample annealed at 800°C indicates a major spinel phase along with the presence of impurities: tenorite (CuO) and rocksalt (MgO). The refinement of the sample annealed at 1000°C indicates the same impurities, along with the emergence of a second (minor) spinel phase.

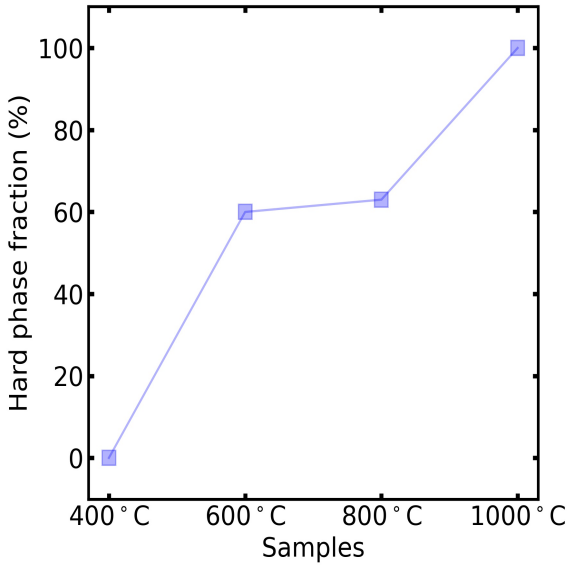


Figure S6.6: The magnetic hard phase fraction obtained from 5 K FORC measurements for all four samples, assuming the sample calcined at 400°C as predominantly soft phase, and the 1000°C annealed sample as hard phase.

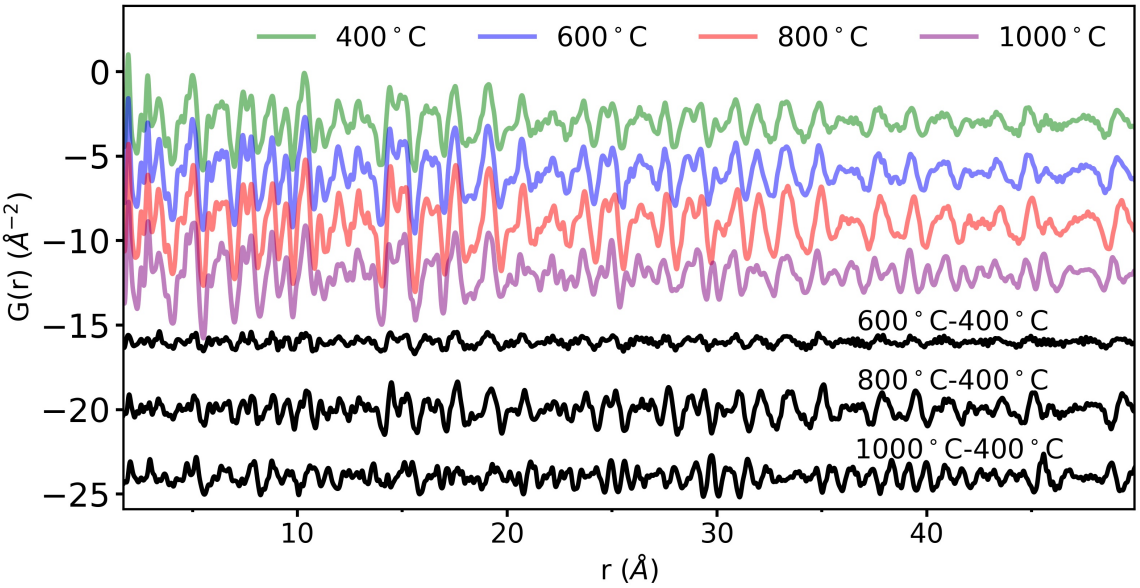


Figure S6.7: PDF data comparison over 1-50 Å for the samples that were calcined at 400°C, and post-annealed at 600°C, 800°C, and 1000°C.

Table S6.1: Rietveld and PDF refinement parameters for the best fitting model results applied for the sample calcined at 400°C and the samples post-annealed at 600°C, 800°C, and 1000°C. The table includes the average scattering length for each site ($\langle b \rangle$), lattice parameter (a), phase percentage (p), oxygen position (u), isotropic atomic displacement parameters (B_{iso}) for the tetrahedral (8b), octahedral (16c), and oxygen (32e) sites, and the resulting refinement goodness-of-fit, R_{wp}. For the Rietveld refinement, the crystalline size (CZ), sample microstrain (MS), and refined magnetic moment (M) are also summarized.

Sample	400°C	600°C	800°C	1000°C
Rietveld Refinement				
$\langle b \rangle_{8b,Zn}$	3.53(23)	3.85(22)	3.96(9)	3.62(19)
$\langle b \rangle_{16c,Fe}$	2.48(11)	2.44(11)	2.62(5)	2.58(9)
a_{Nuc} (Å)	8.05(1)	8.08(001)	8.10(0)	8.07(0)
a_{MgO} (Å)	/	/	4.21(0)	4.23(0)
a_{CuO} (Å)	/	/	3.85(2)	3.18(2)
b_{CuO} (Å)	/	/	3.27(2)	3.01(2)
c_{CuO} (Å)	/	/	3.91(2)	4.32(3)

Table S6.1 Continued

a_{Second} (Å)	/	/	/	8.22(0)
p_{Nuc} (%)	100	100	98	57.24
p_{MgO} (%)	0	0	1.2	7.43
p_{CuO} (%)	0	0	0.8	0.80
p_{Second} (%)	0	0	0	34.54
u (frac.)	0.2371(2)	0.2369(0000)	0.2368(0000)	0.2366(0000)
$B_{iso,8b}$ (Å^2)	0.2744(2755)	0.2698(2523)	0.3223(1249)	0.3348(2471)
$B_{iso,16c}$ (Å^2)	0.1941(2561)	0.2535(2636)	0.2178(1218)	0.1679(2065)
$B_{iso,32e}$ (Å^2)	0.4393(1728)	0.4416(1679)	0.4272(772)	0.3655(1178)
M(μ_B)	0.53	0.28	/	/
CZ (nm)	237(35)	588(197)	948(232)	microscale
MS	0.004(12)	0.009(11)	0.009(5)	0.006(6)
R_{wp} (%)	4.94	6.58	4.07	6.51
PDF Refinement				
$\langle b \rangle_{Nuc,8b,Zn}$	3.45(48)	3.91(53)	3.93(40)	3.70(60)
$\langle b \rangle_{Nuc,16c,Fe}$	2.50(27)	2.48(27)	2.62(32)	2.54(25)
$\langle b \rangle_{Second,8b,Zn}$	6.18(476)	6.75(411)	2.38(567)	4.84(301)
$\langle b \rangle_{Second,16c,Fe}$	5.59(286)	6.47(349)	8.24(623)	3.93(230)
a_{Nuc} (Å)	8.13(1)	8.14(1)	8.16(0)	8.14(1)
a_{Second} (Å)	8.39(9)	8.41(13)	8.50(13)	8.40(12)
p_{Nuc} (%)	83.11	87.54	94.31	84.23
p_{Second} (%)	16.89	12.46	5.69	15.59
$B_{iso,Nuc,8b}$ (Å^2)	0.6992(3116)	0.7011(2611)	0.6863(173)	0.7818(3306)
$B_{iso,Nuc,16c}$ (Å^2)	0.4042(3372)	0.4037(2780)	0.4129(2090)	0.4180(2256)
$B_{iso,Nuc,32e}$ (Å^2)	0.6448(1255)	0.5999(869)	0.6147(918)	0.5952(985)
R_{wp} (%)	11.97	11.59	11.47	10.48

Vita

Originally from China, Xin Wang grew up in Dalian, China. She received her Bachelor's degree in Materials Physics from Chongqing Jiaotong University in 2014 with the award of "Excellent Graduate in Chongqing" and was recommended for postgraduate study based on her excellent academic record. Xin received her Master's degree in Materials Engineering in 2017 with the thesis topic, "Preparation and strain sensing study on graphene/epoxy resin nanoelectrically conductive coating." During the final year of her Master's program, she had the opportunity to serve as a volunteer Chinese teacher in Benin, Africa, teaching both children and undergraduate students for ten months. She came to the University of Tennessee, Knoxville, in 2019 to pursue a Doctor of Philosophy degree in Materials Science and Engineering. Her research focuses on exploring new functional materials, both bulk and nano, specializing in average/local structure-physicochemical property characterization with neutrons and X-rays.

List of Publications

[1] **Xin Wang**, Cameron Sparks Jorgensen, Corisa Kons, Yuanpeng Zhang, Jue Liu, Peter C. Metz, Eleanora Cali, Dustin Allen Gilbert, and Katharine Page. "Impact of thermal annealing on magnetic properties in nano compositionally complex spinel cobaltite - $(Mg_{0.2}Mn_{0.2}Fe_{0.2}Cu_{0.2}Zn_{0.2})Co_2O_4$", under preparation

[2] **Xin Wang**, Harish Singh, Manashi Nath, Kurt Lagemann and Katharine Page. "Excellent bifunctional oxygen evolution and reduction electrocatalysts $(5A_{1/5})Co_2O_4$ and their tunability", *ACS Materials Au* (2024) DOI: 10.1021/acsmaterialsau.3c00088

[3] **Xin Wang**, Peter C. Metz, Eleonora Calì, Palani Raja Jothi, Eric A. Lass, and Katharine Page. "Phase selectivity and stability in compositionally complex ACo_2O_4" *Chemistry of Materials* 35, no. 17 (2023): 7283-7291. DOI: 10.1021/acs.chemmater.3c01647

[4] Bo Jiang, Krishna Chaitanya Pitike, De-Ye Lin, Stephen C. Purdy, **Xin Wang**, Yafan Zhao, Yuanpeng Zhang, et al. "Local cation ordering in compositionally complex Ruddlesden–Popper n= 1 oxides" *APL Materials* 11, no. 5 (2023). DOI: 10.1063/5.0144766

[5] **Xin Wang**, Brianna L. Musicó, Corisa Kons, Peter C. Metz, Veerle Keppens, Dustin A. Gilbert, Yuanpeng Zhang, and Katharine Page. "Local cation order and ferrimagnetism in compositionally complex spinel ferrites" *APL Materials* 10, no. 12 (2022): 121102. DOI: 10.1063/5.0123728

[6] Spurling, R. Jackson, Eric A. Lass, **Xin Wang**, and Katharine Page. "Entropy-driven phase transitions in complex ceramic oxides" *Physical Review Materials* 6, no. 9 (2022): 090301. DOI:10.1103/PhysRevMaterials.6.090301

[7] Bo Jiang, De-Ye Lin, **Xin Wang**, Sverre M. Selbach, and Katharine Page. "Special quasirandom structures description of the local structure of disordered $Bi_{0.5}K_{0.5}TiO_3$" *Journal of Applied Physics* 132, no. 22 (2022): 224101. DOI:10.1063/5.0123468

[8] **Xin Wang**, Bo Jiang, Yuanpeng Zhang, Young-Il Kim, and Katharine Page. "Influence of cation size on the local atomic structure and electronic properties of

Ta perovskite oxynitrides" *Inorganic Chemistry* 60.18 (2021): 14190-14201. DOI: 10.1021/acs.inorgchem.1c01594